Max-Planck-Institut
für Meteorologie

MAX-PLANCK-GESELLSCHAFT

Physical validation and bracket-based dynamical cores for mesoscale NWP models

Ronny Petrik

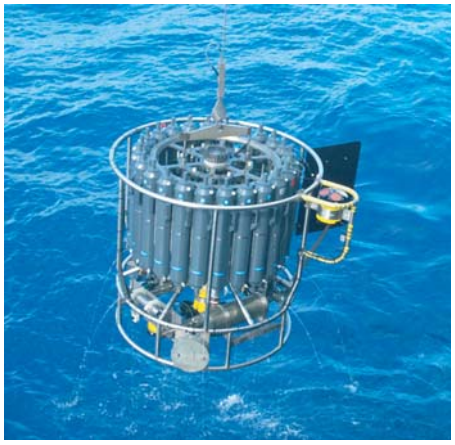

Berichte zur Erdsystemforschung 121/2012

Reports on Earth System Science

Hinweis

Die Berichte zur Erdsystemforschung werden vom Max-Planck-Institut für Meteorologie in Hamburg in unregelmäßiger Abfolge herausgegeben.

Sie enthalten wissenschaftliche und technische Beiträge, inklusive Dissertationen.

Die Beiträge geben nicht notwendigerweise die Auffassung des Instituts wieder.

Die "Berichte zur Erdsystemforschung" führen die vorherigen Reihen "Reports" und "Examensarbeiten" weiter.

Notice

The Reports on Earth System Science are published by the Max Planck Institute for Meteorology in Hamburg. They appear in irregular intervals.

They contain scientific and technical contributions, including Ph. D. theses.

The Reports do not necessarily reflect the opinion of the Institute.

The "Reports on Earth System Science" continue the former "Reports" and "Examensarbeiten" of the Max Planck Institute.

Anschrift / Address

Max-Planck-Institut für Meteorologie
Bundesstrasse 53
20146 Hamburg
Deutschland

Tel.: +49-(0)40-4 11 73-0
Fax: +49-(0)40-4 11 73-298
Web: www.mpimet.mpg.de

Layout:

Bettina Diallo, PR & Grafik

Titelfotos:
vorne:
Christian Klepp - Jochem Marotzke - Christian Klepp
hinten:
Clotilde Dubois - Christian Klepp - Katsumasa Tanaka

Berichte zur Erdsystemforschung 121/2012

Physical validation and bracket-based dynamical cores for mesoscale NWP models

Ronny Petrik

aus Cottbus, Deutschland

Hamburg 2012

Reports on Earth System Science 121/2012

ISSN 1614-1199

Ronny Petrik
Max-Planck-Institut für Meteorologie
Bundesstrasse 53
20146 Hamburg

Als Dissertation angenommen
vom Department Geowissenschaften der Universität Hamburg

auf Grund der Gutachten von
Prof. Dr. K. Heinke Schlünzen
und
Dr. Almut Gassmann

Hamburg, den 13. Januar 2012
Prof. Dr. Jürgen Oßenbrügge
Leiter des Departments für Geowissenschaften

ISSN 1614-1199

Physical validation and bracket-based dynamical cores for mesoscale NWP models

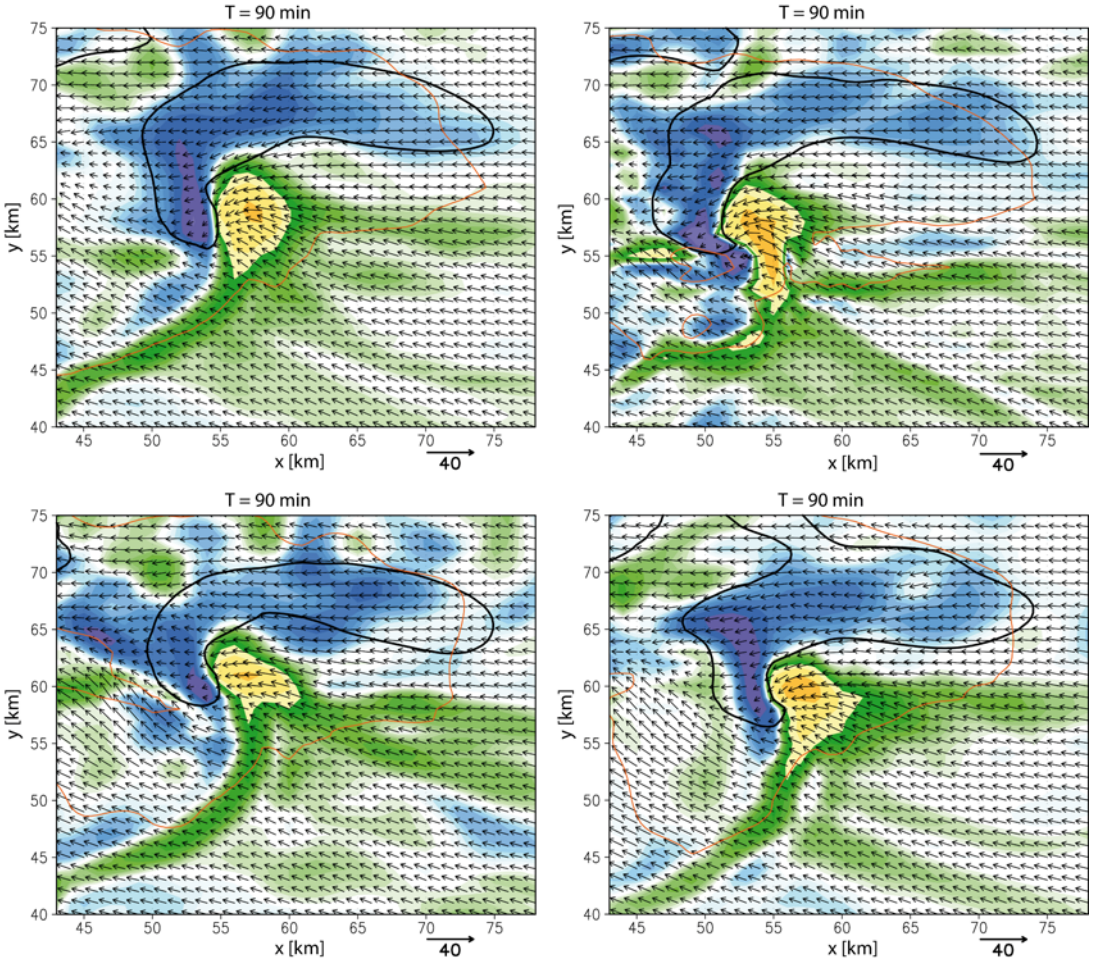

Ronny Petrik

Hamburg 2012

Abstract

In this thesis idealized tests and realistic weather forecasts are used to study the performance of state-of-the art NWP models with respect to their conservation properties and nonlinear dynamics, and to investigate discretization techniques using the Hamiltonian and the Nambu representation of the atmospheric dynamics as tools.
Using a finite volume approach, we develop a model-independent diagnostic tool in order to validate the conservation properties of NWP models with respect to a specific control volume. The control volume is placed at each site in the model domain and is independent of the grid size. Applying the diagnostic tool to the weather forecast model COSMO reveals a good preservation of the water mass, but large errors in energy and total mass conservation. It is shown to which extent errors in the treatment of thermodynamical processes, numerical filters and moisture advection schemes contaminate the sub-domain budgets in idealized model runs and realistic weather forecasts. We find that the largest budget errors arise from an insufficient treatment of diabatic processes in the saturation adjustment, the cloud-microphysical parameterization and the radiation scheme. It is demonstrated that the application of a saturation adjustment scheme under a fixed volume condition is required for models, which use the non-hydrostatic equations and height-based coordinates. Using the saturation adjustment and an extended radiation and cloud-microphysical scheme reduces budget errors in water mass, total mass and energy.
Using the Fourier analysis in terms of the Discrete Cosine Transform (DCT), the representation of nonlinear scale interactions in the NWP model COSMO is investigated. We emulate the high aperiodicity of the limited area model outputs using synthetic fields and test various spectral analysis methods. It is demonstrated that the DCT method offers the best performance in simulating mesoscale spectra following a $k^{-5/3}$-law. Making use of the DCT method, the kinetic energy spectra simulated by the COSMO model is evaluated on observed spectra, which are derived from aircraft measurements taken at the COPS field campaign in summer 2007. We find that the mean spectral variances and the slope of the model spectra averaged over ten forecast days are in good agreement with the observed spectra, but the model is not able to simulate adequately the energy cascade for individual weather events. The evaluation reveals that the model is only capable to resolve adequately the nonlinear interactions down to scales of 20 km, i. e. the effective resolution of the model is seven times the nominal resolution of $\Delta x \approx 2.8$ km. This is consistent with the investigation of the WRF model done by Skamarock (2004). We examine for a cold start configuration that the effective resolution of 20 km is provided after a spin-up time of five hours.
According to the above-mentioned diagnostics, in a further research study discretization techniques are investigated, which maybe offer better conservation properties and allow for a better representation of nonlinear scale interactions. Using the Nambu representation of the atmospheric dynamics as a tool, we construct a discretization scheme (EVT scheme) for the nonlinear term of the momentum equations. The discretization procedure produces large 3-d stencils with extensive reconstructions. We show in an idealized test case that the quality of the EVT solution equals a second order solution. The EVT scheme and, in addition, a scheme based on the Hamiltonian representation of the atmospheric dynamics (Poisson scheme) are validated in the framework of a thunderstorm simulation. We examine that the EVT scheme and the Poisson scheme

resolve the main meteorological features of the thunderstorm and are to some minor extent superior to standard second order discretization schemes. The Poisson solution provides smaller precipitation amounts and a northern drift of the storm relative to the other solutions. We find that the sophisticated EVT and Poisson scheme need the same rate of eddy viscosity as the standard second order schemes, which prefers the high-order upwind-biased advection schemes to resolve small scales.
The Nambu and the Hamiltonian discretization tools seems to be not practical yet for the application to NWP models. With the current discretization setup an measurable improvement to comparable standard discretization schemes could not be achieved. An extension of the discretization procedure to the complete momentum equations may have a positive impact on the model performance. However, the novel sub-domain budget diagnostic developed in this thesis turned out to be very useful. It qualifies the model developer to detect error sources in the model and to improve the provided physical parameterizations and the numerical discretization.

Zusammenfassung

In dieser Arbeit wird anhand von idealisierten Testfällen und realistischen Wettervorhersagen die Güte von aktuellen Wettervorhersagemodellen im Hinblick auf Erhaltungseigenschaften und nichtlinearer Dynamik untersucht. Darüber hinaus werden Diskretisierungsmethoden untersucht, welche eine hamiltonische und eine Nambubeschreibung der Atmosphärendynamik als Werkzeug benutzen.
Unter Verwendung eines finiten Volumenansatzes haben wir ein modellunabhängiges Werkzeug entwickelt, um die Erhaltungseigenschaften in Wettervorhersagemodellen in Bezug auf einzelne Kontrollvolumen zu validieren. Das Kontrollvolumen kann dabei irgendwo in dem Modellgebiet platziert werden und ist unabhängig von der Gitterweite des Modells. Die Anwendung des Diagnoseverfahrens auf das Wettervorhersagemodell COSMO offenbarte, dass die Wassermasse recht gut erhalten wird, wohingegen die Energie und Gesamtmasse überhaupt nicht erhalten sind. In dieser Arbeit wird gezeigt, in welchem AusmaßFehler in der Behandlung von thermodynamischen Prozessen, verschiedene numerische Filter und die Feuchtadvektionsschemata die Bilanzen in einzelnen Teilgebieten des Modells bei idealisierten Modellläufen wie auch realistischen Wettervorhersagen negativ beeinflussen können. Wir finden heraus, dass die größten Bilanzierungsfehler durch eine nicht exakte Implementierung von diabatischen Prozessen innerhalb der Sättigungsadjustierung, den mikrophysikalischen Parameterisierungen und dem Strahlungsschema erzeugt werden. Bezüglich dieser Problematik stellt sich heraus, dass in den nichthydrostatischen Modellen mit höhenbasierter Vertikalkoordinate eine Sättigungsadjustierung verwendet werden muss, die unter der Bedingung eines konstanten Volumens abläuft. Bei Verwendung einer solchen Sättigungsadjustierung und bei entsprechender Erweiterung der Strahlungs- und mikrophysikalischen Parameterisierungen wird eine deutliche Reduzierung der Bilanzierungsfehler der Wassermasse, der Gesamtmasse und der Energie erreicht.
Unter Verwendung der Fourieranalyse in Form der diskreten Kosinustransformation (DCT) wird untersucht, wie gut die nichtlinearen Wechselwirkungsprozesse im Wettervorhersagemodell COSMO widergespiegelt werden. Die starke Aperiodizität der Ausschnittsmodelle wird mit Hilfe von synthetischen Feldern simuliert und verschiedene spektrale Analyseverfahren werden getestet. Wir zeigen, dass die DCT am besten das Verhalten des für die Mesoskala charakteristischen $k^{5/3}$-Spektrums simulieren kann. Mit Hilfe der DCT-Analyse werden die kinetischen Energiespektren des Modells anhand von gemessenen Energiespektren evaluiert. Dazu werden Flugzeugmessungen, welche während des COPS-Experimentes im Sommer 2007 durchgeführt wurden, ausgewertet und spektral aufbereitet. Wir finden heraus, dass die spektrale Varianz und die Neigung des Spektrums bei einer Mittelung über zehn Vorhersagetage gut mit den Messungen übereinstimmen. Allerdings ist das Modell nicht in der Lage, die in der Atmosphäre bei bestimmten Wetterlagen auftretende Energiekaskade realistisch zu simulieren. Desweiteren offenbart die Evaluation, dass das Modell die nichtlinearen Prozesse in der Atmosphäre nur bis zu einer Skala von 20 Kilometern auflösen kann. Dies bedeutet, dass die effektive Auflösung des Modells COSMO siebenmal schlechter ist als die nominale Auflösung von 2.8 Kilometern. Dies ist konsistent mit den Untersuchungen im WRF Modell von Skamarock (2004). In einer Kaltstart-Konfiguration ist die effektive Auflösung allerdings erst nach Beendigung des etwa fünf Stunden umfassenden Spin-up Prozesses verfügbar.

In Anlehnung an die oben erwähnten Diagnostiken wurden im weiteren Verlauf der Arbeit Diskretisierungsverfahren untersucht, bei denen die Erhaltungseigenschaften möglicherweise besser generiert und die nichtlinearen Wechselwirkungen besser im Modell dargestellt werden. Dabei haben wir ein Diskretisierungschema (EVT-Schema) für den nichtlinearen Term der Impulsgleichungen abgeleitet, welches die Nambudarstellung der Atmosphärendynamik als Werkzeug benutzt. Dabei stellt sich heraus, dass das Diskretisierungsverfahren große dreidimensionale Stencil erzeugt auf denen umfangreiche Rekonstruktionen durchgeführt werden müssen. Es wird in einem idealisierten Schwerewellentestfall gezeigt, dass das EVT-Schema dieselbe Genauigkeit und Charakteristik aufweist wie eine Lösung zweiter Ordnung. Weitergehend wird das EVT-Schema zusammen mit einem Poisson-Schema, welches auf der hamiltonischen Darstellung der Atmosphärendynamik beruht, anhand einer Superzellensimulation validiert. Die Auswertung der Modellergebnisse zeigt, dass das EVT-Schema und das Poisson-Schema die wichtigsten meteorologischen Prozesse simulieren. Teilweise sind Strukturen in der EVT- und in der Poisson-Lösung etwas besser aufgelöst als in den Standard-Diskretisierungsschemen zweiter Ordnung. Die Simulation mit dem Poisson-Schema weist wesentlich geringere Niederschlagsmengen auf und die Superzelle driftet gegenüber den anderen Lösungen nach Norden ab. Wir finden heraus, dass selbst die anspruchsvollen EVT- und Poisson-Schemata dieselbe Rate von numerischer Diffusion benötigen wie die Standardschemen zweiter Ordnung. Deshalb sind in dieser Simulation die Aufwind-Standardverfahren hoher Ordnung die beste Wahl, weil sie hier weniger diffusiv auf die kleinen Skalen wirken.
Die Nambu- und Hamiltondiskretisierungsverfahren scheinen nach den bisherigen Stand der Untersuchungen nicht praktikabel für die Anwendung in den numerischen Wettervorhersagemodellen zu sein. In der aktuellen Konfiguration kann eine quantitativ messbare Verbesserung zu vergleichbaren standardmäßig verwendeten Diskretisierungsschemen nicht erreicht werden. Eine Erweiterung der neuen Diskretisierungsverfahren auf die vollständigen Impulsgleichungen könnte einen positiven Effekt auf die Modellqualität haben. Trotz alledem hat sich das in meiner Arbeit entwickelte Bilanzierungsverfahren für Teilgebiete des Modells als sehr nützlich erwiesen. Dieses Diagnosewerkzeug ermöglicht es dem Modellentwickler, Fehlerquellen im Modell zu identifizieren und die im Modell enthaltenen physikalischen Parameterisierungen und numerischen Verfahren zu verbessern.

Contents

1 Introduction

1.1 Setting the scene

Recent state-of-the-art numerical weather predication (NWP) models like WRF (Skamarock et al., 2005), MSM (Saito et al., 2006) and COSMO (formerly known as the Lokalmodell by Steppeler et al., 2003) provide an operational forecast several times a day with a horizontal resolution of about 5 kilometers down to 3 kilometers. Making use of the complete Euler's equation, the NWP models are able to simulate various physical processes and resolve flow regimes on a very wide range of spatial and temporal scales.

Driven by the increase in resolution during the last years, the attention within the NWP model development was focused on the explicit simulation of convective processes. The physical processes occurring in thunderstorms (Bluestein, 2000, 2009) or mesoscale convective systems (MCS) like squall lines (Bluestein and Weisman, 2000; Done et al., 2004; Bryan and Parker, 2010) shall be explicitly resolved by high-resolution models without using a parameterization for the deep convection. Since those phenomena cause material damage and partly result in loss of human live a good forecast will be beneficial to people being affected by severe weather events. Although recent NWP forecasts are performed using resolutions of a few kilometers, the models are often not sufficient to resolve adequately the physical processes being observed within the afore-mentioned small-scale phenomena. Weisman et al. (1997) demonstrated that a horizontal resolution of at least 4 km is needed to simulate the basis structure, mass and momentum transports of an idealized MCS. Bryan et al. (2003) examined that even a resolution of 1 km is not sufficient to adequately simulate the turbulent transports and the energetic transfers among the different horizontal scales.

In order to meet the sophisticated demands of the forecasters, one may increase the resolution of the model forecasts. The desire for a relatively large domain, the wish to perform ensemble runs and the restriction in computer resources preclude resolutions of nearly 1 km and smaller. Even though this high resolutions become feasible in the future, the model developers are still faced with two main challenges when simulating fine-scale structures:

a) A variety of numerical damping mechanisms are used to prevent computational instability (Mesinger and Arakawa, 1976). Thus, the small-scale structures are damped in the model and the effective resolution gets worse (Skamarock, 2004).

b) All the physical processes taking place or rather becoming relevant on the small scales have to be sufficiently considered in the model.

Achieving an improvement with respect to (a) or (b) will hopefully result in a better representation of the small-scale processes in the NWP models without increasing the resolution.

Regarding (a), an exemplary investigation is the one of Arakawa (1966). He introduced a spatial discretization scheme for a barotropic model that overcomes the nonlinear instability without the use of any numerical diffusion. Therefore, the scheme allows for longterm integrations and preserves the amplitude of the physical small-scale structures. The philosophy of the Arakawas scheme is the reasonable and correct representation of the energy flux between spatial structures having different wave numbers, which implies the conservation of the integral properties enstrophy and kinetic energy. Sadourny (1974) and Arakawa and Lamb (1980) examined the robustness and stability of shallow-water models and concluded that the conservation of potential enstrophy is essential to prevent a spurious numerical energy transfer to high wave numbers (nonlinear instability). Arakawa and Lamb (1980) demonstrated that suppressing the spurious numerical energy cascade by an adequate discretization scheme improves the ability of a model to capture the overall flow regime.

Regarding (b), the models considered for the discretization studied by Arakawa, Sadourny and Lamb did not account for the dissipative processes in the atmosphere. The dissipation in the atmosphere has to be treated by physical parameterizations. However, discretization schemes, which require only a small amount or not any numerical diffusion, will improve the physical parameterization of small-scale processes, because the physical dissipation is not bothered by the numerical dissipation.

Motived by the benefits arising for the numerical models by constructing an adequate discretization scheme, the ideas of Arakawa, Sadourny and Lamb were also addressed by some recent studies of the NWP. Tripoli (1992), Tripoli and Mayor (2000) and Janjic et al. (2011) adapted the discretization procedure of enstrophy- and energy-conserving schemes from the shallow-water models to three-dimensional non-hydrostatic compressible models. They were able to derive numerical schemes that improve the representation of nonlinear dynamics on all scales and allow for simulations without excessive numerical dissipation.

A different approach to construct numerical schemes was taken from Salmon (2004, 2005, 2007), Sommer and Névir (2009). They use a Hamiltonian representation (Morrison and Greene, 1980; Morrison, 1998) as well as a Nambu form (a generalization of the Hamiltonian representation, Névir, 1998; Névir and Sommer, 2009) of the original equations as a tool in order to yield discretization schemes. The discretization procedure does not start from the common hydro-thermodynamical equations but from equations expressed by antisymmetric Poisson and Nambu brackets, which involve conservative quantities. Thus, Salmon (2004, 2005) was able to derive straightforward the Arakawa Jacobian for the barotropic model and the energy- and enstrophy-conserving scheme of Arakawa and Lamb (1980) for the shallow-water model. Therefore, the Poisson and Hamiltonian tools allow to understand the intuitive discretization approaches of Arakawa, Sadourny and Lamb on a more general level. Later, Sommer and Névir (2009) showed that a discretization based on a Nambu representation of the shallow-water equations is applicable also to sophisticated geometrical grids.

Towards the application of the Hamiltonian and Nambu tools to recent NWP models, Gassmann and Herzog (2008) proposed a Poisson-Nambu bracket form of the turbulence-averaged Euler equations including diabatic processes. This Nambu-bracket form is in the sense that the diabatic processes and the turbulent friction are added to the brackets as dissipative forcing terms. Thus, Gassmann and Herzog (2008) demonstrated how to overcome the limitations of the original Hamiltonian and Nambu formulation by Morrison (1998) and Névir and Sommer (2009), which are valid only for the ideal fluid. Due to the investigations of Gassmann and Herzog, the Hamiltonian and Nambu tools become applicable also for NWP models.

So far, the application of the Hamiltonian and the Nambu discretization tools to recent weather prediction models was not explored. This gap in knowledge shall be filled in this thesis. The scientific purpose of this thesis is to investigate discretization schemes for state-of-the-art NWP models, which are based on the Hamiltonian and Nambu representation of the three-dimensional non-hydrostatic compressible atmosphere. The focus is on the nonlinear term in the momentum equations, because it is expected to be the most challenging term in the NWP. The work is motivated by the hope to find discretization schemes, which are beneficial to NWP models in the same manner as it was highlighted for the barotrophic and shallow-water models of Arakawa, Sadourny and Lamb.

However, the discretization schemes in the dynamical core of a NWP model are only one part of the whole model. Thus, it has to be carefully considered how to detect or diagnose the model forecast for an intended improvement of the model behavior with respect to specific physical processes. Therefore, a further purpose of this thesis is to explore diagnostic methods, which enables the model developer to gain a deep insight into the impact of modifications to the dynamical core on the model simulations. There are some benchmarks for the dynamical cores in the framework of dry-adiabatic and linear flows, but the realistic weather forecasts are mainly evaluated by a pure check by eye and a comparison of the model output fields with observations. The diagnostic methods explored in this thesis aim to keep the model analysis on a fundamental level, but allow for the analysis of strong nonlinear and diabatic processes as well as realistic weather forecasts. The focus of the diagnostic methods is: (i) on the conservative properties of the model and (ii) on the model quality with respect to nonlinear scale interactions. Such diagnostic is most challenging, because the high-resolution NWP models apply different discretization schemes, a bunch of physical parameterizations, non-physical artificial damping mechanisms and arbitrary boundary conditions on limited domains. The diagnostic methods explored in this thesis hopefully allow to gain useful information about the performance of NWP models.

1.2 Scientific objectives and goals of the thesis

To summarize, the main objectives mentioned in the previous section are:

(O1) to investigate discretization procedures for state-of-the-art NWP models by using Hamiltonian and Nambu tools,

(O2) to explore diagnostic methods in order to measure the performance of NWP models with respect to conservation properties, and

(O3) to explore the quality of a model with respect to nonlinear scale interaction.

The working horse for our model study and model development will be the NWP model COSMO (Steppeler et al., 2003), which is widely used for weather forecasts in the European region. Using the COSMO model, the thesis aims to find answers to the following questions:

- Are the physical constraints (conservation of mass, energy or Ertels potential vorticity) fulfilled in an atmospheric model in spite of the conserved quantities are not treated as prognostic variables in the model equations? What are potential sources in the model causing a violation of the physical constraints? What is the impact on the simulation of the meteorological fields?
- How well are the nonlinear scale interactions resolved in the model? Are there inadequate model formulations or physical parameterizations that have a negative impact on the simulated nonlinear dynamics?
- Is it feasible to construct discretization schemes based on Hamiltonian and Nambu tools for three-dimensional non-hydrostatic and compressible models? Do the ideas of Salmon (2004, 2005, 2007) and Sommer and Névir (2009) become practical also for NWP models?
- What is the impact of a discretization using Hamiltonian and Nambu tools on the meteorological fields and on the nonlinear scale interactions, respectively the energy cascade? Does the schemes allow for reducing the numerical diffusion relative to the standard schemes?
- Does a discretization using Hamiltonian and Nambu tools have a positive impact on the conservation properties?

1.3 Outline of the thesis

According to the objectives (O1) to (O3), the thesis is organized in three chapters as presented in the following. The content of the first chapter is already published in a paper (Petrik et al., 2011). The second and the third chapter are intended to be prepared for a publication. Consequently, each chapter has its own introduction and conclusion. The first and the second chapter are dealing with diagnostic methods for mesoscale NWP models, whereas the third chapter is dealing with discretization schemes using Hamiltonian and Nambu tools.

Chapter 2: In this chapter a diagnostic method is explored, which is capable to verify the conservation properties of a NWP model. Since the high-resolution models apply a bunch of non-physical and computational boundary conditions, the focus of the diagnostics is not on the global conserved quantities integrated over the whole model domain, but on the physical constraints with respect to sub-domains of the model.

The intended use of the diagnostic approach is to detect potential error sources with respect to energy and mass conservation. The diagnostic approach may be essential for the investigation of the hydrological cycle and is especially relevant for models that do not solve equations in flux form and do not apply a finite volume discretization.

Chapter 3: The analysis brought up in **Chapter 2** is extended to the nonlinear dynamics. Therefore a diagnostic method is put forward based on multi-scale statistics in order to analyze nonlinear scale interactions. The diagnostics shall be able to treat the high-resolution limited area models, which provide non-periodic output fields. The multi-scale diagnostic method is meant to analyze the model skills regarding the resolution of small-scale physical processes.

Chapter 4: In this chapter discretization schemes using Hamiltonian and Nambu discretization tools are discussed for their intended use in the COSMO model. Since the temporal and spatial discretization schemes implemented in the NWP models are very complex, the Nambu and the Hamiltonian tools are considered for a specific part of the momentum equations. The focus is on the nonlinear advection term, because it is expected to be the most challenging term in the NWP and most relevant for convective systems. A Nambu discretization is constructed and implemented in the COSMO model. The Nambu discretization scheme and a Poisson discretization scheme (already proposed by Gassmann and Herzog, 2008) are tested in the framework of various flow regimes. The discretization schemes will be evaluated on the standard schemes implemented in the COSMO model using the diagnostic methods examined in **Chapter 2** and **Chapter 3**. Since the Poisson and the Nambu bracket discretization of the nonlinear term involves some physical quantities relevant for the development and evolution of convective storms, we hope to better preserve and represent these structures in the model simulations.

Finally, concluding remarks and an outlook are given in Chapter 5.

2 Validation of a mesoscale weather prediction model using sub-domain budgets

The content of this chapter has been originally taken from the publication of Petrik et al. (2011). The original manuscript was slightly modified for editorial purposes.

2.1 Introduction

When asking for the quality of a mesoscale weather prediction (NWP) model, usually model verification studies are sought after (Roberts and Lean, 2008; Wernli et al., 2009; Skok et al., 2010). There is no doubt that the evaluation of the results obtained by a NWP model on in-situ and remote sensing data observations is important to tackle model deficits. But it is also essential to evaluate the physical adequacy of the model (e. g. the falsification approach as mentioned by Schlünzen, 1997). We devote the work presented in this Chapter to the diagnostics of conservation properties for mesoscale models that use limited domains. State of the art models are very complex to understand, as they are based on the non-hydrostatic compressible equations, complex discretization schemes, extensive physical parameterizations and include various artificial damping mechanisms. Due to their complexity it has become a difficult task to ensure physical constraints like conservation of total energy, Ertel's potential vorticity, and mass. Nevertheless, conservation properties are very important and need to be diagnosed. For example, the water mass budget plays an essential role for the evaluation of the hydrological cycle.

In this paper a diagnostic method is introduced that determines the time evolution of mass and energy relative to sub-domains using a finite volume approach. I. e. those quantities that should be conserved are diagnosed with respect to well-defined control volumes, which are located at some place in the model domain. Here we extend the approach of Doms (2004), who was focusing solely on the moisture mass conservation of the 'Lokalmodell' (today known as COSMO) (Doms and Schaettler, 2002). In contrast to earlier studies by Bryan and Fritsch (2002) and Satoh (2003) we will not investigate the temporal evolution of mass and energy as integrated quantities over the whole model domain, but we use a 'local' perspective on the conservation properties as a benchmark for the physical parameterizations and dynamical cores of non-hydrostatic models. The 'local' perspective provides the opportunity to assess limited area models. These models employ lateral relaxation and upper damping zones, in which the conservation properties are strongly violated. The motivation for our work arises due to the fact that

models like e. g. COSMO (Steppeler et al., 2003), ARPS (Xue et al., 2000) and MM5 (Dudhia, 1993) do not apply a flux form in the model equations, as it is done in the WRF (Skamarock et al., 2005) or METRAS (Schlünzen, 1990; Schlünzen et al., 1996) model. Therefore, conservation is not supposed to be guaranteed by the formulation of the equations.

We use one-dimensional advective tests to analyze the errors of the diagnostic method that develop due to computations on a discrete grid and flux reconstructions. We generalize the diagnostic method for the non-hydrostatic compressible model COSMO, i. e. we determine the budget equations of the quantities water mass, total mass and energy. The diagnostic method shows that large conservation errors are produced during the simulation of thermodynamic processes. Therefore, we investigate the magnitude and the source of the errors. We figure out that non-hydrostatic models using a height-based coordinate must use a saturation adjustment scheme under a fixed volume approach to achieve conservation. Moreover, the diagnostic method shows that the standard diabatic equations of the COSMO model are insufficient for the simulation of explicit moist convection.

The Chapter is structured as follows. In the Section 1.2, a diagnostic method is introduced and it is tested in a simple advection test bed. This method will be generalized to the COSMO model in Section 1.3. In Section 1.4 the performance of the diagnostic method, applied to the standard COSMO model, is shown using idealized cases. In Section 1.5 we present a modified formulation of the thermodynamics that are used in the COSMO model. In Section 1.6 we discuss idealized and realistic simulations using the model physics introduced in Section 1.5. Summary and conclusions are drawn in Section 1.7.

2.2 Description of the diagnostic method

The diagnostic tool is based on the general equation for a scalar quantity ψ in integral form

$$\frac{\partial}{\partial t}\int\limits_V \psi \, dV + \int\limits_{\partial V} \mathbf{f}_\psi \cdot d\mathbf{S} = \int\limits_V q_\psi dV \, . \tag{2.1}$$

This means that a quantity ψ in a volume V can be changed, if a volume source q_ψ or a flux $\mathbf{f}_\psi$ across the boundaries of the volume V occur. To investigate the impact of the model simulated dynamical or physical processes on the sub-domain budgets, the fulfillment of eq. (2.1) needs to be checked. This can be done by discretizing each term in this equation.

2.2.1 Numerical implementation

The expression (2.1) can be numerically approximated as follows (Baldauf, 2008):

$$\int\limits_{CV} \psi \, dV \simeq \sum_{GP \in \mathrm{CV}} \psi_{i,j,k} \, D_{i,j,k} \, \Delta V_{i,j,k} \, , \tag{2.2}$$

where $D_{i,j,k}$ is the Jacobian of the coordinate transformation, and

$$\int_{\partial V} \mathbf{f}_\psi \cdot d\mathbf{S} \simeq \sum_{GP \in \partial V} \mathbf{f}_{\psi;i*,j*,k*} \cdot \Delta\mathbf{S}_{i*,j*,k*} \,. \tag{2.3}$$

$i*$, $j*$ and $k*$ are the positions at the corresponding cell faces. Eq. (2.2) is also used to approximate the term on the right hand side of eq. (2.1). All approximations are second order approximations (Ferziger and Peric, 2002). We calculate the expressions (2.2) and (2.3) in a well-defined control volume (CV) containing the grid points (GP) $i \in [i_{min}, i_{max}]$, $j \in [j_{min}, j_{max}]$ and $k \in [k_{min}, k_{max}]$.

The fluxes $\mathbf{f}_\psi$ have to be reconstructed. Various interpolation methods were tested to calculate the fluxes (Table 2.1). The formulas are given for a one-dimensional flux $F_{i+1/2} = (u\,\psi)_{i+1/2}$ with a well-known normal velocity. Beside the upwind (UDS) and the central difference method (CDS) a third order (QUICK) (e.g. Ferziger and Peric, 2002) and the Lax-Wendroff scheme (LW) (Durran, 1999) are listed.

In real atmospheric conditions where sharp gradients occur, the various approximations possess different flux approximations. Therefore, the behavior of a budget diagnosis with various flux reconstructions has to be investigated in idealized flow tests. We focus exclusively on determining advective fluxes.

2.2.2 Test of the diagnostic tool with exact shifting

As a first test for the diagnostic tool, Baldauf (2008) proposed to shift initial data functions ψ with a constant velocity u_0 through a one-dimensional grid domain (an ideal shifting algorithm). The shifting process is given by the expression

$$\frac{\partial \psi}{\partial t} = \frac{\partial\,(u_0\,\psi)}{\partial x} \,. \tag{2.4}$$

A triangle ψ_{tri} and a pulse function ψ_{pul}

$$\begin{aligned} \psi_{tri}(x) &= \mathrm{MAX}(-10|x+0.25|+1,0) \quad x \in [0,1]\,, \\ \psi_{pul}(x) &= \frac{1}{1+e^{60*(|x-0.25|-0.12)}} \quad x \in [0,1] \end{aligned} \tag{2.5}$$

are shifted inside a domain with 100 grid points in the range $x \in [0,1]$ with different Courant numbers μ. Figure 2.1 displays in an exemplary manner the shifting of the triangle. The functions in eq. (2.5) are shifted through a control volume (CV), which is located in the middle of the domain. It is bound by the grid points $imin = 50$ and $imax = 65$. The number of shifting steps N_T is calculated in such a way that the function can fully pass through the CV.

In order to determine the sub-domain budget of the CV according to the shifting process given by eq. 2.4, the integrated quantities of ψ_{tri} and ψ_{pul} and the corresponding fluxes at the left border $F_{imin-1/2}$ and at the right border $F_{imax+1/2}$ are discretized by using eq. (2.2)-(2.3). The methods used for flux reconstructions at the cell faces are listed in

Table 2.1: Flux reconstruction method and their order of spatial approximation.

Method	Accuracy	Calculation formula
UDS	1	$F^{UDS}_{i+1/2} = \frac{u_{i+1/2}}{2}(\psi_i + \psi_{i+1}) - \frac{\lvert u_{i+1/2}\rvert}{2}(\psi_{i+1} - \psi_i)$
CDS	2	$F^{CDS}_{i+1/2} = \frac{u_{i+1/2}}{2}(\psi_i + \psi_{i+1})$
QUICK	3	$F^{QUICK}_{i+1/2} = \frac{u_{i+1/2}}{16}[9(\psi_{i+1} + \psi_i) - \psi_{i-1} - \psi_{i+2}] - \frac{\lvert u_{i+1/2}\rvert}{16}[3(\psi_{i+1} - \psi_i) + \psi_{i-1} - \psi_{i+2}]$
LW	2	$F^{LW}_{i+1/2} = \frac{u_{i+1/2}}{2}(\psi_i + \psi_{i+1}) - \frac{u^2_{i+1/2}\Delta t}{2\Delta x}(\psi_{i+1} - \psi_i)$

Table 2.1. The temporal discretization of the sub-domain budget is done by an Euler forward method. Thus, the sub-domain budget on the discrete grid reads:

$$\frac{\Psi^{n+1} - \Psi^n}{\Delta t} = -\left(F^n_{imax+1/2} - F^n_{imin-1/2}\right) \text{ , with } \Psi^n = \sum_{GP \in \mathrm{CV}} \psi^n_i \, \Delta x_i \, . \tag{2.6}$$

The sub-domain budget of the quantities Ψ^n_{tri} and Ψ^n_{pul} is not perfectly balanced due to inaccuracies on the discrete grid. To quantify the budget errors the following residual values are defined:

$$\begin{aligned} \mathrm{R} &= \frac{\Psi^{n+1} - \Psi^n}{\Delta t} + \left(F^n_{imax+1/2} - F^n_{imin-1/2}\right) \, , \\ \mathrm{IntR} &= \sum_{n=1}^{N_T} |\mathrm{R}| \, \Delta t \, . \end{aligned} \tag{2.7}$$

Baldauf (2008) showed that even for a perfect shifting process budget errors occur due to flux calculation errors (second term) and volume artifacts (first term on the right hand side of eq. (2.7)). Thus, the integrated residua IntR listed in Table 2.2 are mostly nonzero. Although the shifting is perfect, the diagnostic method does not interpret it as perfect. The measurement of the diagnostic tool using the discretizations in eq. (2.7) is in contradiction to what is going on during the exact shifting process. Only if the Courant number equals one and the flux reconstruction is done by the UDS or the LW method, the budget error is zero. The shortcomings of the low order reconstruction schemes are more pronounced, if the shifting process becomes slower or the non-linear pulse function is used instead of the linear triangle function. In this case, the higher order schemes offer lower residua for small Courant numbers (Table 2.2).

In order to simplify the understanding and comparison of various budget errors, a relative error RE normalized with the temporal average of Ψ^n is introduced (eq. (2.8)):

$$\mathrm{RE} = \frac{\mathrm{IntR}}{\overline{\Psi^n}^{\,t}} \, , \quad \overline{\Psi^n}^{\,t} = \frac{1}{N_T} \sum_{n=1}^{N_T} \Psi^n \, . \tag{2.8}$$

The sensitivity of this error on CV size is shown in Figure 2.2 using the pulse function ψ_{pul}. If the CV-size increases the error RE decreases. Enlarging the CV-size increases the volume relatively more than the total surface area. The determination of the

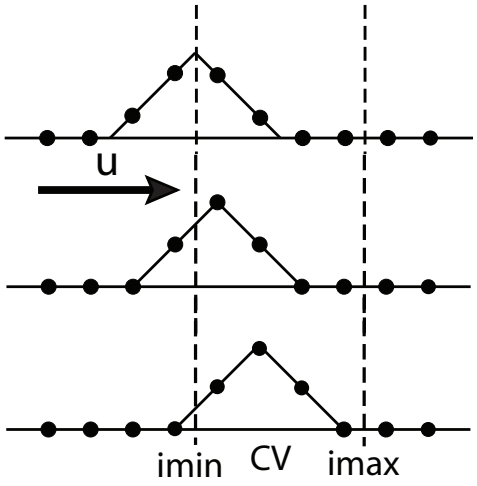

Figure 2.1: A schematic sketch of a triangle shifted one grid point within one time step (Courant number $\mu = 1$) through a discrete grid. The dashed lines indicate the western and eastern boundary of the control volume.

surface flux integral is inaccurate due to flux reconstruction. The volume integral is not affected by flux reconstruction. This means that the impact of inaccurate flux reconstructions will reduce, if the CV gets larger. To obtain reasonable results, the choice of the CV-size must be considered profoundly.

The shift test was extended to two dimensions using a slightly stretched grid to mimic the nonuniform coordinate lines, as they occur in the geographical coordinate system. The integrated residua are qualitatively the same as for the one-dimensional case, which indicates the ability of the diagnostic method to work in more than one dimension.

2.2.3 Test of the diagnostic tool with different numerical advection algorithms

To account for the different numerical integration schemes applied in NWP models, the behavior of the diagnostic tool is applied to different numerical schemes, which

Table 2.2: IntR for an exact shifting with control volume size of 15 grid points. Listed for triangle and pulse function with different Courant numbers μ and flux reconstruction methods.

	triangle			pulse		
Method	μ=0.125	μ=0.5	μ=1	μ=0.125	μ=0.5	μ=1
UDS	0.018	0.010	0	0.017	0.010	0
CDS	0.011	0.011	0.020	0.003	0.010	0.020
QUICK	0.011	0.011	0.020	0.002	0.010	0.020
LW	0.011	0.010	0	0.002	0.001	0

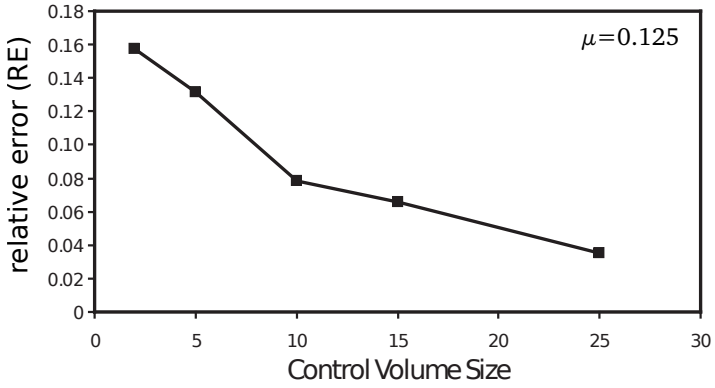

Figure 2.2: Relative error for an exact shifting of the pulse function using various control volume sizes and Courant number $\mu = 0.125$. The results are an average over various budget diagnostics using the flux reconstruction methods from Table 2.1. Values are highly affected from the poor upwind scheme.

compute the advection of the above mentioned functions (eq. 2.5 as initial conditions). The integration is done by a combination of the third-order Runge-Kutta method (Wicker and Skamarock, 2002) used for the temporal discretization and a first order upstream, a second order centered and a fifth order upstream method used for the spatial discretisation: RK3UP1, RK3CN2 and RK3UP5. The budget errors (2.7) are evaluated for the predicted values $\tilde{\psi}_i^n$.

It is obvious that the numerical transport through the control volume as measured by the diagnostic tool is not entirely exact. The numerical advection with any Courant number and test function reveals budget errors (Table 2.3). The IntR is smaller for the numerical advection of the pulse function using the RK3UP5 scheme compared to the ideal shifting case. That is the measurement by the diagnostic scheme is more in agreement with the numerical advection than the pure shifting. In case of the advection of the triangle, the budget errors are also much smaller than for the ideal shifting (not shown here), because the volume artifacts mentioned in Section 2.2.2 also vanish in the numerical integration. Therefore, the sub-domain budgets monitored by

Table 2.3: IntR for advection of a pulse function using different numerical schemes. Listed for different Courant numbers μ and flux reconstruction methods. RK denotes Runge-Kutta scheme, UP upstream and CN centered differences. The numerical schemes are of order 1, 2, 3 or 5. WN indicates white noise.

Numerical-Scheme	UDS	QUICK	LW
RK3UP5, μ=0.5	0.001	0.001	0.001
RK3CN2, μ=0.5	0.011	0.010	0.000
RK3UP1, μ=0.5	0.008	0.024	0.016
RK3UP5WN, μ=0.5	0.026	0.019	0.021
RK2UP5, μ=0.9	0.023	0.072	0.024

the diagnostic tool are better for the numerical advection schemes than for the pure analytical shifting.

We also analyze how the accuracy of the numerical advection scheme influences the budget errors measured by the diagnostic tool. The performance of the advection schemes with a spatial discretization lower than fifth order is tested, i. e. RK3CN2 and RK3UP1 (Table 2.3, row 2-3). Indeed, the diagnostic tool reveals lower sub-domain budget errors concerning the simulations using the higher order schemes compared to the simulations using lower order schemes. The lower the spatial discretization order is, the bigger the IntR is. Especially the very dissipative scheme (RK3UP1) is measured with poor conservation properties concerning the sub-domain CV. An exception is the case, where the advection is simulated by the scheme RK3UP1 and the diagnostic method is based on a UDS flux reconstruction. Then the IntR is influenced by the coincidence between the diagnostic method and the numerical advection scheme.

To simulate numerical artifacts and instabilities and to study their impact on the budget errors, the RK3UP5 solution is disturbed by white noise (RK3UP5WN, amplitude of 0.01) and a Runge-Kutta scheme of second order (e.g. Durran, 1999, p. 53-54) is applied above its theoretical stability threshold (RK2UP5, Courant number of 0.9). In both cases the IntR indicates a bad quality of the numerical solutions (Table 2.3, row 4-5). The white noise leads to at least two times higher and the unstable RK2UP5-scheme leads to at least four times higher IntR-values compared to the undisturbed solution RK3UP5. Examining the results for the white noise test, the reason for good scores with the 'RK3UP5' solution is not only the perfect symmetry of the pulse function, but also the skills of the numerical advection scheme.

In contrast to the sub-domain budget errors discussed above, the monitoring of the budget of ψ with respect to the total domain (i. e. the fluxes on the right hand side of 2.6 are vanishing) does not indicate any problem with the integration. That finding confirms the importance of a sub-domain budget diagnostic regarding conservation properties but also the model performance on a local scale.

2.2.4 Implications of tool tests for its application to complex models

There is no unique discrete analog to the budget relation (2.1). Results from pure shifting and advection tests reveal problems in the budget diagnosis due to the discrete grid and the flux reconstruction. To minimize errors originating from the diagnostic scheme itself, the control volume size has to exceed a threshold that needs to be at least 10 grid points, as depicted in Figure 2.2. In addition, it is concluded that the higher order reconstruction schemes QUICK and LW (Table 2.1) are applicable for the following budget investigations with the COSMO model (the method LW is used hereafter). For boundaries of CV close to the surface or the uppermost model level higher order numerical schemes need to be replaced by lower order methods when reconstructing the fluxes.

Our approach of a budget diagnostics with respect to a specific control volume can be applied to those models, which apply a height-based coordinate, even if those models

contain complex numerical structures. For instance, if a model uses a vertical mass-coordinate, the control volume is not fixed in space in the vertical, but in mass. The interpretation of the budget may then be a bit different. In order to adapt the diagnostic method to a new model one has to consider two things. First, the diagnostic method has to be adapted to the geometry (section 2.3.2). Second, the diagnostic method has to be adapted to the equations or to the conservative variables derived from these equations (also section 2.3.2).

The diagnostic method is designed for model evaluation. It is voluntarily chosen to be in contrast to the elaborated numerical discretization of the model equations that might only partly be budget equations. This allows to detect errors resulting from the model numerics itself. A drawback linked to the diagnostic method is that their error estimators are in favor of those numerical schemes, which are similar to the flux reconstruction applied by the diagnostic method. This issue has to be taken into account when applying the diagnostic method to a model.

2.3 Adaptation of the diagnostic method to the COSMO model

2.3.1 Relevant model numerics for budget diagnostics

A short introduction into the formulation and the numerical discretization of the COSMO is given in the Appendix A. Here we only address those model features, which will be relevant for the application of the diagnostic method introduced in Section 2.2.

Due to the fact that the water mass plays a very important role, we will perform sensitivity studies with respect to the moisture transport schemes that are implemented in COSMO (Förstner et al., 2006):

- an Eulerian flux-form scheme (BOTT) with a positive definite version of Bott's method (Bott, 1989) and a Strang-splitting technique (Durran, 1999, chap. 3) used to solve the multi-dimensional advection
- a tri-cubic Semi-Lagrange (SL) advection scheme with full 3D tri-cubic interpolation within one time step and a multiplicative filling technique (e. g. Staniforth and Cote, 1991)

Moreover, we will study the influence of the numerical filter schemes on the sub-domain budgets. Beside the physical diffusion controlled by the turbulence scheme and the temporally implicit operators describing the vertical advection, there are mainly four damping schemes applied in the COSMO model:

1. A Rayleigh-damping layer is affecting the upper levels of the model domain. The damping layer extends from the top of the domain (22 km) down to 13 km height. Additionally, a lateral relaxation zone is applied with a width of about 50 km.
2. An implicit diffusion is inherent in the discretisation of the horizontal advection operator using an odd order scheme (Wicker and Skamarock, 2002). By default, a fifth order operators is used in the COSMO model.

3. A fourth order Laplacian horizontal diffusion is applied to the prognostic variables. The viscosity coefficient is chosen in such a way that the amplitude of a $2\Delta x$ wave is damped to $1/e$ within two time steps. By default, the viscosity coefficient $\nu_l \approx 1.05 \cdot 10^{10}$ m^4 s^{-1} is applied only at the lateral boundaries.
4. The horizontal divergence damping proposed by Dudhia (1993) is used to damp the horizontally propagating sound waves. By default, the filter coefficient $\nu_d \approx 6 \cdot 10^4$ m^2 s^{-1}.

Taking into account the above mentioned filter mechanisms used in the standard model configuration, a budget analysis is only valid for a control volume far away from the Rayleigh-Damping and lateral boundary zones.

2.3.2 Examination of the budget equations for the COSMO model

The model equations of the COSMO are not in flux form. The continuity equation is transformed to a pressure equation (Appendix A). Therefore, the conservation properties are not explicitly ensured and need to be investigated. Hence, the diagnostic method introduced in Section 2.2 is applied to the COSMO model. We focus on the sub-domain budgets for energy, total mass and water mass, because they are conservative variables in the equation system chosen for the COSMO model. That means the volumic sources and sinks vanish, i. e. the term on the right-hand side of equation (2.1). Only the temporal changes and the boundary fluxes related to the total mass, water mass and total energy have to be determined, i. e. the terms on the left-hand side of equation (2.1). Therefore, the operators in eq. (2.2) and eq. (2.3) have to be transformed to terms of the coordinate system used in COSMO. We have to consider the thermodynamic approximations and the macroscopic reference velocity vector $\mathbf{v}$ used in the COSMO model.

Operators

To diagnose the conservation properties following from eq. (2.1), one needs to define the volume element (eq. 2.2) of a grid box in a left-handed geographical and terrain-following system (Baldauf, 2008):

$$D_{i,j,k}\,\Delta V_{i,j,k} = r^2 \cos\varphi_j \sqrt{G}_{i,j,k} \Delta\lambda \Delta\varphi \Delta\zeta\,, \tag{2.9}$$

The surface integral on the left hand side of eq. (2.3) transforms to

$$\begin{aligned} \int\limits_{\partial V} \psi\, \mathbf{v}\cdot d\mathbf{S} = & \int\limits_{\partial S^{\varphi,\zeta}} \psi u\; r\sqrt{G} d\varphi d\zeta + \int\limits_{\partial S^{\lambda,\zeta}} \psi v\; r\cos\varphi \sqrt{G} d\lambda d\zeta \\ & + \int\limits_{\partial S^{\lambda,\varphi}} r^2 \cos\varphi \left(\frac{J_\lambda}{r\cos\varphi}\psi u + \frac{J_\varphi}{r}\psi v - \psi w \right) d\lambda d\varphi\,. \end{aligned} \tag{2.10}$$

The left-handed terrain-following system is shown in Figure 2.3. The surface $d\mathbf{S}$ is decomposed into $dS^{\lambda,\varphi}$, $dS^{\varphi,\zeta}$ and $dS^{\lambda,\zeta}$, which are the directed surface elements in

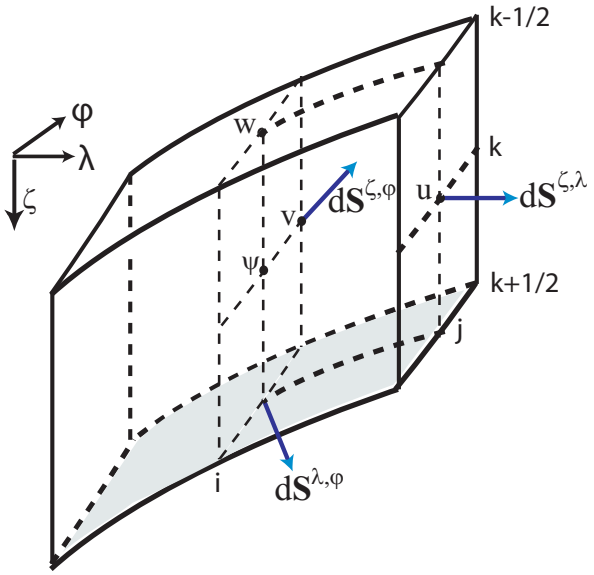

Figure 2.3: A grid box of the COSMO model embedded in a left-handed geographical and terrain-following coordinate system. The coordinates of the system are the geographical longitude λ and latitude φ and the height coordinate ζ, which is decreasing with increased altitude. The scalars Ψ are located at mass mid point (i,j,k). The velocity components u, v and w are staggered on an Arakawa-C/Lorenz grid.

the terrain-following coordinate system. Each integral of eq. (2.10) is discretized by the right hand side of eq. (2.3). The values of ψ at the cell faces are obtained by reconstruction, which was discussed in section 2.2.

Water mass

Wacker and Herbert (2003) and Wacker et al. (2006) studied the budget equations for partial densities of a moist atmosphere, particularly incorporating sedimentation fluxes. Following their approach, the budget of any water component x can be formulated as

$$\frac{\partial \rho_x}{\partial t} = -\nabla \cdot \rho_x \mathbf{v}_{ref} - \nabla \cdot \mathbf{J}_{ref,x} + \sigma_x - \nabla \cdot \mathbf{F}_x \,, \tag{2.11}$$

where ρ_x is the partial mass, σ_x is the internal production rate, e. g. cloud water from a condensation process, and $\mathbf{F}_x$ is the turbulent mass flux. $\mathbf{J}_{ref,x}$ is the diffusion mass flux of the component x relative to the macroscopic reference velocity $\mathbf{v}_{ref}$.

To evaluate the water mass budget in the model runs, the budgets of all partial masses ρ_x given in eq. (2.11) have to be summed up except dry air (abbreviation d). Applying the most sophisticated cloud-microphysics we consider six classes of water: water vapor (v), cloud water (c), cloud ice (i), rain (r), snow (s) and graupel (g). Using the Gaussian theorem, the budget for the water mass M_W

$$M_W = \int_{CV} \sum_{x \neq d} \rho q_x dV \equiv \int_{CV} \rho q_W dV \tag{2.12}$$

is given in a predefined volume CV by

$$\frac{\partial M_W}{\partial t} = -\int\limits_{\partial CV} \rho q_W \mathbf{v}\cdot d\mathbf{S}_{CV} - \int\limits_{\partial S_{CV}^{\lambda,\varphi}} (F_v+F_c+F_i) dS_{CV}^{\lambda,\varphi} + \int\limits_{\partial S_{CV}^{\lambda,\varphi}} a(P_r+P_s+P_g) dS_{CV}^{\lambda,\varphi}\,, \quad (2.13)$$

where ρ is the density of the total air mixture and $S_{CV}^{\lambda,\varphi}$ denotes the surfaces at the top and the bottom of the CV. P_x are the sedimentation fluxes. The water budget with respect to the sub-domain CV as given by eq. (2.13) is derived as follows:

- With respect to the COSMO model, the reference velocity is chosen as a barycentric velocity of total air mixture, i.e.

$$\mathbf{v}_{ref} \equiv \mathbf{v} = \sum \frac{\rho_x}{\rho} \mathbf{v}_x\,, \quad \rho = \sum \rho_x\,, \quad \rho_x = \rho\, q_x\,. \quad (2.14)$$

- The summation over all source rates σ_x vanishes to retain the water mass conservation. The dry air source rate is zero.
- We consider the strictly vertical directed mass fluxes of diffusion and turbulence: $\mathbf{J}_{ref,x} = J_x\mathbf{k}$ and $\mathbf{F}_x = F_x\mathbf{k}$.
- With respect to the precipitating particles, the vertical components of the diffusion fluxes are approximated by the sedimentation fluxes with mean terminal velocities: $J_x = -P_x$, $x = r, s, g$. The sedimentation fluxes cause a compensating lift of all non-precipitating classes (the corresponding fluxes J_d, J_v, J_c and J_i are defined by Catry et al., 2007). The summation over the diffusion fluxes of the water species gives the third term on the right hand side of eq. (2.13). Parameter a is $q_d/(1 - q_r - q_s - q_g)$.
- The turbulent transport of the precipitating particles is disregarded: $F_r = F_s = F_g = 0$.

Taking the impact of water vapor evaporation and precipitation into account, the barycentric velocity is not zero at the surface. Although the earth surface is impermeable for dry air, the diffusive flux of water vapor J_v and the sedimentation flux of the precipitating particles across the Earth surface account for a non-vanishing barycentric velocity at ground (Wacker and Herbert, 2003):

$$w_s = \frac{J_v - P_r - P_s - P_g}{\rho_d}\,. \quad (2.15)$$

Therefore, the turbulent fluxes and precipitation rates of eq. (2.13) have to be multiplied by a factor of ρ/ρ_d, if the lower surface of the CV is equal to the Earth surface.

The water mass budget given by eq. (2.13) is checked by the diagnostic method. If one uses parameterized convection with mass flux schemes, an investigation of the budget given by eq. (2.13) is somewhat restricted in terms of the location of the CV in the three-dimensional space. In this case only the bulk precipitation is available and analysis must be carried out for a control volume with a vertical extent from the model surface to the cloud top.

Total mass

The total mass budget can be derived from expression (2.11) summing up over all components of the air mixture. We use the reference velocity from eq. (2.14) and apply the mass control conditions $\sum \mathbf{J}_{ref,x} = 0$ and $\sum \mathbf{F}_x = 0$ according to Wacker et al. (2006). Then, the budget for the total mass M is given by:

$$\frac{\partial}{\partial t} \int\limits_{CV} \rho dV \equiv \frac{\partial M}{\partial t} = - \int\limits_{\partial CV} \rho \mathbf{v} \cdot d\mathbf{S}_{CV} \,. \tag{2.16}$$

The total mass budget given by eq. (2.16) is checked by the diagnostic method.

The total mass budget given in eq. (2.16) is dependent on the reference velocity. For example, Ooyama (2001) uses a decomposition of the vertical velocity into the velocity of rain water and a velocity related to the motion of the rest of air particles, which is his reference motion. This step would reveal explicitly the vertical precipitation flux divergence in the total mass budget. As already mentioned for the water mass budget, the diffusive flux of water vapor and the sedimentation fluxes of the precipitating particles lead to a non-vanishing barycentric vertical velocity at the ground. If we consider the total mass budget in eq. (2.16) with respect to a control volume, where the lower surface is equal to the Earth surface, then the contribution to the mass flux at the Earth surface (index s) reads explicitly:

$$+\frac{\rho_s}{\rho_{d,s}} \int\limits_{\partial S^s_{CV}} (J_v - P_r - P_s - P_g)\big|_s \, dS^s_{CV} \,. \tag{2.17}$$

Thus, the atmosphere loses mass, if precipitation is higher than evaporation. Although the COSMO and many other models allow for a diffusive water flux from the soil into the atmosphere, they cannot describe the influence of the vertical boundary velocity $w_s \neq 0$ on the prediction of the prognostic variables (e. g. the influence of w_s on the surface pressure Wacker et al., 2006). This leads to a lack in the mass conservation.

Energy

The combination of the hydro-thermodynamical equations for temperature, pressure, momentum and the budget equations for the mass fractions q_x (Steppeler et al., 2003, eq. (1 - 5)) gives the budget for energy diagnostics (Gassmann and Herzog, 2008):

$$\frac{\partial}{\partial t} \int\limits_{CV} \rho E_t dV = - \int\limits_{\partial CV} \left(\rho E_t \mathbf{v} + \overline{\rho \mathbf{v}'' \mathbf{v}''} \cdot \mathbf{v} - p\mathbf{v} + \mathbf{R} + \overline{\rho e'' \mathbf{v}''} \right) \cdot d\mathbf{S}_{CV} \,. \tag{2.18}$$

$\overline{\rho \mathbf{v}'' \mathbf{v}''} \cdot \mathbf{v}$ denotes the transport of the turbulent momentum flux and $\overline{\rho e'' \mathbf{v}''}$ denotes the transport of the turbulent heat flux. $\mathbf{R}$ is the radiative flux and p the pressure. E_t is the total energy per unit total mass. It is the sum of mean kinetic energy $K_m = (u^2 + v^2 + w^2)/2$, potential energy $\Phi = gz$ and internal energy e. The mean turbulent kinetic energy (TKE) is not considered for the energy budget given in eq. (2.18). The

TKE is used for the turbulence closure concept in COSMO to yield turbulent transfer coefficients for momentum and heat. But only the transport of turbulent heat fluxes and turbulent momentum fluxes influence the temporal evolution of total energy.

Out of the radiative flux densities we consider only the vertically directed ones, i. e. $\mathbf{R} = R\mathbf{k}$. It describes the energy gain in the daytime and the cooling of the atmosphere or the cloud backscattering by short-wave and long-wave radiation. The term $p\mathbf{v}$ in eq. (2.18) considers the rate at which work is done by the pressure force (the contraction or expansion of a volume), which changes the internal energy. As already known from mass treatment, surface integrals at the ground must be treated with the barycentric velocity w_s. Consequently, the surface integral at the earth surface (index s) given in eq. (2.18) consists of

$$\rho_s E_{t,s} w_s \qquad \text{and} \qquad p_s \, w_s \, . \tag{2.19}$$

The first term describes, for instance, the input of latent energy to the atmosphere due to strong evaporation fluxes (positive w_s). The second term describes the work done at the Earth surface and used to expand the control volume under the condition that $w_s \neq 0$. We name both effects an energy surface flux hereafter.

The internal energy e results from the common relation between pressure p and enthalpy h:

$$\rho e = \rho h - p \, , \qquad h = \sum h_x q_x \, . \tag{2.20}$$

The enthalpy changes during phase transitions, which is reflected by the heat of vaporisation l_v, fusion l_f and sublimation l_s. The expression for e and h are specified following thermodynamical textbooks (e. g. Emanuel, 1994). But under the condition that different phases of water coexist in the atmosphere, no unique formula for the enthalpy exists. We are following Satoh (2003) to define the origin of the energy e.

In the COSMO model a simplified thermodynamic is applied. I. e., l_v, l_f and l_s are no longer temperature dependent, rather they are fixed at their values at 0°C. This leads to an underestimation of the sensible heat storage (Satoh, 2003). As a consequence of Kirchhoff's law of thermodynamics, the heat capacities of vapor, liquid and frozen particles do not contribute to the total c_p and c_v ($c_p \simeq c_{pd}$ and $c_v \simeq c_{vd}$). This leads to the simplified, but still consistent, expression for the internal energy:

$$e = c_{vd} T + l_v q_v - l_f q_f, \qquad e_s = c_{vd} T, \qquad e_l = l_v q_v - l_f q_f \, . \tag{2.21}$$

e_s is the sensible and e_l the latent heat part of internal energy. The negative sign in the latent heat part describes that latent energy is stored in the water vapor and released by condensation and freezing.

The energy budget given by eq. (2.18) is checked by the diagnostic method. We have to point out here, that the energy budget diagnostic must be consistent with the thermodynamical assumption in a model. With respect to the COSMO model, the energy budget has to be analyzed with the internal energy expression (2.21).

2.4 Investigation of sub-domain budgets for 3-D idealised cases

2.4.1 Definition of residual budget

For our following argumentations it is assumed, that the model (index M) is not perfect and any budget is contaminated by a residuum R_ψ:

$$\left.\frac{\partial \psi}{\partial t}\right|_M = F_\psi|_M + R_\psi \,, \tag{2.22}$$

where F_ψ denotes fluxes and sources defined by the right hand side of the eq. (2.13), (2.16) and (2.18). If $R_\psi > 0$, the model artificially gains mass or energy, whereas $R_\psi < 0$ means, the model erroneously loses energy or mass.

As discussed in Section 2, the temporal discretization in the budget equations is discretized by an Euler Forward method. All required terms are therefore evaluated in the model at the end of a time step.

2.4.2 Experimental setup of the 3-D academic cases

As a first simple test case a single cell convection was chosen for the analysis of the COSMO model. The pre-convective hydrostatic balanced environment is defined by Weisman and Klemp (1982). In order to overcome the convective inhibition the convection is forced using a warm air bubble. The size and amplitude of the bubble used is that defined by Weisman and Klemp (1982).

The simulation is performed on a domain of 100 × 100 grid points with a horizontal grid size of nearly 1.9 km. We use 48 model levels, which are vertically stretched to better resolve the boundary layer. For simplification the Coriolis parameter is set to zero. A short overview about the model configuration is given in Table 2.4.

Table 2.4: Configurations of the COSMO model for the performed experiments. ν_l denotes the Laplacian filter coefficient and ν_d the divergence damping coefficient.

experiment	WKDRY	WKRAIN	REAL
time step [s]	20	20	30
resolution [km]	1.9	1.9	2.8
ν_l [m^4 s^{-1}]	$1.25 \cdot 10^{10}$	$1.25 \cdot 10^{10}$	0
ν_d [m^2 s^{-1}]	$6 \cdot 10^4$	$6 \cdot 10^4$	$6 \cdot 10^4$
Moist. advec.	BOTT	BOTT	BOTT + SL
Physics	no	cloud micro	cloud micro + turbulence + radiation

2.4.3 Case WKDRY - dry convection

A dry convection is simulated. Thus, any phase changes of water vapor are prohibited. In this case q_v might be interpreted as a tracer. But it is not a real passive scalar, because it contributes to the total density of the multiphase atmospheric fluid and also influences the buoyancy of the fluid. In contrast to Weisman and Klemp (1982), the initialized warm air bubble has an amplitude of 10 K.

The thermal bubble rises explosively. Within 6 minutes its center reaches a height of 3000 meters. The maximum vertical velocity is about 10 m s^{-1}. The resulting pressure perturbations, in combination with the motions caused for continuity reasons, lead to a rotation in the y-z-plane (Figure 2.4a).

Cloud formation is suppressed in this case. Although the rising bubble was initialized with a 10 K temperature perturbation in its center, it loses its buoyancy very fast. The resulting descending air cuts the updraft into two pieces, that form sharp wind fronts in the lower atmosphere. Figure 2.4b illustrates such a front 15 km to the north and 24 minutes after initialization. During the first hour the bubble oscillates in a statically stable atmosphere because of the buoyancy force. Later on, this process weakens.

The budget analysis was carried out for a control volume with a horizontal extent of 30 $\times$ 30 grid points and 31 layers in the vertical from Earth surface to nearly 10 km height. The thermal bubble is located in the center of the CV. The total mass fluxes through the boundaries of the volume are shown in Figure 2.5. All the lateral fluxes are the same due to the missing Coriolis force. The fluxes are influenced by gravity and sound wave generation and show a phase shift between the horizontal and vertical fluxes. An upward mass flux at the top of the CV is associated with a vertical integrated horizontal convergence and vice versa.

Since the bubble sucks in the dense air from underneath, i. e. a low level convergence resulting from its buoyancy at the beginning of the simulation, the total mass is increasing rapidly in the control volume. Figure 2.6a shows the sub-domain budget of the total mass. It can be seen that the positive mass change is well explained by the mass fluxes computed at the lateral boundaries. That is the horizontal convergence of mass near the surface is stronger than the loss of mass aloft (Figure 2.5). It is important to note, that the term 'DivFlux_M' in Figure 2.6a summarizes the horizontal and vertical part of the mass fluxes, i. e. the mass divergence as a three-dimensional quantity.

The spin-up phase is disturbed by vigorous oscillations in the levels near the tropopause (12 km). The relative error RE (eq. 2.8) in the simulation is about $7 \cdot 10^{-5}$ and is considered small. The residual curve is smaller than any physical tendency. The remaining error might originate from the inaccuracy of our diagnostic method (see section 2.2).

The water mass is well conserved in the chosen CV (Figure 2.6b). The ascending air increases the mass of moist air and generates a moisture flux convergence. At the time, when the gravity waves and outflow structures reach the CV-boundaries near the surface, the convergence turns into a divergence. The BOTT scheme applied here produces oscillations at the beginning. They originate from splitting errors associated with the multi-dimensionality of the implemented BOTT advection scheme: for efficiency

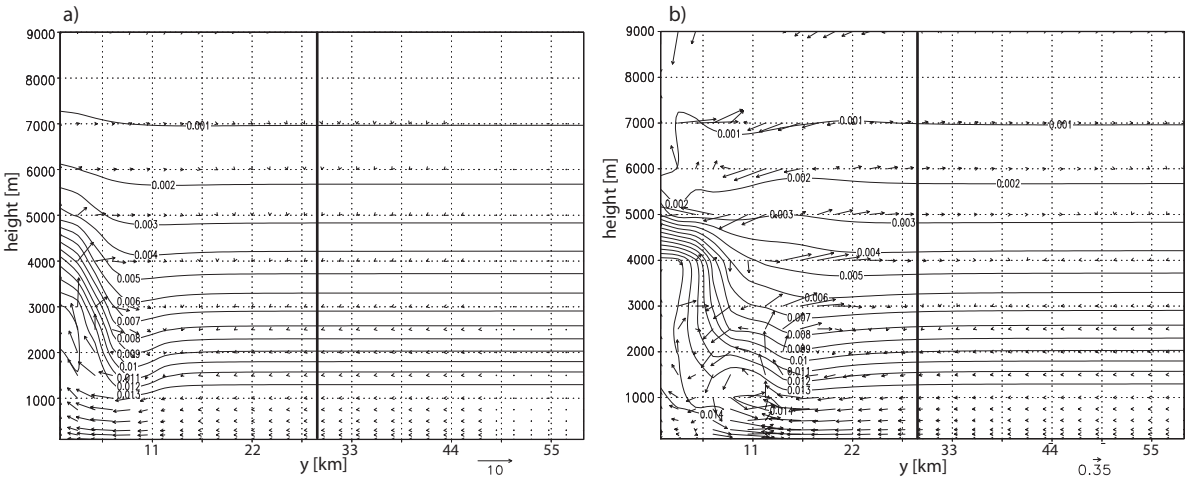

Figure 2.4: Case WKDRY. a) South-North cross-section at x=50 with the center of the convective cell at the left boundary (y=0 km). Specific water vapour [kg kg^{-1}] (contour) and wind vectors at t = 6 min. b) as in a), but at t = 24 min. The thick line indicates the northern boundary of CV.

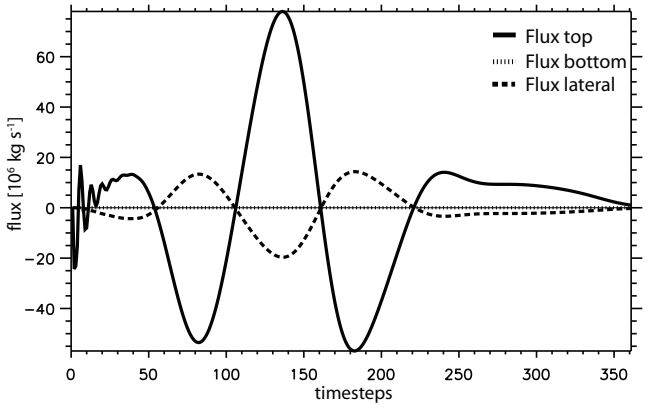

Figure 2.5: Case WKDRY (Δt = 20 s). Total mass fluxes through the boundaries of the CV [kg s^{-1}]. The term 'lateral' is related to the lateral boundary flux at the North.

reasons the splitting steps in the different spatial directions in terms of the Strang-splitting are reduced. If one takes into account the virtual temperature to calculate the CAPE (convective available potential energy, Doswell and Rasmussen, 1994), the numerical perturbation in q_v means a 2 J kg^{-1}-switch in every time step. This is small in comparison to the absolute value, but it could be relevant in meteorological situations with lower CAPE and strong advection processes - e. g. fronts in mountainous regions.

2.4.4 Case WKRAIN - Convection with precipitation

We push further the idealized tests and perform simulations allowing for precipitation physics. A Warm Rain Kessler scheme is used (Doms et al., 2007, Section 5.4) in order

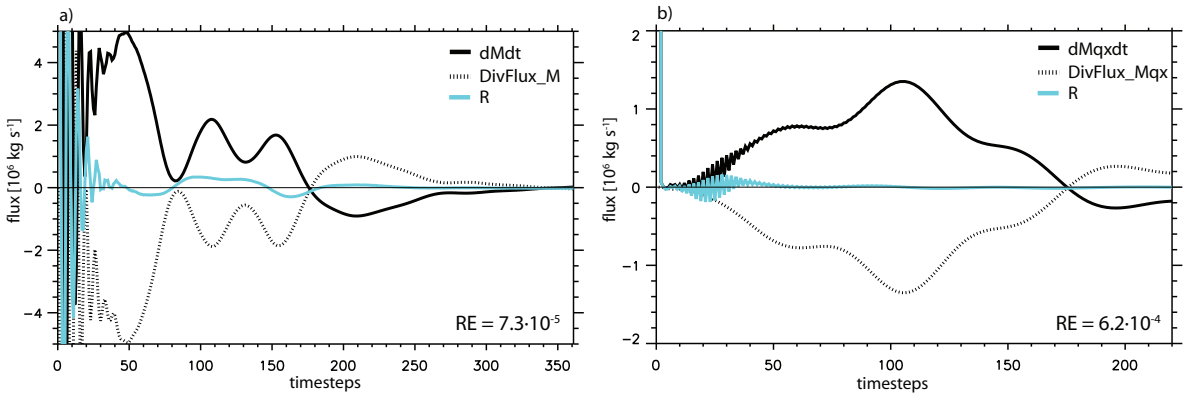

Figure 2.6: Case WKDRY (Δt = 20 s). Sub-domain budgets [kg s^{-1}] of the CV. a) total mass budget (eq. (2.16)) containing mass change (named 'dMdt'), divergence ('DivFlux_M') and residua ('R'). b) water mass budget (eq. (2.12) and (2.13)).

to consider the autoconversion, accretion and evaporation of rainwater. The nucleation of cloud water from the vapor phase is done by a standard saturation adjustment scheme. For more details we refer the reader to Doms et al. (2007, Section 5). The initial atmospheric conditions are slightly modified in comparison to case WKDRY. The surface temperature is $T_s = 297K$. The CAPE is about 1000 J kg^{-1}. The warm air bubble has an initial temperature amplitude of 2 K.

The temporal evolution of the simulation at the center of the convection is shown in Figure 2.7a. The bubble does not rise as fast as in the case WKDRY during the first minutes, because the temperature excess in the bubble center is divided by 5 in comparison to the previous run (Table 2.4). But once the condensation starts, the bubble becomes much warmer due to the latent heat release. The inflow of moist air is nearly two times larger than in the WKDRY run. The temperature excess in the center of the bubble reaches 5 K and the maximum vertical velocity is 17 m s^{-1} after 30 minutes. Above the equilibrium level the moist air dries out and is causing an upper tropospheric outflow divergence. When the formation of rain water starts at about 60 time steps, the liquid water drag increases. This decelerates the flow into the updraft. Later on, the sedimenting rainwater reaches the ground. The precipitation intensifies reaching its maximum rate after 60 min. The developing downdraft cuts off the inflow of moist and dense air and the cell dies.

The total mass budget analysis for the case WKRAIN is presented in Figure 2.8a using the same control volume as in the WKDRY case. Compared to the WKDRY simulation, the total mass budget clearly shows residua with high negative values. The evolution of the total mass during the first hour (the first 180 time steps) is not explained by the mass fluxes which are computed. One possible explanation is that the total mass, which has been supposed conservative without any volumic sources or sinks (right-hand side term of eq. (2.1) vanishes), is not conserved by the model. That means 'fictive' and spurious volumic sources or sinks exist inside the CV due to the discretization or the model approximations. Another explanation is that some 'fictive' inflows or outflows into the CV are present in the model, which should not exist. There is no divergent flux apparent during the first half hour (the first 90 time steps), although the decrease

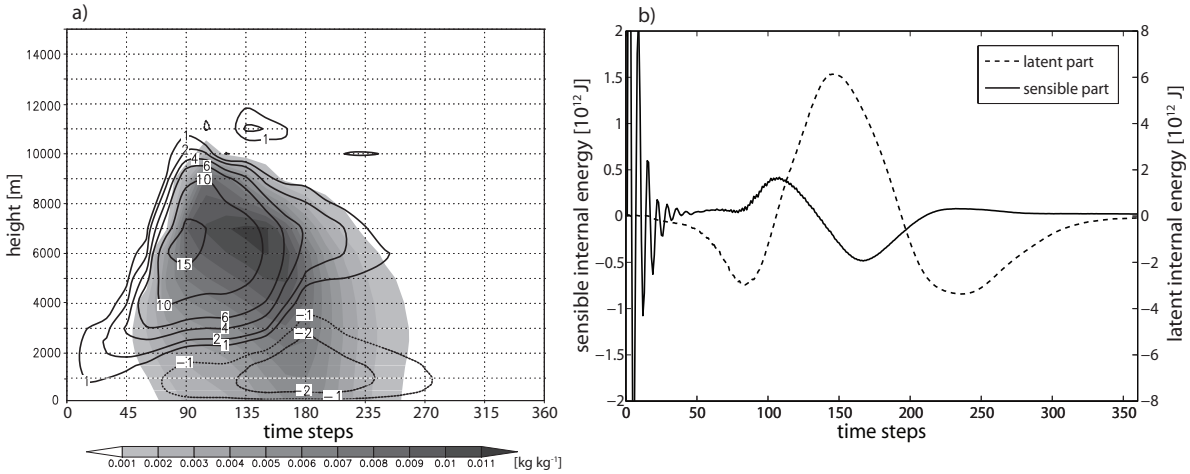

Figure 2.7: Case WKRAIN ($\Delta t = 20$ s). a) Time-height cross section of vertical velocity [m s^{-1}] (contour) and rain water content [kg kg^{-1}] (shaded) at the center of the warm bubble. b) The change in internal energy [J s^{-1}] integrated over the whole CV. The change is decomposed in the sensible heat part and latent heat part of internal energy (eq. (2.21)).

in total mass will imply it.

The error in total mass has its maximum at about 90 time steps. At that time a large amount of latent heat is released and transformed to sensible heat inside the CV (positive diabatic heating, Figure 2.7b). Since the cloud formation process is controlled by standard saturation adjustment scheme, it is supposed to be the main origin for the residual values. We discuss this issue in the Section 2.5.

During the second half of the first hour the residuum curve decreases. Its sign changes after 50 minutes simulation time (150 time steps). At that time, the evaporation of rain water becomes the dominant physical process and causes a negative diabatic heating.

In order to investigate whether the precipitation process also affects the mass and energy conservation, we determine the sub-domain budgets of the total mass by dividing the standard CV into two parts. The first part is located in the lower 2000 m, whereas the second part extends vertically from 2000 m above the ground to the upper boundary of the standard CV at 10000 m. In Figure 2.9a the residual curves concerning the standard CV, the lower and the upper part are shown. In contrast to the mass loss in the middle and upper troposphere, an erroneous mass gain is present in the lower atmosphere. Thus, the negative error inside the cloud is partly compensated by the positive error below the cloud. The error below the cloud implies a problem related to the formulation of microphysical problems which will be discussed in the next section.

The errors in total mass are correlated with energy errors (Figure 2.8b). The total energy change is dominated by changes in the internal energy (eq. (2.21)), whereas the potential and kinetic energy contribute only a small amount to the energy change. The total energy decreases during the first half hour (first 90 time steps). The energy fall is coupled to a strong decrease of latent heat energy due to the condensation of water vapor as depicted in Figure 2.7b. The latent heat release leads to an increase of sensible heat energy. But the rise of sensible heat energy is damped by the decrease

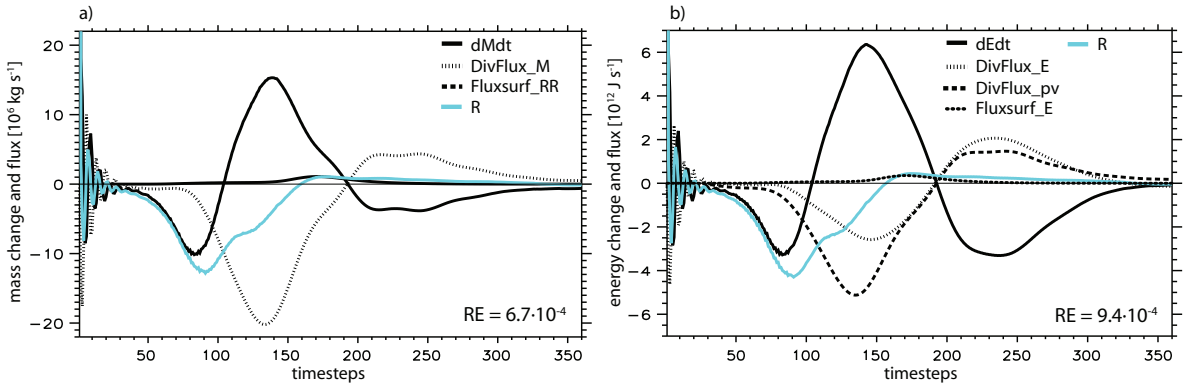

Figure 2.8: Case WKRAIN ($\Delta t = 20$ s). Sub-domain budgets of the CV. a) total mass budget [kg s^{-1}] involving precipitation flux (named 'Fluxsurf_RR', eq. (2.17)) b) total energy [J s^{-1}] budget involving the work done by the CV ('DivFlux_pv') and the energy surface flux ('Fluxsurf_E', eq. (2.18) and (2.19)).

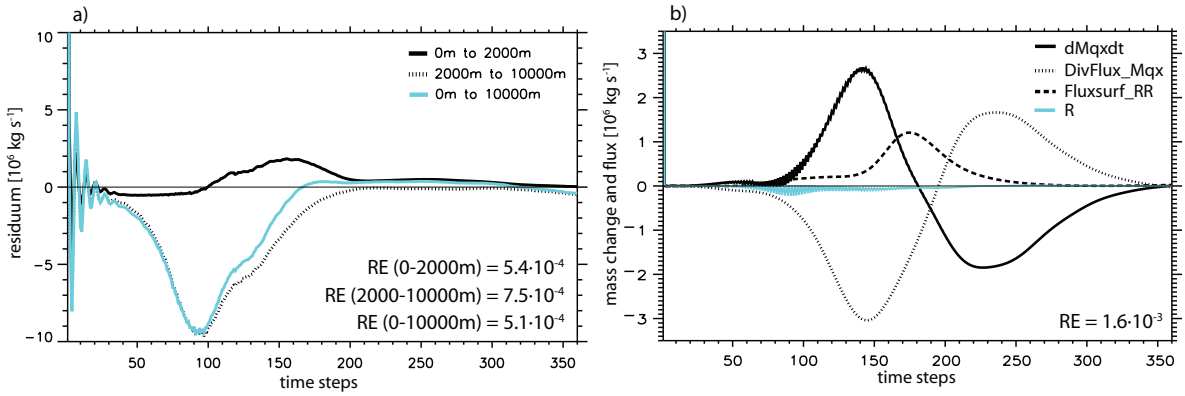

Figure 2.9: Case WKRAIN ($\Delta t = 20$ s). a) Residua of the total mass [kg s^{-1}] shown for various locations of vertical extents of the control volume. b) Sub-domain budget of the water mass [kg s^{-1}] concerning the CV. The precipitation flux is denoted by 'Fluxsurf_RR' (eq. (2.13)).

in total mass and by the initiating evaporation process below and at the top of the cloud. The change of total energy, the energy divergence and the contraction work (third term at the right hand side of eq. (2.18)) do not cancel each other during the first 90 minutes.

Starting 30 minutes into the forecast, the energy sub-domain budget is governed by the change in latent heat energy due to moisture convergence (Figure 2.9b) and the contraction and expansion work of the control volume changing the internal energy. Later on, the drying processes along the cold outflow control the change in internal energy. At the end of the simulation the diabatic heat sources are smaller and the residuum of energy is nearly zero.

In contrast to the total mass and energy, the water mass is well conserved (Figure 2.9b). The moisture divergence, the change in water mass and the precipitation flux are compensating each other. One reason for this good result is that the BOTT algorithm

is written in a conservative flux form and thus it is preferred to have good conservation skills. Another reason comes from the different behavior of water mass and total mass fluxes. Whereas the fluxes of the total mass are dominated by wave structures, the moisture fluxes are mostly advective processes. Thus, small errors in the treatment of gravity waves affect the highly sensitive total mass budget more than the water mass budget.

2.4.5 Sensitivity of sub-domain budgets to moisture advection scheme

In order to study the performance of the two moisture advection schemes implemented in the COSMO model, we analyze the sub-domain budgets concerning the simulation of the case WKRAIN. We test the BOTT-scheme and the Semi-Lagrange (**SL** hereafter) advection scheme. The results are shown in Figure 2.10 for the SL scheme (thick lines) and the BOTT scheme (thin lines). Applying the SL scheme for moisture transport, the moisture convergence induced by the density current is not as strong as for the BOTT scheme. The maximum values of divergence differ by 10 percent after 140 time steps. Nevertheless, the SL scheme produces higher precipitation rates during the first hour. Using the SL scheme a reduced generation of cloud water is present in the mid troposphere which leads to less buoyancy in the updraft channel relative to the BOTT scheme. This implies that the entrainment, respectively the evaporation, at the lower cloud edges is reduced and the sedimentation of rain water is enhanced relative to the BOTT scheme.

It is beneficial for the Semi-Lagrangian scheme that it does not reveal splitting errors, whereas the relative error in water mass conservation is about a factor of two bigger than for the BOTT-scheme ($3.0{\cdot}10^{-3}$ versus $1.6{\cdot}10^{-3}$). Of course, the Semi-Lagrangian scheme is not (water-)mass conserving. Only the global mass over the whole model domain is conserved by a simple multiplicative filling technique (e. g. Staniforth and Cote, 1991). We can speculate that the aforementioned filling technique is not conservative in terms of sub-domain water budgets.

2.4.6 Sensitivity of sub-domain budgets to numerical filters

In order to test the influence of the numerical filter mechanisms on the sub-domain budgets, simulations are carried out in the framework of a modified WKRAIN case. I. e. the precipitation physics is switched off and the CAPE is reduced to 350 J kg^{-1} to prevent from the formation of large wind gradients. We apply the model in four different configurations: with and without Laplacian diffusion ('diff' and 'nodiff') and horizontal divergence damping ('damp' and 'nodamp'). We refer the configuration with horizontal diffusion and divergence damping (configuration 'diff,damp') as the standard experiment.

Clearly, the boundary fluxes are modified by the horizontal diffusion and also by the divergence damping. However, the budgets themselves are not significantly deteriorated. Simulations without diffusion are affected from instabilities appearing after the

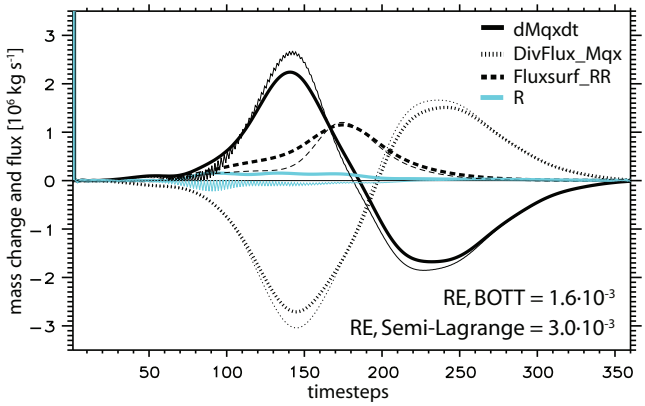

Figure 2.10: Case WKRAIN (Δt = 20 s). Sub-domain budget of the water mass [kg s^{-1}] concerning the CV. Mass change, mass divergence, precipitation flux and residuum using the Semi-Lagrange scheme (thick lines) and the BOTT advection scheme (thin lines). The relative error RE is given in the lower right.

strong convection (beginning at time step 220). The sub-domain budget of total mass (Figure 2.11), which considers the same control volume as in the previous studies, is contaminated. The instability indicates an expected aliasing problem in the model due to missing damping mechanism.

An important result is that the 'nodiff,nodamp' simulation (straight black line) is more stable than the 'nodiff,damp' simulation (long dashed line, Figure 2.11). After 200 time steps the residual curve of the 'nodiff,damp' simulation is often far away from zero and oscillates. This will increase the integrated residua and therefore worsens the conservation properties. As discussed by Gassmann and Herzog (2007), the divergence damping is detrimental to gravity wave modes and thus it does not allow for a proper physical solution.

As far as we investigated the convective test cases, a specific feature of the Semi-Lagrange advection scheme is its sensitivity to the diffusion filter (not shown). There is a significant positive residuum of the water mass conservation, if the diffusive filter is switched off. For example, the relative error RE is 1 % using no filter and 0.3 % using the diffusion filter in the case WKRAIN.

2.4.7 Implications for the simulations WKDRY and WKRAIN

In summary, the diagnostic method applied to the cases WKDRY and WKRAIN is very useful and shows limitations of the COSMO model equations for the simulation of resolved convection. To overcome these limitations we modify the model equations and adapt the physical parameterizations to the modified equations. We introduce the model adaptations in the next section.

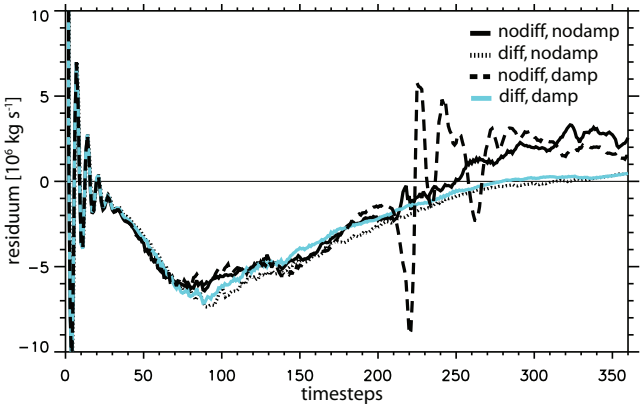

Figure 2.11: Case modified WKRAIN (Δt = 20 s). The temporal evolution of the residua [kg s^{-1}] of the total mass budget. Results are shown for a run with activated or switched off horizontal diffusion (nodiff, diff) and divergence damping (nodamp, damp).

2.5 A modified saturation adjustment and equation set for the COSMO model - the COSMO-MP

In the COSMO model the continuity equation is replaced by a prognostic pressure equation. This does not imply a mass error. But the law of continuity is only fulfilled, if one uses a complete pressure and temperature equation (Gassmann and Herzog, 2008, e. g.):

$$\frac{\partial p^{'}}{\partial t} = -\left(\vec{v}\cdot\nabla_\zeta\right)p^{'} + g\rho_0 w - \frac{c_p}{c_v}p\nabla_\zeta\cdot\vec{v} + \left(\frac{c_p}{c_v}-1\right)Q_h + \frac{c_p}{c_v}Q_m \qquad (2.23)$$

$$\frac{\partial T}{\partial t} = -\left(\vec{v}\cdot\nabla_\zeta\right)T - \frac{p^{'}}{\rho c_v}p\nabla_\zeta\cdot\vec{v} + \frac{1}{\rho c_v}(Q_h+Q_m)\,, \qquad (2.24)$$

The diabatic source term Q_h contains the heating rates due to radiation, turbulent sensible heat fluxes and phase changes controlled by cloud microphysics. Q_m means the mass redistribution as a result of these diabatic processes:

$$Q_m = R_d T\rho\frac{d\alpha}{dT}, \quad \alpha = \left(\frac{R_v}{R_d}-1\right)q_v - q_c - q_i - q_r - q_s - q_g \qquad (2.25)$$

In the recent COSMO model the approximated equations (A.5) and (A.4) are applied instead of the complete temperature and pressure equation (eq. (2.24) and (2.23)). That is the term Q_h is dropped in pressure equation (2.23) and the term Q_m is dropped in eq. (2.23) and eq. (2.24). Consequently, we have to modify the recent COSMO model in order to meet the equations (2.23), (2.24) and thus the law of continuity. Then, a new saturation adjustment technique has to be applied, which is presented in the following Section. According to the simplified thermodynamics of the COSMO model (see eq. (2.21)) we will set c_p and c_v to the constant values c_{pd} and c_{vd} as a consequence of Kirchhoff's law of thermodynamics.

2.5.1 A saturation adjustment scheme under fixed volume condition

The saturation adjustment technique calculates the nucleation rate S^{ce} [kg kg^{-1} s^{-1}] of cloud water from the vapor phase and vice versa. The released latent heat contributes to the diabatic heat source Q_h (eq. (2.24) and (2.23)). The parameterization in COSMO is used for non-precipitating cloud types. If mixed-phase- and ice-phase clouds occur, cloud ice has to be included in the adjustment technique (Lord et al., 1984). Such an extended formulation is not used in the COSMO model. The nucleation and depositional growth of cloud ice are separately formulated in the microphysical schemes (Doms et al., 2007).

The standard saturation adjustment process (**SA**) is assumed to be isobaric and changes the temperature in an atmosphere at rest following the temperature equation (A.5) (Doms et al., 2007, Section 5) in a consistent way. Applying the standard scheme leads to a residuum in the continuity equation (applying the eq. (A.7), (A.4), (A.5), (2.25) to the continuity equation), that is:

$$\frac{\rho T R_v S^{ce}}{p} - \frac{l_v \rho S^{ce}}{T \rho c_{pd}} = -\frac{Q_m}{p} - \frac{Q_h}{T \rho c_{pd}} \,.$$

Using a saturation adjustment technique based on the mass and energy consistent equations (2.23)-(2.24) we derive a new adjustment for temperature and pressure (the modified saturation adjustment approach, **MA**), which differs from the SA scheme as follows:

SA	MA
$\frac{\partial T}{\partial t_{phy}} = \frac{Q_h}{\rho c_{pd}}$	$\frac{\partial T}{\partial t_{phy}} = \frac{1}{\rho c_{vd}}(Q_h + Q_m)$
$\frac{\partial p}{\partial t_{phy}} = 0$	$\frac{\partial p}{\partial t_{phy}} = \frac{c_{pd}}{c_{vd}}(Q_h + Q_m) - Q_h \,,$

(2.26)

where $Q_h = l_v \rho dq_c/dt = l_v \rho S^{ce}$ denotes the latent heat release. $Q_m = -T R_v \rho dq_c/dt = -T R_v \rho S^{ce}$ indicates the mass redistribution of water species. The redefined values of cloud water, vapor, temperature and pressure do not change the water content $q^T = q_v + q_c$ and the density. That is, the same mass remains in the same volume, which is a fixed grid box size in the model domain. In comparison to the SA-scheme, the internal energy e is also kept constant:

$$\rho \frac{de}{dt} + p \nabla \cdot \mathbf{v} = \rho c_{pd} \frac{dT}{dt} - \frac{dp}{dt} - l_v \rho \frac{dq_c}{dt} \,. \tag{2.27}$$

Thus, cloud water generation increases the sensible heat at the expense of the latent heat $c_v \delta T = -l_v \delta q_v$.

If other prognostic variables than p and T are present, the adjustment principle will differ from (2.26). Satoh (2003) uses the sensible part of internal energy and density for the forecast and solves equations in terms of internal energy for the adjusted temperature.

The MA approach considers two cases: the air parcels in a grid box are saturated or not. Assuming that all the cloud water is evaporated, the mixture content can be written as $q^T = q_v^n + q_c^n$ before the adjustment process and $q^T = q_v^{n+1} = q_v^n + q_c^n$ after this process. Taking the temporally discretized equation set (2.26) and using the equation of state, leads to a temperature equation

$$T^{n+1} = \frac{T^n(q_d R_d + q_v^n R_v) - c_p T^n + l_v q_c^n}{(q_d R_d + q_v^{n+1} R_v) - c_p} \,. \tag{2.28}$$

If the specific saturation humidity with respect to water vapor $q_v^{sat}(T) = p_v^{sat}(T)/(\rho R_v T)$ at temperature T^{n+1} is higher than q_v^{n+1}, all water is contained as vapor and the result reads:

$$q_v^{n+1} = q_v^n + q_c^n, \quad q_c^{n+1} = 0, \quad p^{n+1} = \rho R_d T^{n+1} \left\{ 1 + \left(\frac{R_v}{R_d} - 1 \right) q_v^{n+1} - q_x \right\} , \tag{2.29}$$

where q_x denotes the remaining water species.

If supersaturation occurs, vapor and cloud water are in phase equilibrium. The value for q_v^{n+1} is limited to $q_v^{sat}(T^{n+1})$ and the cloud water content can be obtained from the difference $q_v^n + q_c^n - q_v^{sat}(T^{n+1})$. In this case the derived temperature relation from set (2.26) is given by

$$\begin{aligned} &q_v^{sat}(T^{n+1}) \left[R_v T^{n+1} - l_v \right] + T^{n+1} \left[R_d (1 - q_v^n - q_c^n - q_x) - c_p \right] + l_v \left[q_v^n + q_c^n \right] = \\ &T^n \left[q_d R_d + q_v^n R_v \right] - c_p T^n + l_v q_c^n \,. \end{aligned} \tag{2.30}$$

It offers a transcendental equation for temperature, that can be solved with the Newton iteration method. Afterwards, the specific saturation humidity at time step $n+1$ can be calculated with T^{n+1} using the Taylor series expansion:

$$\begin{aligned} q_v^{sat}(T^{n+1}) = q_v^{n+1} &= q_v^{sat}(T^n) + \left. \frac{\partial q_v^{sat}}{\partial T} \right|_n (T^{n+1} - T^n) \\ \frac{\partial q_v^{sat}}{\partial T} &= -\frac{p_v^{sat}(T)}{\rho R_v T^2} + \frac{1}{R_v T \rho} \frac{\partial p_v^{sat}(T)}{\partial T} \,. \end{aligned} \tag{2.31}$$

p_v^{sat} is the saturation vapor pressure with respect to a water surface. The relation for p_v^{sat} is given by the Magnus-formula or can be derived from the Clausius-Clapeyron equation.

2.5.2 Adaption of the physical core of the model

In order to apply the equations eq. (2.23) and (2.24) in COSMO we have to adapt the model formulation to the integration of the Q_h and Q_m terms. This has to be done not only for the saturation adjustment, but for all physical parameterizations.

The diabatic tendencies computed by the physical parameterizations can be decomposed into cloud microphysics ('cmp'), radiation ('rad') and turbulence ('tur'). The diabatic tendency Q_h is:

$$Q_h = Q_h^{cmp} + Q_h^{rad} + Q_h^{tur} \,. \tag{2.32}$$

The integration procedure in the COSMO model is very elaborated with respect to the temporal coupling between the adiabatic core and the physical parameterizations. We refer to Steppeler et al. (2003); Doms and Schaettler (2002); Doms et al. (2007).

We modified the tendencies given by eq. (2.32) in the physical parameterizations in such a way that they coincide with the equations (2.23) and (2.24). That is, Q_h is additionally considered in the pressure equation and Q_m is considered as a tendency in the pressure and temperature equation. Q_m is given by eq. (2.25). For simplification we do not consider the term Q_h^{tur} in terms of its influence on the pressure equation. Furthermore, the contribution of Q_m, which considers turbulent processes, is not taken into account.

The modifications presented in Section 2.5.1 and 2.5.2 are implemented in a new COSMO model named **COSMO-MP**.

2.6 Sub-domain budgets using the modified model COSMO-MP

2.6.1 Case WKRAIN - Convection with precipitation

In order to study the influence of the new model version COSMO-MP introduced in the previous section on the model simulations we consider the case WKRAIN (see section 2.4.4). We perform the same sub-domain budget analysis as it was done in section 2.4.4 using our diagnostic approach from section 2.2.

In Figure 2.12 the total mass and energy budget is shown. Considering the first half hour of the model run, the COSMO-MP simulates a mass and energy divergence that compensates the occurring decrease of total mass and energy. As already mentioned in section 2.4.4, the generation of cloud water is the main process during the first 45 minutes (135 time steps). It is controlled by the saturation adjustment. The modified adjustment implemented in COSMO-MP does not only adjust the temperature during phase transitions. It additionally influences the pressure field due to diabatic heating. The resulting pressure gradients between a cloudy and cloud-free grid box lead to an airflow. Therefore, the phase transitions in a grid box modify the fluxes at the boundaries of the grid cell. The MP-scheme induces a divergent flow and an expanding volume that is consistent to a condensation, respectively heating, in the center of the grid box. This has a positive impact on the total mass and energy budgets (for comparison see Figure 2.8).

Using the diagnostics of sub-domain budgets helps to quantify the positive impact of the new physical formulation in the COSMO-MP model. The residuum of total mass and energy is significantly smaller in comparison to the standard COSMO model. The RE is reduced at least by a factor of two using the COSMO-MP (Table 2.5). The improvement increases, if the amount of CAPE in the atmosphere is larger.

Not only the modified saturation adjustment, but also the modified microphysical core of the COSMO-MP model has a positive impact on the simulation. As already

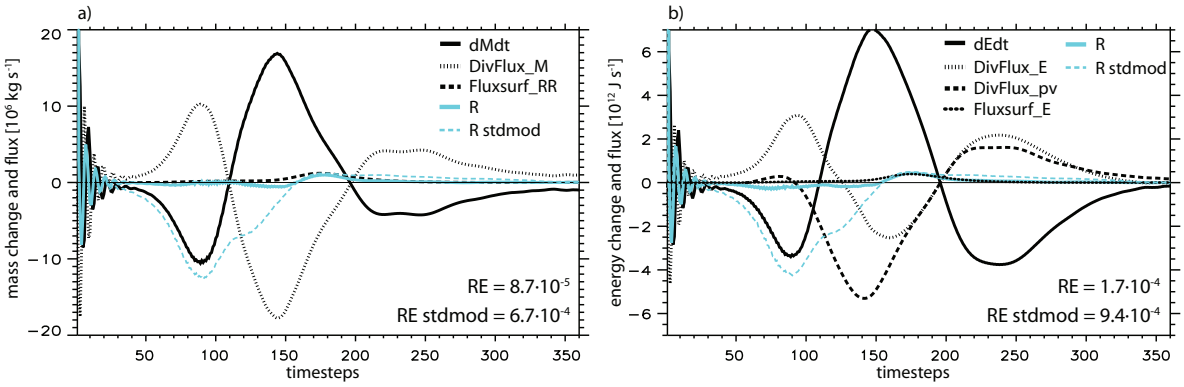

Figure 2.12: Case WKRAIN ($\Delta t = 20$ s). Sub-domain budgets of the total mass and energy concerning the CV. a) and b) as in Figure 2.8a and 2.8b but using the COSMO-MP model. For comparison, the residual curves and the RE of the standard model are given, named 'R stdmod' and 'RE stdmod' respectively.

Table 2.5: RE of energy and total mass budget against the CAPE for case WKRAIN. Values listed for standard model and COSMO-MP.

	Total mass		Energy	
CAPE	COSMO	COSMO-MP	COSMO	COSMO-MP
288 J kg^{-1}	$3.8{\cdot}10^{-4}$	$8.7{\cdot}10^{-5}$	$5.2{\cdot}10^{-4}$	$1.4{\cdot}10^{-4}$
611 J kg^{-1}	$5.0{\cdot}10^{-4}$	$8.5{\cdot}10^{-5}$	$6.8{\cdot}10^{-4}$	$1.4{\cdot}10^{-4}$
1037 J kg^{-1}	$6.7{\cdot}10^{-4}$	$8.9{\cdot}10^{-5}$	$9.3{\cdot}10^{-4}$	$1.7{\cdot}10^{-4}$

mentioned in Section 2.4.4, the generation of rain water and its evaporation in the lower troposphere will be the dominant physical processes in the course of the simulation. Using the COSMO-MP instead of the standard model, the cooling in the downdraft due to evaporation of rain water does influence the pressure inside the grid cells of the model. The COSMO-MP simulates airflows in the evaporation regions, but the standard model does not. Consequently, the standard model erroneously gains mass in the lower atmosphere (Figure 2.9a), whereas the COSMO-MP does not produce any significant error.

The COSMO-MP improves the conservation properties. The implementations introduced in Section 2.5 qualifies the COSMO model to simulate physical processes on scales of resolved convection, which could not be handled by the model equations of the standard COSMO. Nevertheless, there is an inconsistency which remains in the model and which is reflected by the imbalance in the total mass and energy budget between time step 150 and 200 (Figure 2.12). The assumption of a vanishing vertical velocity normal to the Earth surface results in an artificial mass gain by overestimating the positive pressure change near the surface. In order to account for a net mass transfer across the Earth surface due to evaporation and precipitation, Wacker et al. (2006) concluded that a proper boundary condition for the vertical velocity according to eq. (2.15) has to be used in NWP models. Since Lackmann and Yablonsky (2004) examined in model studies that the effect of a mass sink due to precipitation exerts has a

non-negligible influence on the dynamics of a tropical cyclone, we should be motivated to implement the boundary condition (2.15) also into the COSMO model.

The difference between the standard model and the COSMO-MP in terms of the precipitation rate is shown in Figure 2.13. The COSMO-MP simulates a little less rain until 50 minutes compared to the standard model. Later on, the rain rates are slightly higher for the COSMO-MP. The difference might originate from the modified saturation adjustment of COSMO-MP, which releases more latent heat and increases the maximum vertical velocities relative to the standard adjustment (not shown here). I. e. the sedimenting rain water flux in sub-cloud layers is damped by an enhanced intake of moist air, which drops the precipitation rate relative to the standard model. In the subsequent process, the increased generation of cloud water leads to a larger precipitation rate using the COSMO-MP. Nevertheless, the RE of the water mass budget does not change significantly using the COSMO-MP model instead of the standard model.

2.6.2 Case REAL - Realistic test case

Our budget analysis is applied to a real test case to investigate error magnitudes of an operational forecast. The high resolution COSMO model (COSMO-DE, $\Delta x \simeq 2.8$ km) is nested into a low resolution model version (COSMO-EU, $\Delta x \simeq 7.6$ km). A forecast of 30 hours is performed for 12 August 2002 starting at 0 UTC using the COSMO-MP model with BOTT advection (**BOTT-MP**) and the standard model with BOTT-advection (**BOTT-SM**). Additionally, we run the standard model with SL advection (**SL-SM**).

Synoptic overview

During 11 August 2002 the lee cyclone 'ILSE' developed to the south of the Alps and advected moist and warm air, originating from the Mediterranean sea. 'ILSE' propagated as a so-called Vb-cyclone from Italy via the Czech Republic to Poland. At 12 am on 12 August its center was located in South-West Poland (Figure 2.14a). Its occlusion separated the cold air to the west from the moist and warm air to the east. Due to the long lasting phase of orographic lifting and the almost stationary location of 'ILSE' over south-western Poland high amounts of precipitation occurred in the region of Erzgebirge (result of the BOTT-MP model run, Figure 2.14b). At the station Zinnwald-Georgenfeld 312 mm rain were measured within 24 hours (07-07 MEZ). A few days later, a flash flood took place in the Erzgebirge, causing heavy floods along the river Elbe.

Sub-domain budget analysis

The budget analysis is carried out in different control volumes, shown in Figure 2.14b. Each control volume has a horizontal extension of 30 grid points (80 km $\times$ 80 km) and extends from the surface to 9.8 km height. The functionality of the diagnostic tool for

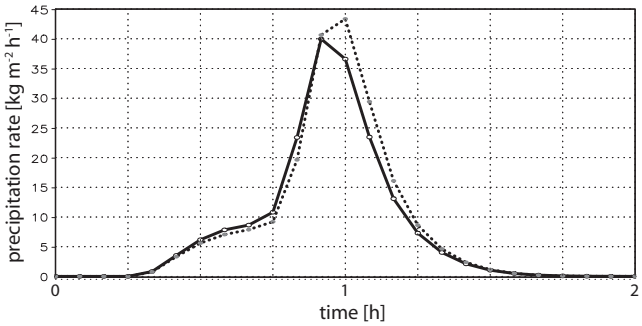

Figure 2.13: Case WKRAIN. Precipitation rate [kg m^{-2} h^{-1}] as a sixteen grid point average using the standard model (solid line) and the COSMO-MP (dotted line).

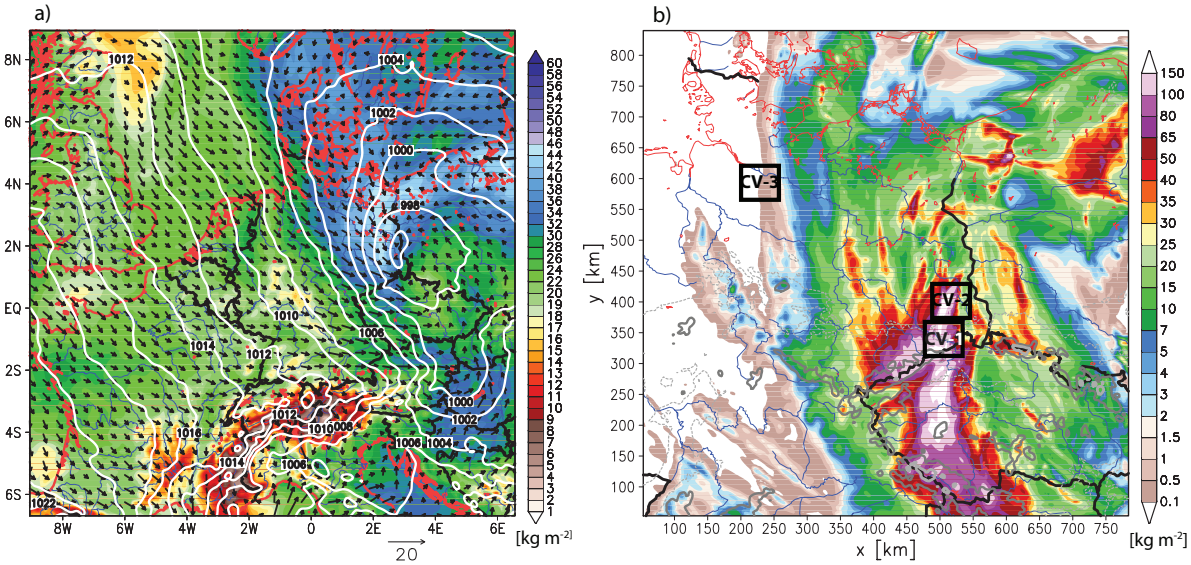

Figure 2.14: REAL test case of 12 August 2002. a) COSMO-EU analysis at 12 UTC for the sea level pressure [hPa] (contour), the column-integrated water vapor [kg m^{-2}] (shaded) and the wind vector [m s^{-1}] at 10 m height. b) High resolution COSMO-DE forecast. The 24 hour accumulated precipitation [kg m^{-2}] (shaded) from 06 UTC of 12 August 2002 until 06 UTC of 13 August 2002. Additionally, the contour line of 500 m height is displayed (gray line). The investigated control volumes (CV) are denoted by a black rectangle and the numbers are the same as used in the text.

mountainous regions was already tested with an ideal shifting inside the COSMO grid (Baldauf, 2008).

CV-1 covers the region windward to the Erzgebirge with Zinnwald-Georgenfeld in its center. When the low reaches the Erzgebirge, the moisture flux into CV-1 becomes stronger than the outgoing moisture flux (8 UTC, Figure 2.15a). This leads to a 3-d moisture flux convergence, which strengthens until 15 UTC. High amounts of precipitation occur. Afterwards the low moves eastward in the forecast (slightly faster than it was observed) and the precipitation rates decrease.

During the first hours of slight prefrontal rain and convection, which is diagnosed by oscillations in the curves of water mass change and mass convergence (Figure 2.15a), the

water mass is well conserved in all three model configurations (BOTT-MP, BOTT-SM, SL-SM). During the strong precipitation event, which is characterized by long phases of high precipitation and convergence rates (from 10 UTC until midnight, Figure 2.15a), the performance is decreasing for BOTT-SM and SL-SM. The RE is 23 % using the BOTT-SM model (brown line, Figure 2.15a) and 16 % using the SL-SM model (gray line). From the point of view of the sub-domain diagnostic, both simulations lost a significant part of the water mass in the CV-1 within one day. 23 % relative error in water mass are equal to 10 kg m^{-2} precipitable water. This might partly explain, why the simulated precipitation differ from the observations in the Zinnwald region. In contrast to the ideal cases, the Semi-Lagrange advection performs better than the BOTT advection, which might hint at the pros of a SL scheme in mountainous regions. It produces no splitting errors.

The water mass budget is much better using the BOTT-MP configuration (blue line, Figure 2.15a). The water mass loss during the heavy precipitation event is significantly decreased. The RE reduces from 23 % to 8 %. Due to the improvement in water mass conservation we further investigated the precipitation forecast. In Figure 2.16a a comparison between observations and model results is shown. The precipitation at Zinnwald-Georgenfeld is increased by 30 % using the BOTT-MP configuration instead of BOTT-SM. This seems to be much more realistic, but we will not draw a conclusion about the forecast skills of both models. Here we only want to mention that the COSMO-MP simulation is physically consistent. Moreover, we test the hypothesis of Dudhia (1993) about the problem of an unrealistic warming of the middle and upper troposphere due to the influence of diabatic effects on the pressure, which is supposed to occur for those models that apply a rigid lid condition. We thus checked vertical profiles of the temperature and compared them with radio sounding data at 06, 12 and 18 UTC at the stations Prag (Figure 2.16b) and Lindberg (here not shown), because at that locations and times high amounts of diabatic heat release are expected due to heavy rainfall. We could not find a signal indicating an unrealistic warming in the COSMO-MP model data.

The total mass and energy is not well conserved in the simulations (see Figure 2.15c,d), but there is a big improvement in the simulations using the BOTT-MP configuration (compare the brown with the blue lines). The RE of total mass is 14 % and the one of the energy is 19 % using the BOTT-SM configuration, whereas the residual values are much smaller using BOTT-MP, i. e. 2 % for the total mass and 3 % for the total energy. The residua in the BOTT-SM simulation are almost larger than any physical tendency, which means a big error.

Mass budget errors and diabatic heating are strongly related (Figure 2.15b). In addition to the latent heat release and latent heat storage from phase changes (black and green line in Figure 2.15b), also radiative heating (red line) is relevant in the real simulation. Therefore, errors in mass and energy conservation of the BOTT-SM scheme can also be explained by shortcomings in simulating the expansion and contraction of a CV by short-wave and long-wave radiation. But we cannot investigate these shortcomings, because the radiative forcing is smaller than the cloud microphysical forcing (Figure 2.15b) during the whole simulation. We only note that the COSMO-MP model is able to resolve these radiative processes. Nevertheless, minor errors are still left when using

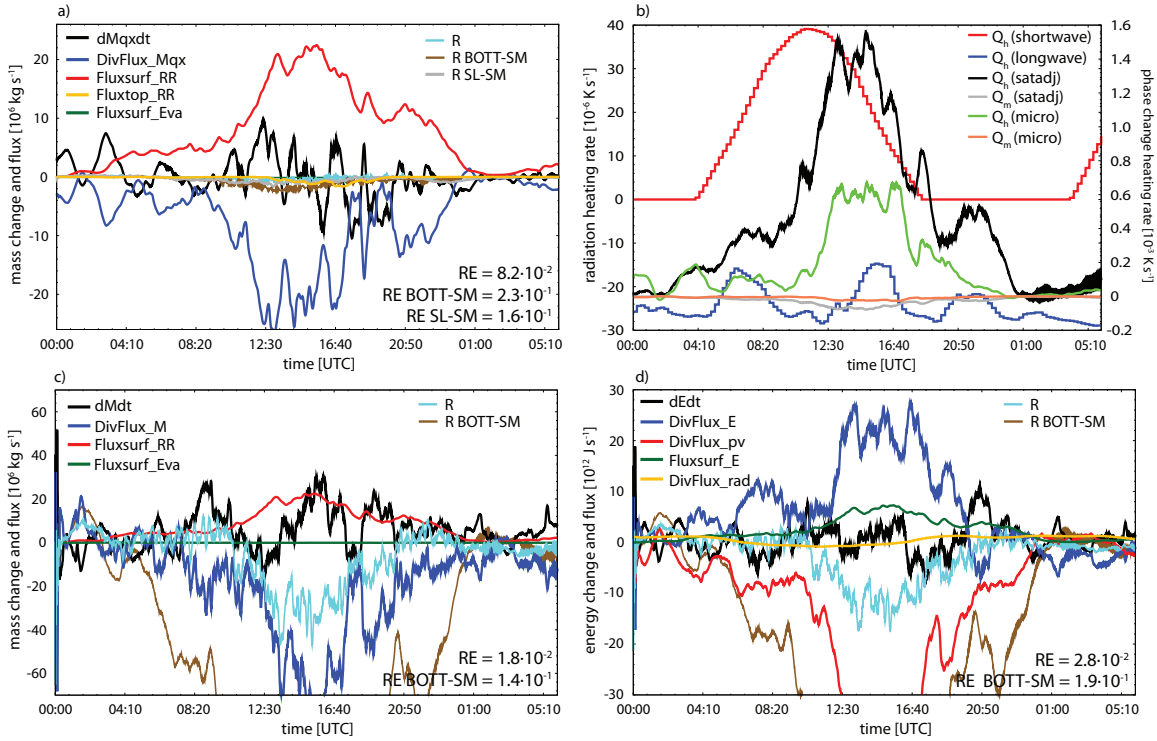

Figure 2.15: Real test case of 12 August 2002. Sub-domain budgets of the CV-1 using the BOTT-MP scheme. The residual curves and the RE of the BOTT-SM and the SL-SM model are denoted by 'R BOTT-SM', 'R SL-SM', 'RE BOTT-SM' and 'RE SL-SM'. a) Water mass budget [kg s^{-1}] involving precipitation flux (Fluxtop_RR) at the top of the CV and evaporation (Fluxsurf_Eva). b) Diabatic heat sources [K s^{-1}] of the temperature equation (2.24) split into parts concerning radiation (short-wave, long-wave), condensation (satadj) and cloud microphysical processes (micro). c) Total mass budget [kg s^{-1}] involving evaporation (Fluxsurf_Eva). d) Total energy budget [J s^{-1}] involving the radiation (DivFlux_rad, eq. (2.19)).

the BOTT-MP. We speculate that the error can be further reduced, if all physical temperature tendencies are analyzed for the real case and a solution is found to make the computations in the dynamics and in the physics coherent (according to eq. (2.24) and (2.23)).

The transport of turbulent sensible heat fluxes and turbulent momentum fluxes (which influence the kinetic energy) do not significantly contribute to the energy budget (eq. (2.18)). They are at least one order of magnitude smaller than the radiation budget (dark yellow line in Figure 2.15d).

Beside the conservation analysis, the budget curves point out processes like warm air advection or the formation of snow by an increase of sensible internal energy and the drying of air masses by a decrease of latent energy.

We also investigated sub-domain budgets with respect to CV-3, which is located to the south of Hamburg (Figure 2.17). In this region, physical processes are fully different to the Zinnwald region. Slight precipitation is present at the beginning of the simulation. A divergent flow is developing in the morning due to the impact of a high propagating

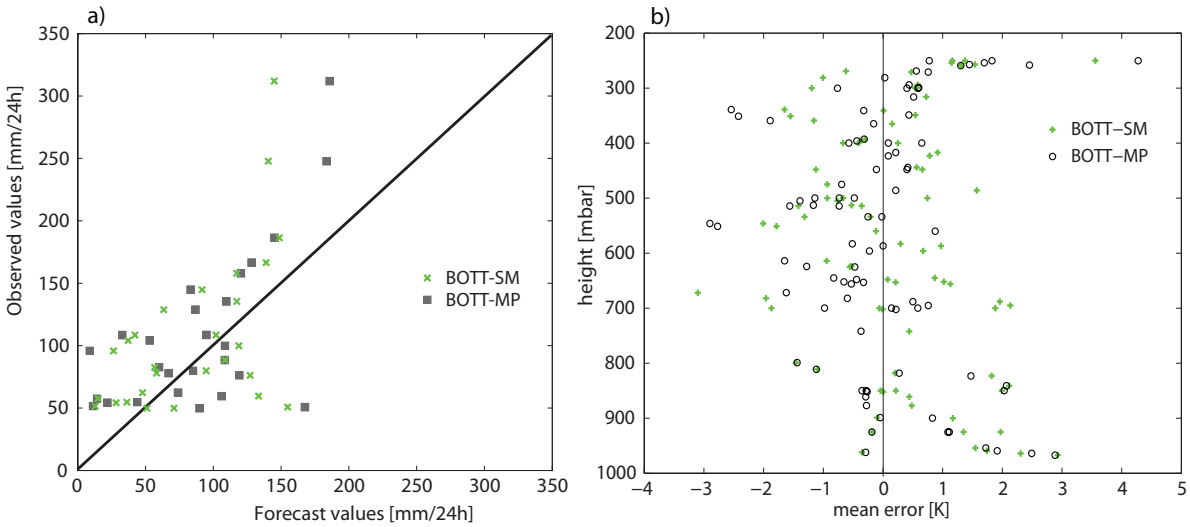

Figure 2.16: a) 24 hours accumulated precipitation from 06 UTC of 12 August 2002 until 06 UTC of 13 August 2002. Scatter plot of the observations and model results using a BOTT-SM (crosses) and a BOTT-MP (rectangles) configuration. Data set of 27 stations near the Erzgebirge. b) Mean error of the temperature [K] using the BOTT-SM (crosses) and the BOTT-MP (rectangles) configuration. The error refers to the data of the radio soundings at the station Prag-Libus at 06, 12 and 18 UTC. The model grid point data were interpolated to the location of Prag-Libus.

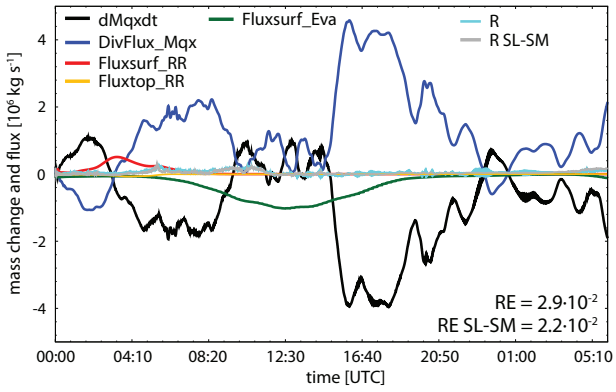

Figure 2.17: As in Figure 2.15a, but for the region to the south of Hamburg (CV-3). Note the different scaling of the ordinate.

eastwards and drying-out the atmosphere. The clear sky shortwave radiation induce an evaporation flux in the afternoon that supplies water vapor for the lower atmosphere and leads to small turbulent perturbations reflected by small-scale oscillations in the water mass change and divergence. Mostly all water mass changes and fluxes are balancing each other. The RE is about 2 % to 3 % for all configurations. The differences of the RE are small, because diabatic processes are mostly irrelevant. Only the radiative heating contributes to small errors in total mass and energy, which are less than one percent for all model configurations, i. e. BOTT-SM, SL-SM and BOTT-MP.

2.7 Summary and Conclusions

This work demonstrates the construction and application of an 'evaluation approach' by which the sub-domain budgets of energy, water mass and total mass can be analyzed in a predefined control volume (CV). As a basic prerequisite we investigate the diagnostic scheme using different discretization methods in an idealistic test bed. An ideal and numerical shifting of various test functions through a control volume has revealed errors originating from discrete grids and flux reconstructions. We defined a configuration for our tool, that minimizes these errors: a Lax- Wendroff- or a third order reconstruction method and a CV-size, that exceeds a critical value of $10\times10\times10$ grid points.

The evaluation method is applied to the mesocale model COSMO. For this purpose we defined the budget equations consistent to the physical formulation of the COSMO. With determining the sources and sinks of mass and energy more complex test cases have been investigated. A rising warm air bubble (Weisman and Klemp, 1982) was used to evaluate the conservation properties of COSMO. The simulations without condensation showed good conservation properties. Slight defects (RE in the order of 10^{-3} %) occur due to the application of an advective form of the discretized thermo-hydrodynamical equations and due to splitting errors associated with the BOTT-transport scheme.

Taking into account condensation and precipitation processes leads to large errors for the sub-domain budgets (RE of 0.1 % within 2 hours) of total mass and its related quantity energy. These imbalances are associated with the water mass redistribution term and the diabatic term, which contributes to the latent heat release in clouds and to the rainwater evaporation in sub-cloud layers (see also the benchmark of Bryan and Fritsch, 2002). Neglecting these terms in the pressure equation suppresses a balancing flow that is consistent with the heating or cooling in the CV. Therefore, we formulated a new saturation adjustment and we modified the equations concerning microphysical and radiative process. These modifications were implemented in a new COSMO model named COSMO-MP. We improved the mass and energy conservation using the COSMO-MP model. We qualified the model to simulate all relevant physical processes on scales of resolved convection, which includes the correct representation of gravity waves. Nevertheless, the sub-domain analysis has also pointed out that a proper boundary condition for the vertical velocity is needed for the COSMO model in order to account for a net mass transfer across the Earth surface due to precipitation and evaporation.

Regarding the water mass, we have diagnosed only a slight impact of the large total mass and energy errors for the cases with condensation and rain physics. Accordingly, the improvement of the water mass conservation using the modified model COSMO-MP instead of the standard model has been less effective (factor 2) in comparison to the total mass. The investigation of the real test case showed an improvement factor of 3, which reduces the numerical error from $10\,\mathrm{kg\,m^{-2}}$ to $3\,\mathrm{kg\,m^{-2}}$ precipitable water within 24 hours. Additionally, the BOTT-scheme has performed better for the Weisman-Klemp-case than the SL-scheme. The SL advection scheme works particularly bad in case of switched off horizontal diffusion (tends to a large positive bias in water mass), but seems to be advantageously in mountainous regions.

In order to study the impact of non-physical damping schemes on the subdomain budgets, we have carried out a sensitivity analysis concerning the frequently used horizontal diffusion and divergence damping. These numerical techniques that stabilize the model run, have not such a large impact as the physical errors. An exception is the horizontal damping used without diffusion. This configuration seems to be at the limit of stability and leads to large relative errors.

Some aspects of our results confirm earlier studies, in which the mass deficit due to neglecting some diabatic heat terms in the equations was mentioned (e. g. Dudhia, 1993; Doms and Schaettler, 2002; Bryan and Fritsch, 2002). We have shown that our analysis of model conservation properties can reveal insight into the model qualities. With our 'evaluation tool' we provide the possibility for diagnosing budgets in any sub-domain inside the model domain. Thus, we can analyze realistic test cases. We have pointed out that the numerical schemes can impact the conservation properties up to the order of 1 %. Furthermore, diabatic processes were identified to be relevant for a reliable mass and energy conservation in a numerical model. The physical treatment of the diabatic processes can impact the conservation properties up to the order of 10 %. Since the diabatic processes are quite generic and the related parameterizations are similar in COSMO and other NWP models, it is relevant to perform similar evaluations for other models. This statement also holds for those written in flux form.

Concerning the operational COSMO model, an alternative formulation of the equations and physical parameterizations as presented in this chapter, might have a positive impact on the model results. A saturation adjustment approach based on our method was tested and evaluated at the German Meteorological Service in the framework of a pre-operational version. Indeed, preliminary studies indicate that the quality of the forecast is improved compared to the standard operational model (Ulrich Blahak, personal communication, 2010).

3 Using spectral decomposition as a performance test for limited area mesoscale models

3.1 Introduction

As well as the budget analysis of sub-domains presented in chapter 2, multi-scale statistics such as Fourier analysis help to verify weather forecast and climate models as demonstrated by Harris et al. (2001), Skamarock (2004) and Laprise et al. (2008). We introduce here the multi-scale statistics methods as an additional 'diagnostic tool' for mesoscale models. The nonlinear scale interactions mainly within the COSMO model are examined in the mesoscale range of nearly 1000 kilometers down to 5 kilometers.

Below the mesoscale range, the statistics of the turbulent flow and the corresponding energy transport due to nonlinear interactions can be described with the three-dimensional turbulence theory of Kolmogorov (1941): energy is transported within the inertial subrange down to smaller scales respectively higher wave numbers k. The energy cascade follows a $k^{-5/3}$ law down to scales, where the energy is converted into molecular heat. The energy spectrum above the mesoscale range is usually explained by two-dimensional turbulence following Kraichnan (1967): at the same time as energy is cascaded from a synoptic-scale source to smaller wave numbers, i.e. an inverse energy inertial range compared to Kolmogorov (1941), enstrophy is cascaded from the synoptic-scale source downscale to higher wave numbers. Within the enstrophy cascade energy transport is suppressed and the energy spectrum follows a k^{-3} law. Observational studies of Julian et al. (1970), Desbois (1975), Boer and Shepherd (1983) and the combined space-time spectra of analyses data by Pratt (1977) provide evidence for a two-dimensional enstrophy cascade and a k^{-3} behaviour of spectral energy in the range between the large-scale waves (a few thousand kilometres) and the low pressure systems (several hundred kilometres).

The spectral distribution of the wind velocity above the boundary layer in the mesoscale was obtained by an observational analysis of Vinnichenko (1970), Gage (1979) and Lilly and Petersen (1983). They found a $k^{-5/3}$ behaviour of the kinetic energy spectra. In more comprehensive studies, Nastrom et al. (1984) and Lindborg (1999) investigated the atmospheric wavenumber spectra of the kinetic energy obtained from aircraft flights over the whole globe. They also found a $k^{-5/3}$ law behavior for scales from a few kilometers up to a few hundred kilometers. Regarding the $k^{-5/3}$ law in the mesoscale range, various hypotheses have been put forward to explain the origin of energy in the spectrum and to describe the turbulent energy transport between the scales. One explana-

tion is, that the energy comes from the large-scale internal gravity waves (VanZandt, 1982; Bacmeister et al., 1996). If these waves break, energy is cascading downscale through the mesoscale spectrum following a $k^{-5/3}$-law (comparable to the Kolmogorov energy inertial range). Another explanation comes from Gage (1979) and Lilly (1983). They assume that the energy input originates from strong shearing instabilities within the jet streams and from convection. Parts of these 3-d energy is transformed to a 2-d stratified turbulence. The energy is transported from small scales to large scales in a two-dimensional inverse-cascading energy inertial range, in the same sense as in the two-dimensional turbulence theory of Kraichnan (1967). Lilly (1989) suggested to describe the behavior of a turbulent flow by using a model with a large-scale and small-scale force, which enter energy in the flow field. One force reflects the baroclinic instability within the long planetary waves and the other force originates from convective instabilities. In between, at the same time an enstrophy flux occurs downscale to high wave numbers and an energy flux takes place up-scale to small wave numbers. The interaction between the two-dimensional enstrophy- and the energy inertial range is very small. Following Lindborg (1999), the small-scale end of the mesoscale spectrum cannot be explained straightforward by two-dimensional turbulence and an energy inertial range.

Keeping in mind the theories about the development of a energy cascade in the mesoscale, we want to examine the energy cascade as predicted from the high-resolution COSMO model. In the first part, we thus invoke the multi-scale Fourier analysis to evaluate the high-resolution COSMO model on the basis of observations derived from aircraft flights over Central and Southwestern Europe, which were part of the Convective Orographic precipitation study (COPS, Wulfmeyer et al., 2008). That is, we prove the ability of the COSMO model to predict feasible characteristics of the kinetic energy spectra at the mesoscale range over a certain region. In contrast to the large-scale analyses of global models done by Boer et al. (1984) and Laursen and Eliasen (1989) and later on the analysis of the transition from the large-scale to the mesoscale done by Koshyk and Hamilton (2001), we focus not purely on the slope of the energy cascade but also investigate the spectral amplitudes of the energy cascade. Skamarock (2004) already investigated the turbulent characteristics of WRF model forecasts using the global and yearly mean spectra of Nastrom et al. (1984) and Lindborg (1999) as a reference. In this study observational data gathered during the COPS campaign are additionally used in order to evaluate the predicted turbulent characteristics of the COSMO model with respect to a specific region and time period. The motivation for our work arises due to the fact that the turbulent characteristics of the atmosphere are highly important for the life cycle of convection.

Since the domain of the COSMO model is limited to horizontal scales of less than 1000 km (5 times smaller than for the WRF model, Skamarock, 2004)), we discuss at the beginning briefly several spectral decomposition methods in terms of the application to limited area model outputs.

In the second part, we extend the analysis of the spectral characteristics of the model to reveal a deep insight into physics and the dynamics of the high resolution COSMO model. As already demonstrated by Lean and Clark (2003), Bryan et al. (2003) and Skamarock (2004), the spectral analysis benefits to estimate the 'true' resolution capa-

bilities. We examine the effective resolution for the COSMO model. Since the effective resolution is defined by the behavior of the spectrum at the small scale end, we explore the influence of numerical damping schemes and physical parameterizations on the model forecast spectra. Furthermore, we analyze how much time the model requires to develop its own mesoscale spectrum during the initial spin-up process, i. e. when the model offers its 'real' high resolution upon an adjustment to observational forcing data with coarse resolution (Skamarock, 2004). It is discussed which processes dominate the spin-up.

3.2 Performance of spectral decomposition methods on limited domains

The spectral decomposition of various atmospheric fields is inherent in many global models due to their global and periodic domain. The determination and evaluation of the model spectrum is straightforward. High-resolution cloud models, simulating convection on small scales, apply simplified lateral boundary conditions. Therefore, they have also been examined using a standard Fourier analysis (Vallis et al., 1996; Lilly et al., 1998; Schröder et al., 2006). When analyzing the mesoscale spectra of limited area forecast models, a number of difficulties arise. Mainly, the atmoshperic fields are no longer periodic on a limited domain. Various approaches have been developed to overcome the problem of aperiodicity.

a) The windowing technique multiplies the physical field by a weighting function that diminishes from one to zero from the central sub-domain to the boundaries. The positive effect is that a Discrete Fourier analysis (DFT) can be performed on the 'windowed' field. The downside of the windowing method is that it also modifies the spectrum of an already periodic field and it cut off data at the lateral boundaries of the physical field. Thus, the windowing technique is applicable only for atmospheric fields on large domains (Salvador et al., 1999), which is in contradiction to the needs for the data analysis of high-resolution limited-area models.

b) Errico (1985) put forward the detrending approach (DDFT). The detrending technique makes a physical field periodic by removing its linear trend. Afterwards, the Fourier analysis is applied to the detrended field. The disadvantage of the detrending method is that it affects the large-scale components of the spectrum and produces line patterns (Errico, 1985; Denis et al., 2002).

c) To circumvent the problem of manipulating the original field prior the application of a Fourier transformation, Ahmed et al. (1974) introduced the discrete cosine transform method (DCT), which was adopted by Denis et al. (2002) for atmospheric model applications. In contrast to the DFT, the spectral decomposition based on the DCT is done using only cosine wave parts but not sine parts. Thus, the DCT is not able to detect a sine function at the same level as the DFT.

We want to discuss shortly, which algorithm is appropriate for analyzing the mesoscale spectra of atmospheric fields on a small model domain.

3.2.1 Variance Spectra using the DCT

The spectrum of any atmospheric field is determined by applying a discrete Fourier transformation (DFT) (Stull, 1988). Although the model output provides two-dimensional fields at various height levels, we want to consider the one-dimensional transformation. Because all spectra derived from observations are obtained from one-dimensional flight paths, we must compare them with the 1-d spectra of the model output. Computing 1-d transformations instead of 2-d transformations allows us to control whether to analyze in x- or in y-direction. We are not forced to convert the two-dimensional field of spectral coefficients to a 1-d spectrum (Errico, 1985; Denis et al., 2002, the binning process). We also produced 1-d spectra from 2-d transformations following Errico (1985) and Denis et al. (2002), but the slope of the spectrum and the amplitude of the spectral variances were not comparable with the observations.

The Fourier analysis transforms any field to spectral coefficients, which are proportional to the variance that is caused by a spatial structure with a specific wave length. If the analysed field is highly aperiodic, the basic functions of the DFT no longer fit to the field and the transformation produces large errors. The discrete cosine transform (DCT) approach applies a symmetrization process to obtain a periodic field, i. e. taking a mirror image of the original field prior the DFT (Ahmed et al., 1974). It was introduced by Denis et al. (2002) for meteorological applications and used by de Ela et al. (2002) for the investigation of regional climate models.

In Figure 3.1a a cosine function is overlapped by a linear function (black line). The DFT method only uses the original function, whereas the DCT analyses additionally the mirror image (blue line). That is, the DCT 'sees' a periodic function containing twice the grid points as the original function.

The largest scales that can be analyzed by the DCT on a grid with N points and with a grid spacing Δx_i have a wavelength

$$\lambda_{max} = 2N\Delta x_i,$$

which is twice the length of the domain. The variance of the highest wave number, k equals $N-1$, can be associated with small-scale structures with a wavelength λ_{min} of nearly $2\Delta x_i$.

The spectral coefficients of the DCT are defined as

$$\begin{aligned} c_{DCT}(k) &= \beta(k) \sum_{i=0}^{N-1} f(i) \cos\left(\pi\, m\, \frac{i+1/2}{N}\right), \text{ with } \beta(k) = \begin{cases} \sqrt{\frac{1}{N}} & , k = 0 \\ \sqrt{\frac{2}{N}} & , k \geq 1 \end{cases}, \\ \sigma^2_{DCT}(k) &= \frac{c_{DCT}(k)^2}{N}. \end{aligned} \tag{3.1}$$

$f(i)$ is the field value at the grid point i and $c_{DCT}(k)$ is the spectral coefficient that corresponds to a wave number k. N indicates the number of grid points. $\sigma^2_{DCT}(k)$ is the variance corresponding to the spectral component $c_{DCT}(k)$.

Since the DCT coefficients only consist of cosine and not sine parts, the DCT cannot detect a sine function on the same level as the DFT, which may be a disadvantage.

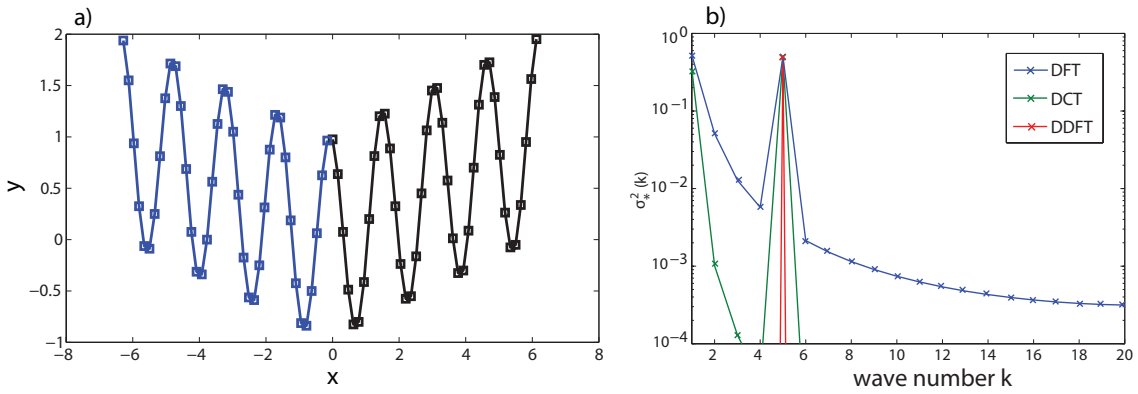

Figure 3.1: a) A cosine function with a linear trend (black) and its mirror image (blue). b) Spectral variances applying the DCT, DFT and DDFT on the black function shown on the left side.

Moreover, one cannot compare the spectral variances determined by the DCT and DFT approach. Denis et al. (2002) suggested to gather the variances of the DCT to have a comparable variance $\sigma^2_\star(k)$:

$$\sigma^2_\star(k) = \frac{\sigma^2_{DCT}(2k-1)}{2} + \sigma^2_{DCT}(2k) + \frac{\sigma^2_{DCT}(2k+1)}{2}\,. \tag{3.2}$$

Using eq. (3.2) and (3.1), we compute the discrete variance spectrum of the function visualized in Figure 3.1a. Figure 3.1b shows the variance $\sigma^2_\star(k)$ derived from the DCT method and also the spectral variances derived from the DFT and from the detrending DFT method (DDFT) by Errico (1985). Note that the spectra are composed of discrete values (the crosses), but the straight lines help to make the diagram readable. The DDFT, as well as the DCT techniques, manage to filter the linear trend, whereas the DFT produces aliasing errors. The lowest gathered mode $k = 1$ of the DCT, which contains not only the mean value but also the mode corresponding to the wave length $\lambda = 2N\Delta x$, absorbs most of the linear trend. We will exclude this mode for the ongoing examinations.

The DDFT does a perfect job for this idealized case. Usually, the aperiodicity of an atmospheric field is not induced by a linear function, but by large-scale structures, which do not fit into the limited domain of a high-resolution model. Therefore, we have pushed the validating test one step further.

3.2.2 Computing spectra of synthetic fields

As already mentioned, observations of the mesoscale spectra show a $k^{-5/3}$ behavior for the kinetic energy followed by a transition region at a few hundred kilometers, in which the spectrum adjusts to a k^{-3} law. We generate synthetic fields, which possess spectral slopes following a $k^{-5/3}$ law and a k^{-3} law, in order to test the different approaches of spectral decomposition. We define a single synthetic field by overlapping N_s cosine

functions

$$y(x) = \sum_{n=1}^{N_s} {k_n}^{-b/2} \cos\left[k_n \left(x + \frac{\Delta x}{2}\right) + \varphi_n\right] \text{ , with } x \in \left[0, \frac{3\pi}{2}\right] , \tag{3.3}$$

where the phase shift φ_n and the wave number k_n are random real numbers in the range of: $\varphi_n \in [-\pi/2, \pi/2]$ and $k_n \in [0.1, N_x - 1]$. The number of cosine functions N_s is set to 150. The phase shift and the wave number are different for every of the 150 cosine functions. The varying phase shift ensures that also sine functions enter our ensemble. The constant b is related to the spectral slope. To simulate high aperiodic fields, we cut off the functions arbitrary at $x = 3\pi/2$. The number of grid points within the domain N_x is 150 and the grid spacing is $\Delta x = \pi/100$. We apply the DCT, DDFT and DFT method to the synthetic function. Afterwards, we repeat our analysis with the next synthetic field. Finally, two ensembles of 2500 synthetic fields are generated: one for parameter $b = -3$ and one for $b = -5/3$. The mean of every spectral coefficient corresponding to a specific wave number is determined.

The variance spectrum of the synthetic fields is shown in Figure 3.2. The reference lines are denoted by black lines and characterize a k^{-3} (straight) and a $k^{-5/3}$ (dashed) law. Note that the lowest displayed mode $k = 2$ can be associated with a wavelength of $\lambda = N_x \Delta x$. The spectrum having a slope of -3 (left lines) is discussed first. The DFT algorithm (blue line) produces large variances for all wave numbers due to aliasing, i.e. the aperiodicity of the large waves is misinterpreted as high wave number components and leads to an artificial energy flux downscale. The artificial cascade follows nearly a k^{-2} law. The DDFT (red line) and the DCT method (green line) give nearly the same spectra. An exception is the region of small wave numbers. The detrending affects the large-scale waves, which leads to higher variances for the DDFT compared to the DCT. Nevertheless, also the DCT analyses depart from what we would expect from our input fields (the black reference line), but it reveals the smallest aliasing errors of all methods. Additionally, the computed spectrum produced by the DDFT and the DCT method tends to have a small upturn at the end of the tail, which may arise from insufficient capabilities to resolve short waves on the grid.

If the predefined synthetic spectrum follows a $k^{-5/3}$ behavior, the aliasing errors of the DFT are significantly reduced but still apparent. The errors of the DDFT method, concerning the modification of the large-scale components, are even more pronounced. This is a big disadvantage for the analysis of spectra on small limited domains. As already mentioned by Denis et al. (2002), a drawback of the DDFT method is that it effects the large-scale components of the spectrum. For instance, the spectrum at low wave-numbers could be misinterpreted as a transition between an energy cascade to an enstrophy cascade.

Emulating dissipation at high wave-numbers

Typically, the ability of NWP models to resolve small scales is limited by damping mechanisms that are needed to dissipate energy at the small-scale waves and to prevent a non-physical build-up of energy. To emulate the dissipation process, we generate

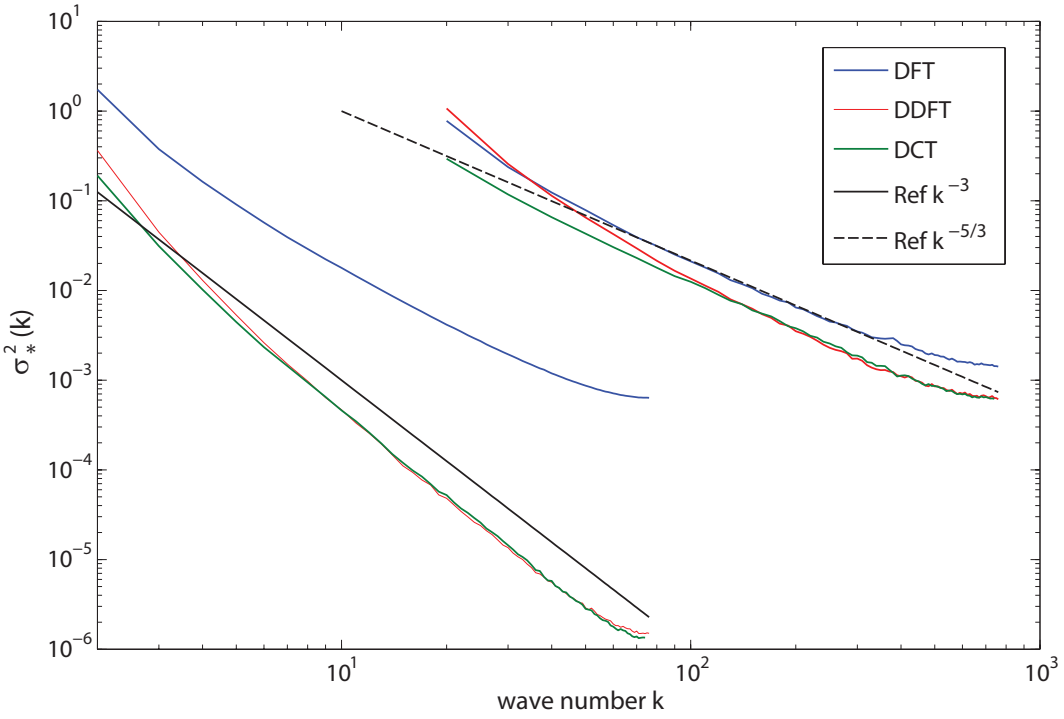

Figure 3.2: Spectral variances of synthetic fields, which have a $k^{-5/3}$- and k^{-3}-law behaviour, using different decomposition methods. The curves corresponding to the $k^{-5/3}$-case are shifted to the right by one magnitude for better visibility.

synthetic fields that are equal to those fields of eq. (3.3), but contain only a small wave-number portion of the spectrum, i. e. $k_n \in [0.1, 15]$. We prescribe a $k^{-5/3}$ behavior of the spectrum ($b = -5/3$).

The spectra computed by the DCT and the DDFT method are shown in Figure 3.3 (straight lines). Both methods show a clear cut-off of the small-scale waves. The DDFT spectrum has an upward tail at high wave-number components which indicates aliasing errors. The slope of the DCT spectrum is nearly perfect for all scales.

Emulating the occurence of isolated structures

Atmospheric fields sometimes show isolated pronounced structures in a certain limited area region, e. g. a convergence line, a foehn front or a jet stream. A spectral analysis of such a field leads to large aliasing errors, which is the so-called leakage problem (Stull, 1988). We simulate this leakage effect by generating synthetic fields equal to those given by eq. (3.3), but contain only a small wave number part ($k_n \leq 15$). In addition, every synthetic field is overlapped by five cosine functions (eq. (3.3), $N_s = 5$) having a wavenumber $k_n \in [6, 13]$. Afterwards, the five functions are set to zero except for one single wave located at the center of the domain.

The spectra computed by the DCT and the DDFT method can be seen in Figure 3.3 (crosses). An energy buildup is induced at the high-wavenumber components due to the isolated structures in the domain center. Assuming that the model spectra decrease rapidly for small-scales due to filter operators, the energy buildup will dominate the

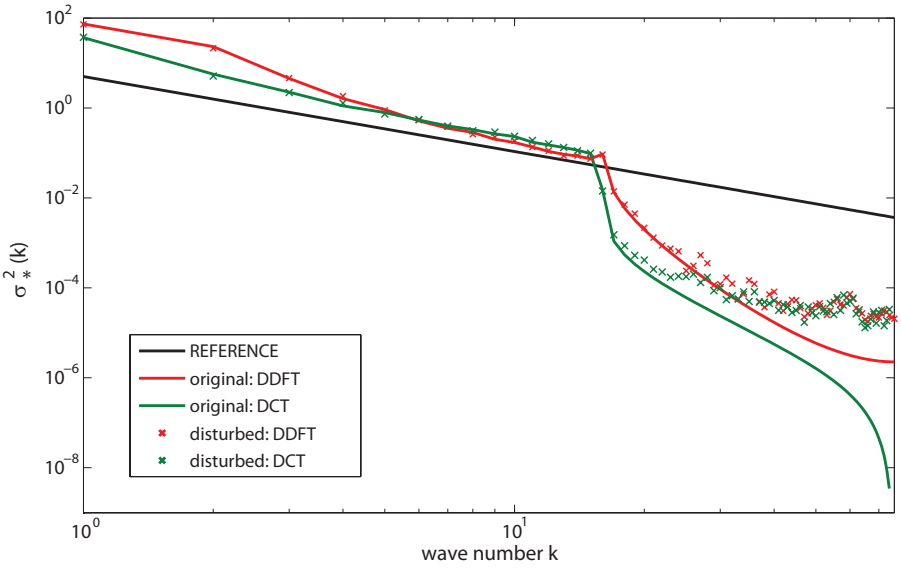

Figure 3.3: Variance spectra of synthetic fields having a $k^{-5/3}$-law behaviour using the DCT (green) and the DDFT method (red). The straight lines denotes the experiment, where the synthetic fields only consist of waves having a small wave-number, i. e. $0.1 \leq k \leq 15$. The crosses correspond to the experiment, where the leakage problem is simulated (see text).

tail of the spectra. That we have to keep in mind in the analysis of numerical model results.

3.2.3 Implication from the experiments with synthetic fields

In summary, we conclude that the DCT method delivers a slightly better performance than the DFFT method and is appropriate for our analysis on the small domain of the COSMO model. If the atmospheric state is dominated by a pronounced structure inside the model domain, one has to be aware to study the spectra in the along-line direction and not in the across-line direction of the phenomenon (Bryan et al., 2003).

3.3 Observational data obtained from aircraft flights

Beside the problem of the spectral decomposition on limited model domains, we will highlight another problem of evaluating and analyzing mesoscale model spectra. The data needed to evaluate model spectra are very rare. If they are not available, it is hard to say that the physical processes simulated by the model and the resulting variance of the energy cascade represent the processes in the real atmosphere.

3.3.1 Available data sets of kinetic energy spectra

The most comprehensive studies about spectra derived from observations are the ones of Nastrom et al. (1984) and Lindborg (1999). They investigated the global and annual

mean of the kinetic energy spectrum using the GASP (Global Atmospheric Sampling Program) and the MOZAIC (Measurements of OZone, water vapour , carbon monoxide and nitrogen oxides by in-service AIrbus airCraft) dataset, which contain a huge amount of aircraft flights. The discrete horizontal kinetic energy density spectrum (for details see Stull, 1988, chap. 8.6) derived by Lindborg (1999) is shown in Figure 3.5 (functional fit denoted by the black line). It is remarkably close to the spectrum of Nastrom et al. (1984) (not shown here) and supports the conclusions drawn by Nastrom et al. (1984). That is, the atmospheric spectrum in the upper troposphere and lower stratosphere strictly follows a line with a slope of $-5/3$ for structures having a wavelength smaller than a few hundred kilometers and a slope of -3 for the larger structures. Nastrom and Gage (1985) highlighted the robustness and universality of the atmospheric spectrum. They found a remarkably small variation of the energy spectrum with respect to season, latitude or altitude and a good agreement to earlier studies by Lilly and Petersen (1983) and Balsley and Carter (1982).

3.3.2 Kinetic energy spectra observed during the COPS campaign

Having the universality of the atmospheric spectra in mind, we will expect that the kinetic energy statistics of the COSMO model forecasts, which focus on the region of Central Europe, are similar to the GASP and MOZAIC spectra. But we will not use the GASP and MOZAIC data as a reference for the atmospheric state to evaluate the model, as it was done by (Skamarock, 2004). In order to get a more detailed picture of the spectral characteristics in Central Europe, we examine the atmospheric spectra obtained during the Convective Orographic precipitation study (COPS, Wulfmeyer et al., 2008) at the summer in 2007. We can benefit from those spectra in two different ways:

- We enhance the knowledge about the mesoscale energy cascades in the upper troposphere over Central Europe.
- We have a much more case specific data set for evaluating the COSMO model data.

We use data of the Falcon aircraft, hosted by the German Aerospace center, that have been obtained as a part of the measurement campaign COPS over the region of Eastern France and Southern Germany. More details about this field campaign and the operating measurement systems are given in Wulfmeyer et al. (2008). The derived energy spectra are based on wind measurements from 17 Falcon flights during the period 8th of July 2007 to 1st of August 2007 (Ehret and Kiemle, 2009). The flight routes are visualized in Figure 3.4. The aircraft was flying in the middle and upper troposphere at an altitude of 5500 m to 11000 m. The long flights took place between southern Germany and Spain or Portugal. The short flights are concentrated over the Black Forest region in southern Germany.

The wind measurements were performed using a nose boom instrumentation linked with the on-board navigation system. The wind data were recorded at a frequency of 10 Hz. Since there were many gaps in the data for the vertical velocity w, we use only the

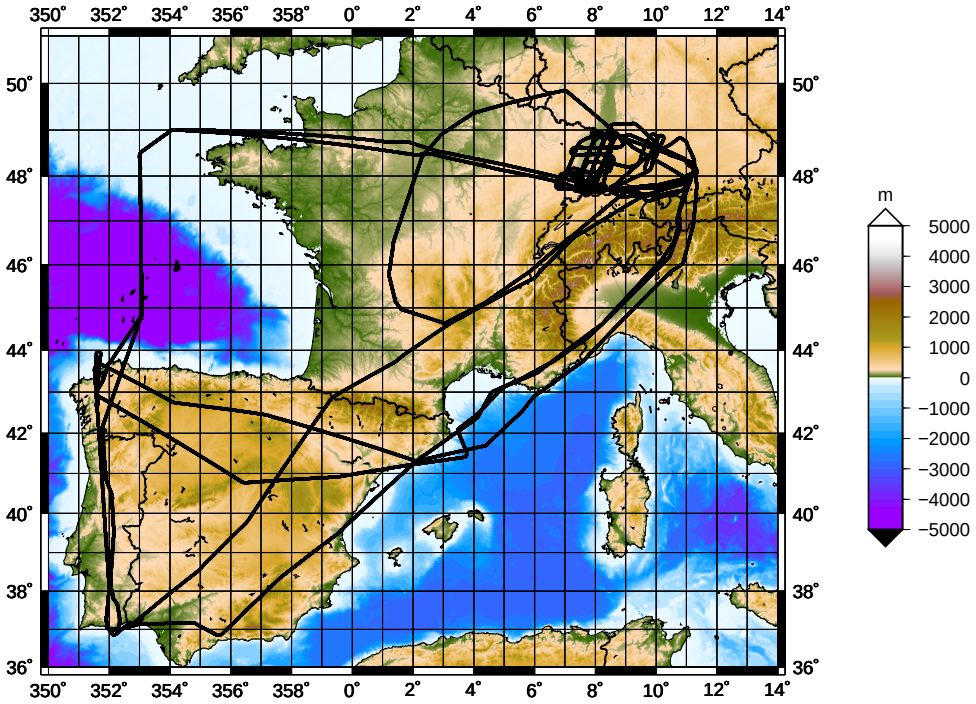

Figure 3.4: Flights of the DLR-Falcon aircraft in the period from 8.7.2007 to 1.8.2007. The black lines illustrate the flight routes. Colours show the topography $[m]$.

horizontal wind components u and v for our observational study. The calculated true airspeed varies in the range of 160 ms^{-1} for the flights at low levels to 200 ms^{-1} at high levels. The typical uncertainty of the wind measurements is 0.5 ms^{-1} depending on the flight maneuver and the initialization of the navigation platform. The navigation data were used to determine the geometrical distances of every data sample along the flight paths. Later on, the data points were arranged on an uniform grid using interpolation. Following Bacmeister et al. (1996), we apply the Taylor-hypothesis of frozen turbulence on the aircraft data, i. e. we assume that the measurements were taken simultaneously. The time between two consecutive measurements is much shorter than the time period of the variations in the atmosphere due to dynamical processes.

The wind data are distinguished in two sets. The first data set considers long flights over Southwestern Europe. We were looking for long flight segments, where the aircraft was flying at least 430 km in one direction without any significant changes in altitude and without any gaps in the data. There are 23 segments that meet these criterion. The DCT (Section 3.2.1) is applied separately on the data set of each flight segment for the zonal wind component u and for the meridional wind component v. The spectral coefficients are averaged over all long flight segments. Afterwards, the spectral coefficients of u and v are used to calculate kinetic energy densities.

The horizontal kinetic energy density spectrum is plotted in Figure 3.5 (crosses). For clarification, not every wave number mode is plotted, but the spectral amplitudes are arranged in wave number bins with logarithmic spacing following Lilly and Petersen (1983). Every single bin combines wave numbers, which differ in their power by 0.05 at most.

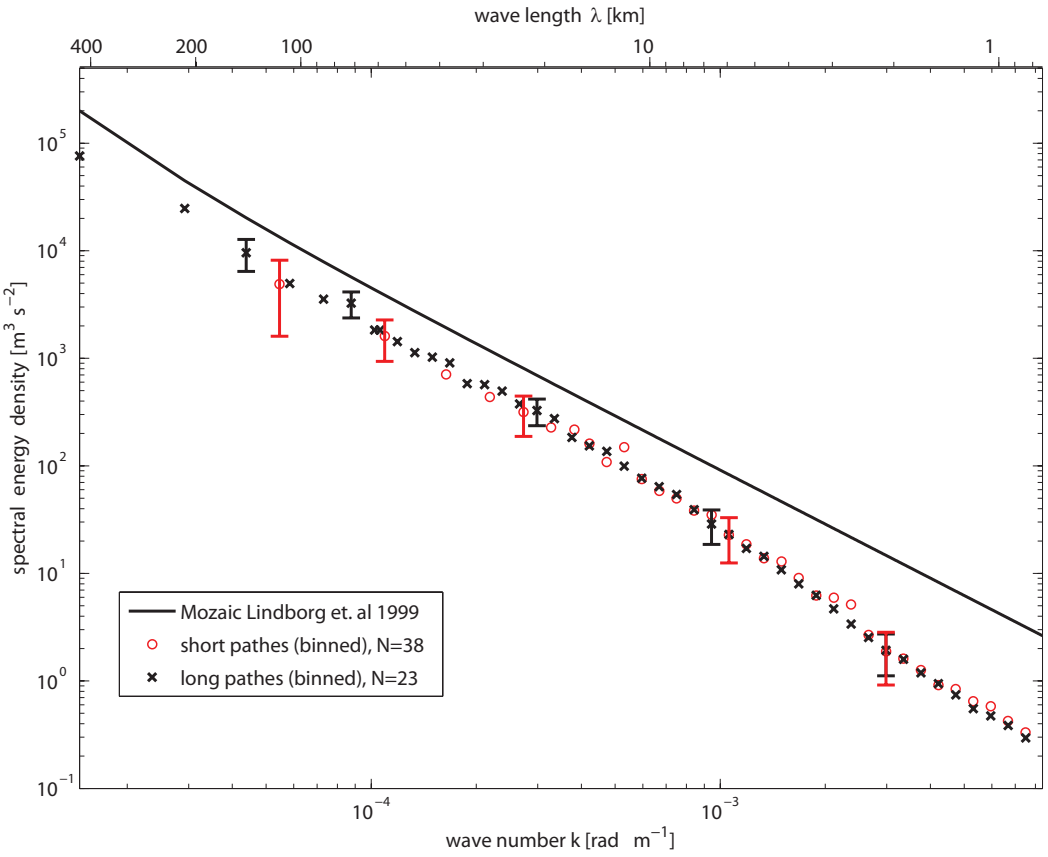

Figure 3.5: Discrete kinetic energy density spectra obtained from the flight data of the DLR falcon aircraft. The spectrum from the long flight routes is denoted by crosses, the short flights are denoted by circles. N denotes the number of short and respectively long flight segments considered for the spectral analysis. The error bars mark two standard deviations normalized by the number of flights. The Lindborg fit is denoted by the black line.

The second data set considers short flights. We select only those flight segments, where the aircraft was flying at least 115 km in nearly one direction. There were 38 segments that met this criterion. We also plot the energy density spectrum of the short flights in Figure 3.5 (circles) using the same calculations as for the long flights. The same binning technique is used as for the long flight paths for a better visualization. For the purpose of comparison, the functional fit of Lindborg (1999) is also included into Figure 3.5.

The limited number of flights does not allow for extensive statistical calculations. Nevertheless, the standard deviations of our results are of about the same magnitude as the mean values of each spectral amplitude, which also holds for the data of the study by Nastrom et al. (1984) and Lilly and Petersen (1983). The uncertainty range of the data is displayed by the error bars in Figure 3.5. The error bars for a specific wave number bin are calculated following Nastrom and Gage (1985), i. e. the error bars indicate the range between the mean spectral amplitude plus and minus two times the standard deviations divided by the number of flights used to form the mean.

The energy cascade of the mesoscale range follows a $k^{-5/3}$ law for wavelengths between 400 km and 8 km considering the data from the long and the short flight segments.

This finding supports the hypothesis of Nastrom and Gage (1985) that the kinetic energy spectra of the free atmosphere has an universal shape with a nearly constant slope and no spectral gap in the mesoscale range. In comparison to the fit of Lindborg (1999) (straight line in Figure 3.5) the spectral amplitudes are about a factor of two smaller. This factor may be not explained by the variance in the data set, but is more a result of the seasonal variability of the energy cascades over South-western and Central Europe. Indeed, the weather in the summer of 2007 was dominated by south-westerly winds and only weak gradients of temperature and geopotential were present at high altitudes (Figure 3.6). Therefore, the development of sharp frontal zones reflected by moderate to strong jet stream winds was suppressed. We assume that this is the reason for the small spectral variances of the mesoscale structures compared to the values of the functional fit by Lindborg (1999), where the atmospheric conditions of autumn and winter season are included. Nastrom and Gage (1985) found only small variations of the spectral amplitudes with respect to the season except for the summer season. They also observed smaller values for the spectral amplitudes during the summer season in comparison to the other seasons.

For wavelengths smaller than 8 km the spectral slope steepens. It is less than -2 for the scales below 8 km. There is no reason for an energy loss due to aliasing by unresolved high frequency motions, because the spectrum in Figure 3.5 is cut at a frequency near 0.3 Hz, which is more than ten times smaller than the Nyquist frequency ($\simeq 10Hz$). We can speculate that the energy input in the range below 8 km is much smaller than the energy input examined by Lilly and Petersen (1983), Lindborg (1999) and Nastrom et al. (1984). As already mentioned, we investigated only a specific summer season and a small area in Europe. Our data contain no strong winter or autumn frontal zones, which induce high variances at small scales due to shearing instabilities inside the jet streams (Kao and Woods, 1964). Gage (1979) showed that inside a polar front jet stream an energy inertial range down to a few kilometers can be formed and the wind variability follows a $k^{-5/3}$ law. In our case study, the energy input at the scales lower than 8 km should originate mainly from convective instabilities, but strong convective events were only observed during two DLR Falcon flights. This could be a reason for the energy decay relative to the Lindborg fit at the smallest scales.

3.4 Model derived spectra versus observations

3.4.1 Model evaluation for a multi-day period

In order to compare the observed spectra presented in Section 3.3 with the model results we use forecast data of the high resolution COSMO model (COSMO-DE, $\Delta x \approx 2.8km$) available at the CERA database (Baldauf et al., 2009). The data has been provided as a part of the MAP D-PHASE campaign (Rotach et al., 2009), which was held in 2007 and coincided with the COPS campaign. The simulations with the COSMO-DE model were performed by the German Weather Service (Deutscher Wetterdienst, DWD). The COSMO-DE model was nested into the COSMO-EU model having a coarser resolution ($\Delta x \approx 7km$). More information about the initialization cycle and the location of the

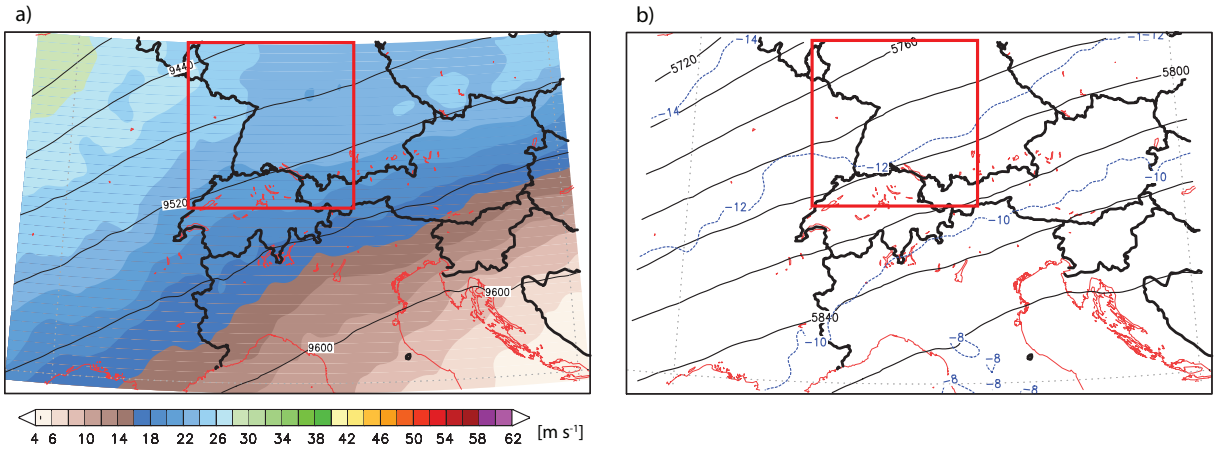

Figure 3.6: The mean synoptic regime at 12 UTC during that days of the COPS compaign, where DLR falcon flights were performed. The rectangle denotes the COPS domain. a) Absolute value of the mean wind vector [m s^{-1}] (shaded) and the mean geopotential [gpm] (contour) at the 300 hPa level. b) The mean temperature [degree Celsius] (blue lines) and the mean geopotential [gpm] (black lines) at the 500 hPa level.

model domains can be found in Rotach et al. (2009). A short introduction into the COSMO model is given in the Appendix A

We examine the hourly forecast data of the COSMO-DE simulations initialized at 00 UTC. We consider the model data with respect to the COPS domain, i. e. the area extends from 47° N to 50 ° N and from 6° N to 11° E (the rectangle in Figure 3.6). To minimize the influence of the spin-up we use only those forecast data, which are at least 6 hours into the forecast. The time period for the spin-up was chosen in accordance with the results presented in section 3.5. We use only model data from those days, at which one aircraft flight was performed. In contrast to the observations, we consider not only the horizontal but also the vertical component of the wind. However, the spectrum of the vertical velocity has no crucial impact on the kinetic energy spectrum.

As already mentioned in Section 3.2, we perform a one-dimensional DCT not only on the observed flight data but also on the model wind fields to calculate the kinetic energy density spectra. Since the aircraft was flying on routes oriented west-east, north-south and diagonal, the spectral transformation is applied on grid point values along the west-east oriented model axis (x-axis) and along the south-north oriented model axis (y-axis). The simulated wind fields are not analyzed diagonally on the model grid, because the grid spacing is different along the x-direction and a diagonal and thus prevents to compare and merge the corresponding spectral coefficients. Moreover, most of the mountain ranges in or near the COPS region are oriented north-east or south-west. Hence, most of the atmospheric structures induced by mountains should be captured by a transformation along the model x-axis and y-axis.

The calculation of the kinetic energy spectra from COSMO data is organized in the following way:

1. We make a spectral decomposition for the wind component u along every west-east oriented grid line and average the spectral amplitudes over the north-south oriented extent of the model domain afterwards.

2. We do the same for the south-north oriented grid lines.

3. We take the mean value of the transformations along the west-east and the south-north oriented grid lines.

4. We perform the steps 1, 2 and 3 for the wind components v and w and derive the discrete kinetic energy spectrum with respect to a specific time step on a specific model level.

5. We repeat this procedure for the time period from 06 UTC to 18 UTC and for all flight days and average the corresponding spectral coefficients.

6. Finally, we average the spectral coefficients vertically over the horizontal model levels located between 5 and 10 km above ground in order to coincide with the range, in which the aircraft flights were performed.

Our philosophy for the evaluation of the model spectra with the observation based spectra is to analyze the multi-scale kinetic energy statistics with respect to a specific region (Eastern France and Southern Germany) and not with respect to local points on specific flight tracks (Ries et al., 2010). Thus, we do not extract model data located on individual flight tracks (which would be problematic due to the high temporal and spatial sampling rate of the aircraft measurements relative to the spatial and temporal resolution of the model output), but we determine a mean model spectrum regarding a specific region and time period and compare it with the mean observed spectrum. Usually, the derived model spectra consist of 10^4 transformations concerning one day, whereas the observed spectra only consist of 10^2. That is, a big discrepancy is present between the number of observational and model data, because the spatial coverage of the flight data is much worse in comparison to the model data. That we have to keep in mind for the further analyses and interpretations.

The model spectrum is plotted in Figure 3.7 (green line) along with the spectra derived from the DLR-flights and the functional fit of Lindborg. The error bars indicate the interval of two standard deviations divided by the number of days used to form the mean value. There is a wide spread among the spectral amplitudes for all wavelength, which is consistent with the spread in the aircraft data (error bars in Figure 3.5). The standard deviations are about the same magnitude as the mean values of each spectral amplitude.

The model fits remarkably well with observations. I. e. the mean kinetic energy statistics of the mesoscale is well represented in the COSMO model with respect to the period from 8.7.2007 to 1.8.2007. For scales larger than 20 km, the spectral variance decreases for increasing wave numbers following a slope, which is about -5/3. For scales lower than 20 km, the model and the observations differ in their spectral behavior. The spectral variances derived from model outputs decay relative to the observed spectra. The point, where the decay starts, was defined as the effective resolution by Skamarock (2004). In terms of the COSMO model, the effective resolution is about seven times bigger than the grid spacing Δx, which is 2.8 km. The scales between Δx and 7 Δx are poorly resolved by the model.

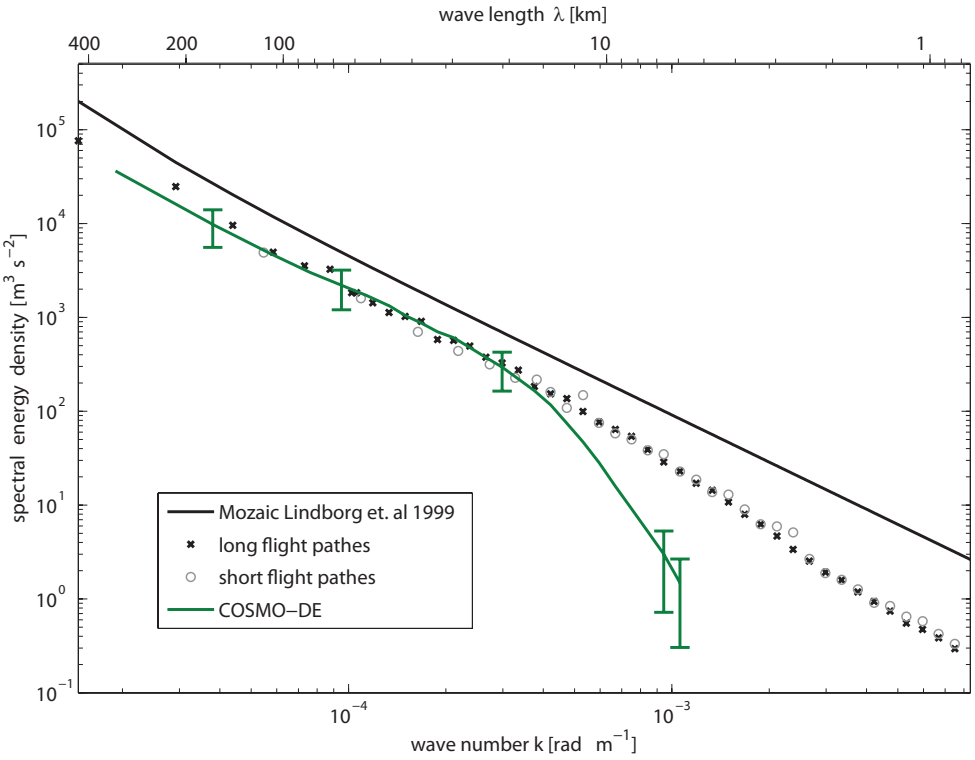

Figure 3.7: Discrete kinetic energy density spectra obtained from the aircraft data and from the COSMO-DE model output. The error bars mark two standard deviations normalized by the number of days. The Lindborg fit is denoted by the black line.

3.4.2 Model evaluation for specific weather regimes

In a more detailed study we have grouped the flight data from the short flight paths into two categories. The first category, denoted by the abbreviation NAW (non-active weather), considers cases where the weather was dominated by a ridge with weak winds in all levels. No precipitation occurred and only some single orographic driven cumulus clouds developed in the COPS region. The second group, denoted by the abbreviation AW (active weather), considers cases where synoptical driven clouds and precipitation were influencing the COPS region. Two flights at the 20th July belong to the AW group. Figure 3.8 shows the COSMO-EU model analysis for the 20th July at 12 UTC. The COPS region is located ahead of a mid- and upper-tropospheric through. A moderate jet stream, embedded into a frontal zone stretching from Southern France to Benelux, is reaching the COPS region. On its left exit cyclogenesis occurred and a surface low developed located over the British Isles. Its cold front and thermally driven mesoscale circulations along the front line influenced the COPS region. Widespread convection and a mesoscale convective system were initialised in the pre-frontal warm and humid air mass, which was characterized by high equivalent potential temperatures. The course of the weather on the 20th July 2007 - the day of the Intensive Observation Period (IOP) 9c during the COPS campaign - was studied in detail by Kottmeier et al. (2008).

The spectra of the flights regarding the AW cases and the NAW cases are given in Figure 3.9 marked as crosses and as dots, respectively. Both spectra possess nearly

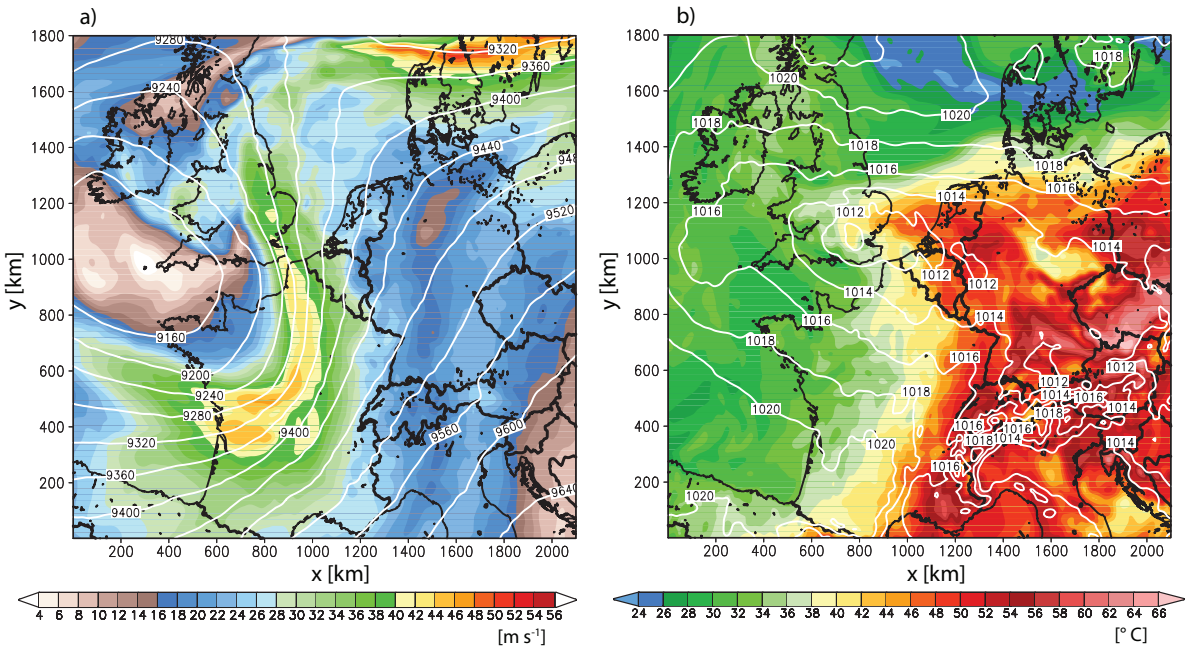

Figure 3.8: COSMO-EU model analysis from 20 July 2007 at 12 UTC. a) The wind speed [m/s] (shaded) and the geopotential height [gpm] (contours) at the 300 hPa level. b) The aequivalent potential temperature [°C] (shaded) at the 850 hPa level and sea level pressure [hPa] (contours).

a $k^{-5/3}$ behavior of the kinetic energy, which is in accordance with an energy inertial range. The amplitudes of the spectral variances of the kinetic energy is much higher for the AW cases relative to the NAW cases for all wavelengths. The high energetic turbulent state of the AW cases might be associated with an energy input due to convective events. We will give a thorough analysis in the next Section.

Another distinctive feature between the AW and NAW cases is the characteristic of the energy cascades for a horizontal scale below 10 kilometers. Concerning the NAW cases we get a slope of nearly -5/2 using a linear fit to the data related to a wavelength smaller than 6 km. Bacmeister et al. (1996) also found a slope of -5/2 for the stratospheric temperature and velocity data in the wavelength range below 6 - 12 km. The $k^{-5/2}$ behaviour is in accordance with predictions for a buoyant sub-range turbulence by the theory of Weinstock (1978), which refers to a stably stratified atmosphere. Since the NAW cases are characterized by an almost stable stratification, Weinstock's theory is likely an explanation for the turbulent behavior at the small scales.

For the AW cases the spectral slope is nearly -2 at the small scales below 6 km. In comparison to the NAW cases, there is a larger portion of energy introduced at the meso-γ-scale. This could be explained by the production of small-scale turbulence due to convective processes or shearing instabilities along the jet stream, which is more pronounced for the AW cases relative to the NAW cases. A more detailed analysis of the turbulent processes on scales of a few kilometers is not given here, because no single turbulence theory can be applied to these scales (Bacmeister et al., 1996; Lindborg, 1999). Bacmeister et al. (1996) and also Lindborg (1999) explored that the velocity spectrum behavior in the range of a few kilometers can neither be explained as

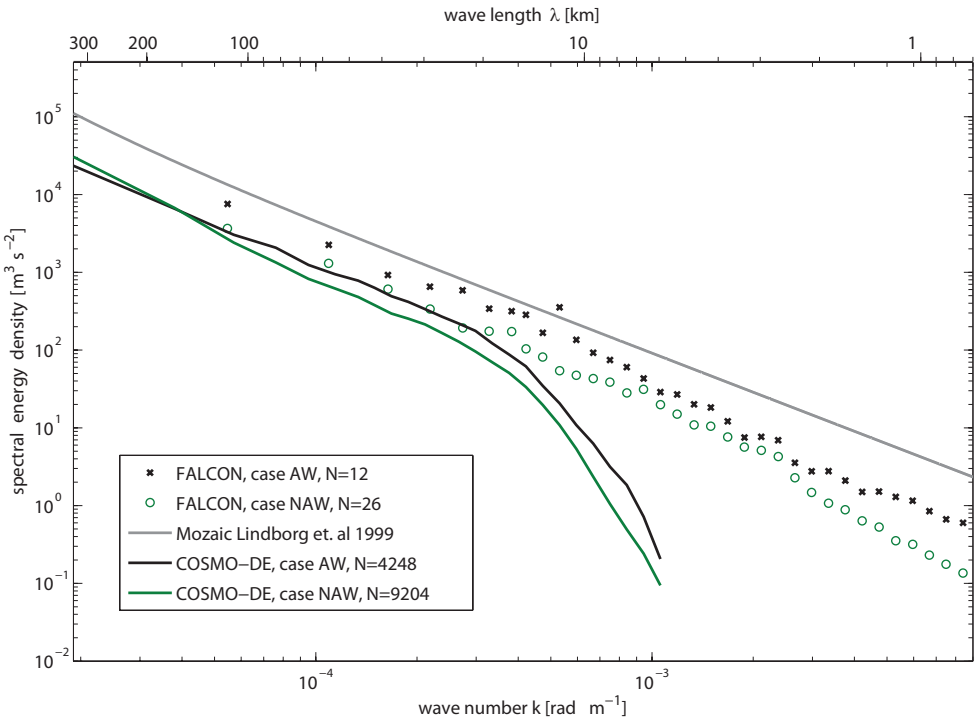

Figure 3.9: Discrete kinetic energy density spectra obtained from the aircraft data and from the COSMO-DE model output with respect to AW cases (strong weather with clouds and precipitation) and NAW cases (no significant weather). N denotes the number of segments considered for the spectral analysis. The Lindborg fit is denoted by the straight gray line.

a two-dimensional energy inertial range nor as a three-dimensional Kolmogorov inertial range.

In order to compare the observed flight spectra with the model spectra regarding the AW cases and the NAW cases, we consider only those wind fields of the model output, which coincide with the time period and the altitude of every individual flight. That is, the spectral coefficients of the simulated wind field are computed exclusively with respect to the model level located near the corresponding flight altitude. The spectral coefficients are averaged temporally according to the flight time. The resulting model spectra with respect to the AW cases and the NAW cases are also plotted in Figure 3.9, marked by the black line (AW) and the green line (NAW). It is important to note that the model spectra for the AW and the NAW cases are in contrast to the model spectrum shown in Figure 3.7, because the latter is a mean over all flight days, over the time period 06 to 18 UTC and over all model levels between 5 km height and 10 km height.

The spectral slope in the model wind data concerning the AW and the NAW cases is consistent with the observations for coarser scales down to the effective resolution limit. There is a gap between the model and the observed spectral amplitudes. More energy is contained by the horizontal structures at all wavelength in the observations than in the model. The gap between model and observed spectra arises to some extent from the fact that the flight tracks covers only some sections of the COPS domain (Figure 3.4), whereas the model data covers the whole COPS domain, i. e. the transformations

used to form the mean spectra are much less in case of the observations compared to the model data. The differences in the spectral amplitudes derived from the model and from the observations are in the range of the error bars displayed in Figure 3.5 and 3.7. Nevertheless, some of the differences concerning the spectra for the AW cases and the NAW cases may result from shortcomings of the COSMO model in the prediction of the turbulent atmospheric state. We will explore in the next Section, whether the differences can be associated with meteorological processes. We focus exclusively on the AW cases, i. e. the two flights at the 20th July 2007.

The turbulent state at the 20th July 2007

In order to gain a deeper insight into the reasons for the discrepancies between model spectra and observed spectra, we put at first the DLR flight paths into the context of the weather regime at the 20th July of 2007 (AW case). For details about the weather regime we refer to Kottmeier et al. (2008).

The first DLR flight is taking place in the morning of the 20th July (**flight track A**), the second is taking place at the noon (**flight track B**). The flight routes are shown in Figure 3.10e and 3.10f. Flight track A is located to the southeast of a large Mesoscale Convective System (MCS hereafter) that has developed over France at the right exit of the jet depicted in Figure 3.8a. The MCS causes a surface pressure fall and the development of a secondary low (the pressure minimum over Western Germany, Figure 3.8b). The cloud structure of the MCS at 9 UTC is shown in the MSG satellite picture 3.10a. At the south-eastern edge of the MCS shower lines are triggered along the windward side of the Vosges (Figure 3.10c). Hence, the observations during the first flight capture the variability of the wind field in a south-westerly flow in front of the afore-mentioned shower lines under almost clear-sky conditions. The aircraft touches the clouds only for some short moments as it is reflected in the observed humidity shown in Figure 3.11a.

Flight track B partly covers a squall line structure and also convective cells over the Southern Black Forest. The squall line structure is depicted in the satellite analyses at 11:45 UTC in Figure 3.10b. It involves single convective cells, which elongate from the Eastern Benelux to Southern Germany in an arc-like structure and produce moderate precipitation (Figure 3.10d). The squall line is associated with the aforementioned MCS, which was propagating northeastwards over the Benelux during the second half of the morning. The deep convective cells along the squall line were initiated to the East of the Rhine Valley at about 11:00 UTC because of mainly four reasons (Kottmeier et al., 2008): (1) a gust front originating from the MCS, which spreads out in the morning over the Vosges and propagates eastwards through the Rhine valley and over the Black Forest and initiates vertical lifting, (2) high potential instability of the air masses in the region of Black Forest and Swabian Jura, (3) vertical motions induced due to orographic features, (4) formation of a convergence zone ahead of a cold front due to thermally driven circulation systems, which develop under the influence of large temperature gradients between cloudy and cloud-free areas (Figure 3.10a). Hence, the observations during the second flight were obtained in a south-westerly flow under the temporary influence of mesoscale convective structures. The aircraft flies rarely

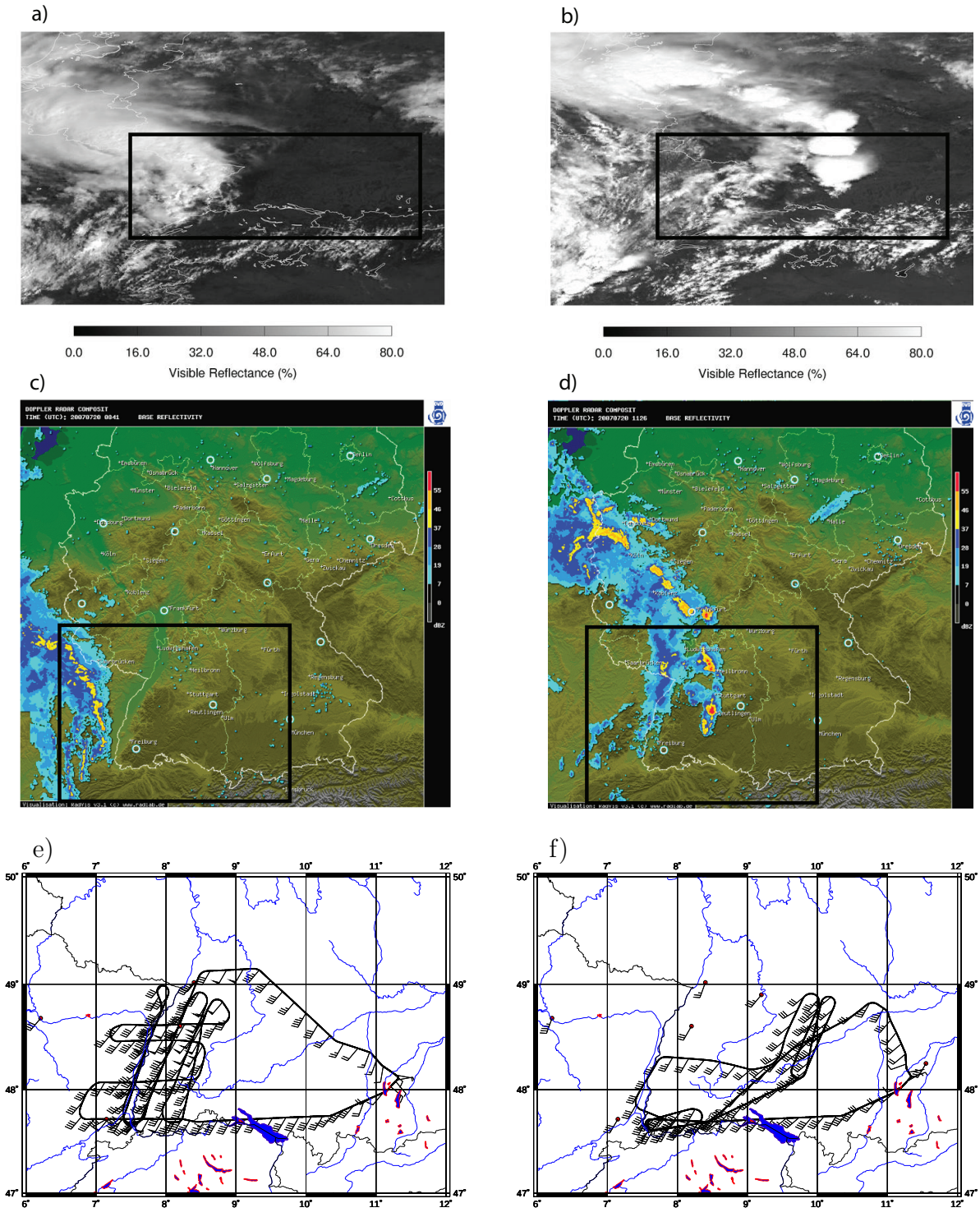

Figure 3.10: COPS campaign, IOP 9, 20th July 2007. The rectangles in the top and middle panel indicate the domain shown in the bottom panel. The visible reflectance [%] derived from Meteosat data at 09:00 UTC (a) and at 11:45 UTC (b) provided by EUMETSAT. The reflectivity [dBZ] derived by the German Radar Network at 09:00 UTC (c) and at 11:45 UTC (d). The flight path A (e) and the flight path B (f) and the observed wind directions. Flight A started at Oberpfaffenhofen to the South-West (9000 m altitude, 06:40 UTC to 09:40 UTC) and flight B started from Oberpfaffenhofen to the South-West (9000 m altitude, 10:50 UTC to 13:20 UTC). The red dots denote the location of a radio sounding station.

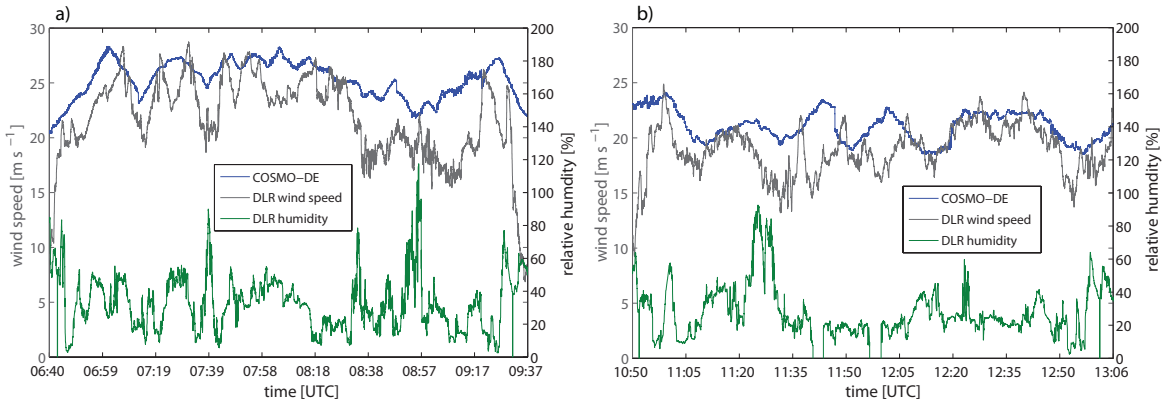

Figure 3.11: a) Observed wind speed (black) and relative humidity (green) at the flight track A at the morning. The wind speed from the output data of the COSMO-DE model is denoted by the blue line. b) as in a), but for the flight track B at noon.

through the clouds (Figure 3.11b), but more frequent above the top of the clouds (vertical resolved soundings not shown here).

Having in mind the weather regime being present during the flight observations, we explore the variances of the wind field observed by the DLR aircraft and compare them with the output of the COSMO-DE model along the flight paths A and B. The observed horizontal wind speed is shown in Figure 3.11 for the flight track A and flight track B. There are a lot of high-frequency and low-frequency perturbations, which imply a high variability of the wind field on all scales concerning both aircraft flights. This is confirmed by the kinetic energy spectrum determined for the AW cases (Figure 3.9). The high variability with respect to flight A may arise from nonlinear processes and mesoscale vortexes in the pre-convective atmosphere, because the convective cells are located some kilometers to the west of the flight route. The high variability with respect to flight B is apparently associated with the convection in the mesoscale cloud systems inside the COPS domain. We have to note here that some of the strong perturbations in the wind field cannot be spatially attributed to radar echoes or reflectance signals in the satellite data, but they characterize the high energetic turbulent state of the upper troposphere in cloud-free regions near convective systems.

In order to examine the variance of the upper tropospheric wind field for the COSMO-DE model, we have reconstructed the FALCON flights by extracting the simulated wind field at the model grid points located near the flight tracks A and B at the level $z = 9\,\mathrm{km}$ and using temporal interpolation of the simulated wind field in order to meet the sampling times on the flight tracks A and B. The result is also plotted in Figure 3.11. The variance of the simulated wind field along both flight tracks is small compared to the observations. This is a possible explanation for the fact that the kinetic energy spectrum derived from model data and shown in Figure 3.9 possesses much smaller amplitudes on all scales compared to the flight observations regarding the AW cases.

Since we have found a small variability of the wind field in the COSMO-DE model compared to the observations and moreover we have associated the observed spectrum

and the observed variability of the wind field with pre-convective clear-sky turbulence at the morning and mesoscale structures at noon, we examined in a subsequent step the meteorological processes resolved by the COSMO-DE model. The COSMO-DE simulation captures the large-scale meteorological structures at the 20th July 2007. It also offers the development of a MCS over Eastern France during the morning of the 20th July, which propagates then to the northeast as reflected in the precipitation pattern shown in Figure 3.12b. Using the precipitation pattern and the vertical integrated cloud water and cloud ice content (not shown here), the MCS is located westerly relative to the radar and satellite analysis (Figure 3.10a and 3.10c). Moreover, the COSMO-DE resolves a cold front with convective precipitation passing the COPS region at the rear side of the MCS. However, the model failed to predict the small-scale features, e. g. the convective clouds and showers in the morning at the Vosges region (Figure 3.10a and 3.10c), the gust front originating from the MCS and the initiation of convection along a squall-line to the East of the Rhine Valley at noon (Figure 3.10b and 3.10d). The vertical integrated cloud water and ice contents (not shown here) and the simulated precipitation in the time period between 07 UTC and 13 UTC (Figure 3.12b) are zero for the central COPS region, whereas the satellite reflectance signals and the radar echoes (Figure 3.10) as well as the rain-gauge network of the German state Baden-Württemberg (Figure 3.12a) clearly indicate deep clouds and precipitation.

We conclude that the gap between the amplitudes of the observed and the model spectra concerning the AW cases shown in Figure 3.9 is related with shortcomings in the weather prediction for the 20th July 2007. On that day the turbulent state and thus the energy cascade in the upper troposphere are poorly represented by the COSMO-DE. In particular, the high multi-scale variance of the observed wind field at the morning under cloud-free conditions is not resolved by the model. This is important to note, because a high energetic turbulent state cannot be identified by radar echoes or satellite reflectance data, but can be evaluated by a spectral analysis of the kinetic energy. Nevertheless, the gap between the model and the observed spectra could also be explained by the uncertainty range for the spectral amplitudes (the error bars in Figure 3.5 and 3.7). It is discussed in the next section, whether the amplitudes in the kinetic energy spectrum are dependent on the model used for the weather forecast at the 20th July 2007.

The turbulent state predicted by various mesoscale models

Having established a link between the insufficient representation of the turbulent state of the upper troposphere and the missing convective initiation over the central COPS region for the COSMO-DE model, an analysis of the kinetic energy spectrum is done with respect to other models. Since the effective resolution serves as a limitation factor concerning the forecast of small-scale phenomena, we are motivated to investigate models having a slightly higher resolution than COSMO-DE. The forecast of the high resolution models MESO-NH2 (Δx = 2.0 km) and COSMO-CH2 (Δx = 2.3 km) are examined regarding the 20th July 2007. A short overview of the corresponding model configurations is given in Table 3.1. The corresponding model output data were provided as a part of the MAP-DPHASE compaign (Rotach et al., 2009). We refer

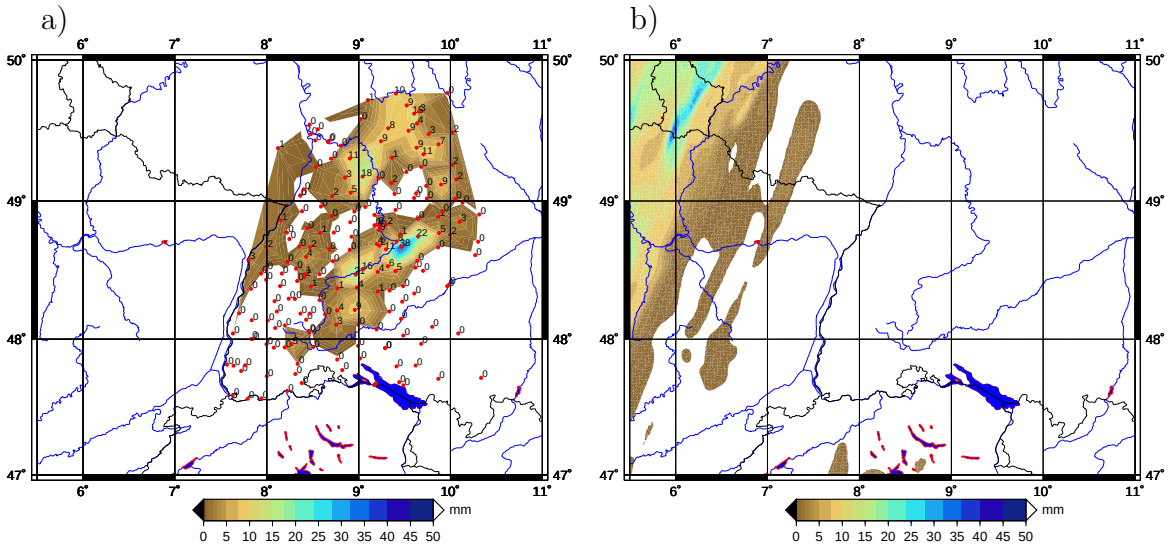

Figure 3.12: COPS campaign, IOP 9, 20th July 2007. a) Precipitation [mm] between 07 UTC and 13 UTC derived from the high-resolution rain gauge network of Baden-Württemberg (provided by the LUBW, Landesumweltamt Baden-Württemberg) b) as a), but the precipitation [mm] predicted by the COSMO-DE model.

Table 3.1: Configurations of three high-resolution models used to perform forecasts during the MAP-DPHASE. Further details can be found in Rotach et al. (2009). L denotes the number of vertical layers, G denotes the number of subdivisions of the standard icosaeder and T denotes the number of spectral coefficients.

model	COSMO-DE	COSMO-CH2	MESO-NH2
resolution	2.8 km	2.3 km	2.0 km
vertical levels	50	60	50
global model forcing	GME, G192L40	IFS, T799L91	IFS, T799L91
resolution of the global model	40 km	32 km	32 km
nesting strategy	one-way COSMO-EU (7 km)	one-way COSMO-CH7 (7 km)	two-way Meso-NH8 (8 km) and Meso-NH32 (32 km)

to Lafore et al. (1998) and Doms et al. (2007) for a detailed documentation about the numerics and physics used in the MESO-NH and respectively the COSMO-CH model.

The discrete kinetic energy spectrum of the COSMO-CH2 and the MESO-NH2 are investigated in the same manner it was done for the COSMO-DE model. That is, the spectral decomposition is done on the COPS domain and for those model output fields, which coincide with the time period and the altitude of the two DLR flights at the 20th July. The kinetic energy spectra derived from the MESO-NH2 and the COSMO-CH2 are plotted in Figure 3.13. The COSMO-DE spectrum, the functional fit of Lindborg and the observed spectrum derived from the FALCON flights regarding the AW case

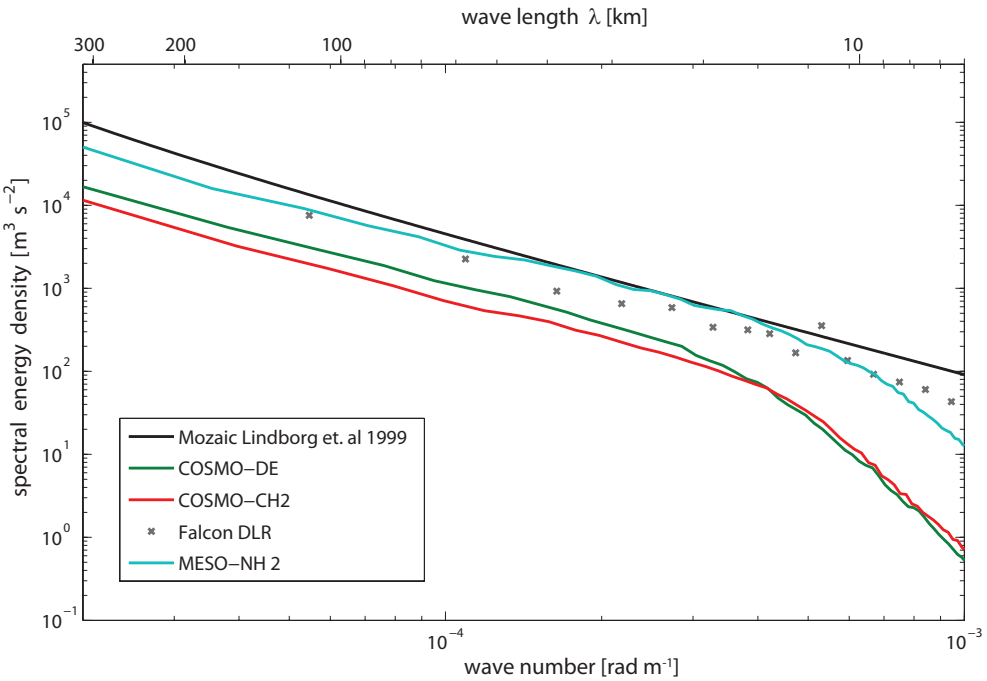

Figure 3.13: Discrete kinetic energy density spectra for the 20th July 2007 obtained from the model output data of COSMO-DE, COSMO-CH2 and MESO-NH2. The model spectra coincide temporally with the observed data of the DLR falcon aircraft (Falcon DLR). The fit of Lindborg (1999) is given for comparison.

are also shown for comparison. The turbulent state of the atmosphere is closer to the observations for the MESO-NH2 model compared to the COSMO models. The MESO-NH2 data possess much more variance at all scales at the upper troposphere, although the initial state (20th July 2007, 00 UTC) reveals the same multi-scale variance of the kinetic energy for all models (not shown here). In particular the COSMO-CH2 and the MESO-NH2 are forced by the same global model, i. e. the IFS of the ECMWF. The MESO-NH2 benefits from its slightly higher resolution ($\approx$ 15 km) relative to the COSMO-DE ($\approx$ 20 km) and thus it is preferred to offer a better performance in predicting fine scale features.

The differences in the kinetic energy spectrum among the models are indeed an indicator for the simulated weather regime. As already noted the COSMO-DE and also the COSMO-CH2 model (not shown here) failed to predict convective initiation at the Vosges mountains in the morning and at the squall line over Baden-Württemberg at noon. Examining the forecast of the MESO-NH2 regarding clouds, precipitation and the wind fields, a gust front is resolved at 12 UTC over Southern Germany (Figure 3.14b), which originates from the cold downdraft of a simulated MCS. The front is stretched south to north at about 8° East and is embedded into a convergence line with convective cells producing moderate rain (Figure 3.14a).

Examining the temporal evolution of the wind gusts observed at the different stations in the Northern Black Forest region (Figure 3.15) reveals that the gust front predicted by the MESO-NH2 is two hours late, but the MESO-NH2 output is more realistic than the COSMO-CH and COSMO-DE output. COSMO-CH and COSMO-DE did not

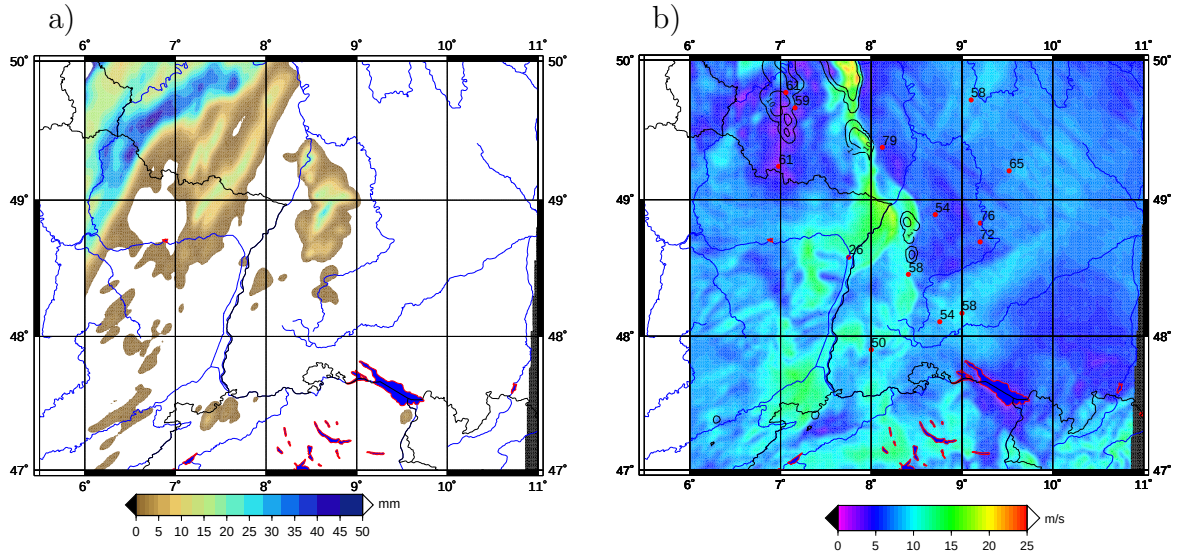

Figure 3.14: COPS domain, 20th July 2007, MESO-NH2 forecast. a) as in Figure 3.12, but for the MESO-NH2 model. b) Simulated wind gusts [$\mathrm{m\,s^{-1}}$] (shaded) at 10 m above ground and the instantaneous rain rate [$\mathrm{kg\,m^{-2}\,h^{-1}}$] (contour levels 1 and 10) are displayed at 12 UTC. The maximums of the one-hourly wind gusts (the numbers at the station points) [$\mathrm{km\,h^{-1}}$] at 12 UTC are given as observed at stations of the German Weather Service.

capture the gust front at all. The increase of the gust speed at 13:00 UTC simulated by COSMO-CH and COSMO-DE is associated with the cold front reaching the COPS region from the West. Driven by the cold front convective initiation occurs in the COSMO-CH forecast and also in the COSMO-DE forecast at 14:00 UTC.

In the case presented here the forecast of the MESO-NH2 is closer to the meteorological processes observed over the central COPS region than the COSMO models. This issue is reflected in the energy cascade predicted by the various models.

Possible explanations for the deficits in the weather forecast and the misrepresentation of the kinetic energy cascade of the COSMO models are briefly given in the following. First, the shortcomings in the COSMO model forecasts can be attributed to the forcing data at the lateral boundaries, which is briefly discussed here. We examined that the MCS is much more pronounced and the upper air forcing (300 hPa divergence and vorticity advection) is much stronger in the morning of the 20th July 2007 regarding the MESO-NH8 simulation compared to the COSMO-EU and COSMO-CH7 model. Examining the tracks of the MCS using the precipitation fields (here not shown) reveals a slight shifting to the east in the MESO-NH8 model compared to the COSMO models. Thus, the MCS has potentially more influence on the region Baden-Württemberg also in the fine-scale MESO-NH2 simulation than in the fine-scale simulations of the COSMO models.

Another possible reason for the different forecast quality of the COSMO models and the MESO-NH2 model is the fact that the physical parameterizations are different. The parameterization may have an impact on the forecast skills, because the convective processes are highly sensitive to turbulent schemes and cloud microphysics. Additionally, the effective resolution may be a limitation factor for the forecast skill. The effective resolution might be insufficient in particular for the COSMO-DE model

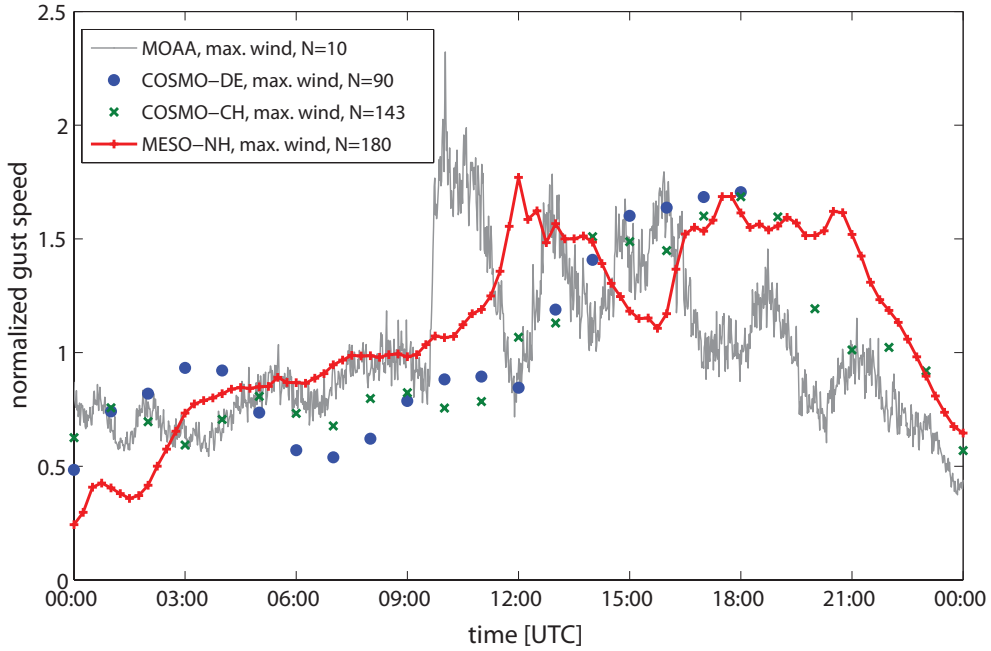

Figure 3.15: COPS domain, IOP 9, 20th July 2007. Observed wind gusts at 3 m above ground and simulated maximum of wind gusts at 10 m above ground. Both time series are normalized by their mean value in order to emphasize the temporal evolution. The MOAA curve is an average over ten different stations spatially distributed over an area of 25 km^2 (Alexander et al., 2009). The area extends from 48°55' N to 48°75' N and from 8°20' E to 8°55' E. The model data are derived from N (given in the legend) grid point values averaged over the observation region. Note that the amplitude of the gust speed cannot be compared among the datasets due to the difference between observation and model level and due to differences in the gust parameterization of the models.

in order to resolve all relevant physical processes, which is highlighted by the huge gap between the simulated and observed energy cascade at the scales smaller than 15 km (Figure 3.13). In contrast to the COSMO-DE model, the COSMO-EU applies a parameterization for deep convection in order to deal with this subgrid-scale process. In the COSMO-EU simulation convection is triggered along a convergence line to the East of the Black forest at noon, which may hint at drawbacks of the COSMO-DE regarding the representation of those small-scale processes that trigger the convection at the 20th July 2007.

3.4.3 Implications from the comparison between observed and predicted kinetic energy spectra

The high resolution model COSMO-DE is able to predict a feasible characteristic of the kinetic energy spectrum for a certain summer period in 2007 at Central Europe (Figure 3.7). The slope and the amplitude of the model spectra are in accordance with the kinetic energy statistics derived from aircraft measurements in the middle and upper troposphere. At the large scales the predicted spectrum of a high resolution model is mainly a footprint of the driving model, but at the small scales the high resolution

model has to develop it own mesoscale spectrum. At very small scales the ability of the COSMO-DE model in resolving a feasible energy cascade is limited to the effective resolution of 20 km, i. e. seven times the nominal resolution $\Delta x \approx 2.8$ km.

A comparison of the model and the observed spectra based on a separation between weather regimes with strong weather and no significant weather reveals differences in the nonlinear dynamics of the upper troposphere (small-scale vortexes, convection and turbulence). One might attribute the differences in the spectral amplitudes between model and observations to the uncertainty range of the multi-scale statistic (the error bars in Figure 3.5), but the differences can also be associated with shortcomings in the weather forecast by the COSMO-DE model over the COPS region as analyzed for a single case during the intensive observation period 9 (20th July 2007). With respect to that single case, a model intercomparison demonstrates that big differences exist concerning the kinetic energy cascades and respectively the nonlinear scale interaction even for a forecast period of 12 hours. The different characteristics of the kinetic energy spectra among the models are associated with big discrepancies in the simulated dynamics and physics at the COPS domain. The MESO-NH2 model, which offers the most realistic representation of the turbulent state of the upper troposphere, tends to resolve some small-scale meteorological processes being observed at the central COPS region, whereas the other failed to predict them. In this context, the spectral analysis may be considered in order to identify the reasons for the model deficits.

3.5 Spectral analysis as a verification method

3.5.1 The Spin-up process

From the point of view of nonlinear scale interactions, a mesoscale model is not only limited due to the discrepancy between nominal and effective resolution, but it also lacks in resolution during the spin-up process. During the spin-up, a high-resolution limited area model is adjusting to the coarsely resolved forcing data provided by the driving model. I. e. the mesoscale model has to develop its own mesoscale spectrum consistent with the turbulent state of the real atmosphere we know from observations (Skamarock, 2004). In the framework of an operational forecast the spin-up does not occur, because the high-resolution models are running in a continuous assimilation cycle. A spin-up is only present in those cases, where assimilation methods designed for high-resolution models are applied to the fine-scale nested model, e. g. the latent heat nudging technique based on radar data (Stephan et al., 2008).

In the framework of scientific purposes an assimilation cycle is not used and thus the spin-up occurs. Taking into account the short forecast period of recent high-resolution models, a rapid spin-up is preferred in order to have a maximum level of usable high-resolution model output. Therefore, the spin-up process is investigated for a cold start configuration in more detail:

1. How long does the spin-up process take, i. e. when is the mesoscale spectrum developed in such a manner that the model offers its 'real' effective resolution?,

2. How does the spin-up process work?

In order to examine these problems and questions, the 30 hour forecast from the 12th August of 2002 is considered, i. e. the Elbe flash flood case which was already discussed in the last chapter (Section 2.6.2). We carry out the same spectral analysis of model data as done in Section 3.4.1. At the initial state (00 UTC) a surface low is located over Northern Austria (Figure 3.16a). At the convergence line clouds develop and rain occurs from the Baltic Sea to Bavaria. The corresponding initial kinetic energy spectrum is shown in Figure 3.16b (gray line). The driving model COSMO-EU provides forcing data with an effective resolution of $\Delta x_{e,g} \approx 60\,\mathrm{km}$, which is eight times larger than the nominal resolution of the COSMO-EU model $\Delta x_{n,g} \approx 7.6\,\mathrm{km}$. At the scales smaller than $\Delta x_{e,g}$ the initial spectrum is obviously decaying against the Lindborg fit. In contrast to the COSMO-EU model, the effective resolution of the COSMO-DE model was estimated to be 7 Δx (Section 3.4.1). Since the COSMO-EU model is running with computational diffusion and the COSMO-DE is not, the small-scale end of the spectrum is more affected in the COSMO-EU simulations relative to the COSMO-DE simulations.

A white noise is present for structures with a wavelength less than the nominal resolution of COSMO-EU, which indicates that the interpolation of the coarse grid to the fine grid does not produce any physical meaningful information. The spectral amplitudes at the small-scale portion of the kinetic energy spectrum are increasing during the first hours of the forecast as depicted by Figure 3.16b. The increase of energy at a special wave number $k^\star$ can take place in three different ways (Skamarock, 2004):

A direct forcing at the wavenumber $k^\star$ due to convection, radiation or perturbations caused by topographic flow interaction,

B downscale energy transfer from smaller wavenumbers to wavenumber $k^\star$

C upscale energy transfer from higher wavenumbers up to wavenumber $k^\star$

Yuan and Hamilton (1994) examined the energy transfer between various modes of the wavenumber spectrum in a shallow water modeling study. They decomposed the flow field into a dynamically balanced vortical and a residual component, which was found to behave nearly as inertia-gravity waves. Their investigations showed that a broadband nonlinear interaction in the energy cascade is coupled to the transfer of energy among gravity wave modes, respectively residual modes. Since the mesoscale is dominated by gravity waves and small scale divergent and rotational flows being not in geostrophic or hydrostatic balance, the processes B and C may quickly fill the spectrum of a high-resolution model. The cascading process depends on the eddy turnover time and thus the time scales are shorter for process C in comparison to process B.

In order to quantify the processes leading to an energy build-up during the spin-up period in the COSMO-DE model, the ratio of the spectral variance $\sigma^2(t,k)$ is calculated at a given time t and with respect to a specific wave number k relative to the value six hours into the forecast:

$$\sigma^2_{RE}(t,k) = \frac{\sigma^2(t,k)}{\sigma^2(t=6h,k)}\,.$$

The ratio σ^2_{RE} is determined from the spectral decomposition of the kinetic energy as a function of the forecast time and the wavelength. σ^2_{RE} is plotted in Figure 3.17 for

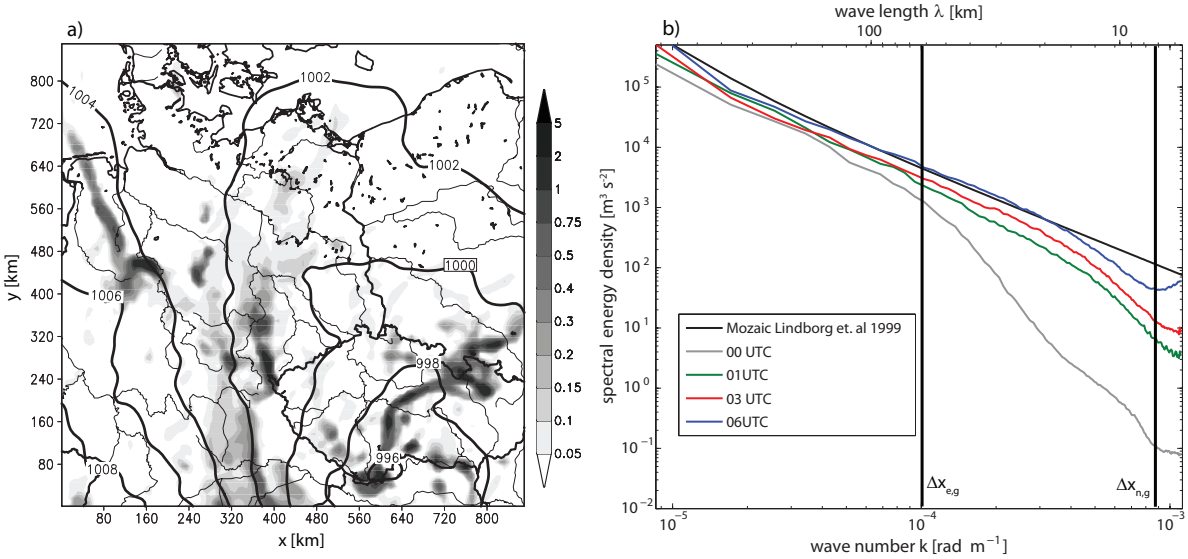

Figure 3.16: a) The initial state of the COSMO-DE forecast at 12th Augunst 2002 at 00 UTC. Sea level pressure (contours) [hPa] and vertically integrated cloud water and cloud ice content (shaded) [kg m^{-2}] are shown. b) Temporal evolution of the kinetic energy density spectrum with respect to the model forecast at the 12th August 2002. The spectra are vertically averaged for the model levels ranging from 3000 m to 9500 m height. The straight black lines denote the nominal and the effective resolution of the COSMO-EU model, i. e. $\Delta x_{n,g}$ and $\Delta x_{e,g}$.

the middle troposphere (a) and the upper troposphere (b). Concerning the middle troposphere, the large scale structures contain mainly the largest σ^2_{RE} values and the largest amount of energy at the initial state. Then, the energy is cascaded down to smaller scales, which is highlighted by the lines. Thus, process B is the main driver for the development of a mesoscale spectrum in the middle troposphere, as it is expected. In addition, process A pushes the spin-up process, which is reflected in the isolated maxima of σ^2_{RE} in Figure 3.17. For instance, the COSMO-DE model generates very rapidly small scale gravity waves and strong wind divergences as the initial large scale flow starts to interact with the topography. After the development of small scale features their energy can be transfered throughout the mesoscale.

Concerning the upper troposphere, process A implies an unrealistic gain of energy at the smallest scales. σ^2_{RE} reaches a value of up to 7 at four hours (not displayed in Figure 3.17b). Although one would expect that fine scale structures originate at the planetary boundary layer in the lower troposphere, we observe here fine scale structures excited at the upper troposphere. The small scale disturbances lead to an unphysical upturn in the kinetic energy spectrum (Figure 3.16b, blue line). Considering the characteristics of the spin-up, we speculate that the unrealistic behavior is caused by reflections of vertically propagating waves at the Rayleigh damping layer as already investigated by Gassmann and Herzog (2007). In order to get rid of the problem one may implement an upper radiative boundary condition (Gassmann and Herzog, 2007) or consider modifications of the numerical filter configurations. The second approach is discussed in Section 3.5.2.

The σ^2_{RE} coefficient is also used in order to determine the time span needed for reaching

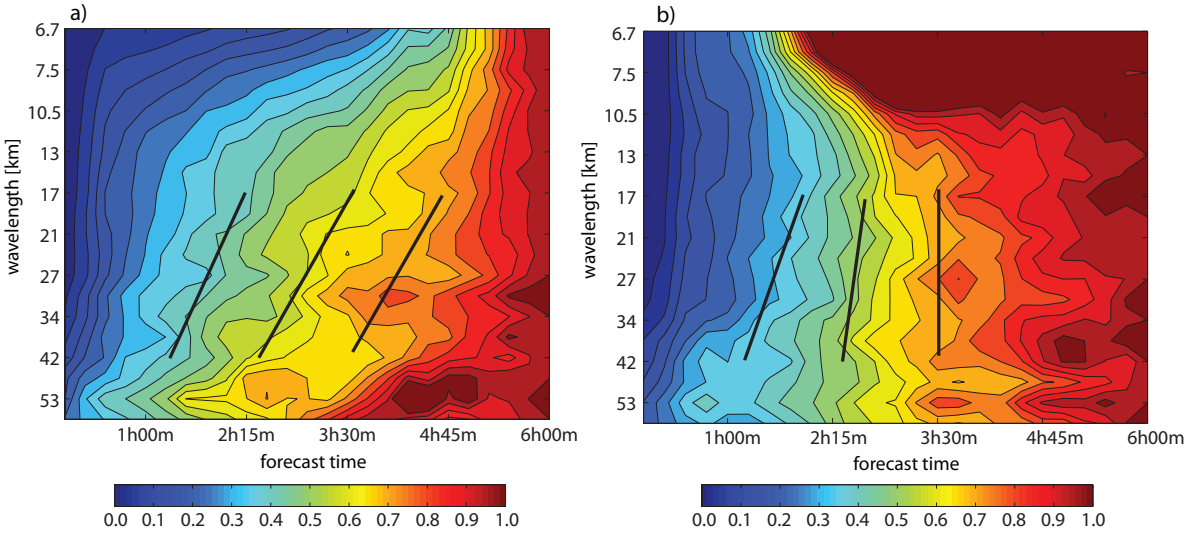

Figure 3.17: σ^2_{RE} dependent on the forecast time and wavelength. (a) Average for the model levels at the middle troposphere (5400 m - 4200 m above ground) and (b) for the model levels at the upper troposphere (9500 m - 7250 m above ground). The lines are tangential to the gradient of σ^2_{RE}.

a fully developed state of the mesoscale spectrum. If the σ^2_{RE} exceeds a threshold value of 0.9, the spin-up process will be defined as finished. Using that definition, the average spin-up time is about 5 hours. Skamarock (2004) estimated roughly by eye the spin-up time for the WRF model to be more than six hours. Indeed our investigations are carried out on a much smaller domain and with a higher resolution compared to the WRF model analysis. The difference in the resolution of the WRF and the COSMO model may lead to differences in the strength of the rotational and divergent modes. Thus, the nonlinear interactions are pushed by the COSMO-DE during the spin-up process. We have to note here, that the definition of spin-up period has to be treated very carefully, because we cannot take into account the influence of a temporally varying large-scale kinetic energy spectrum of the forcing data on the spin-up process.

The time scales of the spin-up process are highly dependent on altitude. We analyzed the σ^2_{RE} coefficient as a function of time for the upper and middle troposphere with respect to one specific wavenumber $k_{30} = 2.1 \times 10^{-4}$ rad m^{-1}, which corresponds to $\lambda \approx 30$ km. The result is listed in Table 3.2. The energy buildup is faster in the middle troposphere than in the upper troposphere during the first two hours of the forecast, whereas the relation is reversed afterwards. An explanation for this behavior is given by the theory of Yuan and Hamilton (1994): the nonlinear energy transfer between various scales is forced by gravity wave modes. We thus examined the modes of the horizontal divergence. The temporal evolution of the divergent mode k_{30} is also given in Table 3.2. Indeed, the variance of the divergence at k_{30} is much larger in the lower troposphere than in the upper troposphere during the first two hours of the forecast. Therefore, the energetic flux throughout the scales is much stronger for the lower levels than for the upper levels. Later on, this relationship is going into reverse, which confirms the theory of Yuan and Hamilton (1994) also in the framework of a mesoscale model.

Table 3.2: Ratio σ^2_{RE} of the kinetic energy and the spectral variance of the horizontal wind divergence σ^2_{div}. All values are related to the wavenumber $k_{30} = 2.1 \times 10^{-4}\,\mathrm{rad\,m^{-1}}$, i. e. $\lambda \approx 30$ km. The model levels 16 to 20 are located between 9500 m to 7300 m altitude, and the levels 28 to 32 are located between 4000 m to 2500 m altitude.

time [hours]	0.25	0.5	1.0	2.0	4.0
σ^2_{RE}, level 16-20	0.08	0.19	0.23	0.41	0.76
σ^2_{RE}, level 28-32	0.21	0.35	0.45	0.70	0.79
σ^2_{div}, level 16-20 [m s^{-2}]	63.2	205.5	301.5	536.5	825.5
σ^2_{div}, level 28-32 [m s^{-2}]	221.5	331.5	460.5	621.5	690.5

3.5.2 Qualification of the strength of the damping mechanisms

Since we found an unrealistic energetic input at the small scale end during the spin-up process (Figure 3.17b) in the upper troposphere, a study about the efficiency of the numerical filters implemented in the COSMO model is needed in order to control and damp the unrealistic wave reflections at the upper Rayleigh damping zone. The numerical filter mechanisms were already introduced in Section 2.3.1. The damping effect of the mechanisms is quantified following Skamarock (2004).

We repeat the simulation for the Elbe flash flood case (12th August 2002) using two modified filter configurations compared to the standard model 'stand'. The simulation 'nodiff' was performed using the standard filter mechanisms except for the horizontal divergence damping. The simulation '4thorder' was performed using the standard filter mechanisms, but applying the fourth order Laplacian diffusion on the total domain. The corresponding discrete energy density spectra are shown in Figure 3.18 at $t = 3.5$ h. Indeed, there is a upturn at the tail of the spectrum using the 'stand' configuration (blue line). The numerical dissipation used in the standard configuration, which originates mainly from the upwind biased advection scheme, is not sufficient to prevent from an artificial gain of energy at the very small-scale end of the spectrum in the upper troposphere. Checking the model output by eye reveals physically inconsistent structures directed along the x-direction, whereas no small scale perturbations are aligned along the y-directions (green-yellow line).

The unrealistic energy build-up can not be damped by the horizontal divergence damping. This numerical filter has no diffusive effect with respect to the kinetic energy (compare the blue and the green line). That is in contrast to the investigations of Skamarock (2004), who found a damping of the spectral variances using a horizontal divergence damping (Skamarock, 2004, Figure 12). As far as we know, the same filter is implemented in the COSMO model and in the WRF model, but the eddy filter coefficient of the COSMO model is smaller by a factor of 1.25 related to the WRF coefficient. Nevertheless, the horizontal divergence damping is useless for our simulation with respect to alleviate the problem of an unrealistic energy build-up at the small scales.

The unphysical input of energy at the small scale end is completely eliminated only,

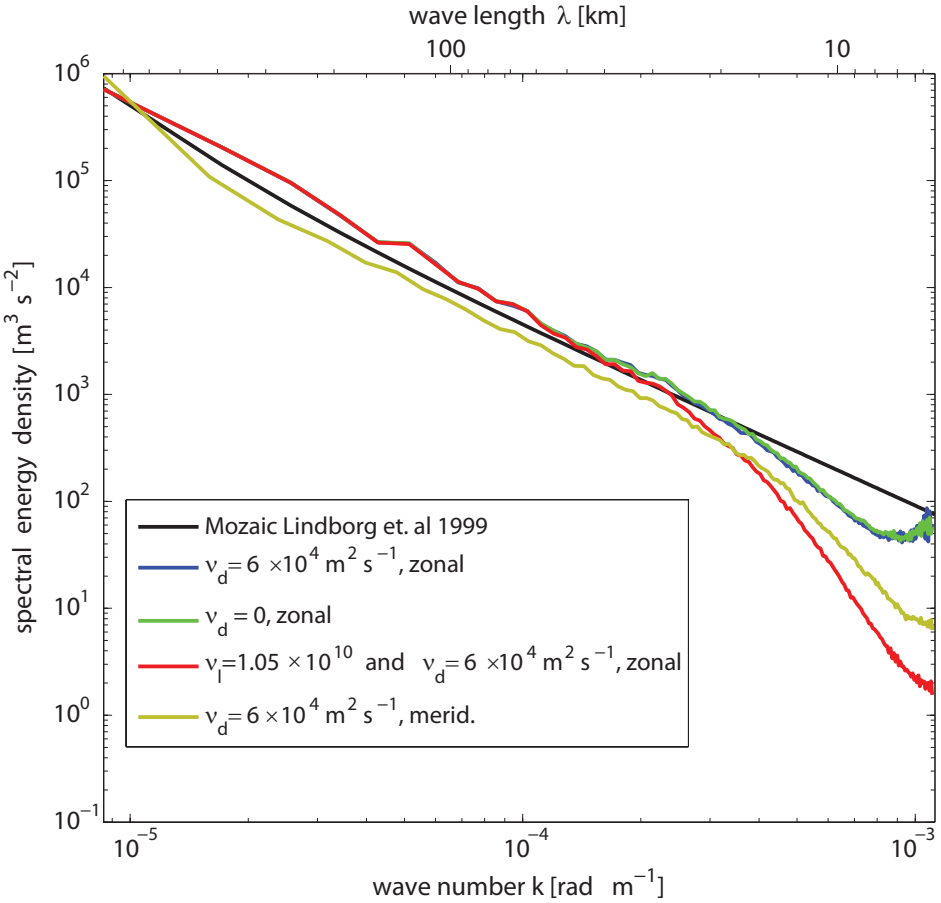

Figure 3.18: Kinetic energy density spectra produced by the model, vertically averaged from 9500 - 3000 m. The spectrum at $t = 3.5$ h for the standard configuration 'stand' (blue line and light green), a configuration with additional Laplacian diffusion '4thorder' (red line) and without any diffusion 'nodiff' (green line). The spectra are performed separately along the x-direction ('zonal') and y-direction 'merid'. ν_d and ν_l denotes the filter coefficient of the fourth order Laplacian diffusion, respectively the divergence damping.

if the simulation is done using the '4thorder' configuration (red line). Then, no small-scale perturbations are generated at the upper troposphere and the spin-up period is physically consistent. A small upturn remains at the tail of the model spectrum due to the misrepresentation of the waves smaller than $4\Delta x$ (Skamarock, 2004). The drawback of the '4thorder' simulation is that the Laplacian diffusion worsens the effective resolution, i. e. from about $7\Delta x = 20$ km using the 'stand' model configuration to about $9\Delta x = 25$ km using the '4thorder' model configuration.

The different behavior of the kinetic energy spectra for model configurations '4thorder' and 'nodiff' allows to draw the conclusion that the small-scale end of the spectrum can be manipulated using various filter coefficients for the Laplacian diffusion. Bryan et al. (2003) already demonstrated with a sensitivity study that the energy cascade at the smallest scales can be created whatever the user wishes. Therefore, care should be taken in the interpretation of the decay of the spectrum relative to theoretical or observed spectra. Conclusions with respect to the model performance using the effective resolution needs to be carefully drawn.

3.6 Summary and Conclusions

We invoke a multi-scale statistic method, namely the Fourier analysis, in order to verify and evaluate a high-resolution limited area model. We concentrate mainly on the wind field of the mid and upper troposphere. Only a few research studies deal with this topic (Denis et al., 2002; Skamarock, 2004), because the spectral decomposition on limited areas is a big challenge due to aperiodicity of the atmospheric fields. Furthermore, observed spectra of wind fields needed for evaluation are very rare. In order to investigate the impact of aperiodic fields on spectral decomposition methods, we performed idealistic tests with synthetic aperiodic fields using the Discrete Cosine Transform (Denis et al., 2002), the Discrete Fourier transform (Stull, 1988) and the detrending method by Errico (1985). Our theoretical investigations showed that the Discrete Cosine Transformation (DCT) offers the best performance in simulating a spectrum following a $k^{-5/3}$-law, which is characteristic for the mesoscale. Therefore, we used the DCT for computing spectra from model data, as well as from measurement data.

We examined aircraft measurements from the COPS field compaign (summer 2007, Southwestern Germany and Eastern France) in order to fill the gap in data needed for a model evaluation based on spectral analysis. That is, in contrast to Skamarock (2004) we did not only consider data on a global and climatological scale, but we also took into account the characteristics of the turbulent state of the atmosphere with respect to the investigated season and region. The observed kinetic energy spectrum derived from the COPS wind data possesses the same slope and shape as the globally and yearly averaged spectra of Nastrom et al. (1984) and Lindborg (1999), but it differs in the amplitude of the spectral variances. This means that the observed spectra over the COPS domain are case specific. This spectra were used as a reference for the model evaluation.

An evaluation of the high-resolution COSMO-DE model on the basis of COPS observations revealed that the energy cascade is well resolved by the model in a climatological sense, i. e. the mean spectra over 10 forecast days is physically consistent and coincides with the mean observed spectra on that days. The spectral analysis points out that the COSMO-DE model is qualified to simulate nonlinear interactions down to scales of $\lambda = 20\,\mathrm{km}$. The effective resolution of the COSMO-DE model is estimated to be seven times the grid spacing Δ, i. e. an improvement by a factor of three compared to the effective resolution of the coarsely resolved forcing model COSMO-EU. The COSMO-DE forecasts are resolving meteorological processes on the meso-β-scale, which are not resolved by the coarse observational analysis and the European COSMO-EU model. The effective resolution of COSMO-DE is in accordance with the investigations of Skamarock (2004) concerning the WRF model. Harris et al. (2001) concluded in his study that model simulations lack in variability at scales smaller than 5 Δ, but their conclusion refer to precipitation data.

Our spectral analysis demonstrated that the COSMO-DE model lacks in the prediction of nonlinear dynamics in the mid and upper troposphere for a specific day and a specific synoptic regime during the COPS campaign. With respect to the 20th July 2007, the spectral variances are two to three times smaller in the model compared

to the observations. On the one hand one can explain the differences because of the uncertainty range of the observations. On the other hand we have examined that the differences between model and observed spectra are associated with shortcomings in the prediction of convective weather over the region of Baden-Württemberg. A model intercomparison showed that COSMO-DE and the high-resolution models COSMO-CH and MESO-NH2 differ in the forecast of the kinetic energy cascade and thus the nonlinear dynamics. The MESO-NH2 offers the most realistic forecast of the kinetic energy cascade and it simulates some important small-scale features being observed on the 20th July 2007. We put forward a possible explanation for the differences in the forecast quality among the models: due to the limitation of the models to its effective resolution the MESO-NH2 (15 km) is preferred to resolve nonlinear dynamics on those scales, which cannot be resolved by COSMO-DE (20 km). However, a further sensitivity study using only one model is needed to investigate more profoundly also the impact of the forcing data, the physical parameterization and the resolution on the forecast skill.

Regarding the effective resolution, we have diagnosed for a cold start configuration that a fully developed state of the mesoscale spectrum is not reached until 5 hours spin-up time has passed. Not until then a consistent high resolution model output is available. The strength of the spin-up is coupled to the divergent modes and is strongly height-dependent.

Moreover, this work emphasizes the importance of the spectral analysis in order to verify the numerical damping schemes. The spectral analysis highlights that the diffusion inherent to the upwind biased advection schemes have a smaller damping effect on the small-scale features than the Laplacian diffusion used for even-order advection schemes, which confirms the results of Skamarock (2004). An upwind biased scheme thus offers a higher effective resolution (20 km compared to 25 km using Laplacian diffusion), but its diffusive operators were not sufficient to prevent instabilities of the COSMO-DE model close to the upper Rayleigh damping zone. Analyzing the instabilities we could detect two inconsistencies in the model: First, the temporal evolution of the kinetic energy spectrum is unphysical at the upper model levels, which shall motivate to implement and test other upper boundary conditions than the rigid lid condition (Gassmann and Herzog, 2007). Second, the divergence damping has no effect on the small-scale end of the spectrum, although the divergent modes are expected to be very high for such high resolutions. Therefore, a further discussion is required to identify qualitatively the impact of the divergence damping scheme on realistic weather forecasts.

4 Discretisation of a mesoscale model using Poisson and Nambu bracket forms

4.1 Introduction

State of the art NWP models are usually based on the Euler equations. Each term of the thermo-hydrodynamical equations is discretized using finite differences, finite volumes or finite element methods. In this study we want to construct the dynamical core of a NWP model, namely the COSMO model, using an equations set based on a Hamiltonian description with Poisson brackets (Gassmann and Herzog, 2008) and the energy-vorticity theory of Névir and Blender (1993) and Névir (1998) involving Nambu brackets.

According to the needs of the NWP, Gassmann and Herzog (2008) derived a Hamiltonian description of the turbulence-averaged compressible non-hydrostatic equations using Poisson brackets, which include all water species and the associated diabatic effects. They have thus extended the Hamiltonian description for an ideal fluid of Morrison and Greene (1980) and Morrison (1998) using Poisson brackets and the energy-vorticity theory of Névir and Blender (1993) and Névir (1998) using Nambu brackets. The energy-vorticity theory is hereinafter referred to as **EVT**.

We employ the Poisson bracket and the Nambu bracket form for two reasons:

(A) the construction of conservative numerical schemes

(B) the representation of three-dimensional vortices

Regarding topic (A), the construction of the numerical analogue of the Poisson and Nambu brackets offers a direct access to the quantities that should be conserved in a model. Salmon (2004, 2005, 2007) impressively adopted the Nambu bracket and Poisson bracket form for model applications, in particular for non-divergent barotropic and shallow-water models. He followed the idea to retain the antisymmetric properties of the brackets during model discretization and established spatial numerical schemes that conserve energy and vorticity-related quantities. Sommer and Névir (2009) applied the Nambu bracket form of Salmon to a shallow-water system on a staggered icosahedral grid and thus derived a conservative scheme regarding total energy and potential enstrophy.

Regarding topic (B), the Poisson bracket and Nambu bracket form of the non-hydrostatic compressible atmosphere incorporates three-dimensional vortex quantities, in particular the helicity in the EVT (Névir and Blender, 1993; Névir and Sommer, 2009). As

pointed out by Etling (1985), Lilly (1986) and Zhemin and Rongsheng (1994), the helicity influences strongly the nonlinear scale interactions. The nonlinear processes are dominating the mesoscale as a transition zone between quasi two-dimensional and three-dimensional flows. Because this scale range is the focus of the NWP models, we are motivated to take up the Poisson bracket and Nambu bracket form of the Euler equations as a basis for the discretization. The benefits of the brackets with respect to the numerical treatment of nonlinear cascades was already demonstrated by Salmon (2005), who derived the Arakawa Jacobian from the Nambu bracket form of a two-dimensional incompressible flow.

From the point of view of the NWP, topic (B) is much more important. In this work we invoke the representation of the nonlinear advection term in Poisson bracket and Nambu bracket form. We will develop and implement discretization schemes based on these brackets in the mesoscale model COSMO: namely a Poisson scheme and an EVT scheme. We will focus exclusively on the spatial discretization. As demonstrated in this Chapter, in both schemes the discretization starts at the level of conservative quantities like mass or energy. The Poisson scheme and the EVT scheme are tested and the model results are discussed in the framework of two idealized cases: an inertia-gravity wave test characterized by weak nonlinear conditions and a supercell simulation developing under strong nonlinear conditions.

This chapter is structured as follows. In Section 4.2 we give an overview on the concept of the Hamiltonian description and the EVT of the continuous Euler equations and the related Poisson and Nambu brackets. In Section 4.3 we explain the discretization procedure, which is applied to the COSMO model in Section 4.4 for idealized test cases. Section 4.5 gives the summary and conclusions.

4.2 The continuous Euler equations based on the Hamiltonian description and the energy-vorticity theory

In this section the Hamiltonian theory and the energy-vorticity theory are discussed with respect to the description of the non-hydrostatic compressible equations. Both theories serve afterwards as a basis for the numerical discretization of the NWP model COSMO.

4.2.1 The Hamiltonian description with Poisson brackets

Morrison and Greene (1980) derived a Hamiltonian description of the magneto- hydrodynamical equations, which was adapted by Morrison (1998) for the atmospheric dynamics. The Euler equations of an adiabatic flow for an ideal fluid in a rotating

frame read:

$$\rho\frac{\partial \mathbf{v}}{\partial t} + \rho\mathbf{v}\cdot\nabla\mathbf{v} = -2\Omega\times(\rho\mathbf{v}) - \nabla p - \rho\nabla\Phi\,, \tag{4.1}$$

$$\frac{\partial \rho}{\partial t} + \mathbf{v}\cdot\nabla\rho = -\rho\nabla\cdot\mathbf{v}\,, \qquad \frac{\partial s}{\partial t} + \mathbf{v}\cdot\nabla s = 0\,, \tag{4.2}$$

where s is the entropy per unit total mass, Φ is the gravitational potential, p is the atmospheric pressure, $\mathbf{v}$ is the velocity vector, Ω is the earth rotation vector and ρ is the density. The entropy equation is equivalent to a conservation of potential temperature.

The non-canonical Hamiltonian form of the equation set (4.1)-(4.2) is given by (Morrison, 1998):

$$\frac{\partial \mathbf{u}}{\partial t} = \underline{\mathbf{D}}\cdot\frac{\delta\mathcal{H}}{\delta\mathbf{u}} =: \{\mathbf{u},\mathcal{H}\}^P\,, \tag{4.3}$$

where δ denotes the functional derivative and $\{,\}^P$ denotes a Poisson bracket. $\mathbf{u}$ is the state vector of the variables u, v, w, ρ and s. The temporal evolution of the state variables is defined by the Hamilton functional $\mathcal{H}$ and the differential matrix operator $\underline{\mathbf{D}}$. The explicit form of $\underline{\mathbf{D}}$ is given in Shepherd (1990). The functional $\mathcal{H}$ is defined as the sum of kinetic, internal and potential energy:

$$\mathcal{H} = \int\limits_V \left(\frac{1}{2}\rho\mathbf{v}^2 + \rho e(\rho,s) + \rho\Phi\right) dV\,, \tag{4.4}$$

where e is the internal energy per unit total mass. The energy-like functional is the only conserved quantity used to construct the general evolution equation (4.3).

The non-canonical representation given by eq. (4.3) is related to the bilinear Poisson bracket (Névir, 1998)

$$\begin{aligned}\{\mathcal{F},\mathcal{H}\}^P =& -\int\limits_V \left(\frac{\delta\mathcal{F}}{\delta\rho}\nabla\cdot\frac{\delta\mathcal{H}}{\delta\mathbf{v}} - \frac{\delta\mathcal{H}}{\delta\rho}\nabla\cdot\frac{\delta\mathcal{F}}{\delta\mathbf{v}}\right) dV - \int\limits_V \left[\frac{1}{\rho}\left(\nabla\times\mathbf{v}+2\Omega\right)\cdot\left(\frac{\delta\mathcal{H}}{\delta\mathbf{v}}\times\frac{\delta\mathcal{F}}{\delta\mathbf{v}}\right)\right] dV \\ & - \int\limits_V \left[\frac{\nabla s}{\rho}\cdot\left(\frac{\delta\mathcal{F}}{\delta s}\frac{\delta\mathcal{H}}{\delta\mathbf{v}}\right) - \frac{\nabla s}{\rho}\cdot\left(\frac{\delta\mathcal{H}}{\delta s}\frac{\delta\mathcal{F}}{\delta\mathbf{v}}\right)\right] dV \\ =:& \quad \{\mathcal{F},\mathcal{H}\}^P_{\rho,\mathbf{v}} + \{\mathcal{F},\mathcal{H}\}^P_{\mathbf{v},\mathbf{v}} + \{\mathcal{F},\mathcal{H}\}^P_{s,\mathbf{v}}\,,\end{aligned} \tag{4.5}$$

where $\mathcal{F}[u]$ is an arbitrary functional dependent on the variables of the state vector. The bracket $\{\mathcal{F},\mathcal{H}\}$ is antisymmetric, i. e. $\{\mathcal{H},\mathcal{F}\} = -\{\mathcal{F},\mathcal{H}\}$. The functional derivatives of the Hamiltonian with respect to the velocity, density and entropy are given by (Névir, 1998):

$$\frac{\delta\mathcal{H}}{\delta\mathbf{v}} = \rho\mathbf{v}\,, \quad \frac{\delta\mathcal{H}}{\delta\rho} = \frac{1}{2}\mathbf{v}^2 + h + \Phi\,, \quad \frac{\delta\mathcal{H}}{\delta s} = \rho T\,, \tag{4.6}$$

where $h = e + p/\rho$ is the enthalpy per unit total mass.

Using the functional derivatives (4.6) one can rewrite the equation system (4.1) and (4.2) as follows:

$$\frac{\partial\mathbf{v}}{\partial t} = \{\mathbf{v},\mathcal{H}\}^P\,, \quad \frac{\partial\rho}{\partial t} = \{\rho,\mathcal{H}\}^P\,, \quad \frac{\partial s}{\partial t} = \{s,\mathcal{H}\}^P\,. \tag{4.7}$$

The relation between the Eulerian form given by (4.1) and (4.2) and the Hamiltonian description can only be obtained, if some integration by parts is done. In addition, boundary terms associated with volume integrals must vanish, i. e. the boundary condition

$$\int_V \nabla \cdot \boldsymbol{\psi}\, dV = 0\,, \quad \text{or equivalent:} \quad \int_{\partial V} \boldsymbol{\psi} \cdot d\mathbf{S}_b = 0 \tag{4.8}$$

has to be valid for an arbitrary vector-valued function $\boldsymbol{\psi}$. $d\mathbf{S}_b$ is the surface oriented normal to the boundary ∂V. A discussion about the required boundary conditions can be found in Morrison (1998, page 490) and Bannon (2003, Section 3).

Having in mind that our investigation is focusing on the representation of the nonlinear interaction, the Euler equations of momentum are derived from the Poisson form given in eq. (4.7) using the bracket definition (4.5), the functional derivatives (4.6) and the mathematical laws and assumptions given as follows:

- The functional derivatives $\frac{\delta \mathbf{v}}{\delta \rho}$ and $\frac{\delta \mathbf{v}}{\delta s}$ are zero.
- Integration by parts and the boundary condition (4.8) is applied to the $\{\mathbf{v}, \mathcal{H}\}^P_{\rho,\mathbf{v}}$ part of the Poisson bracket.
- The functional derivative of the velocity field $\mathbf{v}$ with respect to $\mathbf{v}$ gives the Dirac Delta function. The reader is referred to Morrison (1998) and Lange (2002) for details about functional derivatives.
- The volume integral of the product of a Dirac Delta function and a vector valued field is assumed to turn into the vector valued field (Lange, 2002).

Thus, we get the following sequence of transformations:

$$\begin{aligned}
\frac{\partial \mathbf{v}}{\partial t} =& \{\mathbf{v}, \mathcal{H}\}^P_{\rho,\mathbf{v}} + \{\mathbf{v}, \mathcal{H}\}^P_{\mathbf{v},\mathbf{v}} + \{\mathbf{v}, \mathcal{H}\}^P_{s,\mathbf{v}} \\
=& -\int_V \left[\frac{\delta \mathbf{v}}{\delta \mathbf{v}} \cdot \nabla \left(\frac{1}{2}\mathbf{v}^2 + h + \Phi\right)\right] dV - \int_V \left[\frac{1}{\rho}\frac{\delta \mathbf{v}}{\delta \mathbf{v}} \cdot (\nabla \times \mathbf{v} + 2\Omega) \times (\rho \mathbf{v})\right] dV \\
&+ \int_V \left[\rho T \frac{\delta \mathbf{v}}{\delta \mathbf{v}} \cdot \frac{\nabla s}{\rho}\right] dV \\
=& -\frac{1}{\rho}(\nabla \times \mathbf{v} + 2\Omega) \times (\rho \mathbf{v}) - \nabla\left(\frac{1}{2}\mathbf{v}^2\right) + \boldsymbol{\chi}(h, \Phi, s, T)\,.
\end{aligned} \tag{4.9}$$

The vector valued function $\boldsymbol{\chi}$ summarizes all thermodynamical terms and the acceleration due to gravity. Only the $\{\mathcal{F}, \mathcal{H}\}_{\rho,\mathbf{v}}$ and the $\{\mathcal{F}, \mathcal{H}\}_{\mathbf{v},\mathbf{v}}$ part of the Poisson bracket contribute a relevant part to the nonlinear advection term, which is recovered in the derivation (4.9) by the Lamb transformation:

$$\mathbf{v} \cdot \nabla \mathbf{v} + 2\Omega \times \mathbf{v} = \frac{1}{\rho}(\nabla \times \mathbf{v} + 2\Omega) \times (\rho \mathbf{v}) + \nabla\left(\frac{1}{2}\mathbf{v}^2\right)$$

It is important to note here that the Poisson bracket form unveils clearly the absolute potential vorticity flux in the equation of motion, which is hidden in the Eulerian form

given by eq. (4.1). In addition, the vorticity contribution due to the Earth rotation is inherently linked to the vorticity field.

With respect to the NWP, multiphase diabatic and turbulent friction processes remain hidden in the non-canonical Hamiltonian form (4.7). Gassmann and Herzog (2008) proposed to extend the Poisson bracket description of an ideal fluid by the so-called physical brackets (eq. 47, 48), which guarantee for energy conservation in the moist turbulent case. They employed the virtual potential temperature and not the entropy as a pressure-like variable. Nevertheless, their Hamiltonian description of the nonlinear advection term is the same as given by derivation (4.9), i. e. their formulation for the $\{\mathcal{F},\mathcal{H}\}_{\rho,\mathbf{v}}$ and the $\{\mathcal{F},\mathcal{H}\}_{\mathbf{v},\mathbf{v}}$ part of the Poisson bracket do not differ from the definitions in eq. (4.5).

The $\{\mathcal{F},\mathcal{H}\}_{\rho,\mathbf{v}}$ and the $\{\mathcal{F},\mathcal{H}\}_{\mathbf{v},\mathbf{v}}$ bracket parts are used as a basis for the discretization of the nonlinear advection term in a mesoscale NWP model, which is discussed in Section 4.3.3.

4.2.2 The energy-vorticity theory

A characteristic feature of the matrix operator $\underline{\mathbf{D}}$ (eq. (4.3)) and the related Poisson bracket is its singularity. This singularity is related to Casimir functionals $\mathcal{C}$ that commute with the Hamiltonian $\mathcal{H}$ (Morrison, 1998; Névir, 1998):

$$\underline{\mathbf{D}} \cdot \frac{\delta \mathcal{C}}{\delta \mathbf{u}} = 0 \qquad \Rightarrow \qquad \frac{\partial \mathcal{C}}{\partial t} = \{\mathcal{C},\mathcal{H}\} = 0\,. \tag{4.10}$$

Therefore, the Casimir functionals are itself global conserved quantities. The Casimir functionals of a compressible adiabatic fluid, which fulfill eq. (4.10), are the mass-weighted integrals

$$\mathcal{M} = \int_V \rho dV\,, \quad \mathcal{S} = \int_V \rho s dV\,, \quad \mathcal{P}_a = \int_V \rho \Pi_a dV\,, \tag{4.11}$$

where Π_a is the Ertels potential vorticity:

$$\Pi_a = \frac{(\nabla \times \mathbf{v} + 2\Omega) \cdot \nabla s}{\rho}\,.$$

The occurrence of Casimir functionals means a reduction of the degree's of freedom. I. e., from the physical point of view, that the temporal evolution of the variables $\mathbf{v}$, ρ and s is not independent in the Eulerian space. To eliminate the singularity of the differential operator $\underline{\mathbf{D}}$ and the related Poisson bracket, Névir and Blender (1993) generalized the Hamiltonian dynamics and introduced the so-called energy-vorticity theory (EVT) (also refer to Névir, 1998; Névir and Sommer, 2009). In the framework of the EVT Névir and Blender (1993) proposed to describe the thermodynamics of a compressible adiabatic fluid with three trilinear Nambu brackets: an energy-helicity bracket $\{\mathcal{F},h_a,\mathcal{H}\}^N$,

an energy-mass bracket $\{\mathcal{F},\mathcal{M},\mathcal{H}\}^N$ and an energy-entropy bracket $\{\mathcal{F},\mathcal{S},\mathcal{H}\}^N$. The brackets are defined as follows (Névir and Sommer, 2009):

$$\{\mathcal{F},h_a,\mathcal{H}\}^N = -\int\limits_V \left[\frac{1}{\rho}\frac{\delta\mathcal{F}}{\delta\mathbf{v}}\cdot\left(\frac{\delta h_a}{\delta\mathbf{v}}\times\frac{\delta\mathcal{H}}{\delta\mathbf{v}}\right)\right]dV\,, \tag{4.12}$$

$$\{\mathcal{F},\mathcal{M},\mathcal{H}\}^N = -\int\limits_V \left[\frac{\delta\mathcal{F}}{\delta\mathbf{v}}\frac{\delta\mathcal{M}}{\delta\rho}\cdot\nabla\frac{\delta\mathcal{H}}{\delta\rho}+\frac{\delta\mathcal{F}}{\delta\rho}\nabla\cdot\left(\frac{\delta\mathcal{M}}{\delta\rho}\frac{\delta\mathcal{H}}{\delta\mathbf{v}}\right)\right]dV+\mathrm{cyc}(\mathcal{F},\mathcal{M},\mathcal{H})\,, \tag{4.13}$$

$$\{\mathcal{F},\mathcal{S},\mathcal{H}\}^N = -\int\limits_V \left[\frac{\delta\mathcal{F}}{\delta\mathbf{v}}\frac{\delta\mathcal{S}}{\delta\rho}\cdot\nabla\frac{\delta\mathcal{H}}{\delta\sigma}+\frac{\delta\mathcal{F}}{\delta\sigma}\nabla\cdot\left(\frac{\delta\mathcal{S}}{\delta\rho}\frac{\delta\mathcal{H}}{\delta\mathbf{v}}\right)\right]dV+\mathrm{cyc}(\mathcal{F},\mathcal{S},\mathcal{H})\,. \tag{4.14}$$

cyc(.,.,.) denotes cyclic permutations (refer to eq. (4.17)). $\sigma=\rho s$ is the entropy and h_a is the absolute global helicity given by:

$$h_a=\frac{1}{2}\int\limits_V \mathbf{v}_a\cdot\boldsymbol{\xi}_a\,,\quad \mathbf{v}_a=\mathbf{v}+\Omega\times\mathbf{r}\,,\quad \boldsymbol{\xi}_a=\nabla\times\mathbf{v}+2\Omega\,. \tag{4.15}$$

We refer to $\boldsymbol{\xi}_a$ as the absolute three-dimensional vorticity vector.

The functional derivatives of the Hamiltonian $\mathcal{H}$ and the global quantities $\mathcal{M}$, $\mathcal{S}$, h_a with respect to the state variables read (Névir, 1998):

$$\begin{array}{lllllllll}
\dfrac{\delta\mathcal{H}}{\delta\mathbf{v}} &=& \rho\mathbf{v}\,, & \dfrac{\delta\mathcal{H}}{\delta\rho} &=& \dfrac{1}{2}\mathbf{v}^2+e+\dfrac{p}{\rho}-Ts+\Phi\,, & \dfrac{\delta\mathcal{H}}{\delta\sigma} &=& T\\
\dfrac{\delta\mathcal{M}}{\delta\mathbf{v}} &=& 0\,, & \dfrac{\delta\mathcal{M}}{\delta\rho} &=& 1\,, & \dfrac{\delta\mathcal{M}}{\delta\sigma} &=& 0\\
\dfrac{\delta\mathcal{S}}{\delta\mathbf{v}} &=& 0\,, & \dfrac{\delta\mathcal{S}}{\delta\rho} &=& s\,, & \dfrac{\delta\mathcal{S}}{\delta\sigma} &=& 1\\
\dfrac{\delta h_a}{\delta\mathbf{v}} &=& \boldsymbol{\xi}_a\,, & \dfrac{\delta h_a}{\delta\rho} &=& 0\,, & \dfrac{\delta h_a}{\delta\sigma} &=& 0
\end{array} \tag{4.16}$$

In order to derive the functional derivatives of the absolute global helicity the boundary condition (4.8) is assumed to be valid.

The Nambu representation is only satisfied, if the Nambu brackets given in eq. (4.12)-(4.14) are completely antisymmetric, i. e. the condition $\{\mathcal{F},\mathcal{G},\mathcal{H}\}^N=-\{\mathcal{G},\mathcal{F},\mathcal{H}\}^N=\{\mathcal{G},\mathcal{H},\mathcal{F}\}^N$ is fulfilled. The energy-helicity bracket is antisymmetric due to the mathematical properties of the scalar triple product. The antisymmetry of the energy-mass and energy-entropy bracket is recovered, if all cyclic permutations $\mathrm{cyc}(\mathcal{F},\mathcal{M},\mathcal{H})$ and $\mathrm{cyc}(\mathcal{F},\mathcal{S},\mathcal{H})$ are taken into account. These additional terms are given here for the energy-mass bracket:

$$\begin{aligned}\mathrm{cyc}(\mathcal{F},\mathcal{M},\mathcal{H}) = &-\int\limits_V \left[\frac{\delta\mathcal{H}}{\delta\mathbf{v}}\frac{\delta\mathcal{F}}{\delta\rho}\cdot\nabla\frac{\delta\mathcal{M}}{\delta\rho}+\frac{\delta\mathcal{H}}{\delta\rho}\nabla\cdot\left(\frac{\delta\mathcal{F}}{\delta\rho}\frac{\delta\mathcal{M}}{\delta\mathbf{v}}\right)\right]dV\\ &-\int\limits_V \left[\frac{\delta\mathcal{M}}{\delta\mathbf{v}}\frac{\delta\mathcal{H}}{\delta\rho}\cdot\nabla\frac{\delta\mathcal{F}}{\delta\rho}+\frac{\delta\mathcal{M}}{\delta\rho}\nabla\cdot\left(\frac{\delta\mathcal{H}}{\delta\rho}\frac{\delta\mathcal{F}}{\delta\mathbf{v}}\right)\right]dV\end{aligned} \tag{4.17}$$

Indeed, all terms vanish in eq. (4.17) using the functional derivatives in eq. (4.16) and the needed boundary condition (4.8). But if we permute $\mathcal{F}$ and $\mathcal{M}$ in the energy-mass bracket, we yield nonzero terms for the cyc$(\mathcal{M},\mathcal{F},\mathcal{H})$ part of the $\{\mathcal{M},\mathcal{F},\mathcal{H}\}^N$ bracket:

$$\{\mathcal{M},\mathcal{F},\mathcal{H}\}^N = \mathrm{cyc}(\mathcal{M},\mathcal{F},\mathcal{H}) = -\int_V \left[\frac{\delta\mathcal{H}}{\delta\mathbf{v}}\frac{\delta\mathcal{M}}{\delta\rho}\cdot\nabla\frac{\delta\mathcal{F}}{\delta\rho} + \frac{\delta\mathcal{H}}{\delta\rho}\nabla\cdot\left(\frac{\delta\mathcal{M}}{\delta\rho}\frac{\delta\mathcal{F}}{\delta\mathbf{v}}\right)\right] dV\,. \tag{4.18}$$

Taking into account the rule of the integration by parts and the boundary condition (4.8), one can derive the expression

$$\int_V A\nabla\cdot\boldsymbol{\psi}\,dV = -\int_V \boldsymbol{\psi}\cdot\nabla A\,dV\,, \tag{4.19}$$

which is valid for an arbitrary function A and a vector valued function $\boldsymbol{\psi}$. Applying the transformation (4.19) to the terms cyc$(\mathcal{M},\mathcal{F},\mathcal{H})$ given in eq. (4.18) reveals that the bracket $\{\mathcal{M},\mathcal{F},\mathcal{H}\}^N$ is equivalent to $-\{\mathcal{F},\mathcal{M},\mathcal{H}\}^N$. I. e. the energy-mass bracket is antisymmetric because of (a) the duality between the divergence and the gradient operator (eq. (4.19)) and (b) because of the terms occurring in the cyclic permutations cyc$(\mathcal{F},\mathcal{M},\mathcal{H})$ (eq. (4.17)). That also holds for the energy-entropy bracket.

The temporal evolution of an arbitrary functional $\mathcal{F}[\mathbf{v},\rho,\sigma]$ in a compressible adiabatic fluid is given by the sum of all three brackets in eq. (4.12)-(4.14) (Névir, 1998):

$$\frac{\partial\mathcal{F}}{\partial t} = \{\mathcal{F},h_a,\mathcal{H}\}^N + \{\mathcal{F},\mathcal{M},\mathcal{H}\}^N + \{\mathcal{F},\mathcal{S},\mathcal{H}\}^N\,. \tag{4.20}$$

The global integrated quantities mass, enstrophy and the absolute helicity constitute the governing equations on the same level as the Hamiltonian $\mathcal{H}$. That is in contrast to the non-canonical Hamiltonian description given by eq. (4.3), where the Casimir functionals are hidden (Névir, 1998).
The Euler equations (4.1) and (4.2) are obtained by setting $\mathcal{F}=\mathbf{v}$, $\mathcal{F}=\rho$ and $\mathcal{F}=\sigma$ in eq. (4.20):

$$\begin{aligned}\frac{\partial\mathbf{v}}{\partial t} &= \{\mathbf{v},h_a,\mathcal{H}\}^N + \{\mathbf{v},\mathcal{M},\mathcal{H}\}^N + \{\mathbf{v},\mathcal{S},\mathcal{H}\}^N\,,\\ \frac{\partial\rho}{\partial t} &= \{\rho,\mathcal{M},\mathcal{H}\}^N\,, \qquad \frac{\partial\sigma}{\partial t} = \{\sigma,\mathcal{S},\mathcal{H}\}^N\,.\end{aligned} \tag{4.21}$$

The continuity equation and the first law of thermodynamics are defined by one bracket, whereas the momentum equation is made up by the sum of all three trilinear Nambu brackets. In the case of a barotropic compressible flow the momentum equation is constituted only by the energy-helicity and the energy-mass bracket. Only in the case of an incompressible and barotropic flow the momentum equation is constituted by the energy-helicity bracket alone (Névir, 1998).

Focusing on the nonlinear scale interaction in the framework of the energy-vorticity theory, we need to consider the energy-helicity and the energy-mass bracket. We reveal the nonlinear advection term $\mathbf{v}\cdot\nabla\mathbf{v}$ in the Euler momentum equations from the Nambu

bracket form (4.21) using the following sequence of transformations:

$$\begin{aligned}\frac{\partial \mathbf{v}}{\partial t} =& -\int\limits_V \left[\frac{1}{\rho}\frac{\delta \mathbf{v}}{\delta \mathbf{v}}\cdot\left(\frac{\delta h_a}{\delta \mathbf{v}}\times\frac{\delta \mathcal{H}}{\delta \mathbf{v}}\right)\right] dV - \int\limits_V \left[\frac{\delta \mathbf{v}}{\delta \mathbf{v}}\frac{\delta \mathcal{M}}{\delta \rho}\cdot\nabla\frac{\delta \mathcal{H}}{\delta \rho} + \frac{\delta \mathbf{v}}{\delta \rho}\nabla\cdot\left(\frac{\delta \mathcal{M}}{\delta \rho}\frac{\delta \mathcal{H}}{\delta \mathbf{v}}\right)\right] dV \\ & - \int\limits_V \left[\frac{\delta \mathbf{v}}{\delta \mathbf{v}}\frac{\delta \mathcal{S}}{\delta \rho}\cdot\nabla\frac{\delta \mathcal{H}}{\delta \sigma} + \frac{\delta \mathbf{v}}{\delta \sigma}\nabla\cdot\left(\frac{\delta \mathcal{S}}{\delta \rho}\frac{\delta \mathcal{H}}{\delta \mathbf{v}}\right)\right] dV \\ =& -\frac{\boldsymbol{\xi}_a}{\rho}\times(\rho\mathbf{v}) - \nabla\left(\frac{1}{2}\mathbf{v}^2\right) + \boldsymbol{\chi}(h,\Phi,s,T)\,.\end{aligned} \tag{4.22}$$

The vector valued function $\boldsymbol{\chi}$ summarizes all thermodynamical terms and the acceleration due to gravity. We made use of the same assumptions and mathematical rules as for the derivation (4.9). The first terms on the right hand side constitute the nonlinear advection term using the Lamb transformation as discussed for the Hamiltonian description. Keeping in mind the importance of the helicity for analysing rotational flows (Etling, 1985) and its influence on nonlinear scale interactions (Lilly, 1986), it might help to explicitly represent the energy-helicity bracket in the framework of the model discretization.

As already discussed for the Hamiltonian form (4.3), the multiphase diabatic and turbulent processes are not yet incorporated in the Nambu bracket formulation (4.20). Although some adaptations to the brackets are needed to incorporate the full-physics into the energy-vorticity theory, the composition of the nonlinear advection term on the level of the brackets does not change. Hence, the Nambu brackets $\{\mathcal{F}, h_a, \mathcal{H}\}^N$ and $\{\mathcal{F}, \mathcal{M}, \mathcal{H}\}^N$ serves as a basis for the discretization of the nonlinear advection term in a mesoscale NWP model. We introduce the discretization procedure in the Section 4.3.2.

4.3 Obtaining local discretisation procedures from the contineous Bracket forms

In the previous Section we introduced the Hamiltonian and the energy-vortex representation of the Euler equations. In particular, the main goal was to find the bracket description for the nonlinear dynamics. Both bracket representations offer the opportunity to design new discretization schemes benefiting from the mathematical properties of the Poisson and Nambu brackets. In contrast to Gassmann and Herzog (2008), we confine ourself to the nonlinear part of the model equations, because it is expected to be the most challenging part for the short-term NWP.

The guideline for the following discretization is that we need to transfer the antisymmetric properties of the brackets to their discretized analogues. Salmon (2004, 2005, 2007) already proposed computational methods that preserve the antisymmetric properties of the Poisson and Nambu brackets during the discretization process. He developed new numerical schemes for 2-d barotropic and shallow-water models and could derive the Arakawa Jacobian based on the Nambu bracket philosophy.

The application of the Poisson and Nambu brackets to state-of-the-art models is challenging due to the complex geometry and the staggered grids. Having in mind the implementation of the bracket philosophy to the COSMO model, we focus our investigation on the Arakawa-C/Lorenz grid staggering. We discuss exclusively the spatial discretization.

4.3.1 The COSMO grid

A detailed description of the COSMO model grid is given in Steppeler et al. (2003) and Doms and Schaettler (2002). Here, only the aspects relevant to our spatial discretization are introduced. The grid is a quadrilateral grid. I. e. the irregular physical space and its curvilinear terrain-following Earth surface are mapped onto a regular computational grid, which is subdivided into grid boxes with a well-defined horizontal and vertical extent:

- $r \cos \Delta\lambda$: grid spacing in West-East direction,
- $r\Delta\varphi$: grid spacing in North-South direction,
- $-\sqrt{G}\Delta\zeta$: grid spacing in vertical direction,

where r is the Earth radius. λ, φ and ζ denotes the longitude, latitude and the height coordinate and $\sqrt{G}$ is a geometrical factor of a terrain-following system (Doms and Schaettler, 2002). In order to study the bracket-based discretization approaches, we assume a Cartesian grid space and do not further consider the terrain-following terms. Then, the dimensions of the grid boxes changes to:

$$r\cos\Delta\lambda = \text{const.} \Rightarrow \Delta x \quad r\Delta\varphi = \text{const.} \Rightarrow \Delta y \quad -\sqrt{G}\Delta\zeta \Rightarrow \Delta z \tag{4.23}$$

The horizontal and vertical cross section of a model grid box is shown in Figure 4.1. The prognostic variables are staggered on an Arakawa-C / Lorenz grid. The center of every grid box is the mass mid point denoted by the indices (i, j, k), where i and j corresponds to the x-direction and the y-direction, respectively, and k is related to the vertical z-coordinate. The index k is defined to increase when the height decreases. All scalar variables are located at the mass mid point, whereas the velocity components u, v and w are staggered by half a grid point and located at the cell faces. The notations for the COSMO grid are listed in Table 4.1.

With respect to the differential operators, the grid can be interpreted as a composition of a primal and a dual grid. The divergence operator is defined with regard to the primal grid (bounded by a straight line, Figure 4.1). The curl operator is defined regarding the dual grid (bounded by a dotted line).

4.3.2 The EVT scheme

Keeping in mind the energy-vorticity theory (EVT), the related Nambu form given by eq. (4.21) and the derivation in eq. (4.22), a discretization of the energy-helicity bracket $\{\mathcal{F}, h_a, \mathcal{H}\}$ and the energy-mass bracket $\{\mathcal{F}, \mathcal{M}, \mathcal{H}\}$ and the corresponding functionals and functional derivatives need to be specified.

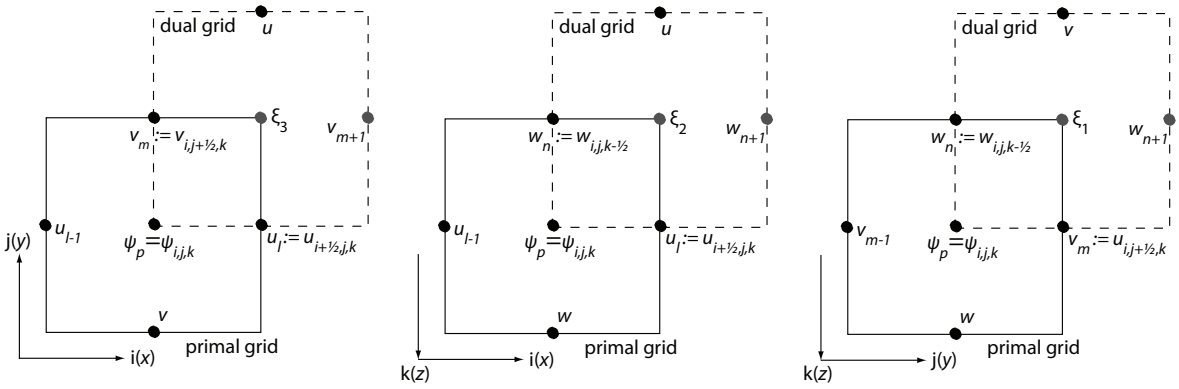

Figure 4.1: Positions of the variables on the COSMO grid. The horizontal $x-y$ cross section (left), the vertical $x-z$ cross section (middle) and $y-z$ cross section (right) are shown. The primal grid is denoted by the rectangle with a straight line, the dual grid is denoted by the rectangle with a dashed line.

Table 4.1: Notation of the COSMO model grid.

index	description	index	description
l	position of components	m	position of components v
n	position of components w	p	position of mass mid points
c	corner points $(i+\frac{1}{2}, j+\frac{1}{2}, k+\frac{1}{2})$	N	number of global grid points
τ_x	3-d volume with the center at position x	$F(p)$	cell faces belonging to the grid box p
$A(x)$	2-d surface with the center at position x	ξ_1	position of vorticity in the y-z plane
ξ_2	position of vorticity in the x-z plane	ξ_3	position of vorticity in the x-y plane

The functionals

The integrals inherent in the functionals are approximated by a sum over grid boxes following the approach of Salmon (2004). We first consider the Hamiltonian $\mathcal{H}$ given by eq. (4.4). It is replaced by

$$H_p = \sum_{p=1}^{N} \left[\left(\frac{1}{2} \rho \mathbf{v}^2 \right)_p + (\rho e)_p + (\rho \Phi)_p \right] \tau_p \,, \tag{4.24}$$

where subscript p denotes the grid location and N the grid point number given in Table 4.1. The internal energy and the potential energy part of the Hamiltonian H_p are omitted in the subsequence, because both parts do not contribute to the nonlinear advection term (eq. (4.22)).

In order to discretize the inner product $\frac{1}{2}\rho\mathbf{v}^2$ of the Hamiltonian H_p the ansatz of

Gassmann and Herzog (2008) is used:

$$\left(v^2\right)_P = \frac{1}{2}\sum_{l\in F(p)} u_l^2 + \frac{1}{2}\sum_{m\in F(p)} v_m^2 + \frac{1}{2}\sum_{n\in F(p)} w_n^2 := \overline{u_l^2}^x\Big|_p + \overline{v_m^2}^y\Big|_p + \overline{w_n^2}^z\Big|_p\,, \tag{4.25}$$

where l, m, n denotes the grid locations and $F(p)$ the cell faces given in Table 4.1. Eq. (4.25) defines not only the approximation for the inner product, but also the reconstruction from the cell faces of a grid box to the mass point p (Figure 4.1). Applying eq. (4.25) to eq. (4.24), the discretized Hamiltonian H_p reads:

$$H_p = \sum_{p=1}^{N}\left[\frac{1}{2}\rho_p\left(\overline{u_l^2}^x\Big|_p + \overline{v_m^2}^y\Big|_p + \overline{w_n^2}^z\Big|_p\right)\right]\tau_p\,. \tag{4.26}$$

For obtaining the discretized functional of the absolute helicity h_a (eq. (4.15)), we need to specify its position on the grid. Because the helicity is a scalar triple product, i. e. $h_a \sim \mathbf{v}\cdot\nabla\times\mathbf{v} \sim \mathbf{v}\times\xi$, each of the vector components of the velocity and the vorticity are reconstructed on the same position on the grid prior to the scalar multiplication. In order to be consistent in defining the functionals, we locate the functional of the absolute helicity h_a at the mass mid point p:

$$h_{a,p} = \frac{1}{2}\sum_{p=1}^{N}\left[\left(\mathbf{v}+\boldsymbol{\Omega}\times\mathbf{r}\right)_p\times\left(\boldsymbol{\xi}+2\boldsymbol{\Omega}\right)_p\right]\tau_p\,. \tag{4.27}$$

We do not allow for a rotating sphere, i. e. $\boldsymbol{\Omega}=0$ and $h_{a,p}\to h_p$.

The definition of a discretized $\boldsymbol{\xi}$ implies a definition of the curl of the velocity field. As mentioned by Salmon (2005) and Sommer and Névir (2009) the model designer is free in selecting a spatial discretization for the differential operators as long as antisymmetry of the Nambu brackets is guaranteed. We choose a second order curl operator as a first guess, which has the same accuracy as the second order divergence operator implemented in the COSMO model in order to solve the temperature and pressure equation (Doms and Schaettler, 2002). Using the generalized Gauss theorem

$$\int_V d\tau\nabla\times\mathbf{v} = \int_{\partial V} d\mathbf{S}\times\mathbf{v}$$

and taking into account the simplified Cartesian model grid depicted in Figure 4.1, the components of the discretized curl operator are given by:

$$\begin{aligned}
\left(\nabla\times\mathbf{v}\cdot\mathbf{e}_x\right)_{\xi_1} &= \left(\partial_y w - \partial_z v\right)_{\xi_1} \to \frac{1}{A(\xi_1)}\left(\sum_{n\in\mathcal{E}(\xi_1)} w_n^\Gamma dz + \sum_{m\in\mathcal{E}(\xi_1)} v_m^\Gamma dy\right) := \omega_1\\
\left(\nabla\times\mathbf{v}\cdot\mathbf{e}_y\right)_{\xi_2} &= \left(\partial_z u - \partial_x w\right)_{\xi_2} \to \frac{1}{A(\xi_2)}\left(\sum_{l\in\mathcal{E}(\xi_2)} u_l^\Gamma dx + \sum_{n\in\mathcal{E}(\xi_2)} w_n^\Gamma dz\right) := \omega_2\\
\left(\nabla\times\mathbf{v}\cdot\mathbf{e}_z\right)_{\xi_3} &= \left(-\partial_y u + \partial_x v\right)_{\xi_3} \to \frac{1}{A(\xi_3)}\left(\sum_{l\in\mathcal{E}(\xi_3)} u_l^\Gamma dx + \sum_{m\in\mathcal{E}(\xi_3)} v_m^\Gamma dy\right) := \omega_3\,.
\end{aligned} \tag{4.28}$$

ω_1, ω_2 and ω_3 are defined on the dual grid (Figure 4.1), which corresponds to the surfaces $A(\xi_1)$, $A(\xi_2)$ and $A(\xi_3)$. The line integral Γ is directed counterclockwise along the edges $\mathcal{E}(\xi_1)$, $\mathcal{E}(\xi_2)$ and $\mathcal{E}(\xi_3)$ of the dual grid and incorporates the velocity components u_l^Γ, v_m^Γ and w_n^Γ. Using the definition (4.28) the helicity at the mass mid point is approximated by:

$$h_p = \frac{1}{2}\sum_{p=1}^{N}\left[\overline{u_l}^x\big|_p \cdot \overline{\omega_1}^{y,z}\big|_p + \overline{v_m}^y\big|_p \cdot \overline{\omega_2}^{x,z}\big|_p + \overline{w_n}^z\big|_p \cdot \overline{\omega_3}^{x,y}\big|_p\right]\tau_p\,. \tag{4.29}$$

Finally, we give the representation for the mass functional:

$$M_p = \sum_{p=1}^{N}\rho_p\tau_p \tag{4.30}$$

The functional derivatives

The functional derivatives has to be transformed to its discrete analogue. Keeping in mind the definition of a functional derivative (Lange, 2002), the discrete operator turns out to be a partial derivative approximated by the functional 'difference quotient'

$$\frac{\delta\mathcal{G}}{\delta\psi} \to \frac{1}{\tau_\nu}\frac{\partial G}{\partial\psi_\nu} = \frac{1}{\tau_\nu}\lim_{\Delta\psi_\nu\to 0}\frac{G[\psi_n + \Delta\psi\eth_{n,\nu}] - G[\psi_n]}{\Delta\psi_\nu}\,, \tag{4.31}$$

where G is a functional dependent on many discrete functions ψ_n. G is differentiated with respect to the specific function ψ_ν and $\Delta\psi_\nu$ is a small variation of the function ψ_ν. $\eth$ is the Kronecker symbol defined as:

$$\eth_{n,\nu} = \begin{cases} 0, n \neq \nu \\ 1, n = \nu \end{cases}\quad .$$

We explicitly compute the functional derivatives of H_p, h_p and M_p with respect to the velocity components and the density using definition (4.31). The derivative of H_p with respect to the velocity vector is decomposed into:

$$\frac{\partial H_p}{\partial\mathbf{v}} = \frac{\partial H_p}{\partial u}\mathbf{e}_x + \frac{\partial H_p}{\partial v}\mathbf{e}_y + \frac{\partial H_p}{\partial w}\mathbf{e}_z$$

The functional 'difference quotient' of H_p with respect to u at the specific grid location $l\star$ reads:

$$\begin{aligned}\frac{\delta\mathcal{H}}{\delta u} \to \frac{1}{\tau_{l\star}}\frac{\partial H_p}{\partial u_{l\star}} &= \frac{1}{\tau_{l\star}}\lim_{\Delta u_{l\star}\to 0}\left\{\frac{1}{\Delta u_{l\star}}\left[\sum_{p=1}^{N}\tau_p\frac{1}{2}\rho_p\,\overline{\left(u_l + \Delta u_l\eth_{l,l\star}\right)^2}^x\Big|_p - \sum_{p=1}^{N}\tau_p\frac{1}{2}\rho_p\,\overline{\left(u_l\right)^2}^x\Big|_p\right]\right\} \\ &= \frac{1}{\tau_{l\star}}\lim_{\Delta u_{l\star}\to 0}\left\{\frac{1}{\Delta u_{l\star}}\sum_{p=1}^{N}\tau_p\frac{1}{2}\rho_p\frac{1}{2}\sum_{l\in F(p)}2u_l\Delta u_l\eth_{l,l\star}\right\}\,,\end{aligned}$$

where the summation rule $\overline{a+b} = \overline{a} + \overline{b}$ is applied, and the terms $\mathcal{O}(\Delta {u_{l\star}}^2)$ are disregarded. The limit of H_p is reached here regardless of the magnitude of $\Delta u_{l\star}$. Only two values are picked up during the summation process due to the discrete Delta distribution:

$$\frac{1}{\tau_{l\star}} \frac{\partial H_p}{\partial u_{l\star}} = \frac{u_{l\star}}{2\tau_{l\star}} \left(\tau_{p1}\rho_{p1} + \tau_{p2}\rho_{p2}\right) := u_{l\star}\ \overline{\rho_p}^{x_\tau}\big|_{l\star}\ , \tag{4.32}$$

where $p1$ and $p2$ are the two mass mid points to the left and to the right of $l\star$. The discrete derivative gives exactly the mass flux through the boundaries of the cell face belonging to the location $l\star$. The expression (4.32) holds for all grid locations l under the condition that (a) the mass flux $u_l\ \overline{\rho_p}^{x_\tau}\big|_l$ is zero at the lateral boundaries or (b) the mass fluxes at the lateral boundary are balancing each other (requires τ, $\rho\ u_l$ to be periodic in the x-direction). Both boundary conditions are thus consistent with the condition 4.8 used for the continuous case.

It turns out that the functional derivatives helps to define the averaging operators. If the model designer has decided to use an arithmetic mean for the reconstruction of cell face values to mass mid points as done for the calculation of the kinetic energy (eq. (4.25)), then the reconstruction from mass mid points to the cell faces is automatically generated during the calculation of the functional derivatives: The right hand side of eq. (4.32) reveals a volume weighted mean. The notations $\overline{\cdots}^x\big|_p$ and $\overline{\cdots}^{x_\tau}\big|_l$ are used hereafter in order to indicate both averaging operators

$$\overline{\psi_l}^x\Big|_p = \frac{1}{2} \sum_{l \in F(p)} \psi_l\,, \quad \overline{\psi_p}^{x_\tau}\Big|_l = \frac{1}{2\tau_l} \sum_{p \in F(l)} \tau_p \psi_p\,. \tag{4.33}$$

The calculation of the discrete derivatives of H with respect to v, w and ρ are straightforward:

$$\frac{1}{\tau_m}\frac{\partial H}{\partial v_m} = v_m\ \overline{\rho_p}^{y_\tau}\big|_m\ , \quad \frac{1}{\tau_n}\frac{\partial H}{\partial w_n} = w_n\ \overline{\rho_p}^{z_\tau}\big|_n \tag{4.34}$$

and

$$\frac{1}{\tau_p}\frac{\partial H}{\partial \rho_p} = \frac{1}{2}\left(\overline{u_l^2}^x\Big|_p + \overline{v_m^2}^y\Big|_p + \overline{w_n^2}^z\Big|_p\right)\ . \tag{4.35}$$

In order to calculate the derivations of the helicity functional we use the same vectorial decomposition for $\frac{\partial h_p}{\partial \mathbf{v}}$ as we did for $\frac{\partial H_p}{\partial \mathbf{v}}$. Because the velocity fields u_l, v_m and w_n are linked with the averaging and curl operators in the definition of the helicity functional (eq. (4.29)), the calculation of the partial derivatives is extensive. Thus, only the results are given here:

$$\begin{aligned}
\frac{\delta h}{\delta u} \to \frac{1}{\tau_l}\frac{\partial h_p}{\partial u_l} &= \frac{1}{2}\,\overline{\overline{\omega_1}^{y,z}\big|_p}^{x_\tau}\Big|_l + \frac{1}{2\tau_l}\,\overline{\partial_y\left(\tau_p\ \overline{w_n}^z\big|_p\right)}^{x,y}\Big|_l - \frac{1}{2\tau_l}\,\overline{\partial_z\left(\tau_p\ \overline{v_m}^y\big|_p\right)}^{x,z}\Big|_l\ ,\\
\frac{\delta h}{\delta v} \to \frac{1}{\tau_m}\frac{\partial h_p}{\partial v_m} &= \frac{1}{2}\,\overline{\overline{\omega_2}^{x,z}\big|_p}^{y_\tau}\Big|_m + \frac{1}{2\tau_m}\,\overline{\partial_z\left(\tau_p\ \overline{u_l}^x\big|_p\right)}^{y,z}\Big|_m - \frac{1}{2\tau_m}\,\overline{\partial_x\left(\tau_p\ \overline{w_n}^z\big|_p\right)}^{x,y}\Big|_m\ ,\\
\frac{\delta h}{\delta w} \to \frac{1}{\tau_n}\frac{\partial h_p}{\partial w_n} &= \frac{1}{2}\,\overline{\overline{\omega_3}^{x,y}\big|_p}^{z_\tau}\Big|_n + \frac{1}{2\tau_n}\,\overline{\partial_x\left(\tau_p\ \overline{v_m}^y\big|_p\right)}^{x,z}\Big|_n - \frac{1}{2\tau_n}\,\overline{\partial_y\left(\tau_p\ \overline{u_l}^x\big|_p\right)}^{y,z}\Big|_n\ .
\end{aligned} \tag{4.36}$$

We have applied the sum manipulations $\sum a_p\ \overline{b_l}\big|_p^x = \sum \overline{a_p}\big|_l^x\ b_l$ and $\sum a_p \partial_x b_l = -\sum b_l \partial_x a_p$ to the helicity functional, i. e. we tacitly take into account (a) no flux or (b) periodic

flux conditions at the lateral boundaries (the discrete analogue to eq. (4.8)). The requirement of specific boundary conditions for calculating the discrete functional derivatives (4.36) would be a drawback if a regional model simulates under realistic weather conditions.

A lot of averaging occurs for the discrete partial derivatives given in eq. (4.36) mainly due to the Arakawa-C / Lorenz grid staggering, which might result in a smoothing of the prognostic fields. Nevertheless, our discretization procedure rests on global quantities and yields here a splitting of the partial derivatives of the helicity functional into three mixture terms. These terms ensure a consistent representation of the energy-helicity Nambu bracket (eq. (4.12)).

Finally, we give the discrete functional derivatives of M_p with respect to ρ and $\mathbf{v}$:

$$\frac{1}{\tau_p}\frac{\partial M_p}{\partial \rho_p} = 1\,, \qquad \frac{1}{\tau_q}\frac{\partial M_p}{\partial v_q} = 0 \quad \text{with} \quad q = l, m, n\,. \tag{4.37}$$

$\{\mathcal{F}, h_a, \mathcal{H}\}$ - the energy-helicity bracket

Making use of a vectorial decomposition concerning the expressions $\frac{\delta \mathcal{F}}{\delta \mathbf{v}}$, $\frac{\delta h_a}{\delta \mathbf{v}}$ and $\frac{\delta \mathcal{H}}{\delta \mathbf{v}}$, the scalar triple product of the energy-helicity bracket (eq. (4.12)) can be rewritten in component notation. The discretized analogue to this component notation is obtained by reconstructing every vector of the scalar triple product to the same location on the grid. We decide to calculate the energy-helicity bracket at the mass mid point p using the averaging operator defined by eq. (4.33):

$$\begin{aligned}
\{F, h_p, H_p\}^N = &- \sum_{p=1}^{N} \frac{\tau_p}{\rho_p} \overline{\frac{1}{\tau_l}\frac{\partial F}{\partial u_l}}^{x}\Bigg|_p \left[\overline{\frac{1}{\tau_m}\frac{\partial h_p}{\partial v_m}}^{y}\Bigg|_p \overline{\frac{1}{\tau_n}\frac{\partial H_p}{\partial w_n}}^{z}\Bigg|_p - \overline{\frac{1}{\tau_n}\frac{\partial h_p}{\partial w_n}}^{z}\Bigg|_p \overline{\frac{1}{\tau_m}\frac{\partial H_p}{\partial v_m}}^{y}\Bigg|_p \right] \\
&- \sum_{p=1}^{N} \frac{\tau_p}{\rho_p} \overline{\frac{1}{\tau_m}\frac{\partial F}{\partial v_m}}^{y}\Bigg|_p \left[\overline{\frac{1}{\tau_n}\frac{\partial h_p}{\partial w_n}}^{z}\Bigg|_p \overline{\frac{1}{\tau_l}\frac{\partial H_p}{\partial u_l}}^{x}\Bigg|_p - \overline{\frac{1}{\tau_l}\frac{\partial h_p}{\partial u_l}}^{x}\Bigg|_p \overline{\frac{1}{\tau_n}\frac{\partial H_p}{\partial w_n}}^{z}\Bigg|_p \right] \\
&- \sum_{p=1}^{N} \frac{\tau_p}{\rho_p} \overline{\frac{1}{\tau_n}\frac{\partial F}{\partial w_n}}^{z}\Bigg|_p \left[\overline{\frac{1}{\tau_l}\frac{\partial h_p}{\partial u_l}}^{x}\Bigg|_p \overline{\frac{1}{\tau_m}\frac{\partial H_p}{\partial v_m}}^{y}\Bigg|_p - \overline{\frac{1}{\tau_m}\frac{\partial h_p}{\partial v_m}}^{y}\Bigg|_p \overline{\frac{1}{\tau_l}\frac{\partial H_p}{\partial u_l}}^{x}\Bigg|_p \right] .
\end{aligned} \tag{4.38}$$

The partial derivatives are given by the eq. (4.32), (4.34) and (4.36).

The antisymmetry of the bracket (4.38) is obvious, regardless of the choice for F. The mathematical structure of the scalar triple product guarantees that any onefold permutation in F, h_p or H_p yields the bracket $-\{F, h_p, H_p\}$ and any twofold permutation yields $\{F, h_p, H_p\}$.

$\{\mathcal{F}, \mathcal{M}, \mathcal{H}\}$ - the energy-mass bracket

The energy-mass bracket is discretized based on eq. (4.13):

$$\begin{aligned}\{F, M_p, H_p\}^N = &- \sum_{p=1}^{N} \tau_p \frac{1}{\tau_p}\frac{\partial F}{\partial \rho_p}\left[\nabla \cdot \left(\frac{1}{\tau_p}\frac{\partial M_p}{\partial \rho_p}\frac{1}{\tau_{\mathbf{v}}}\frac{\partial H_p}{\partial \mathbf{v}}\right)\right]_p \\ &- \sum_{p^\star=1}^{N} \tau_{p^\star}\left(\frac{1}{\tau_{p^\star}}\frac{\partial F}{\partial \mathbf{v}}\frac{1}{\tau_p}\frac{\partial M_p}{\partial \rho_p}\right)_{p^\star} \cdot \nabla \frac{1}{\tau_p}\frac{\partial H_p}{\partial \rho_p} + cyc(F, M_p, H_p)\,,\end{aligned} \tag{4.39}$$

where $p^\star$ are the model grid locations at the cell faces (locations of the velocity components) corresponding to the needs of the Nabla operator. The discretized bracket is defined at different grid locations p and $p^\star$, which can be avoided by rewriting the energy-mass bracket (4.13) in a pure divergent form using the transformation given in eq. (4.19). Then, we yield a second option for the discretization of the energy-mass bracket:

$$\begin{aligned}\{F, M_p, H_p\}^N = &- \sum_{p=1}^{N} \tau_p \frac{1}{\tau_p}\frac{\partial F}{\partial \rho_p}\left[\nabla \cdot \left(\frac{1}{\tau_p}\frac{\partial M_p}{\partial \rho_p}\frac{1}{\tau_{p^\star}}\frac{\partial H_p}{\partial \mathbf{v}}\right)\right]_p \\ &+ \sum_{p=1}^{N} \tau_p \frac{1}{\tau_p}\frac{\partial H_p}{\partial \rho_p}\left[\nabla \cdot \left(\frac{1}{\tau_p}\frac{\partial M_p}{\partial \rho_p}\frac{1}{\tau_{p^\star}}\frac{\partial F}{\partial \mathbf{v}}\right)\right]_p + cyc(F, M_p, H_p)\,.\end{aligned} \tag{4.40}$$

It is convenient to define the energy-mass bracket at the mass mid point p (eq. (4.40)) in order to match the location of the discretized energy-helicity bracket (4.38). However, both energy-mass bracket forms result in the same discretization of the nonlinear part of the momentum equation.

As already mentioned for the analytical case, the antisymmetry of the $\{F, M_p, H_p\}^N$ bracket is not obvious. It is only revealed, if the permutations $cyc(F, M, H)$ are explicitly written down and the duality between the gradient and the divergence operator exist (eq. (4.19)). In order to proof this duality for the numerical application, we examine exemplarily the second term on the right hand side of eq. (4.40). The Nabla operator and the discrete functional derivative of H_p with respect to $\mathbf{v}$ are decomposed into:

$$\begin{aligned}\nabla =& \nabla_x \mathbf{e}_x + \nabla_y \mathbf{e}_y + \nabla_z \mathbf{e}_z \\ \frac{1}{\tau_{\mathbf{v}}}\frac{\partial H_p}{\partial \mathbf{v}} =& \frac{1}{\tau_l}\frac{\partial H_p}{\partial u_l}\mathbf{e}_x + \frac{1}{\tau_m}\frac{\partial H_p}{\partial v_m}\mathbf{e}_y + \frac{1}{\tau_n}\frac{\partial H_p}{\partial w_n}\mathbf{e}_z\,.\end{aligned}$$

Then, we rewrite the second term on the right hand side of eq. (4.40) using the sum

rule $\sum_p a_p \partial_x b_l = -\sum_l b_l \partial_x a_p$ and setting $\frac{1}{\tau_p}\frac{\partial M_p}{\partial \rho_p} = 1$ (eq. (4.37)):

$$
\begin{aligned}
&+ \sum_{p=1}^{N} \tau_p \frac{1}{\tau_p}\frac{\partial H_p}{\partial \rho_p}\left[\nabla \cdot \frac{1}{\tau_{p^\star}}\frac{\partial F}{\partial \mathbf{v}}\right]_p \\
&= \sum_{p=1}^{N} \tau_p \frac{1}{\tau_p}\frac{\partial H_p}{\partial \rho_p}\left\{\left[\nabla_x\left(\frac{1}{\tau_l}\frac{\partial F}{\partial u_l}\right)\right]_p + \left[\nabla_y\left(\frac{1}{\tau_m}\frac{\partial F}{\partial v_m}\right)\right]_p + \left[\nabla_z\left(\frac{1}{\tau_n}\frac{\partial F}{\partial w_n}\right)\right]_p\right\} \\
&= -\sum_{l=1}^{N}\frac{1}{\tau_l}\frac{\partial F}{\partial u_l}\cdot\nabla_x\frac{\partial H_p}{\partial \rho_p} - \sum_{m=1}^{N}\frac{1}{\tau_m}\frac{\partial F}{\partial v_m}\cdot\nabla_y\frac{\partial H_p}{\partial \rho_p} - \sum_{n=1}^{N}\frac{1}{\tau_n}\frac{\partial F}{\partial w_n}\cdot\nabla_z\frac{\partial H_p}{\partial \rho_p} \\
&:= -\sum_{p^\star=1}^{N}\left(\frac{1}{\tau_{p^\star}}\frac{\partial F}{\partial \mathbf{v}}\right)\cdot\nabla\frac{\partial H_p}{\partial \rho_p}\,.
\end{aligned}
\tag{4.41}
$$

Here, we imply specific boundary conditions due to the manipulation of the sum. As discussed earlier for the discrete functional derivatives of H_p (eq. (4.32)), the manipulation of the sum requires boundary conditions equivalent to the analytical case (eq. (4.8)).

The divergence operator indeed turns into a gradient operator during the transformations given in eq. (4.41). The duality between the divergence and the gradient operator is only satisfied, if the model designer discretizes both operators in the same manner, i. e. the same accuracy. The divergence operator implemented in the COSMO model is second order:

$$
\begin{aligned}
\nabla\cdot\mathbf{A}\big|_p =& \frac{1}{\tau_p}\left\{\left(A^x_{l2} - A^x_{l1}\right)\Delta y\Delta z + \left(A^y_{m2} - A^y_{m1}\right)\Delta x\Delta z + \left(A^z_{n2} - A^z_{n1}\right)\Delta x\Delta y\right\} \\
:=& \nabla_x A^x + \nabla_y A^y + \nabla^z A^z\,,
\end{aligned}
\tag{4.42}
$$

where $\mathbf{A}$ is an arbitrary vector field $\mathbf{A} = A^x\mathbf{e}_x + A^y\mathbf{e}_y + A^z\mathbf{e}_z$. The indices $l1$ and $l2$ corresponds to the cell face positions to the West and to the East of the mass mid point p. $m1$, $m2$, $n1$ and $n2$ refer to the locations to the North, to the South, to the top and to the bottom of the mass mid point p (Figure 4.1). We straightforwardly derive a numerical expression for the gradient operator based on the divergence operator (4.42) due to transformations given in eq. (4.41):

$$
(\partial_x, \partial_y, \partial_z)^T = \left(\left.\frac{\psi_{p1} - \psi_p}{\Delta x}\right|_l, \left.\frac{\psi_{p2} - \psi_p}{\Delta y}\right|_l, \left.\frac{\psi_{p3} - \psi_p}{\Delta z}\right|_l\right)^T\,,
$$

where $p1$, $p2$ and $p3$ are the adjacent mass mid points relative to the location p.

Having defined the gradient operator as a dual operator to the divergence, the antisymmetry of the energy-mass bracket is guaranteed: If we permute F and H_p in the energy-mass bracket $\{F, M_p, H_p\}^N$ (eq. (4.39)) and apply the transformations given in eq. (4.41) to the permuted bracket $\{H_p, M_p, F\}^N$, we yield an expression equal to $-\{F, M_p, H_p\}^N$ except for the locations p and $p^\star$. The term antisymmetry is meant here in an approximated sense, i. e. the antisymmetry is approximated by the differential operators.

Obviously the trilinear energy-mass bracket degenerates to a bilinear Poisson bracket, if the functional derivative of the mass with respect to the density is skipped because it is one (eq. (4.37)). Then, the discretized energy-mass Nambu bracket $\mathcal{F},\mathcal{M},\mathcal{H}^N$ is equivalent to the discretized $\{\mathcal{F},\mathcal{H}\}^P_{\rho,\mathbf{v}}$ part of the Poisson bracket (eq. (4.5)). From this point of view, it seems that we do not gain any benefits using the discretized energy-mass Nambu bracket (eq. (4.40)) in comparison to the discretized analogue of the Poisson bracket part $\{\mathcal{F},\mathcal{H}\}_{\rho,\mathbf{v}}$.

The nonlinear parts of the momentum equations

Having in mind the discretized brackets (4.38) and (4.39), we derive the numerical bracket form of the nonlinear part of the Euler equations by mapping the functional F to the local points of the velocity components:

$$F^u = \sum_{l=1}^{N} \frac{u_l}{\tau_l}\eth_{l,l\star}\tau_l = u_{l\star}\,, \quad F^v = \sum_{m=1}^{N} \frac{v_m}{\tau_m}\eth_{m,m\star}\tau_m = v_{m\star}\,, \quad F^w = \sum_{n=1}^{N} \frac{w_n}{\tau_n}\eth_{n,n\star}\tau_n = w_{n\star}\,.$$

The discrete functional derivatives of F^u, F^v and F^w with respect to the density ρ_p is zero. The derivatives with respect to the velocity components u_l, v_m and w_n gives the Delta Dirac function:

$$\begin{aligned} \frac{\delta\mathcal{F}}{\delta u} &\to \frac{1}{\tau_l}\frac{\partial F^u}{u_l} = \frac{1}{\tau_l}\lim_{\Delta u_l\to 0}\left\{\frac{u_{l\star}+\Delta u_{l\star}\eth_{l\star,l}-u_{l\star}}{\Delta u_l}\right\} = \frac{\eth_{l\star,l}}{\tau_l}\,, \\ \frac{\delta\mathcal{F}}{\delta v} &\to \frac{1}{\tau_m}\frac{\partial F^v}{v_m} = \frac{\eth_{m\star,m}}{\tau_m}\,, \quad \frac{\delta\mathcal{F}}{\delta w} \to \frac{1}{\tau_n}\frac{\partial F^w}{w_n} = \frac{\eth_{n\star,n}}{\tau_n}\,. \end{aligned} \tag{4.43}$$

Upon inserting the derivatives (4.43) into eq. (4.38) and (4.39) and using the evolution equation (4.20) one obtains prognostic equations for the velocity components at local grid points. I. e. starting from the discretization of the Nambu brackets and the related functionals as the global quantity mass, one ends up automatically with an evolution equation for local grid points. The prognostic equation for the velocity component u reads:

$$\begin{aligned} \frac{\partial u_{l\star}}{\partial t} = &-\frac{1}{\rho_p}\left[\overline{\overline{\frac{1}{\tau_m}\frac{\partial h_p}{\partial v_m}}^{y}\Big|_p\ \overline{\frac{1}{\tau_n}\frac{\partial H_p}{\partial w_n}}^{z}\Big|_p} - \overline{\overline{\frac{1}{\tau_n}\frac{\partial h_p}{\partial w_n}}^{z}\Big|_p\ \overline{\frac{1}{\tau_m}\frac{\partial H_p}{\partial v_m}}^{y}\Big|_p}\right]^{x_\tau}\Bigg|_{l\star} \\ &-\frac{1}{\tau_{l\star}}\partial_x\left(\frac{\tau_p}{2}\,\overline{u_l^2}^{x}\Big|_p + \frac{\tau_p}{2}\,\overline{v_m^2}^{y}\Big|_p + \frac{\tau_p}{2}\,\overline{w_n^2}^{z}\Big|_p\right) + \mathcal{L}(u)\,, \end{aligned} \tag{4.44}$$

The first terms on the right hand side constitute the nonlinear advection term, whereas $\mathcal{L}(u)$ summarizes the remaining linear terms of the momentum equation (see the Appendix A for $\mathcal{L}(u)$ in terms of the COSMO model).

The derivation of the nonlinear part of the v and w equation is straightforward:

$$\begin{aligned} \frac{\partial v_{m\star}}{\partial t} = &-\frac{1}{\rho_p}\left[\overline{\overline{\frac{1}{\tau_n}\frac{\partial h_p}{\partial w_n}}^{z}\Big|_p\ \overline{\frac{1}{\tau_l}\frac{\partial H_p}{\partial u_l}}^{x}\Big|_p} - \overline{\overline{\frac{1}{\tau_l}\frac{\partial h_p}{\partial u_l}}^{x}\Big|_p\ \overline{\frac{1}{\tau_n}\frac{\partial H_p}{\partial w_n}}^{z}\Big|_p}\right]^{y_\tau}\Bigg|_{m\star} \\ &-\frac{1}{\tau_{m\star}}\partial_y\left(\frac{\tau_p}{2}\,\overline{u_l^2}^{x}\Big|_p + \frac{\tau_p}{2}\,\overline{v_m^2}^{y}\Big|_p + \frac{\tau_p}{2}\,\overline{w_n^2}^{z}\Big|_p\right) + \mathcal{L}(v)\,, \end{aligned} \tag{4.45}$$

$$\frac{\partial w_{n\star}}{\partial t} = -\frac{1}{\rho_p}\left[\overline{\left.\overline{\frac{1}{\tau_l}\frac{\partial h_p}{\partial u_l}}^{x}\right|_p \overline{\left.\frac{1}{\tau_m}\frac{\partial H_p}{\partial v_m}\right|_p}^{y} - \left.\overline{\frac{1}{\tau_m}\frac{\partial h_p}{\partial v_m}}^{y}\right|_p \overline{\left.\frac{1}{\tau_l}\frac{\partial H_p}{\partial u_l}\right|_p}^{x}}^{z_\tau}\right]_{n\star} - \frac{1}{\tau_{n\star}}\partial_z\left(\frac{\tau_p}{2}\left.\overline{u_l^2}^{x}\right|_p + \frac{\tau_p}{2}\left.\overline{v_m^2}^{y}\right|_p + \frac{\tau_p}{2}\left.\overline{w_n^2}^{z}\right|_p\right) + \mathcal{L}(w)\,, \tag{4.46}$$

The discretization scheme given by the equations (4.44), (4.45) and (4.46) is referred as the **EVT scheme**.

Implementation of the EVT scheme

The bracket discretization scheme given by the equations (4.44), (4.45) and (4.46) implies extensive averaging and differential calculations on widespread stencils. For instance, the stencil related to the term

$$\left.\overline{\overline{\frac{1}{\tau_n}\frac{\partial H_p}{\partial w_n}}^{z}}\right|_p\Bigg|_{l\star}^{x_\tau} = \left.\overline{\overline{w_n\,\overline{\rho_p}|_n^{z_\tau}}^{z}}\right|_p\Bigg|_{l\star}^{x_\tau} \tag{4.47}$$

on the right hand side of eq. (4.44) involves 4 vertical velocity values and 6 density values at different locations on the grid (Figure 4.2). The stencil will be even much broader and much more complex with respect to those terms in eq. (4.44), which involve the partial derivatives with respect to helicity h_p. Thus, implementing the broad and complex stencils in the source code of the EVT scheme may be very vulnerable to programming errors.

In order to prevent errors originating from coding the complex stencils explicitly for each term of the eq. (4.44) - (4.46) (indexing errors), the construction of the stencils with respect to the averaging and differential operators are managed by recursive algorithms. They perform much slower on the computer than an algorithm with explicit coded stencils, but deliver a readable, structured and much less error-prone code.

Considering the big stencils implied by the EVT scheme, one needs to specify suitable boundary conditions. Free slip conditions for the kinetic energy, the mass flux and the curl of the velocity field are defined at the top and the bottom of the model domain, which are non-penetrative rigid lids.

Towards a bracked-based EVT scheme in operational NWP models

In this section problems with the EVT scheme are addressed, which arise on the complex model grids used for operational NWP.

To achieve an algorithm practicable for operational NWP, one needs to consider the terrain-following Earth surface. This is often done using terrain-following coordinates (Doms and Schaettler, 2002, e. g.) If one transfers the discretization of the Euler momentum equations in the framework of the energy-vorticity theory to terrain-following coordinates, the discretization will be much more complicate to derive than the EVT scheme on a Cartesian grid because of three reasons:

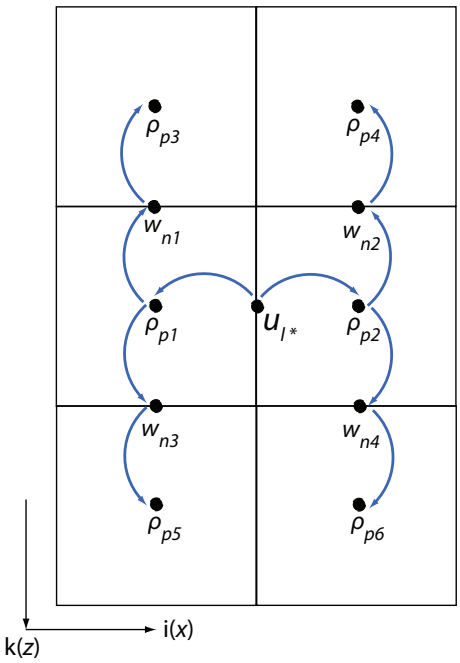

Figure 4.2: The growth of the stencil related with the term (4.47) is depicted starting from the position $l\star$.

(1) The terrain-following coordinate system is non-orthogonal. The contravariant and covariant base vectors have to be considered for the decomposition of a vector into components.

(2) Additional computational effort originates from metric terms, e. g. the Euler equations (3.134) in Doms and Schaettler (2002).

(3) The mathematical properties of the scalar triple product, which guarantees the antisymmetry of the energy-helicity bracket $\{\mathcal{F}, h_a, \mathcal{H}\}^N$ (eq. (4.12)), may not be ensured on computational non-cartesian grids. That is the rules for the scalar and cross product are only valid if both vectors are defined at the same location, which is hard to achieve for a discretized version of $\{\mathcal{F}, h_a, \mathcal{H}\}^N$ based on terrain-following coordinates. The widespread stencils of a EVT scheme in terrain-following coordinates prevent to have the discretized vector components at the same locations.

In summary, it is highly demanding to transfer the analytic properties of the Nambu brackets to its discretized analogues using terrain-following coordinates. However, we do not consider the terrain-following coordinates in the experiments discussed in Section 4.4 and 4.5.

4.3.3 The Poisson scheme

Keeping in mind the Poisson bracket form of the Euler equations given by eq. (4.7) and (4.9), one could also derive a numerical scheme for the nonlinear advection term, which is closely connected with the EVT scheme introduced in the Section 4.3.2.

Gassmann and Herzog (2008, Section 5) proposed a discretization scheme based on the $\{\mathcal{F},\mathcal{H}\}^P_{\rho,\mathbf{v}}$ and $\{\mathcal{F},\mathcal{H}\}^P_{\mathbf{v},\mathbf{v}}$ part of the Poisson bracket given in eq. (4.5). The $\{\mathcal{F},\mathcal{H}\}^P_{\rho,\mathbf{v}}$ part is defined at the mass mid points, whereas the $\{\mathcal{F},\mathcal{H}\}^P_{\mathbf{v},\mathbf{v}}$ part is located at the corners $c=(i+1/2,j+1/2,k+1/2)$ of a grid box (Gassmann 2009, personal communication). Following this ansatz, the explicit discretization of the momentum equation for the components u, v and w can be obtained by:

(a) using the discretized Hamiltonian H_p and it discrete functional derivatives already introduced in Section 4.3.2,

(b) discretizing the Poisson bracket parts $\{\mathcal{F},\mathcal{H}\}^P_{\rho,\mathbf{v}}$ and $\{\mathcal{F},\mathcal{H}\}^P_{\mathbf{v},\mathbf{v}}$ and the associated differential operators (refer to (4.28) and (4.42)),

(c) setting the functional $F^u=u_{l\star}$, $F^v=v_{m\star}$ and $F^w=w_{n\star}$ and determine the derivatives with respect to u_l, v_m and w_n (refer to eq. (4.43)).

Finally, the discretized momentum equations read:

$$\begin{aligned}\frac{\partial u_{l\star}}{\partial t} =& -\frac{1}{\tau_{l\star}}\,\overline{\frac{\tau_c}{\overline{\rho_p}^{x,y,z}\big|_c}\left[\overline{\omega_2}^{y}\big|_c\,\overline{\overline{\rho_p}^{z}\big|_n\,w_n}^{x,y}\Big|_c-\overline{\omega_3}^{z}\big|_c\,\overline{\overline{\rho_p}^{y}\big|_m\,v_m}^{x,z}\Big|_c\right]}^{y,z}\Bigg|_{l\star}\\ &-\frac{1}{\tau_{l\star}}\partial_x\left(\frac{\tau_p}{2}\,\overline{u_l^2}^{x}\Big|_p+\frac{\tau_p}{2}\,\overline{v_m^2}^{y}\Big|_p+\frac{\tau_p}{2}\,\overline{w_n^2}^{z}\Big|_p\right)+\mathcal{L}(u)\,,\end{aligned}\tag{4.48}$$

$$\begin{aligned}\frac{\partial v_{m\star}}{\partial t} =& -\frac{1}{\tau_{m\star}}\,\overline{\frac{\tau_c}{\overline{\rho_p}^{x,y,z}\big|_c}\left[\overline{\omega_3}^{z}\big|_c\,\overline{\overline{\rho_p}^{x}\big|_l\,u_l}^{y,z}\Big|_c-\overline{\omega_1}^{x}\big|_c\,\overline{\overline{\rho_p}^{z}\big|_n\,w_n}^{x,y}\Big|_c\right]}^{x,z}\Bigg|_{m\star}\\ &-\frac{1}{\tau_{m\star}}\partial_y\left(\frac{\tau_p}{2}\,\overline{u_l^2}^{x}\Big|_p+\frac{\tau_p}{2}\,\overline{v_m^2}^{y}\Big|_p+\frac{\tau_p}{2}\,\overline{w_n^2}^{z}\Big|_p\right)+\mathcal{L}(v)\,,\end{aligned}\tag{4.49}$$

$$\begin{aligned}\frac{\partial w_{n\star}}{\partial t} =& -\frac{1}{\tau_{n\star}}\,\overline{\frac{\tau_c}{\overline{\rho_p}^{x,y,z}\big|_c}\left[\overline{\omega_1}^{x}\big|_c\,\overline{\overline{\rho_p}^{y}\big|_m\,v_m}^{x,z}\Big|_c-\overline{\omega_2}^{y}\big|_c\,\overline{\overline{\rho_p}^{x}\big|_l\,u_l}^{y,z}\Big|_c\right]}^{x,y}\Bigg|_{n\star}\\ &-\frac{1}{\tau_{n\star}}\partial_z\left(\frac{\tau_p}{2}\,\overline{u_l^2}^{x}\Big|_p+\frac{\tau_p}{2}\,\overline{v_m^2}^{y}\Big|_p+\frac{\tau_p}{2}\,\overline{w_n^2}^{z}\Big|_p\right)+\mathcal{L}(w)\,.\end{aligned}\tag{4.50}$$

The first terms on the right hand side constitute the nonlinear advection term, whereas $\mathcal{L}(u)$ summarizes the remaining linear terms of the momentum equation (see the Appendix A for $\mathcal{L}(u)$ in terms of the COSMO model). ω_1, ω_2 and ω_3 are the vorticity components given in eq. (4.28).

The discretization scheme given by the equations (4.48), (4.49) and (4.50) is referred as the **Poisson scheme**.

4.3.4 Implications for the application to the NWP models

An overview about the specific features of the bracket formulations with respect to the nonlinear advection term is given in Table 4.2. A comparison is done with the standard discretization scheme implemented in the COSMO model, i. e. the advection form in eq. (A.1)-(A.3).

Table 4.2: Features of the various representations concerning the nonlinear advection term of the momentum equation. The properties of the Poisson scheme are discussed in Gassmann and Herzog (2008). The term antisymmetric* refers to an antisymmetry in an approximated sense.

method	Advection form (COSMO-DE)	Poisson scheme	EVT scheme
analytical basic concept	momentum equations in advection form: $\mathbf{v} \cdot \nabla \mathbf{v}$	Hamiltonian description of the momentum equations with Poisson brackets (Lamb transformation)	energy-vorticity theory of the momentum equations with Nambu brackets (Lamb transformation)
explicit discretization of / discretization starts from	advection operator	total energy, mass + brackets	total energy, mass, helicity + brackets
mathematical properties of the discretized brackets	-	two antisymmetric bilinear brackets	a twofold antisymmetric trilinear bracket + a antisymmetric* bilinear bracket
physical quantities obtained during the discretization	mass flux, vorticity components	mass flux, vorticity flux	mass flux, vorticity flux
Conditions required to derive the numerical scheme	no	periodic or penetrative boundary conditions	as for the Poisson scheme
local accuracy of the scheme	second to sixth order gradient operator (user-defined)	second order rotation and divergence operator	as for the Poisson scheme
Stencil	advection calculated along lines in 3 directions	many involved grid points form a cubic shape	as for the Poisson scheme, but a little bit more widespread
Diffusion inherent in the discretization	inherent diffusion for the odd order advection schemes, no diffusion for even order	potential smoothing due to extensive reconstructions	as for the Poisson scheme
numerical algorithm	easy and readable code, fast algorithm, easy implementation of vertical implicit schemes	complicate and error-prone code, slow algorithm, elaborate implementation of vertical implicit schemes	complicate and error-prone code, very slow algorithm, elaborate implementation of vertical implicit schemes

An discretization scheme based on the conservation form of the Euler equations

$$\frac{\partial(\rho u_j)}{\partial t} = \sum_i \frac{\partial(\rho u_i u_j)}{\partial x_i} + \mathcal{L}(u_j)\,,$$

which is implemented in the WRF (Skamarock et al., 2005) and the METRAS (Schlünzen, 1990; Schlünzen et al., 1996) model, is not discussed in Table 4.2. This approach might be categorized between the 'advection form' and the 'Bracket schemes', because it is based on the momentum conservation, but it does not use global quantities to carry over the conservation properties to a numerical scheme.

The 'EVT' and the 'Poisson' scheme are implemented in the COSMO-MP version of the COSMO model, which was introduced in Section 2.5. Having as a reference the standard discretization of the nonlinear advection term in the COSMO model, we will analyze how the numerical 'Poisson' and the 'EVT' scheme are influencing the flow. The explicit representation of vortex quantities and the related splitting into rotational and irrotational flows might help to better resolve rotational flows, e. g. in convective systems, and the nonlinear transfer of energy and vorticity-like quantities throughout the mesoscale. Nevertheless, we have to proof that the brackets related to the rotational flow parts are not producing kinetic energy. In particular, we need to keep in mind that the derivation of the bracket schemes requires specific boundary conditions (eq. (4.8)).

4.4 Gravity wave initiation and propagation - weak nonlinearity

In order to validate the implementation of the 'EVT' and the 'Poisson' scheme, we first simulate the propagation of inertia-gravity waves as described by Skamarock and Klemp (1994). The test case is designed for comparing quantitatively the model results with the analytic solutions of the linearized Euler equations with Boussinesq and incompressible approximations. Thus, the flow is evolving under weak nonlinear conditions.

4.4.1 Experimental setup

The propagation of waves is simulated in a periodic two-dimensional channel with a length of $L = 300\,\mathrm{km}$. The vertical extent of the channel is $H = 10\,\mathrm{km}$ with impermeable and free-slip upper and lower boundaries at $z = 0, H$. A stable-stratified atmosphere of constant Brunt-Väisälä frequency $N = 0.01\,\mathrm{s}^{-1}$ is predefined in the channel with $\theta(z = 0) = 300\,\mathrm{K}$ and $p(z = 0) = 1000\,\mathrm{hPa}$. The initial atmosphere is hydrostatically balanced and horizontally homogeneous. A constant wind of $U = 20\,\mathrm{m\,s}^{-1}$ is initiated inside the whole domain and transports the gravity waves.

The waves are excited by a small perturbation θ_p of the initial potential temperature:

$$\Theta_p(x, z, 0) = \Delta\theta_p\, a^2\, \frac{\sin(\pi z/H)}{a^2 + (x - x_c)^2}\,, \tag{4.51}$$

where the amplitude $\Delta\theta_p = 0.1\,\mathrm{K}$, the half-width $a = 5\,\mathrm{km}$ and $x_c = \frac{L}{3}$. Since the potential temperature is not a prognostic variable in the COSMO model, we have adjusted the temperature according to eq. (4.51). The inertial effect of the excited waves on a rotating frame is not considered, i. e. the Coriolis parameter f is set to zero.

The model simulations are carried out on a grid with a horizontal spacing of 500 m. The aspect ratio $\Delta z/\Delta x$ equals one. Thus, the domain consists of 600×20 grid points. Four different configurations of the COSMO model are considered (see the Appendix for a short model description), which are listed in Table 4.3. The simulation using the standard configuration of the COSMO model ('Adv5th') serves as the reference for the model runs using the 'Poisson' and the 'EVT' scheme. Beside the 'Adv5th' configuration, which deals with a fifth-order explicit horizontal and third-order implicit vertical discretization for the nonlinear advection operator, we also perform simulations using a second order full explicit discretization of the advection operator (configuration 'Adv2nd'). The 'Adv2nd' configuration is supposed to be the best to compare the runs using an advection form of the nonlinear advection term with the runs using a Nambu or a Poisson bracket description of the nonlinear advection term. Due to problems with the implicit vertical advection scheme we are forced to implement a Rayleigh damping layer for the uppermost level in the reference configuration 'Adv5th'.

4.4.2 Structure and propagation of the gravity waves

The results of the model runs are shown in Figure 4.3 at $t = 3000\,\mathrm{s}$ for the perturbation θ, which is meant as the deviation from the initial potential temperature. The solution of the 'Adv2nd' run is nearly identical to the 'Poisson' solution and is not shown here. The model simulations are evaluated with the analytic solution of the linearized incompressible Boussinesq model by Skamarock and Klemp (1994) (Figure 4.3a). All model

Table 4.3: Characteristics of the model configurations used for the inertia-gravity wave test. The accuracy of the advection operator with respect to the 'Adv5th' scheme is meant as formal accuracy, because it refers only to the gradient operator and not to the complete advection operator.

configuration	Adv5th	Adv2nd	Poisson	EVT
timestep	Δt(big) = 6 s / Δt(small) = 1.5 s			
numerical filters	horizontal divergence damping, $\nu_d \approx 1.6 \cdot 10^4\ \mathrm{m^2\ s^{-1}}$; no Laplacian diffusion, $\nu_d = 0$			
accuracy of horizontal / vertical advection schemes	fifth order explicit / third order implicit	second order explicit / second order explicit	rotation and divergence second order explicit	
damping mechanism	one Rayleigh damping layer	no	no	no

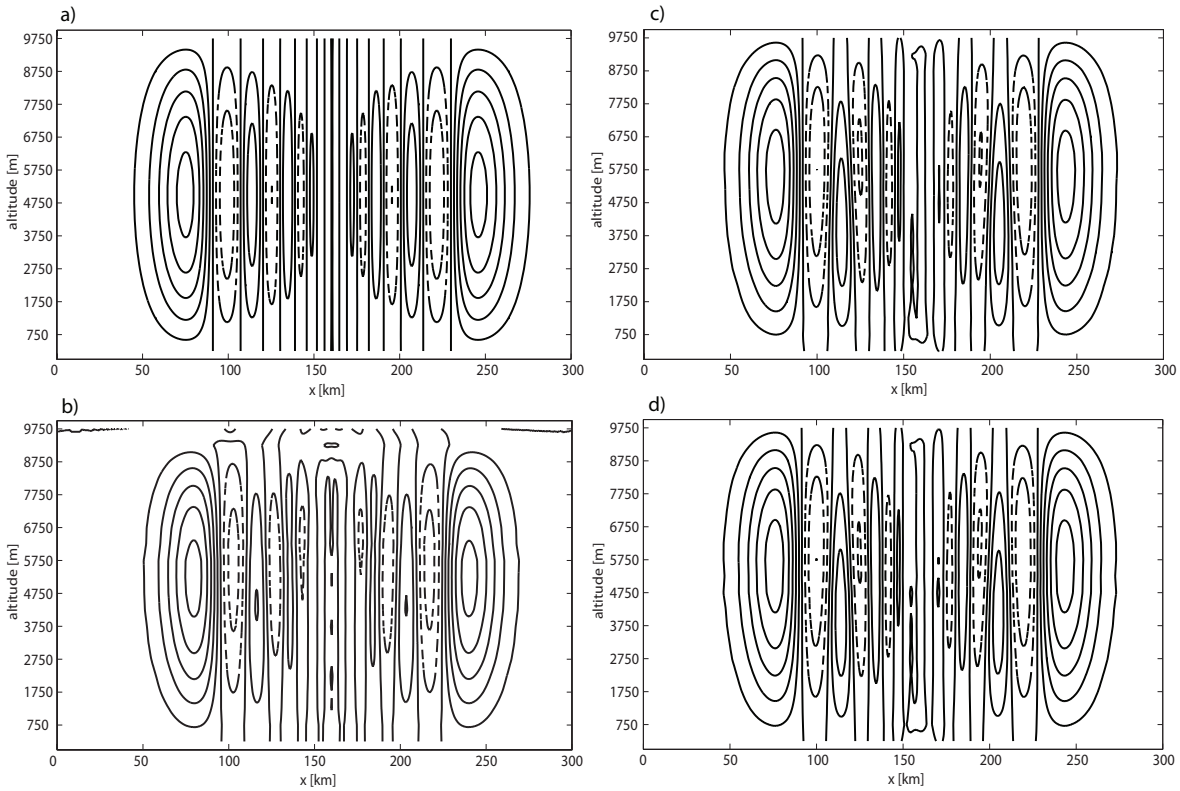

Figure 4.3: Cross section of the perturbation θ for the inertia gravity wave test at $t = 3000$ s. A domain of 600×20 grid points is shown. The contour interval is 0.05 K. a) The analytic solution and b) the model solution using the 'Adv5th' configuration, c) the 'Poisson' configuration and d) the 'EVT' configuration. The 'Adv2nd' model solution is identical to the 'Poisson' solution and is not shown here.

outputs match almost the analytic solution except for the reference solution 'Adv5th'. Since the 'Adv5th' configuration involves a Rayleigh damping layer in the uppermost level, the reflection of the gravity waves at the model top and its propagation and amplitude is damped (Figure 4.3b). Furthermore, the analytic solution is symmetric at the axis $z = H/2$, but the model solutions are not. A possible explanation was given by Skamarock and Klemp (1994): Some of the differences in the symmetry properties arise from the fact that the non-hydrostatic compressible models, for instance the COSMO model, do not account for a Boussinesq approximated atmosphere and apply a full x- and height-dependent density field to all Euler equations.

A more detailed insight into the gravity wave generation and propagation is provided by the one-dimensional profile of perturbation θ in Figure 4.4 at $t = 3000$ s. The profile is taken at an altitude of 4750 meters, which is located near the epicenter of the strongest buoyancy oscillations. There is a good agreement between the analytic (dashed line) and the model solutions 'Poisson' (blue line) and 'EVT' (red line). Nevertheless, both model solutions are slightly distorted in comparison to the analytic solution near the epicenter, which is situated at $x \approx 160$ km. Accordingly, the symmetry properties of the 'Poisson' and 'EVT' solutions are biased, which is depicted by the symmetric

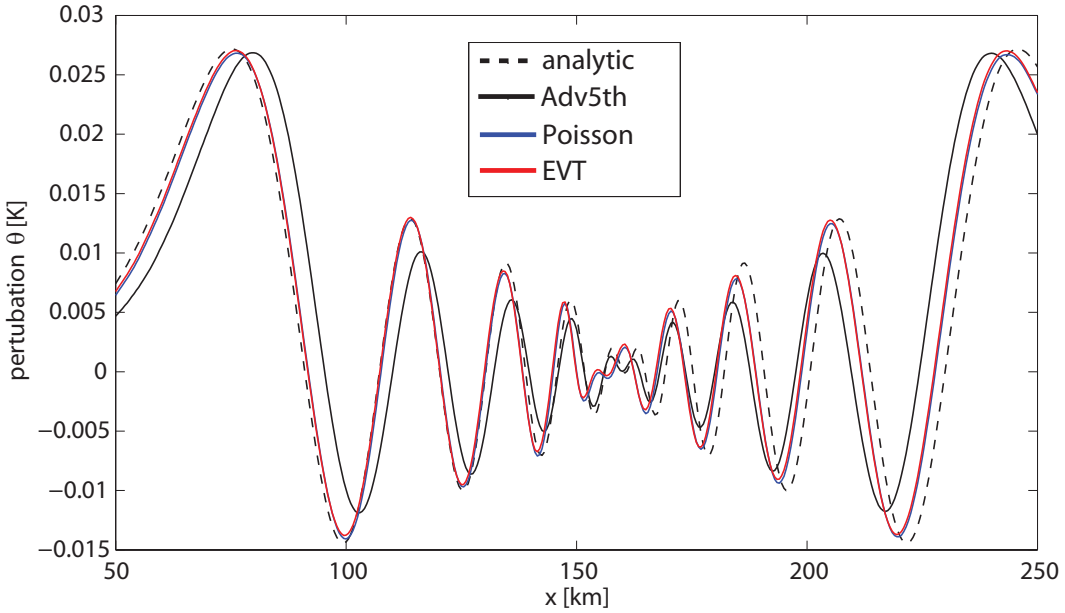

Figure 4.4: 1-d profile of the perturbation θ at an altitude of 4750 m for the inertia gravity wave test at $t = 3000$ s. The displayed grid is 400 grid points. The 'Adv2nd' model solution is nearly identical to the 'Poisson' solution and is not shown here.

square error E_s^2 given in Table 4.4. E_s^2 is determined by the expression

$$E_s^2 = \sum_{i=1}^{200} \left[\theta'(x_s + i\Delta x) - \theta'(x_s - i\Delta x)\right]^2 ,$$

where x_s is the position of the symmetry axis and is obtained in such a way that it gives the optimal value for E_s^2, respectively the minimal value. The 'Poisson' and the 'EVT' symmetric error E_s^2 are nearly identical to the 'Adv2nd' solution, which indicates the bracket-based schemes behave as a second order scheme with respect to the resolution of the gravity wave generation.

As already mentioned, the 'Adv5th' model run is affected by the Rayleigh damping layer at the uppermost level. Thus, big differences between model and analytic solution occur regarding the amplitude and phase speed of the propagating gravity waves (Figure 4.4). Nevertheless, due to the high level of accuracy the 'Adv5th' configuration is preferred to resolve the excited oscillations. Therefore, the symmetry performance is enhanced and the E_s^2 index is small in comparison to the runs with low accuracy ('Adv2nd', 'Poisson' and 'EVT').

The location of the symmetry axis x_s is different for all model runs (Table 4.4). The 'Adv5th' simulation provides the smallest phase shift between the epicenter location in the model and the analytic solution. In particular, the 'EVT' configuration offers a phase shift of about two to three times Δx, which is even one grid point more than for the 'Poisson' solution. The discrepancy between the two bracket-based schemes results from the different treatment of the rotational parts of the flow: e. g. in the 'EVT' scheme the energy-helicity is located at the mass mid point and in the 'Poisson'

Table 4.4: Performance of the model configurations used for the inertia gravity-wave test. The term timing refers to the computational time required for a one hour gravity-wave simulation. The timings of the 'EVT' and the 'Poisson' simulation are influenced by the recursive algorithm building up the stencils (Section 4.3.2).

configuration	Analytic solution	Adv5th	Adv2nd / Poisson	EVT
symmetry axis x_s	160.5 km	160.0 km	159.75 km	159.25 km
E_s^2	0.0 K^2	4.3×10^{-5} K^2	4.4×10^{-4} K^2	5.0×10^{-4} K^2
RE of subdomain budget [%/100]	-	2.5×10^{-5}	3.1×10^{-5}	3.1×10^{-5}
timing	-	122 s	117 s / 1891 s	1752 s

scheme the $\{\mathcal{F}, \mathcal{H}\}^P_{\mathbf{v},\mathbf{v}}$ part of the Poisson bracket is located at the grid box corner (Section 4.3.2 and Section 4.3.3). Considering the spatial distribution of the rotational modes with respect to the x-z plane (Figure 4.5a), a phase shift of the rotational wind field to the left is observed in the 'EVT' solution in comparison to the 'Poisson' solution. Consequently, the advection of velocity is also different for the 'EVT' and the 'Poisson' solution, i. e. a slightly different dispersion relation for the simulated gravity waves. Thus, the 'EVT' scheme delivers a little bit worse performance compared to the 'Adv2nd' and the 'Poisson' scheme with respect to the gravity wave propagation.

4.4.3 Sub-domain analysis of the gravity-wave propagation

Pushing further the validation of the bracket-based schemes, the numerical algorithms are tested for artificial sources or sinks of energy. Therefore, we invoke the sub-domain budget analysis for testing the principles of conservation on a local scale as discussed in Chapter 2. The energy related fluxes of a sub-domain are examined and plotted in Figure 4.5b. The sub-domain is bounded by the coordinates $x = 120\,\text{km}$, $x = 140\,\text{km}$ and $z = 2.5\,\text{km}$, $z = 7.5\,\text{km}$. In order to achieve a better visualization the energy change is plotted using thin lines (dark green for the 'Adv5th' and light green for the 'Poisson' simulation). It turns out that the sub-domain budgets are almost the same in the 'Adv2nd', 'Poisson' and 'EVT' runs. The 'Adv5th' configuration offers more smoothed mass fluxes and changes, which may originate from the high accuracy and the inherent diffusion of the fifth-order advection scheme. However, all numerical schemes have only a small residua: The RE of the total energy budget is about 3×10^{-5} (Table 4.4). The residual curve possesses small oscillations at the beginning of the simulation originating from the spin-up process, but there are no big budget errors. Thus, it is concluded that the bracket-based schemes does not produce strong artificial sources or sinks of energy in case of the weak nonlinear test.

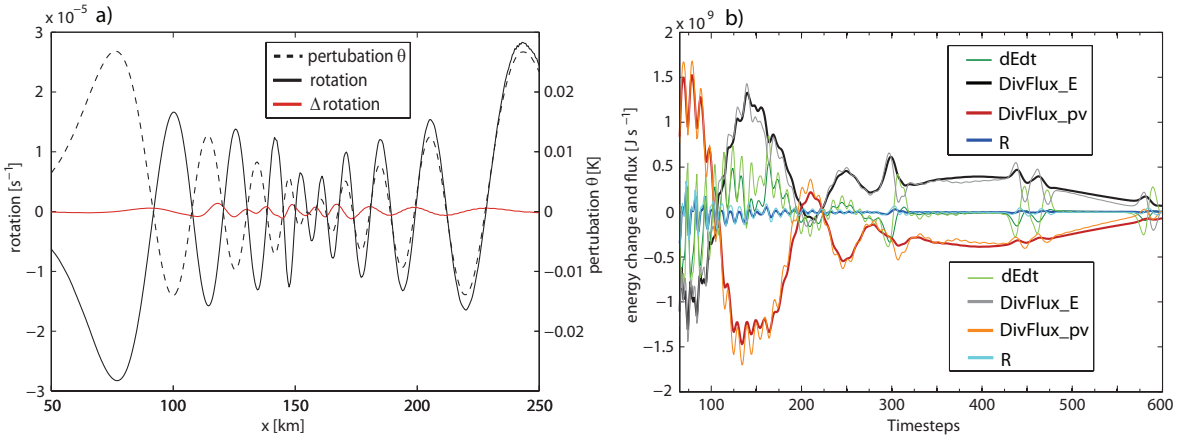

Figure 4.5: a) 1-d profile of the perturbation θ and the rotation of the wind field at an altitude of 4750 m for the 'Poisson' configuration at $t = 3000$ s. Δ rotation indicates the difference in rotation between 'EVT' and 'Poisson' configuration. The displayed grid is 400 grid points. b) Sub-domain budget of total energy using the 'Adv5th' configuration (black, dark red and blue) and the 'Poisson' configuration (gray, orange and light blue). The abbreviations in the legend are equal to the ones used for the sub-domain analysis in Chapter 2.

4.4.4 Implications for simulations under weak nonlinear conditions

In summary, the numerical schemes 'Poisson' and 'EVT' work fine in the framework of the inertia-gravity wave test. Although the stencils of the 'EVT' and the 'Poisson' scheme are very complex, no numerical smoothing could be identified in the solutions, but a small phase shift for the 'EVT' scheme (1.5 Δx within 50 minutes) relative to the reference solution 'Adv5th' of the COSMO model. The bracket-based schemes behave as the 'Adv2nd' scheme with respect to the symmetric properties and the spatial resolution of the gravity waves. The numerical algorithms of the 'EVT' and the 'Poisson' scheme are much more computational expensive than the numerical algorithms of the 'Adv5th' and 'Adv2nd' scheme. We have to note here, that the computing performance of the 'Poisson' and the 'Nambu' simulation could be improved by coding the stencils explicitly (as it is the case for the 'Adv5th' and 'Adv2nd' scheme), but the code would be very vulnerable to indexing errors as already mentioned in Section 4.3.2.

In the framework of the inertia-gravity test case we dealt more or less with the propagation of waves advected with a constant velocity through the domain. The differences in the simulations between the bracket-based schemes and the standard advection schemes are very small because of the weak nonlinear scale interaction. But this is no indicator for the model behavior with respect to strong nonlinear flows, which is discussed in the next section.

4.5 Evolution and dynamics of a supercell thunderstorm - strong nonlinearity

Keeping in mind that the bracket-based 'Poisson' and 'EVT' scheme incorporate three-dimensional vortex quantities, three-dimensional rotational flows are simulated with the COSMO model in a preliminary test. The generation of rotational flows in a three-dimensional non-hydrostatic model can be achieved mainly by two forcing mechanisms. First, the rotational flow is evolving inside a large-scale baroclinic wave, which is excited by small perturbations of the wind field in a baroclinic and hydrostatic balanced atmosphere (e. g. Jablonowski and Williamson, 2006). Second, the rotational flow is embedded in supercell storms, which are initiated with an isolated warm thermal (Klemp and Wilhelmson, 1978; Weisman and Klemp, 1982) or along a thermal line (Weisman et al., 1988; Bluestein, 2000). Since the supercell storms develop under strong nonlinear conditions and much faster as the baroclinic waves, the rotation is forced using the second mechanism.

Our modeling philosophy is to simplify the interpretation of the results. Therefore, we perform a storm simulation using a single warm thermal as proposed by Klemp et al. (1981).

4.5.1 Experimental setup

The storm simulation is mainly initialized following Klemp et al. (1981). The simulation was designed to study the evolution and structure of the Del City Storm as observed by the NSSL radar network in the late afternoon of 20th May 1977 (Ray et al., 1981). The initial model environment is defined based on radio soundings at Ft. Sill and at Elmore City. The vertical profiles of wind, temperature and dew point are depicted in Figure 4.6. The temperature and humidity profile are adjusted at the top of the PBL to increase the convective inhibition, because we hope to suppress the triggering of secondary convection along the outflow boundaries (Bluestein, 2000). The observed wind profile is modified in such a way that the storm remains in the centre of the model domain. The moist convection in the atmosphere is initiated with a thermal bubble, which possesses in its center a temperature excess of 4 K compared to the environmental air (Klemp et al., 1981).

The simulation of the Dell City storm is performed on a single CPU, because the numerical algorithm for the Poisson and EVT scheme is not parallelized. The simulation is carried out on a model domain, which extends 120 km in each horizontal direction. The horizontal grid spacing is 1 km. The domain consists of 34 vertical levels with a grid spacing of 500 m. The vertical extend of the model domain is 17 km with impermeable and free-slip upper and lower boundaries. Thus, the integration is done on 120 $\times$ 120 $\times$ 34 grid points. A Rayleigh-damping zone is implemented and extends from 12 km height up to the model top. In addition, a lateral relaxation zone with a width of 20 km is used to damp reflections of gravity waves that are excited by the convective storm inside the computational domain.

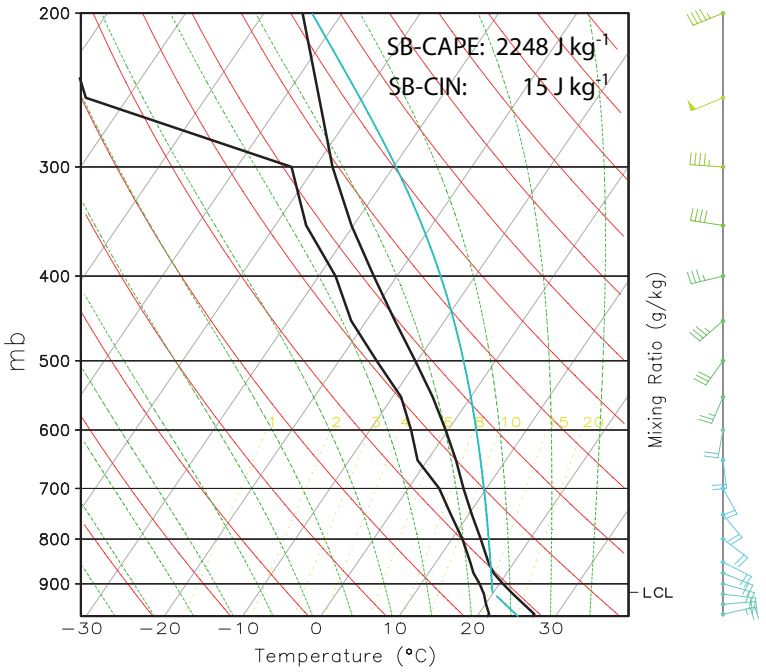

Figure 4.6: Skew-T log-p diagram of the initial model atmosphere with respect to the Del City storm test case. Temperature and dew point [° C] are denoted by the black lines and the horizontal winds by the wind barbs. The blue line displays the temperature of an air parcel lifted from the earth surface. 'LCL' is the lifting condensation level.

The numerical integration is done with a time step of 6 seconds using the Runge-Kutta time integration scheme (for more model details see Appendix A). The simulation ends after two hours. The turbulence scheme of Raschendorfer (2001) and a six class cloud microphysical scheme are used to treat the physical processes. Radiative processes are not considered and the Coriolis parameter is set to zero. As already done for the inertia-gravity wave test case, the results of four different model configurations (Table 4.3) are examined and compared. In contrast to the inertia-gravity wave test, a fourth-order Laplacian diffusion is turned on for all prognostic variables (Section 2.3.1). The eddy viscosity coefficient is $\nu_l \approx 8.5 \cdot 10^8\,\mathrm{m^4\,s^{-1}}$. Since the configuration 'Adv5th' is expected to be capable to prevent nonlinear instability because of the diffusion inherent in the fifth-order upwind scheme (Wicker and Skamarock, 2002), the eddy viscosity coefficient is set to zero for the reference simulation 'Adv5th'.

4.5.2 Temporal evolution of the supercell thunderstorm in the reference simulation 'Adv5th'

The thermal bubble is initialized in the model domain at $x = 75\,\mathrm{km}$ and $y = 45\,\mathrm{km}$. Afterwards, strong moist and deep convection is developing due to the rising thermal bubble. The temporal evolution of the convective system is depicted by Figure 4.7 for all model configurations. At first, we focus on the results from the reference COSMO simulation 'Adv5th' (the black lines). After 30 minutes the maximum vertical velocity inside the mid-level updraft reaches $16\,\mathrm{m\,s^{-1}}$ (Figure 4.7a). The low-level vorticity has

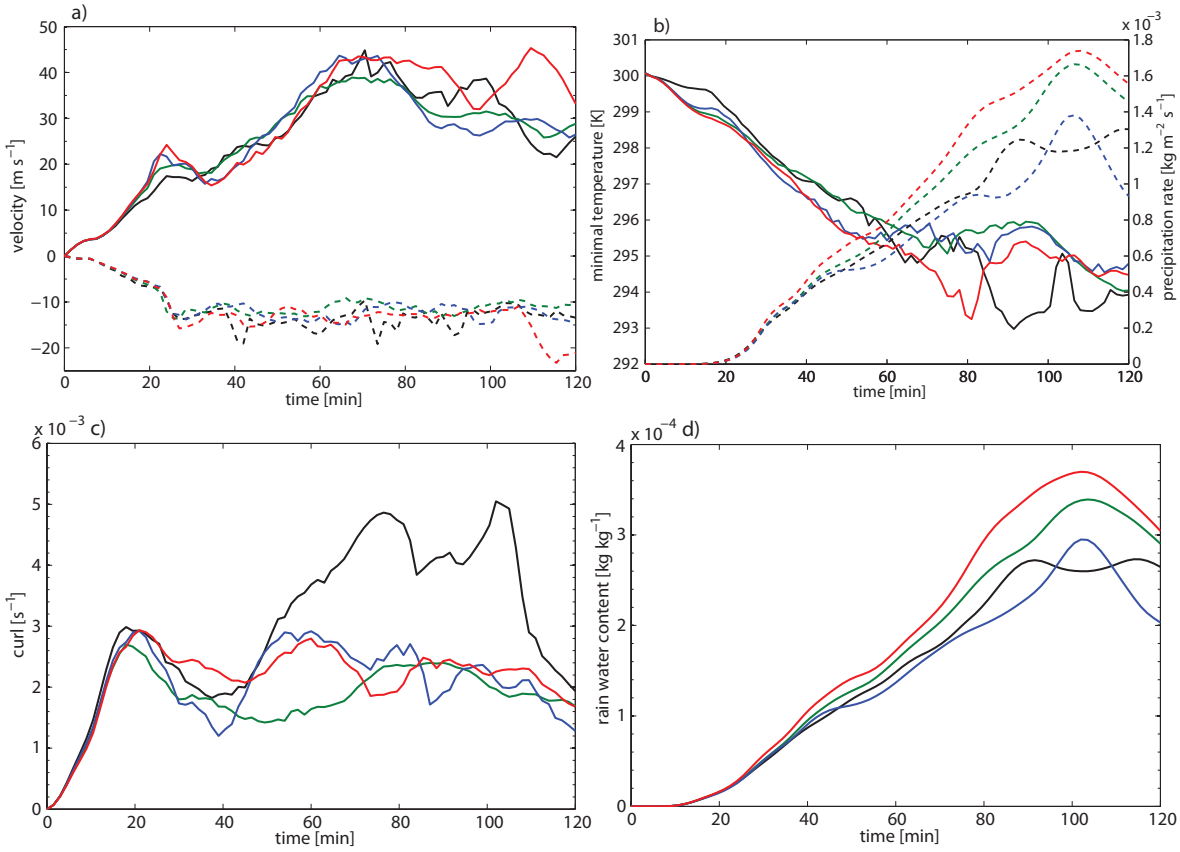

Figure 4.7: Simulated temporal evolution of the Del City storm using the configuration 'Avd5th' (denoted by the black line), 'Adv2nd' (green), 'Poisson' (blue) and 'EVT' (red). Only the central 50 km × 50 km region is considered. a) Maximum vertical wind speed [m s^{-1}] (solid lines) and minimum vertical wind speed [m s^{-1}] (dashed lines) at all levels. b) Minimum temperature at the 250 m level [K] (solid lines) and mean instantaneous precipitation rate [kg m^2 s^{-1}] (dashed lines). c) Maximum vertical vorticity [s^{-1}] (on a x-y plane) at the lowest 1750 m. d) Mean rain water content [kg kg^{-1}] at the lowest 1750 m.

increased up to $3{\cdot}10^{-3}$ s^{-1} after 20 minutes due to the twisting of horizontal vortexes to vertical vortexes under vertical wind shear conditions (Figure 4.7c). The precipitation generated by the convective cell cools the lower levels (Figure 4.7b) and forms a strong downdraft, which is -3 m s^{-1} at 1000 m above ground. The downdraft starts to split the low-level updraft, which is described in detail by Wilhelmson and Klemp (1978) and Weisman and Klemp (1982).

After one hour, two storms are present in the simulation, which are 15 km apart and located on the right side and on the left side of the initial updraft. The structure of the storms is shown in Figure 4.8a,b. Only data from the central 55 km × 55 km region are considered for the plot. The storm on the right side becomes more intense than the storm on the left side, i. e. the maximum updraft velocity is 35 m s^{-1} for the right cell and only 12 m s^{-1} for the left cell. The clockwise curvature of the wind hodograph in the environmental air favors the growth of the right-moving storm compared to the left-moving storm (Klemp et al., 1981; Rotunno and Klemp, 1982). At the northern

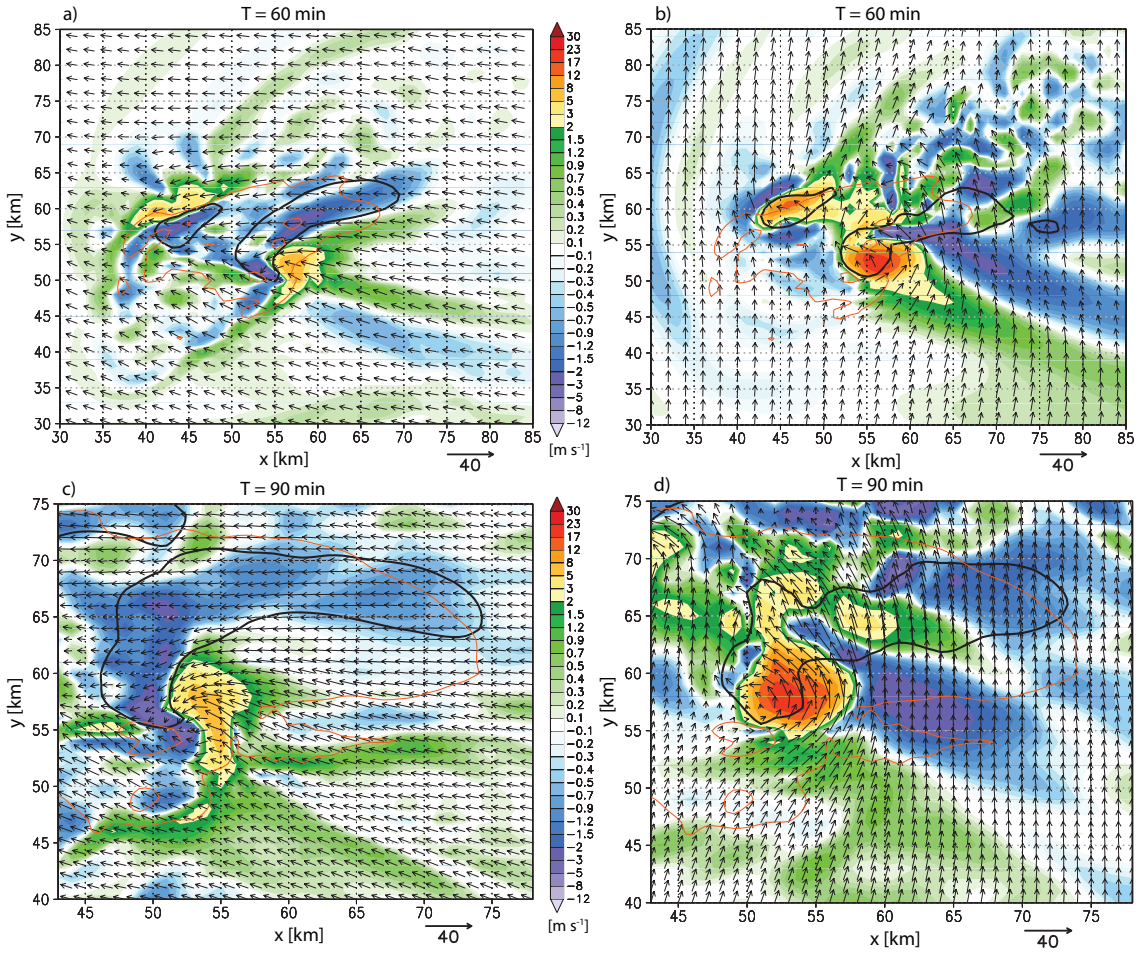

Figure 4.8: X-y cross-section of the simulated Del City storm using the reference configuration 'Adv5th'. a) Vertical velocity [m s^{-1}] (shaded), the horizontal wind [m s^{-1}] (vectors) and the rain water level of 7 g kg^{-1} (black line) at the level z = 1 km and at 60 min. The red line denotes the -1 K temperature pertubation at the lowest model level (z = 250 m). The scale of the wind vectors is given in the lower right. The central 55 km × 55 km model domain is displayed. b) as in a), but at the level z = 4 km and at 60 min. The black line denotes the 15 g kg^{-1} rain water contour. c) and d), as in a) and b), but at 90 min and for the central 35 km × 35 km region.

flank of the right-moving storm a strong downdraft has established at the lower and mid levels. The cold outflow is spreading out near the ground and forms a gust front extending from the Northeast to the Southwest of the convective system, which is depicted by the -1 K temperature perturbation in Figure 4.8. Since strong convergence is forced along the cold front, the storm updraft is supplied with additional moist and warm inflow.

At 60 minutes the strongest downdraft region at the lower levels is located on the west side of the updraft, i. e. the rear flank downdraft (RFD, (Markowski, 2002)). The outflow is nearly 5 K colder as the environmental air at 250 m above ground, which implies high wind speeds in the low level outflow. The horizontal wind field displays strong cyclonic rotation inside the storm. At this time the rotation is about $3.6{\cdot}10^{-3}\,\mathrm{s}^{-1}$. After 75 minutes, the storm has reached its mature stage and possesses the strongest updraft and low-level rotation during the whole simulation period. The storm structure remains nearly steady-state until the convective system decays.

The storm structure at 90 minutes is shown in Figure 4.8c,d. Only data from the central 35 km $\times$ 35 km are considered. The left-moving storm is located far to the northwest of the right-moving storm and produces precipitation along a convergence line, which is not discussed further. The downdraft and the precipitating water along the RFD of the right-moving storm has wrapped around the rotating updraft at its southern flank and forms a well-defined hook structure (Markowski, 2002). The cold outflow has progressed further east and south relative to the storm. Consequently, the warm inflow into the updraft declines. Starting at about 100 minutes, the maximum updraft velocity and later on the rain water and the precipitation rate decrease. The decay of the storm is faster in our simulation in comparison to (Klemp et al., 1981) due to the fact that we use a modified and more stable atmospheric profile, which was introduced in Section 4.5.1.

The trend of the minimum temperature, maximum vertical velocity and low-level vorticity in Figure 4.7 reveals some high maximal values during the second half of the reference COSMO simulation. They are related with unphysical $2\Delta x$ structures. The simulation is at the limit of stability. This issue is discussed in Section 4.5.5.

4.5.3 Impact of the EVT and Poisson scheme on the supercell storm

Considering the temporal evolution of the storm as shown in Figure 4.7, only a few distinctive features are revealed among the different model configurations, which are examined in the following. We measure the performance of the 'Poisson' and 'EVT' scheme on the 'Adv5th' simulation and involve additionally the results of 'Adv2nd' simulation for the purpose of comparison as already done for the inertia-gravity wave test.

Supercell dynamics

During the first half of the simulation all configurations give nearly the same results. At 60 minutes the 'Adv2nd', 'Poisson' and 'EVT' simulations predict two split storms

(Figure 4.9, left panel), which is in accordance with the 'Adv5th' simulation. Small differences among the simulations can be seen in particular for the low-level wind field in the storm region. Examining the low-level vorticity field predicted by the four different model schemes at 60 minutes (Figure 4.10), the strength and the orientation of the dipole structure in the updraft and downdraft region of the right-moving storm (x = 58 km and y = 53 km) differ from each other. The 'Adv5th' scheme produces the strongest and most extending updraft rotation, because it benefits from the high accuracy and the small amount of numerical damping inherent in the fifth order advection scheme. The differences in the orientation of the dipole may be associated with the phase shift examined for the gravity wave test case (Table 4.4).

The 'Poisson' and the 'EVT' schemes resolve a strong cyclonic vortex between the left-moving and the right-moving storm at 60 minutes. The enhancement of the rotation southeast to the left-moving storm might influence the dynamics of the cell relative to the 'Adv5th' and 'Adv2nd' simulations. Since the left-mover was not observed by the radar (Ray et al., 1981) on the 20th May 1977 and Klemp et al. (1981) refer to its small production rate of rain-water content in their model simulation, this issue is not discussed further.

The mature stage of the right-moving supercell storm at 90 minutes is displayed in Figure 4.9 (right panel) for the three schemes 'Adv2nd', 'Poisson' and 'EVT'. Since the storm has reached a nearly steady-state at this time, we are able to compare adequately the model results with the reference run 'Adv5th' (Figure 4.8c). All schemes capture the downdraft and updraft regions of the right-moving supercell, but the cell is shifted slightly to the northeast using the 'Adv5th' scheme. As noted earlier, a small hook-echo is present in the rain water and vertical velocity field of the 'Adv5th' simulation. The 'EVT' and the 'Poisson' integration also indicate a small hook-echo structure in the RFD region southwest to the updraft at 90 minutes. That is, the downdraft is extending to the east at the southern flank of the updraft. At this time the 'Adv2nd' solution does not offer a hook-like feature at all. This implies that the 'EVT' and 'Poisson' simulations have a slightly higher effective resolution than the 'Adv2nd' simulation, which is discussed in Section 4.5.5.

Precipitation and storm tracks

The temporal evolution of the simulated precipitation is qualitatively the same for all numerical schemes (Figure 4.7b). The magnitude of the precipitation rates differ among the simulations during the second half of the simulation. In the 'Poisson' simulation the instantaneous precipitation rate at 90 minutes is reduced by 50 percent compared to the 'EVT' simulation. The two-hour accumulated precipitation is shown in Figure 4.11. The 'Poisson' scheme produces the least precipitating supercell compared to the other schemes and reveals two maxima at the western part of the right-moving cell, but an explanation for this behavior cannot be given in this preliminary study. Nearly the same amount of precipitation is predicted by the 'EVT' and the 'Adv2nd' scheme nearly at the same region, whereas the reference simulation 'Adv5th' gives some less precipitation amounts shifted slightly to the west.

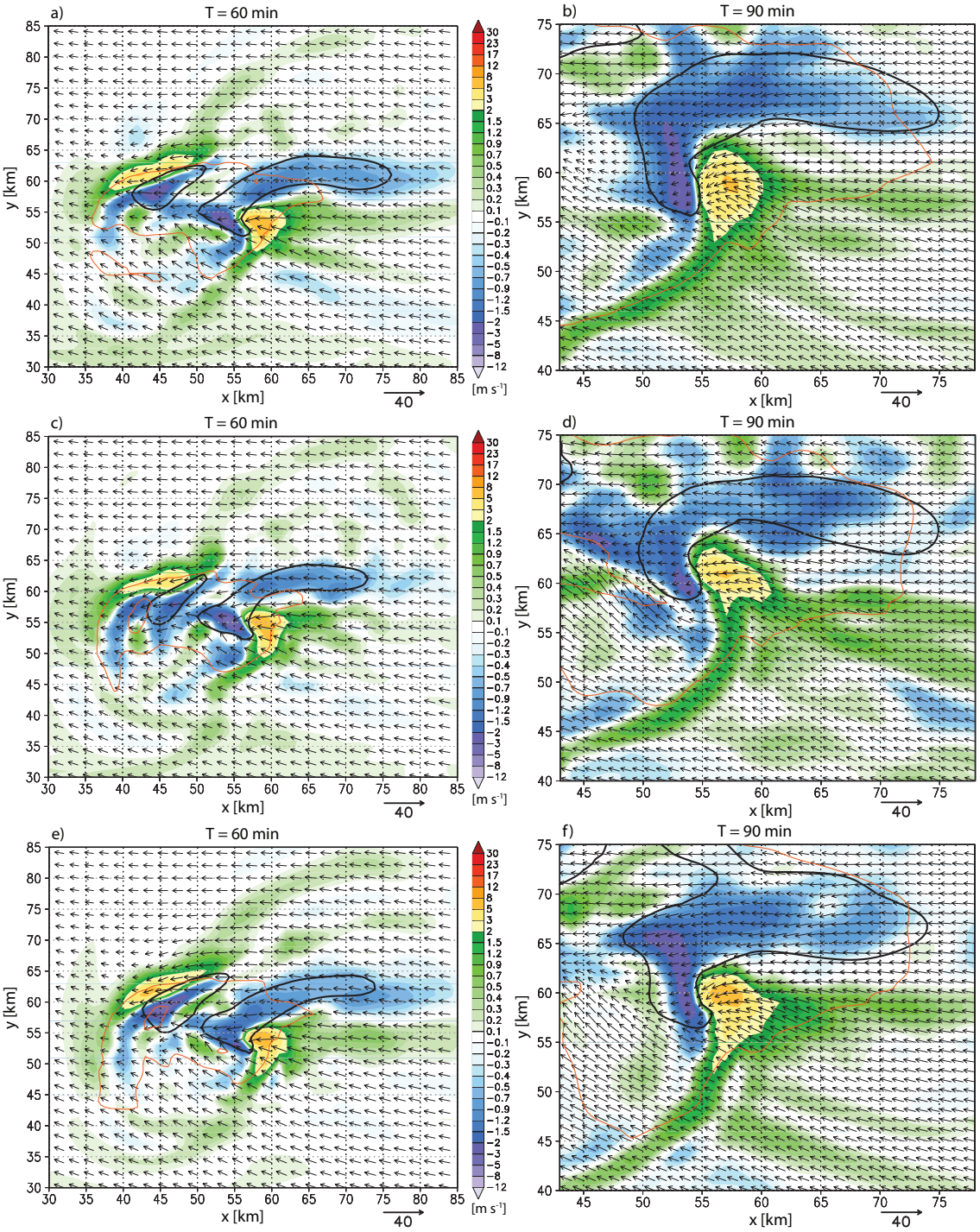

Figure 4.9: X-y cross-section of the simulated Del City storm using three different configurations. a) and c) and e) as in Figure 4.8a, but for the 'Adv2nd', the 'Poisson' and the 'EVT' scheme. b) and d) and f) as in Figure 4.8c, but for the 'Adv2nd', the 'Poisson' and the 'EVT' scheme.

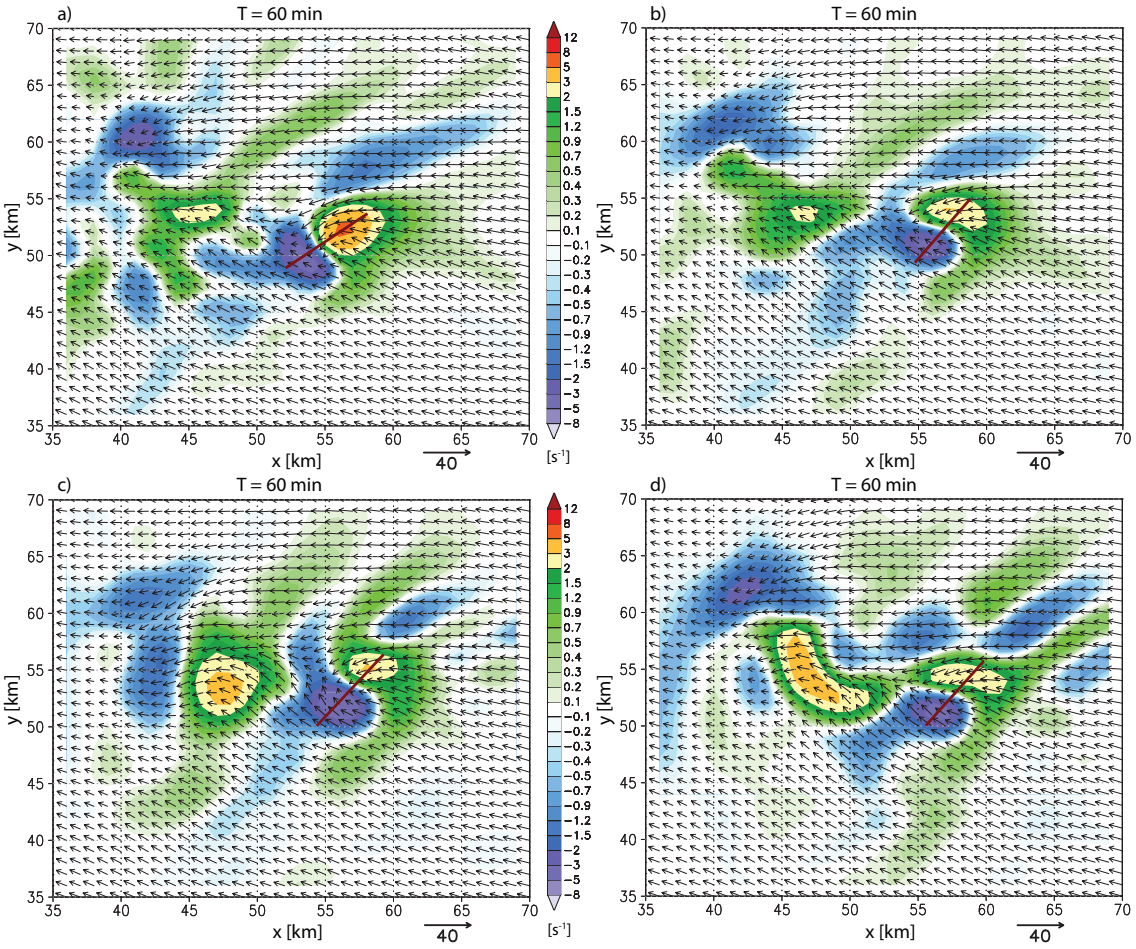

Figure 4.10: X-y cross-section of the simulated Del City storm using a) the 'Adv5th', b) the 'Adv2nd', c) the 'Poisson' and d) the 'EVT' configuration. The third component of the vorticity $[10^{-3}\,\mathrm{s}^{-1}]$ (shaded) and the horizontal wind (vectors) are displayed for the central 35 km × 35 km region at the level z = 1 km and at 60 min. The scale for the wind vectors is given in the lower right. The dark red line denotes the dipole axis of the right-moving storm.

In order to investigate the track of the supercell storm in the different simulations, the position of the maximum updraft at 4000 m above the ground is determined regarding the right-moving storm. The location of the maximum updraft region is listed in Table 4.5 at 60, 90 and 120 minutes. During the first 90 minutes the storm track is nearly identical in the 'EVT', 'Poisson' and 'Adv2nd' simulation, but a little bit shifted to the west in the reference run 'Adv5th'. Starting at 90 minutes the storm in the 'Poisson' simulation is obviously propagating to the North relative to the other simulations. The drift to the North in the 'Poisson' simulation is associated with the rain water occurring at the northern part of the right-moving cell: The amount of rain water is reduced at the mid troposphere in the 'Poisson' simulation relative to the others (Figure 4.7d and Figure 4.9), which might push the storm cell to the North by the southern wind regime at the mid levels.

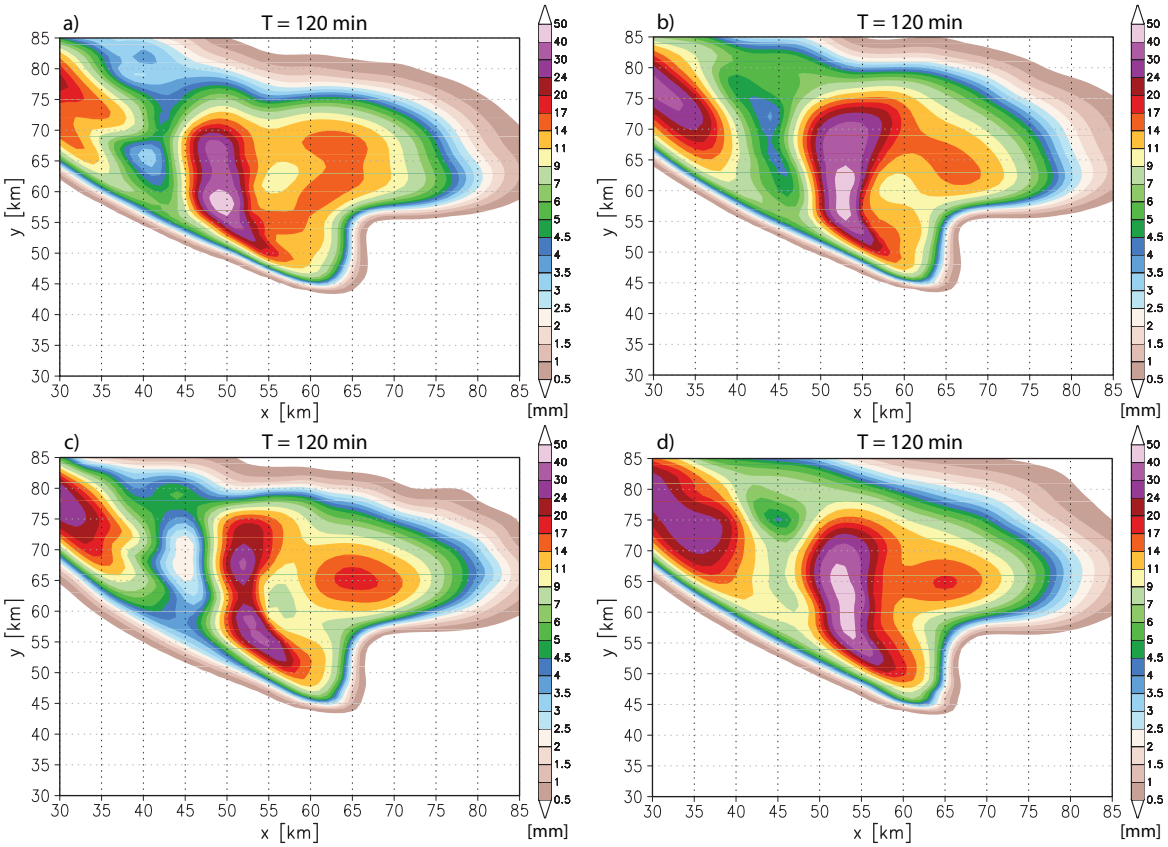

Figure 4.11: Two-hour accumulated precipitation [mm] (shaded) for the simulated Del City storm using a) the 'Adv5th', b) the 'Adv2nd', c) the 'Poisson' and d) the 'EVT' configuration.

Table 4.5: Characteristics of the right-moving cell concerning the Del City supercell storm simulation. The location of the maximum updraft at the level z = 4 km and the maximum accumulated precipitation over two hours is given.

configuration	Adv5th	Adv2nd	Poisson	EVT
Updraft location [km] at 60 min	x=56 / y=52	x=58 / y=53	x=58 / y=54	x=58 / y=53
at 90 min	x=53 / y=58	x=56 / y=59	x=56 / y=61	x=56 / y=59
at 120 min	x=52 / y=63	x=56 / y=64	x=55 / y=70	x=57 / y=64
Maximum precipitation [mm]	49	46	32	45

4.5.4 Physical validation by the sub-domain budget method

In order to test whether the physical fluxes developing in the environment of the supercell storm are consistent with the temporal change in the water, energy and mass

reservoir inside the supercell, we invoke the sub-domain budget analysis discussed in Chapter 2. The energy budget is considered and validated exemplary for the simulations 'Adv5th', 'Adv2nd', 'Poisson' and 'EVT' scheme. The energy related fluxes and the energy change are determined for a certain sub-domain, which is bounded by the coordinates $x = 40\,\mathrm{km}$, $x = 75\,\mathrm{km}$, $y = 45\,\mathrm{km}$, $y = 80\,\mathrm{km}$ and $z = 0.5\,\mathrm{km}$, $z = 8.5\,\mathrm{km}$. Thus, the right-moving supercell storm is developing mainly inside the monitored sub-domain.

The sub-domain budget of energy is plotted in Figure 4.12. For the sake of clarity, only the budget for the 'Poisson' simulation is shown. The turbulent fluxes of momentum and heat and the energetic flux at the surface are not displayed (see Chapter 2 for energy related fluxes), because they do not significantly contribute to the budget (magnitude $10^{10}\,\mathrm{J\,s^{-1}}$). Additionally, the residua are shown for the 'Adv5th' (cyan), the 'Adv2nd' (purple) and the 'EVT' (yellow) scheme. It turns out that the energy budget is well balanced for the 'Poisson' scheme as well as for the 'EVT' scheme: The energy related fluxes are physically consistent with the temporal change in energy. The energetic fluxes differ among the the various simulations (not shown), but the residua are almost the same in all configurations. All numerical schemes produce only a small relative error (RE) of about 0.1 %. The residual curve of the 'Adv5th' simulation offers small-scale oscillations at time step 400, which are related to instabilities discussed further in Section 4.5.5.

4.5.5 Effective resolution versus robustness

In order to determine the effective resolution of the different model runs, we perform the same spectral analysis as used for the model evaluation and verification in Chapter 3. The effective resolution refers to that part of the kinetic energy spectrum, where the model spectrum is decaying against the spectrum known from observations or theoretical considerations. The focus is here on the mature stage and along the West-East axis of the supercell storm, i. e. the spectral decomposition is done at the 5000 m level along the x-direction at the section x$\in$ [35 km, 75 km], which is reflected by a high variance in the vertical velocity field. The spectra are averaged along the y-direction over fifteen West-East oriented line segments. To obtain robust energy spectra, the model output is analyzed in the time range 70 minutes to 90 minutes after the initialization. The kinetic energy spectra derived from the simulations using the 'Adv5th', the 'Adv2nd', the 'Poisson' and the 'EVT' scheme are plotted in Figure 4.13a. The spectra highlight two main aspects:

(A) The 'Adv2nd', the 'Poisson' and the 'EVT' simulation possess nearly the same kinetic energy spectra,

(B) the reference simulation 'Adv5th' possesses the highest effective resolution.

Regarding the aspect (A), the kinetic energy spectrum predicted by the three schemes decays against the reference spectrum at wavelength $\lambda \approx 5\,\mathrm{km}$. Thus, the effective resolution is the same for the 'Adv2nd', the 'Poisson' and the 'EVT' solution. We draw the conclusion that the extensive reconstruction on big stencils inherent in the 'Poisson' and 'EVT' scheme (Section 4.3.4) does not worsen the effective resolution compared

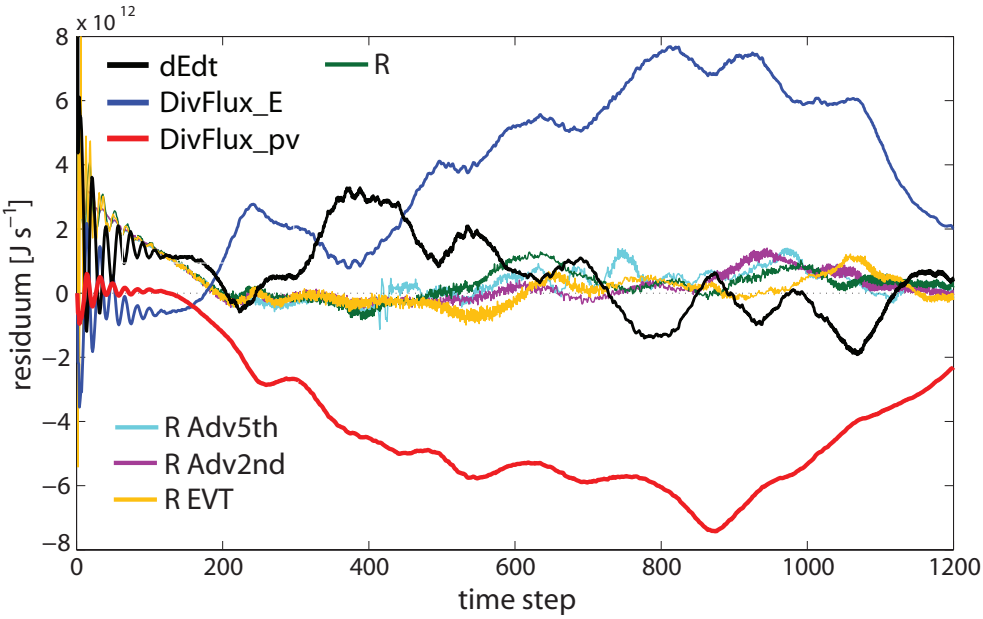

Figure 4.12: Sub-domain budget of the energy with respect to the Dell City storm simulation in the environment of the right-moving cell. The energy budget is displayed for the 'Poisson' simulation: the energy change (black), the energy flux divergence (dark blue), the flux due to work done by the control volume (red) and the residuum (green). In addition, the residua of the numerical schemes 'Adv5th', 'Adv2nd' and 'EVT' are shown (color code in the legend). The relative error for all configurations is given as follows: RE 'Adv5th' $\approx 1.0 * 10^{-3}$, RE 'Adv2nd' $\approx 0.9{*}10^{-3}$, RE 'Poisson' $\approx 1.0{*}10^{-3}$ and RE 'EVT' $\approx 0.9{*}10^{-3}$, . The sub-domain budget analysis is discussed in detail in Chapter 2.

to the 'Adv2nd' scheme. The impact of the extensive reconstruction on the smallest resolved scales seems to be smaller than the impact of the Laplacian diffusion. The Laplacian diffusion used for the 'Adv2nd', 'Poisson' and 'EVT' configuration damps severely the small-scales and thus prevents for example simulating sufficiently the aforementioned hook echo.

Although one obtains the same effective resolution from the kinetic energy spectra of the 'Adv2nd', the 'Poisson' and the 'EVT' simulation, a conclusion about the ability of those three models to resolve fine-scale structures needs to be carefully considered. One cannot distinguish for a specific spectral amplitude the portion belonging to the physical structures from the portion belonging to spurious numerical cascades. The spurious numerical cascades originate from nonlinear instability (Mesinger and Arakawa, 1976). The computational energy cascade can be controlled by an adequate treatment of integral constraints, e. g. energy or enstrophy, during the discretization process as highlighted by Arakawa (1966), Sadourny (1974) and Arakawa and Lamb (1980) for two-dimensional flows and by Tripoli (1992) and Janjic et al. (2011) for three-dimensional flows. Tripoli (1992) argued that a sophisticated discretization of the nonlinear advection term based on enstrophy conservation reduces the numerical cascade down to the smallest resolvable scales. In that case, more amplitude of the spectral variances is retained on the resolvable and physical structures. Taking into account the nearly identical spectra of the 'Adv2nd', the 'Poisson' and the 'EVT' sim-

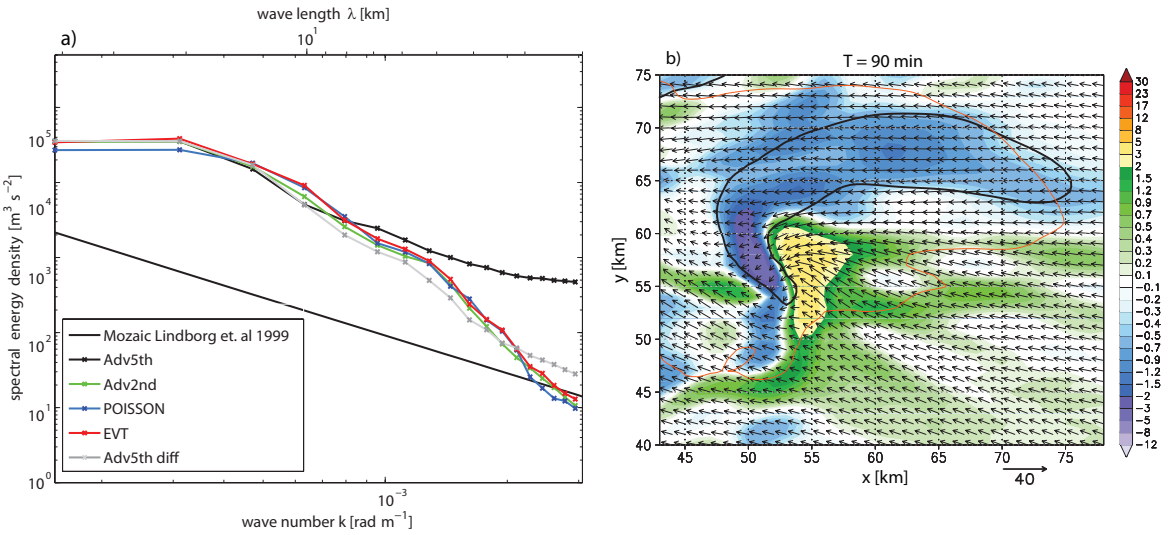

Figure 4.13: a) The discrete kinetic energy density spectra at the model level z = 5000 m for different model configurations. The spectra are averaged over the time span t = 70 min to t = 90 min. Further details about the Lindborg fit and the spectral analysis can be read in Chapter 3. b) As in Figure 4.8c, but using the 'Adv5th diff' configuration.

.

ulation but the small differences concerning the resolution of the hook-echo structure (Figure 4.9), the 'Poisson' and the 'EVT' scheme may retain more amplitude of the small-scale spectral variances on the physical structures than the 'Adv2nd' scheme.

Regarding the aspect (B), the reference simulation 'Adv5th' is preferred to resolve small-scale features as the hook echo, because of the missing Laplacian diffusion. Nevertheless, the small-scale end of the spectrum indicates no decaying variance at all. A slight energy buildup at the smallest scales is present. The diffusion inherent in the odd-order advection scheme is not sufficient to prevent the energy buildup at the small-scale end due to spurious energy cascades. The maximum horizontal wind speeds exceeds occasionally 180 m s^{-1} in the reference simulation 'Adv5th'. However, the simulation does not crash, because the damping mechanism of the odd-order advection scheme becomes strong in those regions where high Courant numbers occur (Wicker and Skamarock, 2002). The effective resolution might be the best for the reference run, but the model output and also the simulation itself is contaminated with unphysical $2\Delta x$ structures.

In order to yield a more robust reference run, a simulation is performed using the 'Adv5th' configuration, but applying additionally Laplacian diffusion on all prognostic variables (configuration 'Adv5th diff'). The eddy viscosity coefficient is the same as used for the other experiments, i. e. $\nu_l \approx 8.5 \cdot 10^8$ m^4 s^{-1}. The spectrum obtained from the 'Adv5th diff' simulation is also plotted in Figure 4.13a. Spectral variance is lost for structures having a size of less than 10 km relative to the 'Adv5th' simulation. This also holds for the above-mentioned hook structure. At 90 minutes the hook echo is nearly smoothed out and much weaker using the 'Adv5th diff' scheme (Figure 4.13b) than for the 'Adv5th' scheme (Figure 4.8) and the strength of the updraft rotation is decreased. The storm structure at the RFD is close to the one predicted by the 'Poisson' and the

'EVT' scheme. Therefore, the quality of the 'Poisson' and the 'EVT' solution with respect to the resolved small-scale features becomes identical to the solution 'Adv5th diff'.

4.5.6 Implications from the supercell storm simulation

The 'Poisson' and the 'EVT' scheme resolve well the main features of the Dell City supercell storm known from the observations of Ray et al. (1981) and the model simulation performed by Klemp et al. (1981): the storm splitting process, the rotating updraft, the forward flank downdraft and the rear flank downdraft at the right-moving cell. The sub-domain budget in the environment of the storm is well balanced and physically consistent for the 'Poisson' and the 'EVT' simulation. Moreover, the 'Poisson' and the 'EVT' scheme tend to simulate a hook-echo structure during the mature stage of the right-moving storm, which is not present in the 'Adv2nd' simulation. The difference among the 'Adv2nd', the 'Poisson' and the 'EVT' scheme with respect to the fine-scale phenomena hook-echo is not reflected in the behavior of the kinetic energy spectrum at the small-scales. However, the spectral decomposition analysis does not allow to separate the portion belonging to physical structures from the portion originating from a spurious numerical cascade.

The reference solution 'Adv5th' provides a well resolved hook echo and a higher effective resolution than the 'Adv2nd', the 'Poisson' and the 'EVT' solution due to the missing Laplacian diffusion. Nevertheless, the reference simulation is contaminated with unphysical small-scale noise. To prevent this noise, Laplacian diffusion was applied also to the 'Adv5th' simulation ('Adv5th diff'), which leads to a solution for the mature stage of the storm comparable to the 'Poisson' and the 'EVT' solution. Therefore, care should be taken in the interpretation of the decay of the spectrum relative to theoretical or observed spectra. Possible conclusions with respect to the model performance using the effective resolution need to be carefully drawn. Bryan et al. (2003) also concludes from sensitivity studies concerning the magnitude of the Laplacian numerical diffusion that the cascade at the smallest scales can be manipulated and created whatever the user wishes.

Although the 'Poisson' and the 'EVT' scheme implies big stencils with numerous averaging operators (eq. (4.44)-(4.46) and eq. (4.48)-(4.50)), the 'Poisson' and 'EVT' simulations offer the same spectral variance of the kinetic energy at the small scales as the 'Adv2nd' scheme. However, 'Poisson' and the 'EVT' suffer from the Laplacian diffusion required for a robust simulation in the same manner as the 'Adv2nd' and the 'Adv5th diff' simulation. It was hoped that the implementation of antisymmetric brackets into the 'EVT' and 'Poisson' scheme and the related discretization of three-dimensional vortex quantities as well as the kinetic energy improves the representation of scale-interactions and thus the simulation of the nonlinear cascades. However, the same rate of artificial diffusion is required as for the standard advection scheme 'Adv2nd' in order to prevent from a spurious energy cascade. One explanation for this behavior is given in Section 4.5.7.

4.5.7 Artificial kinetic energy production by the 'EVT' and 'Poisson' scheme

Since the 'Poisson' and the 'EVT' scheme are designed to resolve separately the rotational and irrotational parts of the flow and the discretization process refers explicitly to the kinetic energy and three-dimensional vorticity quantities, it was hoped to better resolve the nonlinear transfer of energy and vorticity-like quantities. In particular a spurious downscale energy transfer shall be reduced by the 'Poisson' and 'EVT' scheme. Thus a further supercell simulation was performed using a smaller eddy viscosity coefficient for the 'EVT' and the 'Poisson' scheme (not shown here), but there is no indicator that the 'EVT' and the 'Poisson' scheme prevent from a numerical aliasing effect. That is, reducing the eddy viscosity coefficient leads to an energy build-up at the small scale end and unphysical wave structures appear in the model output at the same level as it is observed for the 'Adv2nd' scheme. One possible explanation is given in the following.

Hollingsworth et al. (1983) investigated the stability of multi-level shallow water models, which apply energy- and enstrophy-conserving numerical schemes to the vector invariant form of the momentum equations. That is, the flow is split into rotational and irrotational parts, which is comparable with the discretization methods used for the 'EVT' and 'Poisson' scheme. Hollingsworth et al. (1983) identified an instability due to a spurious momentum source (HW-instability, hereafter). The momentum source originates from the non-cancellation of certain terms in the linearized form of the discretized shallow-water momentum equations. In order to test for the HW-instability in an approximate manner with respect to the 'Poisson' and the 'EVT' scheme, we compare the linearized form of the continuous momentum equation (4.1) with the linearized form of the discretized momentum equation, i. e. eq. (4.48)-(4.50) for the 'Poisson' scheme and eq. (4.44)-(4.46) for the 'EVT' scheme. We depart from an exact analysis and focus only on the nonlinear part of the u equation for the sake of simplicity.

The linearization is done around a state, which is comparable to the initial conditions of the supercell storm (Figure 4.6): $u = \hat{u}_z + u'$, $\hat{u}_z = u(z)$, $v = \hat{v}_z + v'$, $\hat{v}_z = v(z)$, $w = w'$ and $\omega_i = \omega_i'$. The perturbations are assumed to be small and y-independent as well as z-independent. The grid box volume τ and the density ρ are constant. The linearized form of the continuous u equation (4.1) is given by:

$$\frac{\partial u'}{\partial t} = \hat{v}_z \partial_x v' - \partial_x \left(\hat{u}_z u'\right) - \partial_x \left(\hat{v}_z v'\right) , \tag{4.52}$$

where the first and the third term on the right hand side cancel each other. Applying the linearization on the discretized equation (4.48) yields:

$$\frac{\partial u'}{\partial t} = \overline{\hat{v}_z}^{z} \partial_x v') - \partial_x \left(\overline{\hat{u}_z u'}^{x}\right) - \hat{v}_z \partial_x v' . \tag{4.53}$$

In contrast to the continuous case, the first and the third term on the right side of finite difference equation (4.53) do not cancel each other. That also holds for the 'EVT' scheme. The linearized form of the finite difference equation (4.44) is:

$$\frac{\partial u'}{\partial t} = \hat{v}_z \overline{\partial_x v'}^{x,x} - \partial_x \left(\overline{\hat{u}_z u'}^{x}\right) - \hat{v}_z \partial_x v' . \tag{4.54}$$

Even in the linearized case the finite form of the momentum equations offer a spurious source of momentum and kinetic energy as well, if one uses the 'EVT' and the 'Poisson' scheme. The extensive and sophisticated techniques used to derive the discretization methods 'Poisson' and 'EVT' from a bracket representation of the momentum equations violate the conservation of momentum.

It is tested, whether the formal non-conservation of momentum in the sense of Hollingsworth et al. (1983) can be detected somehow in the supercell storm simulation. Since the analysis of linearized equations is not valid for strong perturbations, one cannot transfer the problem of HW-instability straightforward to the supercell storm test case. Nevertheless, an indicator for the spurious generation of momentum might be a modified storm simulation, which is performed without initializing the warm thermal. Then, only some small perturbations are expected to develop in the atmosphere characterized by a strong vertical wind shear (Figure 4.6). Thus, simulations were done over one hour without using a warm thermal as convective forcing. The 'Adv5th', the 'Poisson' and the 'EVT' configuration are used without Laplacian diffusion. The deviation of the wind components u and w from the initial state are displayed in Figure 4.14 at 60 minutes. The results of the reference run 'Adv5th' reveal that small perturbations are developing in the model domain, although no forcing of momentum will be apparent in the continuous case. The deviations from the initial state are much stronger for the 'EVT' and the 'Poisson' scheme, which implies artificial momentum sources inherent in both schemes. These artificial source of momentum and energy will explain the fact that the 'Poisson' and the 'EVT' scheme also become unstable, if the eddy viscosity coefficient is decreased below the value used for the 'Adv2nd' scheme.

4.6 Summary and Conclusions

In this work a discretization technique is investigated, which refers to the Hamiltonian description of the continuous Euler equations and to the energy-Vortex theory (EVT). That means the momentum equations, the continuity and the pressure-like thermodynamic equation are constituted by antisymmetric brackets. We have focused on the bracket description of the nonlinear term in the momentum equations, because it is expected to be the most challenging term for numerical weather prediction models.

The nonlinear term is represented by two bilinear Poisson brackets using the Hamiltonian description (Gassmann and Herzog, 2008) and by two trilinear Nambu brackets using the EVT. The Poisson as well as the Nambu brackets involve the global integrated kinetic energy and a global integrated vortex-like quantity: the three-dimensional absolute vorticity in case of the Poisson brackets and the absolute helicity in case of the Nambu brackets. Thus, the non-linear term is split into a rotational and irrotational part and can be recovered by the Lamb transformation. Therefore, the vorticity process is clearly unveiled in the equation of motion, which is hidden in the advective or flux form typically used as a basis for the discretization in recent mesoscale models (Doms and Schaettler, 2002; Schlünzen, 1990; Skamarock et al., 2005). Moreover, the vorticity contribution due to the Earth rotation is inherently linked to the vorticity field.

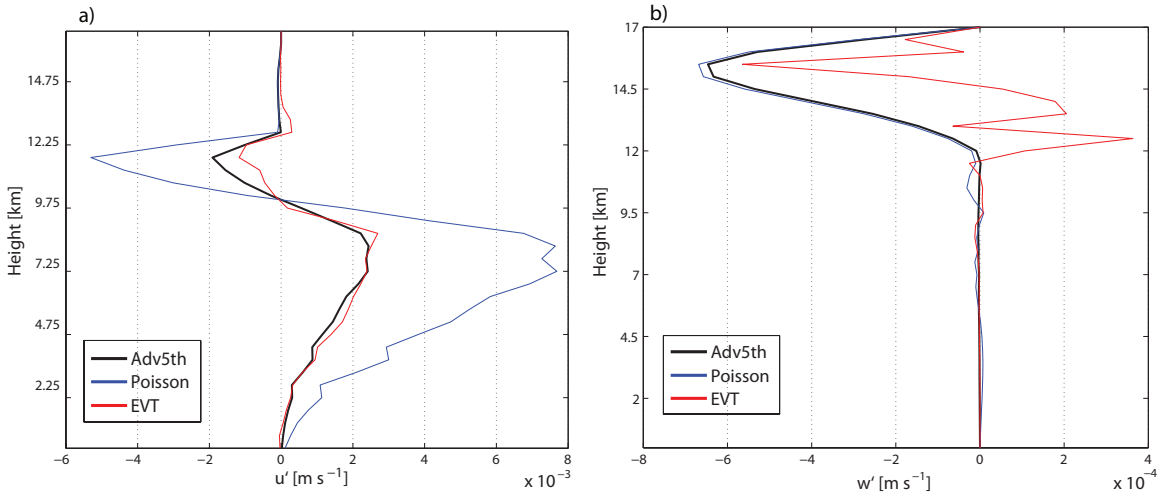

Figure 4.14: Vertical profile of the deviation u' [m s^{-1}] (a) and w' [m s^{-1}] (b) from the initial state with respect to the Del City storm simulation initialized without a warm thermal.

The EVT and the related Nambu brackets are used to derive a discretization for the nonlinear part of the momentum equations. The discretization refers to the following steps: (1) the definition of the global functionals mass, energy and absolute helicity, (2) the determination of the discrete functional derivatives, which constitute then an energy-mass and an energy-helicity bracket and (3) the transfer of the symmetric properties of the continuous brackets to the discretized analogues. In the EVT scheme the discretized energy-helicity bracket is purely antisymmetric, but the energy-mass bracket is antisymmetric in an approximated sense. Finally, the discretization process leads to a prognostic equation at a specific grid point: the numerical scheme is called the 'EVT' scheme. The characteristics of the 'EVT' scheme are the extensive reconstructions on wide-spread three-dimensional stencils, whereas the standard approaches used to discretize the advection form of the nonlinear term possess only small and two-dimensional stencils. The drawbacks of the wide-spread three-dimensional stencils are the exhausting coding and the difficulties in defining efficient implicit time integration methods.

The 'EVT' scheme is implemented into the operational and mesoscale NWP model COSMO (Steppeler et al., 2003). In addition, a discretization based on the Hamiltonian description of the nonlinear part of the momentum equations (Gassmann and Herzog, 2008) is considered for the COSMO model. The related numerical scheme is called the 'Poisson' scheme. The 'EVT' and the 'Poisson' scheme were tested for two different flow regimes: (a) the excitation and propagation of gravity waves under weak non-linear conditions and (b) the simulation of a supercell thunderstorm with strong nonlinear scale interactions. The results of the 'EVT' and 'Poisson' scheme were compared with the standard schemes of the COSMO model, i. e. an ad-hoc discretization of the nonlinear advection operator with second order or fifth order accuracy.

With respect to the gravity wave test case, the 'EVT' and the 'Poisson' scheme gave qualitatively the same solution as the standard schemes, but the EVT solution offers a small phase shift of the gravity waves compared to the other numerical schemes.

The accuracy of the 'EVT' and 'Poisson' solution are quite similar to a second order standard solution, which is in accordance with the definition of the curl and gradient operators in the 'EVT' and 'Poisson' scheme. Although the stencil of the 'EVT' scheme is wide-spread, it does not imply an high local accuracy as it will be the case for a large stencil in the standard schemes. The runtime performance are much worse for the 'EVT' and the 'Poisson' scheme due to the extensive reconstructions inherent in both schemes.

The preliminary study of the Dell City supercell thunderstorm reveals that the 'Poisson' and the 'EVT' scheme resolve the main meteorological processes being observed and simulated for the Dell City storm (Ray et al., 1981; Klemp et al., 1981). The energetic fluxes in the environment of the supercell storm are physically consistent with the temporal changes of the energy inside the supercell storm. In comparison to the second order standard scheme, the 'EVT' and the 'Poisson' schemes tend to resolve a hook-like structure at the RFD region of the right-moving cell for a long time span. A further analysis has to be done to understand the three-dimensional vortex dynamics and forcing at the RFD and hook region for the different numerical schemes. The preliminary result suggests that more amplitude at a certain scale is retained on the resolvable and physical structures using the 'EVT' and the 'Poisson' scheme relative to the second order standard scheme, which would support the findings of Tripoli (1992). Tripoli (1992) argued that the enstrophy-related scheme, which he proposed, reduces the spurious enstrophy and energy cascade down to the smallest resolvable scales.

The best resolution of small-scale features as the hook echo is provided by the simulation using the fifth order standard scheme, because it benefits from its substantially less numerical diffusion compared to the other schemes. However, an examination of the fifth order solution showed that the numerical diffusion is too small to prevent unphysical short-wave structures in the model results. Repeating the fifth order simulation using the same rate of eddy viscosity as for the other schemes results in a solution qualitatively comparable to the 'EVT' and 'Poisson' solutions.

The shortcomings of the 'Poisson' and the 'EVT' scheme with respect to the resolution of the small-scale features are caused by (i) the extensive reconstructions inherent in both schemes and (ii) the Laplacian diffusion used for the simulations. Regarding (i), a loss of spectral variance at the smallest resolvable scales cannot be detected in the 'Poisson' and the 'EVT' solution when comparing with the standard seconder order solution. Regarding (ii), the Laplacian diffusion was explored to be required for a robust 'Poisson' and 'EVT' simulation. The storm simulations with reduced eddy viscosity showed that a spurious energy cascade is not only present in the standard schemes, but is also present in the sophisticated 'Poisson' and the 'EVT' scheme. Both bracket-based schemes do not prevent an energy build-up at the small scale end and unphysical structures in the output fields. The 'Poisson' and the 'EVT' scheme suffer from a spurious source of momentum in the sense of Hollingsworth et al. (1983). Hollingsworth et al. (1983) and Tripoli and Mayor (2000) propose solutions to overcome the Hollingsworth instability. Further investigations are needed in order to qualify the bracket-based schemes for suppressing spurious cascades and energetic transfers. One possible solution is the redefinition of the discretized brackets and the involved functionals (Gassmann, personal communication, 2011). Another improvement for the

'EVT' and 'Poisson' scheme might be achieved by considering not only the spatial but also the temporal discretization (Gassmann and Herzog, 2008).

Pushing forward the numerical schemes introduced here towards the application to a real weather forecast would mean to tune the computationally expensive algorithms, in particular in the case of terrain-following coordinates. Moreover, one has to examine the impact of non-periodic boundaries on bracket-based schemes like 'EVT' and 'Poisson', because they are derived under the condition of vanishing fluxes at the boundaries of the model. Above all, a further understanding of the Nambu brackets and their mathematical properties will be beneficial for numerical schemes derived from the EVT, which is an ongoing project of Hantel (personal communication, 2010).

5 Conclusions and Outlook

5.1 Conclusions

The questions brought up in Section (1.2) of the introduction are discussed.

Are the physical constraints (conservation of mass, energy or Ertels potential vorticity) fulfilled in an atmospheric model although the conserved quantities are not treated as prognostic variables in the model equations?

In order to monitor the conservation properties of a recent NWP model, a diagnostic method was developed in this thesis, which analyzes the weather forecast with respect to specific sub-domains located somewhere in the model domain. The so-called sub-domain budget method (**SDBM**) evaluates whether the temporal evolution of the quantities water mass, energy or total mass inside a sub-domain is physically consistent with the energy- and mass-related fluxes through the boundaries of the sub-domain. The SDBM analyzes not only the conservation properties, but measures also the physical quality of a NWP model with a resolution of one time step. That is in contrast to the common diagnostic approach, which monitor quantities that should be conserved by integrating them over the whole model domain (e. g. the analysis proposed by Bryan and Fritsch, 2002). I depart from the common diagnostic approaches by using the SDBM, because it is considered to be a more sustainable way to get rid of the complexity of the NWP models when adequately monitoring the conservation properties also for realistic weather forecasts. Such models apply a bench of physical parameterizations, discretization schemes, non-physical damping mechanisms and arbitrary boundary conditions.
Applying the SDBM to the COSMO model revealed good conservation properties in case of dry-adiabatic processes. That is an encouraging result because the COSMO model is not formulated in flux form like the METRAS (Schlünzen, 1990; Schlünzen et al., 1996) or the WRF (Skamarock et al., 2005) model, but in advective form. The conservation properties of the model get worse, if simulations are performed that allow for phase transitions, precipitation processes and subgrid-scale turbulence.

What are potential sources in the model causing a violation of the physical constraints? What is the impact on the simulation of the meteorological fields?

Using the SDBM, I examined physical inconsistencies in the model mainly because of three reasons:

- The radiation scheme and the cloud-microphysical schemes including the saturation adjustment do not sufficiently treat diabatic moisture sources and mass redistribution terms. i. e. the schemes do not allow for an adjustment of the atmospheric pressure in those grid cells, where latent heat or sensible heat is released.

- There are potential deficits of the Semi-Lagrangian moisture advection scheme (Staniforth and Cote, 1991) and shortcomings of the Eulerian BOTT advection scheme (Bott, 1989) in steep mountainous terrain.
- The common divergence damping Dudhia (1993) used in a configuration with no Laplacian diffusion deteriorates the robustness of the model.

In order to improve the conservation properties but also the physical quality of the model simulations, I put forward a new saturation adjustment scheme under a fixed volume condition for NWP models, which use the non-hydrostatic compressible equations and a height-based vertical coordinate. In addition, I have proposed a modification for the microphysical and the radiation scheme in such a manner that both schemes account adequately for the diabatic moisture source term and a mass redistribution term in the prognostic equations. The implementation of the new schemes into the COSMO model reduced the error in total mass, energy and water mass and qualified the model to resolve more physical processes on scales of resolved convection.
Typically, the sub-domain budgets are stronger affected by inappropriate physical parameterizations than by artificial damping mechanisms or insufficient numerical discretization scheme. Nevertheless, the commonly used divergence damping may lead to large errors in sub-domain budgets if used without Laplacian diffusion. That result may be relevant for state-of-the-art NWP models, because the recent weather forecasts tend to use model configurations with the diffusion inherent in the upwind-biased advection schemes, but with no Laplacian diffusion. Furthermore, the Semi-Lagrangian moisture advection scheme of the COSMO model (Förstner et al., 2006) causes large positive residua in the water mass budget for strong convective events, in particular for simulations with switched-off Laplacian diffusion. The Eulerian BOTT scheme (Förstner et al., 2006) written in flux form has performed better in case of strong convective events, but it seems to be disadvantageous in mountainous regions due to splitting errors associated with multidimensionality (Skamarock, 2006).

How well are the nonlinear scale interactions resolved in the model?

In order to analyze the nonlinear scale interaction in the COSMO model, I invoke the multi-scale statistics in terms of the Fourier analysis. Having in mind that the high-resolution NWP models perform the simulations on limited areas (1000 km for the high-resolution COSMO model), I explored in this thesis various spectral decomposition methods regarding their capability to handle sufficiently the aperiodicity of the model output fields. My investigations using synthetic fields pointed out that the Discrete Cosine Transform (**DCT**, Denis et al., 2002) offers the best performance in simulating spectra, which are characteristic for the mesoscale, i. e. spectra following a $k^{-5/3}$-law. Making use of the DCT analysis, I evaluated the nonlinear kinetic energy cascade simulated by the COSMO model on observations taken at the COPS field campaign in the summer 2007. In contrast to the investigations of Skamarock (2004), I did not restrict my evaluation to the globally and yearly averaged data of Nastrom et al. (1984) and Lindborg (1999), but I have also accounted for the atmospheric dynamics with respect to a specific region and season. The evaluation of the model spectra on the observed spectra revealed that

- the energy cascade is well resolved by the model on a 'climatological scale', i. e.

the mean simulated spectra over ten forecast days coincides with the observed ones,

- the model is able to adequately represent nonlinear scale interactions down to scales of $\lambda \approx$20 kilometers, i. e. the effective resolution is seven times the nominal resolution of Δx=2.8 km (in accordance with the WRF model, Skamarock, 2004),
- the model is not able to predict adequately the energy cascades with respect to specific synoptic regimes being present during the COPS campaign.

Are there inadequate model formulations or physical parameterizations that have a negative impact on the simulated nonlinear scale interactions?

The model is only capable to sufficiently resolve the nonlinear scale interactions in the mesoscale range down to scales of 20 km, if specific conditions are satisfied:

- If the model is not running in a continuous assimilation cycle, the high-resolution COSMO requires a spin-up time of five hours in order to develop its own mesoscale spectrum based on the coarse resolved analysis of the driving model,
- Only a model configuration using an upwind-biased advection scheme provides the effective resolution of 20 kilometers, because in this configuration the spectral amplitudes at the high wave numbers have been least affected by numerical diffusion (in accordance with (Skamarock, 2004)). The effective resolution get worse for model configurations using Laplacian diffusion. Surprisingly, the kinetic energy spectrum is not affected by the divergence damping.
- The energy cascade is unphysical at the levels located directly below the upper Rayleigh damping zone. These levels may be influenced by vertical propagating gravity waves being reflected from the Rayleigh damping zone back to the lower levels. An application of a radiative upper boundary condition may prevent such reflections (Gassmann and Herzog, 2007).

The application of the SDBM and DCT analysis demonstrated, how relevant this diagnostic methods are in order to tackle deficits in state-of-the-art NWP models. The shortcomings discussed in this thesis are related to the COSMO model, but the physical parameterizations and the numerical schemes are quite similar in the COSMO and other NWP models. Since the SDBM as well as the DCT analysis are model-independent, it is relevant to perform similar evaluations for other NWP models. However, the SDBM and the DCT analysis have some drawbacks when measuring the model performance. First, all physical fluxes relevant for the budget of energy or mass have to be taken into account and extracted from the model by the SDBM algorithm, e. g. all horizontal subgrid-scale turbulent fluxes in case of three-dimensional turbulence parameterization. Second, the SDBM algorithm and the related error estimators and measures are in favor to those model numerics, which use the same kind of discretization for advective processes as the SDBM uses for the calculation of the boundary fluxes through the subdomains. Third, the DCT analysis cannot distinguish for a specific spectral amplitude, which portion belongs to physical and resolvable structures and which portion belongs to a spurious numerical cascade. Therefore, care should be taken in particular for the interpretation of the decay of the model spectrum at the high wave numbers relative to theoretical or observed spectra. Possible conclusions with respect to the effective

resolution and the resolution of the nonlinear scale interaction need to be carefully drawn: the user may manipulate the energy cascade at the smallest resolvable scales to their needs by changing the magnitude of numerical diffusion.

Is it feasible to construct discretization schemes based on Hamiltonian and Nambu tools for three-dimensional non-hydrostatic and compressible models? Do the ideas of Salmon (2004, 2005, 2007) and Sommer and Névir (2009) become practical also for NWP models?

Motivated by the successful application of the Hamiltonian and Nambu tools to two-dimensional models by Salmon (2004, 2005, 2007) and Sommer and Névir (2009), I have investigated in this thesis such tools for the intended use in three-dimensional NWP models. The benefits of a discretization using the Hamiltonian and Nambu tools is that the conservation is guaranteed for the quantities that are involved in a bracket formulation. Another benefit for the NWP models is the implementation of three-dimensional vortex quantities inherently linked to the brackets. Using them on the level of Poisson or Nambu brackets may have a positive impact on the representation of vortices in the model simulation. Moreover, the implementation of the helicity in the framework of the energy-vorticity theory of Névir and Sommer (2009) might be beneficial for models to resolve the evolution and development of convection. Lilly (1986) highlighted the importance of helicity for convective long-lived storms.
I have put forward in this thesis a discretization scheme (**EVT** scheme) for the nonlinear advection term of the momentum equations based on the Nambu form of the non-hydrostatic compressible equations, i. e. the energy-vorticity theory of Névir and Sommer (2009). Taking into account the complexity of the design and discretization schemes in a NWP model, the focus was only on the nonlinear term. However, the nonlinear term is very challenging for NWP models and very important for mesoscale models. The discretization of the nonlinear term revealed that the application of the Nambu tools to three-dimensional models is not straightforward to the same degree as it was demonstrated by Salmon (2005) and Sommer and Névir (2009). The reason for this is that the three-dimensional Arakawa-C / Lorenz grid allows for many degrees of freedom where to define the brackets and the related global quantities mass, helicity and energy. I defined a discrete energy-helicity, which refers to the rotational part of the flow, and the energy-mass bracket, which refers to the gradient of kinetic energy. The first is purely antisymmetric. The second is antisymmetric in an approximated sense, i. e. the antisymmetry is approximated by the differential operators.
The differential operators occurring in the discretized brackets are approximated by finite differences using second order accuracy. My investigations with an idealized gravity-wave test case showed the accuracy of the 'EVT' solution were quite similar to a second order standard solution.
The bracket-based EVT scheme causes a wide-spread three-dimensional stencil originating from a large number of reconstructions on the Arakawa-C/Lorenz grid. This stencil is associated with some drawbacks. First, the EVT scheme is complicate to code and computational expensive. Second, the extensive reconstructions may lead to a smoothing of the meteorological fields. Third, the complex stencils make it difficult to apply vertical implicit schemes.

What is the influence of a discretization using Hamiltonian and Nambu tools on the

meteorological fields and on the nonlinear scale interactions, respectively the energy cascade? Does the schemes allow for reducing the numerical diffusion relative to the standard schemes?

In order to study the numerical discretization of the nonlinear term in terms of a Nambu bracket representation, I have explored the EVT scheme in a preliminary test environment using a strong single cell thunderstorm and extreme wind shear instability. I validated the EVT solution on the standard advection schemes implemented in the COSMO model. In addition to the EVT scheme, I have considered a **Poisson** scheme for the application to the NWP model COSMO. The Poisson scheme is based on the Hamiltonian representation of the nonlinear term of the momentum equations, which refers to two bilinear antisymmetric Poisson brackets. The Poisson scheme was already proposed within the scope of theoretical considerations by Gassmann and Herzog (2008).
The EVT and the Poisson scheme resolve the main meteorological features of the thunderstorm. The Poisson solution produces less rain in the thunderstorm region and a faster propagating right-moving storm compared to the other solutions. In addition, I have explored small differences among the model solutions occurring in the region of the small-scale hook echo associated with the RFD of the thunderstorm: The EVT and the Poisson scheme offer a slightly better resolution than a standard advection scheme using second order accuracy. A further DCT analysis of the kinetic energy spectrum revealed nearly the same characteristics of the spectral variances for the EVT, the Poisson and the second order standard scheme. Furthermore, I have discovered that the extensive reconstructions inherent in the EVT and also in the Poisson scheme does not cause any detrimental damping effects on the smallest resolvable scale.
Nevertheless, the EVT and the Poisson scheme require the same rate of Laplacian diffusion as the standard second order scheme, i. e. a spurious numerical cascade is present also in the sophisticated EVT and Poisson solutions leading to nonlinear computational instability. Thus, the ability of the EVT and Poisson model to simulate a reasonable energy cascade for the smallest resolvable scales was strongly limited. I have demonstrated that the EVT and the Poisson scheme may suffer from a spurious source of momentum in the sense of Hollingsworth et al. (1983). As long as the bracket-based EVT and Poisson schemes are not further improved, the upwind-biased fifth order advection scheme is the reference in NWP models for simulating adequately the nonlinear dynamics over a preferably wide range of the mesoscale. I have found out that the upwind-biased scheme offers the best performance because of its comparatively small inherent diffusion. Anyhow, the thunderstorm experiments revealed that a small amount of eddy viscosity is needed for the upwind-biased schemes to yield physically reasonable and robust model simulations.

Does a discretization using Hamiltonian and Nambu tools have a positive impact on the conservation properties?

Unfortunately, the answer is no. Using the SDBM method, I have demonstrated that the physical parameterizations and not the numerical discretization schemes have the biggest impact on the sub-domain budget in the framework of short-range weather forecasts. From the theoretical point of view, a discretization scheme based on Nambu tools is able to conserve algebraic exactly the conservative quantities involved in the brackets

(Sommer and Névir, 2009; Névir and Sommer, 2009). Instead of a full discretization procedure involving all terms and Nambu brackets related to the compressible non-hydrostatic equations, I considered in the EVT scheme only the nonlinear terms of the momentum equations. An exact conservation is no longer guaranteed for the EVT scheme.

5.2 Outlook

This thesis give important answers, but also raises many questions, which have to be addressed in future research projects. There are mainly three topics, which are worth to study further:

A The impact of the strong violation in mass and energy detected by the SDBM should be further analyzed in operational weather forecasts. An alternative formulation of the cloud-microphysical and the radiation schemes as discussed in Chapter 2 might have a positive impact on the model results. A saturation adjustment approach based on our method is tested and evaluated at the German Weather Service in the framework of a pre-operational version (Ulrich Blahak, personal communication, 2010).

B Further investigations of the turbulence parameterizations shall be done using the SDBM and the DCT analysis. In particular the SDBM enables a deep insight into the most complex model parameterizations, because it is capable to analyze the physical quality of the weather forecast on very small sub-domains with a resolution of one time step. Examining the impact of various turbulence closure concepts and the related turbulent fluxes on the sub-domain budgets may be very important for the water mass and thus the whole hydrological cycle. Since the turbulent parameterizations do not only specify the subgrid-scale fluxes but also control the scale interaction and the energetic transfer between the resolved and the unresolved scales, an investigation of the energy cascades using the DCT analysis may be beneficial to understand the impact of the turbulence parameterizations with respect to mixing processes, in particular in regions with strong convective processes.

C The investigations with respect to the bracket-based EVT and Poisson scheme were more or less preliminary. My analysis refers to the implementation of the schemes and a rough evaluation on standard schemes implemented in a recent NWP model. Further investigations are required and may focus on the quality of the schemes to prevent spurious numerical cascades and the nonlinear instability. An extension of the discretization procedure from the nonlinear term to the pressure gradient term or the complete momentum equations may be beneficial for the bracket-based schemes. Another focus should be on the representation of the three-dimensional vortex quantities involved in the EVT and the Poisson scheme. In particular, for the EVT scheme the question arises to what extent this scheme influences the organization of convection and the nonlinear transfer of energy and helicity in the framework of idealized and realistic runs with multi-cell storms. Such experiments demand to push forward the EVT and Poisson schemes towards

real weather forecasts, which should be done carefully. The bracket based schemes are derived under the condition of vanishing or periodic fluxes at the model boundaries. Above all, a further comprehensive mathematical investigation of the Nambu brackets is indispensable to construct further discretization schemes. This is the ongoing project of Hantel (personal communication, 2010).

Acknowledgements

First of all, I thank the DFG (German Research Foundation) for founding this work. The last months of my work were founded by the MPI. Many thanks to Jochem Marotzke for making this possible.

I want to thank my supervisors K. Heinke Schlünzen and Almut Gassmann. I didn't get around to publish a paper without the professional guiding through K. Heinke Schlünzen. The thesis would not have been finished without the motivation and the scientific advice of Almut Gassmann. Many thanks for their understanding for my personal problems I was faced with during my PHD.

I am grateful to Hans-Joachim Herzog for attending my PHD time with useful advices and critical reading of my manuscripts. Thank you for your help with respect to the report for the DFG. He motivated me very often in situations, where I had almost given up.

I would also like to thank the people at the German Meteorological Service that were open to problems with the COSMO model and gave me some useful advices, in particular Michael Baldauf, Ulrich Schättler and Ulrich Blahak. Without their help, the COSMO and some diagnostic routines would still not run on the parallel computer systems at the DKRZ.

I also thank Janek Zimmer, Marco Rastelli, Florian Rauser, Aiko Voigt, Björn Fock, Malte Uphoff and Hinnerk Ries for the scientific discussions about my topic. I am indebted to Peter Düben, Werner Bauer, Verena Grützun, Kevin Sieck, Almut Gassmann, K. Heinke Schlünzen and Laura Niederdrenk for critical reading my PHD manuscript.

The PHD students at the MPI provided an incredible surrounding to me. I loved the discussions about the really important things of life in the kitchen and elsewhere, the table tennis matches and the social after-work activities. I owe thanks to the people who support me in eaten up my cake and singing with me in the choir:
Aiko Voigt, Alberto Elizalde, Alexander Beitsch, Chao Li, Claas Teichmann, Daniel Hernández Deckers, Daniela Matei, Eleftheria Exarchou, Fanny Adloff, Felix Landerer, Florian Rauser, Freja Vamborg, Verena Grützun, Helge Gößling, Helmuth Haak, Iris Ehlert, Jaison Thomas Ambadan, Jens Kieser, Juliane Otto, Jürgen Kröger, Karl-Hermann Wieners, Kathrin Riemann-Campe, Kay Hübner, Kevin Sieck, Laura Niederdrenk, Malte Heineman, Marco Restelli, Maria Paz Chidichimo, Mario Krapp, Max Popp, Michael Botzet, Nils Fischer, Nina Wilkens, Peter Düben, Peter Korn, Rosina Grimm, Stefan Hagemann, Steffen Tietsche, Stephan Lorenz, Veronika Gayler, Werner Bauer, Wolfgang Müller, Zoltan Szuts.

In particular, I would like to thank Iris Ehlert and Werner Bauer. You are the reason I survived the PHD. I will never forget your help during my stay at the MPI.

The most interesting discussions during my PHD were about synoptical meteorology. I thank to the few people who allow for such discussions at the MPI - Jens Kieser and Alexander Beitsch - and at the Meteorological Institute - Hinnerk Ries, Peter Hoffmann and Kathrin Riemann-Campe.

A big thank goes to my lunch group: Nina Maaß, Steffen Grünler, Antje Tittebrandt, Anne-Christin Anweiler, Sascha Hölig, Manfred Brath and Martin Scharffenberg. Nothing could be more relevant for the human race than our discussion during the lunch time at the mensa and the stays at the Pony bar.

I thank my dear mother, father, brother and sister for their mental support and their help to survive this PHD. Dear mother, I was crying in your arms but you found a way to motivate me again and again.

I address the last words to my family. Dear Bine, thank you for supporting me all the time during my PHD. You were taking care of our two children so often when I was sitting over my thesis in the afternoons and evenings. A lot of weekends you traveled around with the two children to give me the freedom to finish the PHD. Dear Kolya and Paula, your laughing was so important to understand what is really important in my life. I love you all.

A Formulation of the COSMO model

The COSMO model (Doms and Schaettler, 2002; Doms et al., 2007; Steppeler et al., 2003) is a compressible non-hydrostatic NWP model used for operational forecasts on limited domains by several European Meteorological services. High resolution model versions of the COSMO, e. g. the COSMO-DE, run without parameterized deep convection and shall explicitly resolve extreme and small-scale weather phenomena like squall lines, fog and foehn storms.

The model solves the non-hydrostatic primitive equation system that approximates a shallow atmosphere (following the Penn State-NCAR Mesoscale Model MM5, Dudhia, 1993). The prognostic variables are the temperature T, the pressure p, the three-dimensional wind field $\mathbf{v}$ and the partial masses of the water constituents q_x. The thermodynamic variables are separated into base-state variables and deviations from the base state (quantities with a $'$). The base state is assumed to be horizontally homogeneous, dry and at rest. The dynamic equations of the COSMO model are given in Steppeler et al. (2003, eq. (9 - 15)) and are also written down here explicitly:

$$\frac{\partial u}{\partial t} = -\left(\vec{v}\cdot\nabla_\zeta\right)u + \frac{uv}{r}\tan\varphi - \frac{1}{\rho r\cos\varphi}\left(\left.\frac{\partial p'}{\partial\lambda}\right|_\zeta + \frac{J_\lambda}{\sqrt{G}}\frac{\partial p'}{\partial\zeta}\right) + fv + M_u \quad \text{(A.1)}$$

$$\frac{\partial v}{\partial t} = -\left(\vec{v}\cdot\nabla_\zeta\right)v - \frac{u^2}{r}\tan\varphi - \frac{1}{\rho r}\left(\left.\frac{\partial p'}{\partial\varphi}\right|_\zeta + \frac{J_\varphi}{\sqrt{G}}\frac{\partial p'}{\partial\zeta}\right) - fu + M_v \quad \text{(A.2)}$$

$$\frac{\partial w}{\partial t} = -\left(\vec{v}\cdot\nabla_\zeta\right)w + \frac{1}{\rho\sqrt{G}}\frac{\partial p'}{\partial\zeta} + B + M_w \quad \text{(A.3)}$$

$$\frac{\partial p'}{\partial t} = -\left(\vec{v}\cdot\nabla_\zeta\right)p' + g\rho_0 w - \frac{c_{pd}}{c_{vd}}p\nabla_\zeta\cdot\vec{v} \quad \text{(A.4)}$$

$$\frac{\partial T}{\partial t} = -\left(\vec{v}\cdot\nabla_\zeta\right)T - \frac{1}{\rho c_{vd}}\left(p\nabla_\zeta\cdot\vec{v}\right) + \frac{Q_h}{\rho c_{pd}} \quad \text{(A.5)}$$

$$\frac{\partial q_x}{\partial t} = -\mathbf{v}\cdot\nabla q_x + \frac{1}{\rho}\frac{\partial P^x}{\partial z} + S^x + M_{q^x}\,. \quad \text{(A.6)}$$

The approximations used to derive the model equations (A.1)-(A.6) are given in Doms and Schaettler (2002). A short legend to the symbols is given in Table A.1. The model equations are solved on a terrain-following coordinate system with a generalized height-coordinate ζ. The slope of the coordinate surfaces are expressed by the elements $J_\lambda \equiv \partial z/\partial\lambda$, $J_\varphi \equiv \partial z/\partial\varphi$ (for $\zeta = const.$) and $\sqrt{G} \equiv -\partial z/\partial\zeta$. The density ρ is derived from the equation of state

$$\begin{aligned} p &= \rho\left(R_d q_d + R_v q_v\right)T \\ &= \rho R_d\left\{1 + (\frac{R_v}{R_d} - 1)q_v - q_l - q_f\right\}T\,, \end{aligned} \quad \text{(A.7)}$$

Table A.1: Legend to the symbols and definitions used for the model equations.

Symbol	Meaning
r	Earth radius
φ	geographical latitude
ζ	generalized height-coordinate of the terrain-following coordinate system
J_λ, J_φ and $\sqrt{G}$	geometrical elements of the terrain-following coordinates
∇_ζ	three-dimensional Nabla operator with respect to the terrain-following coordinates
ρ	total density of the air mixture
f	Coriolis parameter
M_u, M_v, M_w	source terms due to turbulent mixing of momentum
M_{q^x}	source terms due to turbulent mixing of the water constituents
B	buoyancy term
P^x	precipitation fluxes
S^x	microphysical sources and sinks
c_{pd}	specific heat capacity at constant pressure
c_{vd}	specific heat capacity at constant volume
Q_h	diabatic heat sources originating from turbulent heat fluxes, radiation and cloud mircophysics.

where R_d and R_v denote the gas constants for dry air and water vapor, respectively. The indexes v, l and f stand for the water vapor, the liquid water and the solid water phase.

An overview about the model grid and the numerical discretization is given in Steppeler et al. (2003). We have to note, that the recent dynamical core of the model is discretized using a third order Runge-Kutta scheme (Wicker and Skamarock, 2002) for time integration, which is combined with a time-splitting method to separate between slow processes like advection and fast processes related to fast wave propagation (as in Wicker and Skamarock, 2002). By default, the horizontal part of the advection operator in the model equations (Steppeler et al., 2003, eq. (9 - 15)) is discretized with fifth-order upwind scheme. The vertical part of the advection operator is treated implicitly using a Crank-Nicolson scheme and an accuracy of third order. The accuracy is meant as a formal accuracy, i. e. only the gradient operator is fifth order, respectively third order.

The recent cloud microphysical scheme considers six water components: water vapour, cloud water, cloud ice, rain, snow and 'graupel'. The cloud microphysics are represented by a bulk water-continuity model (Doms et al., 2007, Section 5). The precipitation is treated prognostically in the COSMO model. This allows for drifting the hydrometeors

during their way to the ground (Gassmann, 2002).

For simulations with grid spacing more than 5 km the deep and shallow moist convection is parameterized by the Tiedtke mass flux scheme (Tiedtke, 1989). For model applications on the meso-γ scale with grid spacings less than 5 km the deep moist convection is explicitly resolved.

The turbulent fluxes are subgrid-scale processes and have to be parameterized. A diagnostic level 2 closure (according to Mellor/Yamada) and two different second order closure schemes (level 2.5), which apply the prognostic equation of the turbulent kinetic energy, are implemented in COSMO. A more detailed overview on the model physics is given in Steppeler et al. (2003, section 4) and an extensive description can be found in Doms et al. (2007).

List of Figures

List of Tables

Bibliography

Ahmed, N., T. Natarajan, and K. R. Rao, 1974: Discrete cosine transform. *IEEE Trans. Comput.*, **C-23**, 90–93.

Alexander, G., S. Hoelzl, and F. Schueller, 2009: cops_nmet_ui: meteorological data from automatic weather stations run by university of innsbruck during cops 2007. URL `http://cera-www.dkrz.de/WDCC/ui/Compact.jsp?acronym=cops_nmet_ui`, last access on December 2011, URL `http://cera-www.dkrz.de/WDCC/ui/Compact.jsp?acronym=cops_nmet_ui`, last access on December 2011.

Arakawa, A., 1966: Computational design for long-term numerical integration of the equations of fluid motion: Two-dimensional incompressible flow. part i. *J. Comp. Phys.*, **1**, 119–143.

Arakawa, A. and V. R. Lamb, 1980: A potential enstrophy and energy conserving scheme for the shallow water equations. *Mon. Wea. Rev.*, **109**, 18–37.

Bacmeister, J., S. Eckermann, P. Newman, L. Lait, K. Chan, M. Loewenstein, M. Proffitt, and B. Gary, 1996: Stratospheric horizontal wavenumber spectra of winds, potential temperature, and atmospheric tracers observed by highaltitude aircraft. *J. Geophys. Res.*, **101(D5)**, 9441–9470.

Baldauf, M., 2008: A tool for testing conservation properties in the COSMO-model. COSMO Newsletter No. 7, Deutscher Wetterdienst, 7–17 pp., Offenbach a. M., Germany.

Baldauf, M., et al., 2009: dphase_lmk: Lmk (cosmo-de) high resolution model forecasts run by dwd for the map d-phase project. URL `http://cera-www.dkrz.de/WDCC/ui/Compact.jsp?acronym=dphase_lmk`, last access in December 2011, URL `http://cera-www.dkrz.de/WDCC/ui/Compact.jsp?acronym=dphase_lmk`, last access in December 2011.

Balsley, B. B. and D. A. Carter, 1982: The spectrum of atmospheric velocity fluctuations at 8 km and 86 km. *Geophys. Res. Lett.*, **9**, 465–468.

Bannon, P. R., 2003: Hamiltonian description of idealized binary geophysical fluids. *J. Atmos. Sci.*, **60**, 2809–2819.

Bluestein, H. B., 2000: A tornadic supercell over elevated, complex terrain: The divide, colorado, storm of 12 july 1996. *Monthly Weather Review*, **128 (3)**, 795–809, doi: 10.1175/1520-0493(2000)128⟨0795:ATSOEC⟩2.0.CO;2, URL `http://journals.ametsoc.org/doi/abs/10.1175/1520-0493%282000%29128%3C0795%3AATSOEC%3E2.0.CO%3B2`.

Bluestein, H. B., 2009: The formation and early evolution of the greensburg, kansas, tornadic supercell on 4 may 2007. *Weather and Forecasting*, **24**, 899–920.

Bluestein, H. B. and M. L. Weisman, 2000: The interaction of numerically simulated supercells initiated along lines. *Mon. Wea. Rev.*, **128**, 3128–3149.

Boer, G. J., N. A. McFarlane, R. Laprise, J. D. Henderson, and J.-P. Blanchet, 1984: The canadian climate centre spectral atmospheric general circulation model. *ATMOSPHERE-OCEAN*, **22 (4)**, 430–473.

Boer, G. J. and T. G. Shepherd, 1983: Large-scale two-dimensional turbulence in the atmosphere. *J. Atmos. Sci.*, **40 (1)**, 164–184.

Bott, A., 1989: A positive definite advection scheme obtained by nonlinear renormalization of the advective fluxes. *Mon. Wea. Rev.*, **117**, 1006–1015.

Bryan, G. H. and J. M. Fritsch, 2002: A benchmark simulation for moist nonhydrostatic numerical models. *Mon. Wea. Rev.*, **130**, 2917–2928.

Bryan, G. H. and M. D. Parker, 2010: Observations of a squall line and its near environment using high-frequency rawinsonde launches during vortex2. *Mon. Wea. Rev.*, **138**, 4076–4097.

Bryan, G. H., J. C. Wyngaard, and J. M. Fritsch, 2003: Resolution requirements for the simulation of deep moist convection. *Monthly Weather Review*, **131 (10)**, 2394–2416, doi:10.1175/1520-0493(2003)131⟨2394:RRFTSO⟩2.0.CO;2, URL `http://journals.ametsoc.org/doi/abs/10.1175/1520-0493%282003%29131%3C2394%3ARRFTSO%3E2.0.CO%3B2`.

Catry, B., J.-F. Geleyn, M. Tudor, P. Bénard, and A. Trojákova, 2007: Flux-conservative thermodynamic equations in a mass-weighted framework. *Tellus*, **59A**, 71–79.

de Ela, R., R. Laprise, and B. Denis, 2002: Forecasting skill limits of nested, limited-area models: A perfect-model approach. *Monthly Weather Review*, **130 (8)**, 2006–2023, doi:10.1175/1520-0493(2002)130⟨2006:FSLONL⟩2.0.CO;2, URL `http://journals.ametsoc.org/doi/abs/10.1175/1520-0493%282002%29130%3C2006%3AFSLONL%3E2.0.CO%3B2`.

Denis, B., J. Ct, and R. Laprise, 2002: Spectral decomposition of two-dimensional atmospheric fields on limited-area domains using the discrete cosine transform (dct). *Monthly Weather Review*, **130 (7)**, 1812–1829, doi:10.1175/1520-0493(2002)130⟨1812:SDOTDA⟩2.0.CO;2, URL `http://journals.ametsoc.org/doi/abs/10.1175/1520-0493%282002%29130%3C1812%3ASDOTDA%3E2.0.CO%3B2`.

Desbois, M., 1975: Large-scale kinetic energy spectra from eulerian analysis of eole wind data. *J. Atmos. Sci.*, **32 (9)**, 1838–1847.

Doms, G., 2004: Test of the moisture mass conservation in LM. COSMO Newsletter No. 3, Deutscher Wetterdienst, 179–185 pp., Offenbach a. M., Germany.

Doms, G., J. Foerstner, E. Heise, H.-J. Herzog, M. Raschendorfer, R. Schrodin, T. Reinhardt, and G. Vogel, 2007: A description of the nonhydrostatic Regional Model LM - part II: Physical Parametrization. DWD Documentation, Deutscher Wetterdienst, 140 pp., Offenbach a. M., Germany.

Doms, G. and U. Schaettler, 2002: A description of the nonhydrostatic Regional Model LM - part I: Dynamics and Numerics. DWD Documentation, Deutscher Wetterdienst, 140 pp., Offenbach a. M., Germany.

Done, J., C. A. Davis, and M. Weisman, 2004: The next generation of nwp: explicit forecasts of convection using the weather research and forecasting (wrf) model. *Atmospheric Science Letters*, **5**, 110–117.

Doswell, C. A. and E. N. Rasmussen, 1994: The effect of neglecting the virtual temperature correction on cape calculation. *Wea. Forecasting*, **9**, 625–629.

Dudhia, J., 1993: A nonhydrostatic version of the penn state-ncar mesoscale model: Validation tests and simulation of an atlantic cyclone and cold front. *Mon. Wea. Rev.*, **121**, 1493–1513.

Durran, D. R., 1999: *Numerical Methods for Wave Equations in Geophysical Fluid Dynamics*. 1st ed., Texts in Applied Mathematics, Springer-Verlag, 465 pp.

Ehret, G. and C. Kiemle, 2009: cops_adlr_data: data from falcon research aircraft run by dlr/ipa during cops 2007. URL `http://cera-www.dkrz.de/WDCC/ui/Compact.jsp?acronym=cops_adlr_data`, last access on December 2011, URL `http://cera-www.dkrz.de/WDCC/ui/Compact.jsp?acronym=cops_adlr_data`, last access on December 2011.

Emanuel, K. A., 1994: *Atmospheric Convection*. 1st ed., Oxford University Press, 580 pp.

Errico, R. M., 1985: Spectra computed from a limited area grid. *Mon. Wea. Review*, **113 (9)**, 1554–1562, doi:10.1175/1520-0493(1985)113⟨1554:SCFALA⟩2.0.CO;2, URL `http://journals.ametsoc.org/doi/abs/10.1175/1520-0493%281985%29113%3C1554%3ASCFALA%3E2.0.CO%3B2`.

Etling, D., 1985: Some aspects of helicity in atmospheric flows. *Beitr. Phys. Atmosph.*, **58**, 88–100.

Ferziger, J. H. and M. Peric, 2002: *Computational Methods for Fluid Dynamics*. 3d ed., Motion and Motion Systems, Springer-Verlag, 423 pp.

Förstner, J., M. Baldauf, and A. Seifert, 2006: Courant number independent advection of the moisture quantities for the LMK. COSMO Newsletter No. 6, Deutscher Wetterdienst, 1–14 pp., Offenbach a. M., Germany.

Gage, K. S., 1979: Evidence far a k5/3 law inertial range in mesoscale two-dimensional turbulence. *J. Atmos. Sci.*, **36 (10)**, 1950–1954.

Gassmann, A., 2002: Nummerische Verfahren in der nichthydrostatischen Modellierung und ihr Einfluss auf die Güte der Niederschlagsvorhersage. Ph.D. thesis, University of Bonn, 96 pp.

Gassmann, A. and H.-J. Herzog, 2007: A consistent time-split numerical scheme applied to the nonhydrostatic compressible equations. *Monthly Weather Review*, **135 (1)**, 20–36.

Gassmann, A. and H.-J. Herzog, 2008: Towards a consistent numerical compressible nonhydrostatic model using generalized hamiltonian tools. *Quart. J. Roy. Meteor. Soc.*, **134**, 1597–1613.

Harris, D., E. Foufoula-Georgiou, K. K. Droegemeier, and J. J. Levit, 2001: Multiscale statistical properties of a high-resolution precipitation forecast. *Journal of Hydrometeorology*, **2 (4)**, 406–418, doi:10.1175/1525-7541(2001)002⟨0406:MSPOAH⟩2.0.CO;2, URL `http://journals.ametsoc.org/doi/abs/10.1175/1525-7541%282001%29002%3C0406%3AMSPOAH%3E2.0.CO%3B2`.

Hollingsworth, A., P. Kallberg, V. Renner, and D. M. Burridge, 1983: An internal symmetric computational instability. *Quart. J. R. Meteorol. Soc.*, **109**, 417–428.

Jablonowski, C. and D. L. Williamson, 2006: A baroclinic instability test case for atmospheric model dynamical cores. *Quart. J. Roy. Meteor. Soc.*, **132**, 2943 – 2975.

Janjic, Z., T. Janjic, and R. Vasic, 2011: A class of conservative fourth-order advection schemes and impact of enhanced formal accuracy on extended-range forecasts. *Mon. Wea. Rev.*, **139**, 15561568.

Julian, P. R., W. M. Washington, L. Hembree, and C. Ridley, 1970: On the spectral distribution of large-scale atmospheric kinetic energy. *J. Atmos. Sci.*, **27 (3)**, 376–387.

Kao, S.-K. and H. D. Woods, 1964: Energy spectra of meso-scale turbulence along and across the jet stream. *J. Atmos. Sci.*, **21**, 513 – 519.

Klemp, J. B. and R. B. Wilhelmson, 1978: The simulation of three-dimensional convective storm dynamics. *Journal of the Atmospheric Sciences*, **35 (6)**, 1070–1096, URL http://journals.ametsoc.org/doi/abs/10.1175/1520-0469%281978%29035%3C1070%3ATSOTDC%3E2.0.CO%3B2.

Klemp, J. B., R. B. Wilhelmson, and P. S. Ray, 1981: Observed and numerically simulated structure of a mature supercell thunderstorm. *Journal of the Atmospheric Sciences*, **38 (8)**, 1558–1580, doi:10.1175/1520-0469(1981)038⟨1558:OANSSO⟩2.0.CO;2, URL http://journals.ametsoc.org/doi/abs/10.1175/1520-0469%281981%29038%3C1558%3AOANSSO%3E2.0.CO%3B2.

Kolmogorov, A. N., 1941: Evaluating mesoscale nwp models using kinetic energy spectra. *Monthly Weather Review*, **32 (1)**, 141.

Koshyk, J. N. and K. Hamilton, 2001: The horizontal kinetic energy spectrum and spectral budget simulated by a high-resolution troposphere stratosphere mesosphere gcm. *J. Atmos. Sci.*, **58 (4)**, 329–348.

Kottmeier, C., et al., 2008: Mechanisms initiating deep convection over complex terrain during cops. *Meteorol. Z.*, **17**, 931–948, doi:10.1127/0941-2948/2008/0348.

Kraichnan, R. H., 1967: Inertial ranges in twodimensional turbulence. *Phys. Fluids*, **10 (417)**, 1417–1423.

Lackmann, G. M. and R. M. Yablonsky, 2004: The importance of the precipitation mass sink in tropical cyclones and other heavily precipitating systems. *Journal of the Atmospheric Sciences*, **61 (14)**, 1674–1692, doi:10.1175/1520-0469(2004)061⟨1674:TIOTPM⟩2.0.CO;2, URL http://journals.ametsoc.org/doi/abs/10.1175/1520-0469%282004%29061%3C1674%3ATIOTPM%3E2.0.CO%3B2.

Lafore, J. P., et al., 1998: The meso-nh atmospheric simulation system. part i: adiabatic formulation and control simulations. *Annales Geophysicae*, **16 (1)**, 90–109, doi:10.1007/s00585-997-0090-6, URL http://www.ann-geophys.net/16/90/1998/.

Lange, H.-J., 2002: *Die Physik des Wetters und des Klimas. Ein Grundkurs zur Theorie des Systems Atmosphre*. Reimer, 625 pp.

Laprise, R., et al., 2008: Challenging some tenets of regional climate modelling. *Meteorol. Atmos. Phys.*, **100**, 3–22.

Laursen, L. and E. Eliasen, 1989: On the effect of the damping mechanisms in an atmospheric general circulation model. *Tellus*, **41A**, 385–400.

Lean, H. W. and P. A. Clark, 2003: The effects of changing resolution on mesoscale modelling of line convection and slantwise circulations in fastex iop 16. *Quart. J. Roy. Meteorol. Soc.*, **129**, 2255–2278.

Lilly, D. K., 1983: Stratified turbulence and the mesoscale variability of the atmosphere. *J. Atmos. Sci.*, **40 (3)**, 749–761.

Lilly, D. K., 1986: The structure, energetics and propagation of rotating convective storms. part ii: Helicity and storm stabilization. *J. Atmos. Sci.*, **43**, 126–140.

Lilly, D. K., 1989: Two-dimensional turbulence generated by energy sources at two scales. *J. Atmos. Sci.*, **46 (13)**, 2026–2030.

Lilly, D. K., G. B. Droegemeier, K. Droegemeier, and P. Bartello, 1998: Stratified turbulence in the atmospheric mesoscales. *Theoret. Comput. Fluid Dynamics*, **11**, 139–153.

Lilly, D. K. and E. L. Petersen, 1983: Aircraft measurements of atmospheric kinetic energy spectra. *Tellus*, **35A**, 379–382.

Lindborg, E., 1999: Can the atmospheric kinetic energy spectrum be explained by two-dimensional turbulence? *J. Fluid Mech.*, **388**, 259–288.

Lord, S., H. Willoughby, and J. Piotrowicz, 1984: Role of parameterized ice-phase microphysics in an axisymmetric nonhydrostatic tropical cyclone model. *J. Atmos. Sci.*, **41**, 2836–2848.

Markowski, P. M., 2002: Hook echoes and rear-flank downdrafts: A review. *Monthly Weather Review*, **130 (4)**, 852–876, doi:10.1175/1520-0493(2002)130⟨0852:HEARFD⟩2.0.CO;2, URL `http://journals.ametsoc.org/doi/abs/10.1175/1520-0493%282002%29130%3C0852%3AHEARFD%3E2.0.CO%3B2`.

Mesinger, F. and A. Arakawa, 1976: Numerical methods used in atmospheric models. *GARP Publications Series*, WMO/ICSU, Vol. 1, 71.

Morrison, P. J., 1998: Hamiltonian description of the ideal fluid. *Rev. Mod. Phys.*, **70**, 468–519.

Morrison, P. J. and J. M. Greene, 1980: Noncanonical hamiltonian density formulation of hydrodynamics and ideal magnetohydrodynamics. *Phys. Rev. Lett.*, **45**, 790 – 794.

Nastrom, G. D. and K. S. Gage, 1985: A climatology of atmospheric wavenumber spectra of wind and temperature observed by commercial aircraft. *J. Atmos. Sci.*, **42 (9)**, 950–960, doi:10.1175/1520-0469(1985)042⟨0950:ACOAWS⟩2.0.CO;2, URL `http://journals.ametsoc.org/doi/abs/10.1175/1520-0469%281985%29042%3C0950%3AACOAWS%3E2.0.CO%3B2`.

Nastrom, G. D., K. S. Gage, and W. H. Jasperson, 1984: Kinetic energy spectrum of large-and mesoscale atmospheric processes. *Nature*, **310**, 36–38.

Névir, P., 1998: *Die Nambu-Felddarstellungen der Hydro-Thermodynamik und ihre Bedeutung für die dynamische Meteorologie*. Habilitationsschrift at Freie Universität Berlin, 317 pp.

Névir, P. and R. Blender, 1993: A nambu representation of incompressible hydrodynamics using helicity and enstrophy. *J. Phys. A: Math. Gen.*, **26A**, L1189 – L1193.

Névir, P. and M. Sommer, 2009: Energyvorticity theory of ideal fluid mechanics. *J. Atmos. Sci.*, **66**, 2073–2084.

Ooyama, K. V., 2001: A dynamic and thermodynamic foundation for modeling the moist atmosphere with parameterized microphysics. *Mon. Wea. Rev.*, **58**, 2073–2102.

Petrik, R., M. Baldauf, H. Schlünzen, and A. Gassmann, 2011: Validating of a mesoscale weather prediction model using sub-domain budgets. *Tellus A*, **63 (4)**, 707–726, doi:10.1111/j.1600-0870.2011.00528.x, URL http://dx.doi.org/10.1111/j.1600-0870.2011.00528.x.

Pratt, R. W., 1977: Space-time kinetic energy spectra in mid-latitudes. *J. Atmos. Sci.*, **34 (7)**, 1054–1057.

Raschendorfer, M., 2001: The new turbulence parameterisation of lm. COSMO Newsletter No. 1, Deutscher Wetterdienst, 89–97 pp., Offenbach a. M., Germany.

Ray, P., B. Johnson, K. Johnson, J. Bradberry, J. Stephens, K. Wagner, R. Wilhelmson, and J. Klemp, 1981: The morphology of several tornadic storms on 20 may 1977. *Journal of the Atmospheric Sciences*, **38 (8)**, 1643–1663, doi:10.1175/1520-0469(1981)038⟨1643:TMOSTS⟩2.0.CO;2, URL http://journals.ametsoc.org/doi/abs/10.1175/1520-0469%281981%29038%3C1643%3ATMOSTS%3E2.0.CO%3B2.

Ries, H., K. H. Schlünzen, B. Brümmer, M. Claussen, and G. Müller, 2010: Impact of surface parameter uncertainties on the development of a trough in the fram strait region. *Tellus A*, **62 (4)**, 377–392, doi:10.1111/j.1600-0870.2010.00451.x, URL http://dx.doi.org/10.1111/j.1600-0870.2010.00451.x.

Roberts, N. M. and H. W. Lean, 2008: Scale-selective verification of rainfall accumulations from high-resolution forecasts of convective events. *Monthly Weather Review*, **136 (1)**, 78–97, doi:10.1175/2007MWR2123.1, URL http://journals.ametsoc.org/doi/abs/10.1175/2007MWR2123.1, http://journals.ametsoc.org/doi/pdf/10.1175/2007MWR2123.1.

Rotach, M. W., et al., 2009: Map d-phase: Real-time demonstration of weather forecast quality in the alpine region. *Bulletin of the American Meteorological Society*, **90 (9)**, 1321–1336, doi:10.1175/2009BAMS2776.1, URL http://journals.ametsoc.org/doi/abs/10.1175/2009BAMS2776.1.

Rotunno, R. and J. B. Klemp, 1982: The influence of the shear-induced pressure gradient on thunderstorm motion. *Monthly Weather Review*, **110 (2)**, 136–151, doi:10.1175/1520-0493(1982)110⟨0136:TIOTSI⟩2.0.CO;2, URL http://journals.ametsoc.org/doi/abs/10.1175/1520-0493%281982%29110%3C0136%3ATIOTSI%3E2.0.CO%3B2.

Sadourny, R., 1974: The dynamics of finite-difference models of the shallow-water equations. *J. Atmos. Sci.*, **32**, 680–689.

Saito, K., et al., 2006: The operational jma nonhydrostatic mesoscale model. *Mon. Wea. Rev.*, **134**, 1266–1298.

Salmon, R., 2004: Poisson-bracket approach to the construction of energy- and potential-enstrophy-conserving algorithms for the shallow-water equations. *J. Atmos. Sci.*, **61**, 2016–2036.

Salmon, R., 2005: A general method for conserving quantities related to potential vorticity in numerical models. *Nonlinearity*, **18**, R1–R16.

Salmon, R., 2007: A general method for conserving energy and potential enstrophy in shallow-water models. *J. Atmos. Sci.*, **64**, 515–531.

Salvador, R., , J. Calb, and M. M. Milln, 1999: Horizontal grid size selection and its influence on mesoscale model simulations. *J. Appl. Meteor.*, **38 (9)**, 1311–1329, doi: 10.1175/1520-0450(1999)038⟨1311:HGSSAI⟩2.0.CO;2, URL `http://journals.ametsoc.org/doi/abs/10.1175/1520-0450%281999%29038%3C1311%3AHGSSAI%3E2.0.CO%3B2`.

Satoh, M., 2003: Conservative scheme for a compressible nonhydrostatic model with moist processes. *Mon. Wea. Rev.*, **131**, 1033–1049.

Schlünzen, K. H., 1990: Numerical studies on the inland penetration of sea breeze fronts at a coastline with tidally flooded mudflats. *Contrib. Atmos. Phys.*, **63**, 243–256.

Schlünzen, K. H., 1997: On the validation of high-resolution atmospheric mesoscale models. *J. Wind Eng. Ind. Aerodyn.*, **67-68**, 479–492.

Schlünzen, K. H., K. Bigalke, C. Lüpkes, U. Niemeier, and K. Salzen, 1996: Concept and realization of the mesoscale transport- and fluid-model 'METRAS'. METRAS Techn. Rep 5, Meteorologisches Institut, Universität Hamburg, 156 pp., Universität Hamburg, Germany.

Schröder, G., K. H. Schlünzen, and F. Schimmel, 2006: Use of (weighted) essentially non-oscillatory advection schemes in a mesoscale model. *Quart. J. R. Meteorol. Soc.*, **132**, 1509–1526.

Shepherd, T., 1990: Symmetries, conservation laws, and hamiltonian structure in geophysical fluid dynamics. *Adv. Geophys.*, **32**, 287–338.

Skamarock, W. C., 2004: Evaluating mesoscale nwp models using kinetic energy spectra. *Monthly Weather Review*, **132 (12)**, 3019–3032.

Skamarock, W. C., 2006: Positive-definite and monotonic limiters for unrestricted-time-step transport schemes. *Mon. Wea. Rev.*, **134**, 2241–2250.

Skamarock, W. C. and J. B. Klemp, 1994: Efficiency and accuracy of the klemp-wilhelmson time-splitting technique. *Mon. Wea. Rev.*, **122**, 2623–2630.

Skamarock, W. C., J. B. Klemp, J. Dudhia, D. O. Gill, D. M. Barker, W. Wang, and J. G. Powers, 2005: A description of the Advanced Research WRF version 2. NCAR Tech. Note, Mesoscale and Microscale Meteorology Devision NCAR, 100 pp., Boulder, Colorado, USA.

Skok, G., J. Tribbia, and J. Rakovec, 2010: Object-based analysis and verification of WRF model precipitation in the low- and midlatitude Pacific Ocean. *Monthly Weather Review*, **138 (12)**, 4561–4575, doi:10.1175/2010MWR3472.1, URL `http://journals.ametsoc.org/doi/abs/10.1175/2010MWR3472.1`, `http://journals.ametsoc.org/doi/pdf/10.1175/2010MWR3472.1`.

Sommer, M. and P. Névir, 2009: A conservative scheme for the shallow-water system on a staggered geodesic grid based on a nambu representation. *Q. J. R. Meteorol. Soc.*, **135**, 485–494.

Staniforth, A. and J. Cote, 1991: Semi-lagrangian integration schemes for atmospheric model - a review. *J. Geophys. Res..*, **119**, 2206–2223.

Stephan, K., S. Klink, and C. Schraff, 2008: Assimilation of radar-derived rain rates into the convective-scale model cosmo-de at dwd. *Quart. J. Roy. Meteor. Soc.*, **134**, 1315–1326.

Steppeler, J., G. Doms, U. Schättler, H. W. Bitzer, A. Gassmann, U. Damrath, and G. Gregoric, 2003: Meso-gamma scale forecasts using the nonhydrostatic model LM. *Meteor. Atmos. Phys.*, **82**, 75–96.

Stull, R. B., 1988: *An Introduction to Boundary Layer Meteorology*. Springer Netherlands, 295–329 pp.

Tiedtke, M., 1989: A comprehensive mass flux scheme for cumulus parameterization in large scale models. *Mon. Wea. Rev.*, **117**, 1779–1799.

Tripoli, G. J., 1992: A non-hydrostatic mesoscale model designed to simulate scale interaction. *Mon. Weather Rev.*, **120**, 1342–1359.

Tripoli, G. J. and S. D. Mayor, 2000: Numerical simulation of the neutral boundary layer: A comparison of enstrophy conserving with momentum conserving finite difference schemes. *Proceedings of 14th Symposium on boundary layers and turbulence, 711 Aug, Aspen, CO.*, 376–379, URL `http://lidar.ssec.wisc.edu/papers/conferences/ekman_blt2000.pdf`, last access in December 2011.

Vallis, G. K., G. J. Shutts, and M. E. B. Gray, 1996: Balanced mesoscale motion and stratified turbulence forced by convection. *Quart. J. Roy. Meteor. Soc.*, **123**, 1621–1652.

VanZandt, T. E., 1982: A universal spectrum of buoyancy waves in the atmosphere. *Geophys. Res. Lett.*, **9 (5)**, 575–578.

Vinnichenko, N. K., 1970: The kinetic energy spectrum in the free atmosphere - 1 second to 5 years. *Tellus*, **22A**, 158–166.

Wacker, U., T. Frisius, and F. Herbert, 2006: Evaporation and precipitation surface effects in local mass continuity laws of moist air. *J. Atmos. Sci.*, **63**, 2642–2652.

Wacker, U. and F. Herbert, 2003: Continuity equations as expressions for local balances of masses in cloudy air. *Tellus*, **55**, 247–254.

Weinstock, J. D., 1978: On the theory of turbulence in the buoyancy subrange of stably stratified flows. *J. Atmos. Sci.*, **35**, 634–649.

Weisman, M. L. and J. B. Klemp, 1982: The dependence of numerically simulated convective storms on vertical wind shear and buoyancy. *Mon. Wea. Rev.*, **110**, 504–520.

Weisman, M. L., J. B. Klemp, and R. Rotunno, 1988: Structure and evolution of numerically simulated squall lines. *Journal of the Atmospheric Sciences*, **45 (14)**, 1990–2013, doi: 10.1175/1520-0469(1988)045⟨1990:SAEONS⟩2.0.CO;2, URL `http://journals.ametsoc.org/doi/abs/10.1175/1520-0469%281988%29045%3C1990%3ASAEONS%3E2.0.CO%3B2`.

Weisman, M. L., W. C. Skamarock, and J. B. Klemp, 1997: The resolution dependence of explicitly modeled convective systems. *Mon. Wea. Rev.*, **125**, 527–548.

Wernli, H., C. Hofmann, and M. Zimmer, 2009: Spatial forecast verification methods intercomparison project: Application of the sal technique. *Weather and Forecasting*, **24 (6)**, 1472–1484, doi:10.1175/2009WAF2222271.1, URL http://journals.ametsoc.org/doi/abs/10.1175/2009WAF2222271.1.

Wicker, L. J. and W. C. Skamarock, 2002: Time-splitting methods for elastic models using forward time schemes. *Mon. Wea. Rev.*, **130**, 2088–2097.

Wilhelmson, R. B. and J. B. Klemp, 1978: A numerical study of storm splitting that leads to long-lived storms. *Journal of the Atmospheric Sciences*, **35 (10)**, 1974–1986, doi:10.1175/1520-0469(1978)035⟨1974:ANSOSS⟩2.0.CO;2, URL http://journals.ametsoc.org/doi/abs/10.1175/1520-0469%281978%29035%3C1974%3AANSOSS%3E2.0.CO%3B2.

Wulfmeyer, V., et al., 2008: Research campaign: The convective and orographically induced precipitation study. *Bulletin of the American Meteorological Society*, **89 (10)**, 1477–1486, doi:10.1175/2008BAMS2367.1, URL http://journals.ametsoc.org/doi/abs/10.1175/2008BAMS2367.1.

Xue, M., K. K. Droegemeier, and V. Wong, 2000: ARPS - a multiscale nonhydrostatic atmospheric simulation and prediction tool. part I : Model dynamics and verification. *Meteor. Atmos. Physics.*, **75**, 161–193.

Yuan and Hamilton, 1994: Equilibrium dynamics in a forced-dissipative f-plane shallow-water system. *J. Fluid. Mech.*, **280**, 369–394.

Zhemin, T. and W. Rongsheng, 1994: Helicity dynamics of atmospheric flow. *Advances in Atmospheric Sciences*, **11**, 175–188.



ISSN 1614-1199